Nanophotonic integration and engineering of defect qubits in diamond

Srivatsa Chakravarthi

A dissertation
submitted in partial fulfillment of the
requirements for the degree of

Doctor of Philosophy

University of Washington

2022

Reading Committee:

Kai-Mei Fu, Chair

Arka Majumdar

Mo Li

Program Authorized to Offer Degree:
Department of Electrical and Computer Engineering

©Copyright 2022
Srivatsa Chakravarthi

University of Washington

Abstract

Nanophotonic integration and engineering of defect qubits in diamond

Srivatsa Chakravarthi

Chair of the Supervisory Committee:
Kai-Mei Fu
Department of Electrical and Computer Engineering

Solid-state defect qubits are emerging as a promising candidate for quantum information processing. A fundamental resource for quantum information is entanglement between distant qubit nodes. Several quantum platforms have demonstrated entanglement generation between two physically separated qubits. However, a scalable platform to efficiently entangle multiple qubits remains elusive. Optically addressable defect qubits in diamond such as the nitrogen-vacancy (NV) and the silicon-vacancy (SiV) centers serve as the foundation of this thesis. The crucial components of optically interfaced defect qubit platforms are high-fidelity initialization, manipulation and readout of the qubit spin state accomplished using photoluminescence on an optical cycling transition. Here, we demonstrate significant steps towards realizing these components with a gallium phosphide (GaP) on diamond hybrid photonic platform. Utilizing individual defect qubits created by targeted defect formation process, experimental results on various defect-photonic coupling geometries are presented. Enhanced photon collection efficiency is measured for implanted NV centers coupled to disk-resonators and inverse-designed photon extraction devices. One of the main challenges encountered with coupled NV devices is the significant spectral instability. By performing large-scale automated resonant spectroscopy on the implanted NV centers, we determine that defect-surface interactions are the dominant source of the observed spectral instability. This leads us to consider the SiV center in diamond, which exhibits inherent protection from electric field fluctuations arising by its inversion symmetry within the diamond lattice. We demonstrate coupling of SiV centers to 1-D photonic crystal cavities (PhC) fabricated in GaP. To avoid perturbation of the

diamond surface, we fabricate the PhCs on a separate chip and integrate with SiV centers in diamond by a stamp-transfer technique. Ancillary components for a single chip architecture such as single photon detectors, coherent frequency-conversion and passive photonics utilizing GaP are also demonstrated. These results establish GaP-on-diamond as a suitable platform for efficiently interfacing defects qubits with nanophotonic devices for scalable entanglement generation.

NANOPHOTONIC INTEGRATION AND ENGINEERING OF DEFECT QUBITS IN DIAMOND

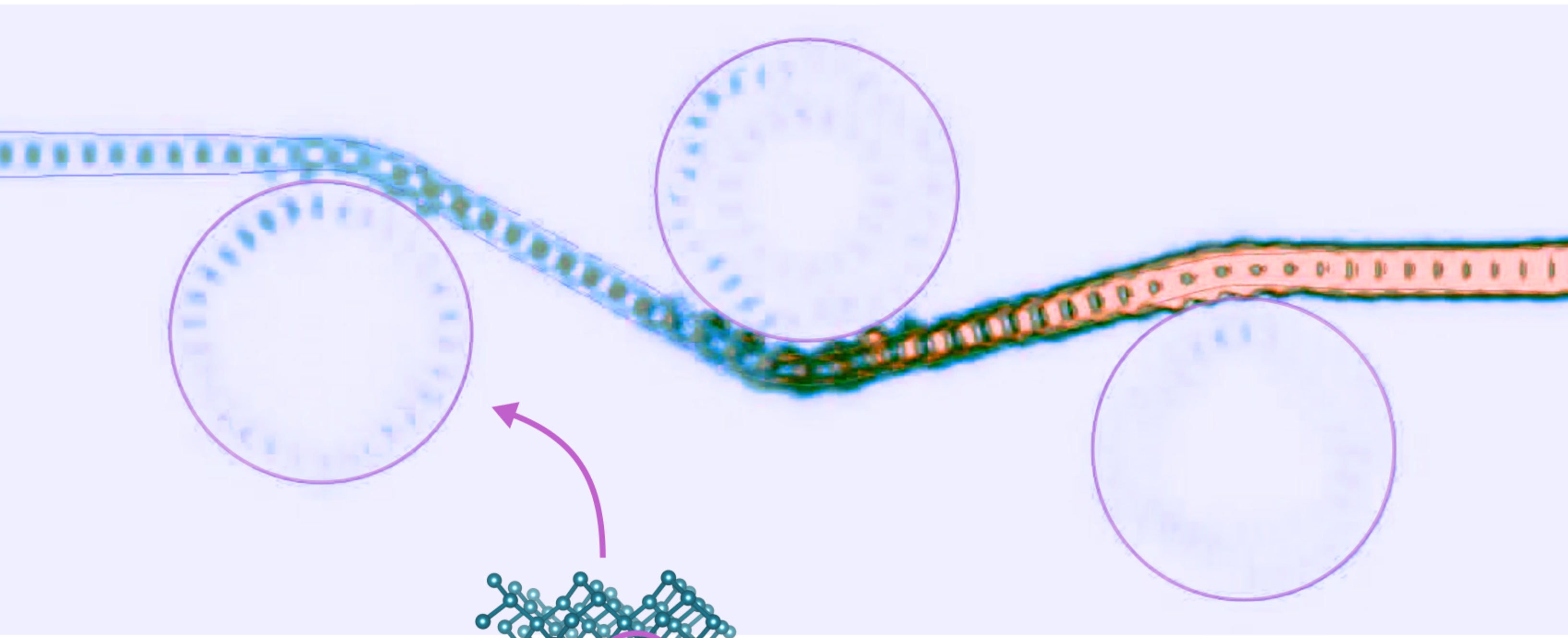

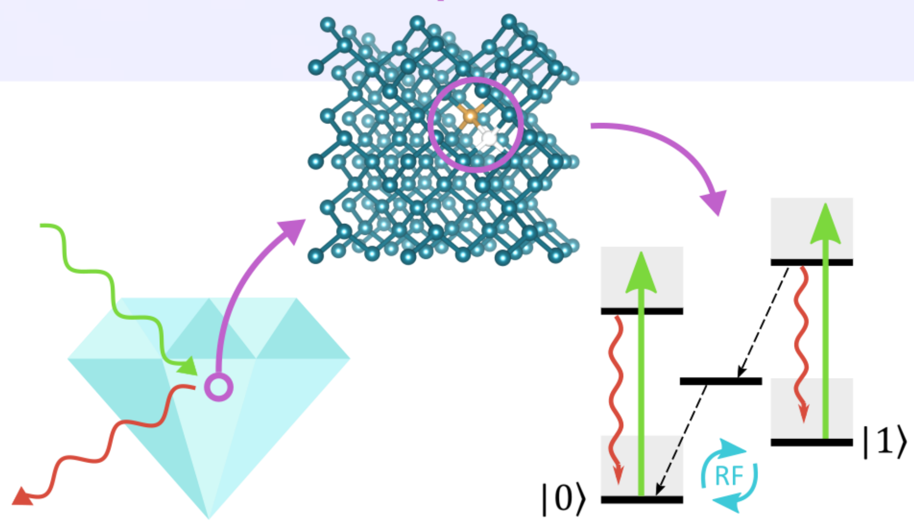

SRIVATSA CHAKRAVARTHI

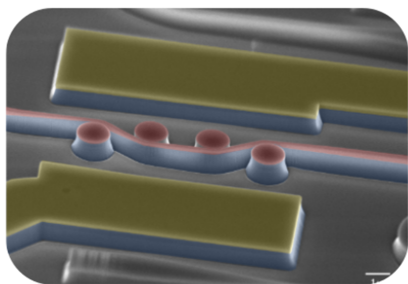

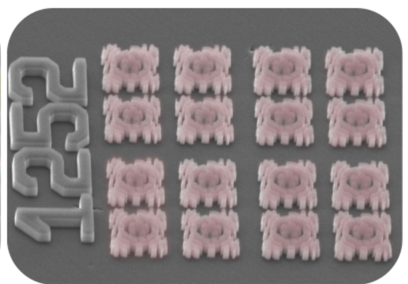

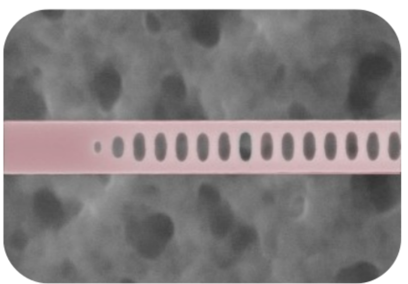

TABLE OF CONTENTS

Page

List of Figures . . . v

List of Tables . . . xv

Chapter 1: Introduction . . . 1
- 1.1 Background . . . 1
- 1.2 Overview of this thesis . . . 4

Chapter 2: Theory . . . 7
- 2.1 Solid-state qubits in diamond . . . 7
  - 2.1.1 Diamond host material . . . 7
  - 2.1.2 The NV center in diamond . . . 7
  - 2.1.3 The SiV center in diamond . . . 11
- 2.2 Photon-mediated entanglement protocol . . . 13
- 2.3 Gallium phosphide for hybrid nanophotonics . . . 15

Chapter 3: Integration of NV centers with GaP disk resonators and dynamic stabilization 18
- 3.1 Introduction . . . 19
- 3.2 Hybrid GaP-on-diamond photonic resonators . . . 19
  - 3.2.1 Fabrication process and device yield . . . 19
  - 3.2.2 Characterization of cavity-coupled NV centers . . . 23
- 3.3 Spectral behavior of cavity-coupled NV centers and stark tuning . . . 23
- 3.4 Dynamic feedback stabilization of NV transitions . . . 25
  - 3.4.1 Voltage Feedback Algorithm . . . 27
  - 3.4.2 Stabilization results . . . 27
- 3.5 Summary and outlook . . . 28

Chapter 4: Formation of NV centers by annealing . . . 31
- 4.1 Introduction . . . 32
- 4.2 Confocal photoluminescence maps of NV centers . . . 32

4.2.1 Optical measurement setup . . . 33
4.2.2 Data analysis techniques . . . 34
4.3 Study of NV annealing dynamics . . . 37
4.3.1 Appearances of NV centers . . . 38
4.3.2 Disappearances of NV centers . . . 40
4.3.3 Orientation changes of NV centers . . . 43
4.4 Summary and outlook . . . 45

Chapter 5: Inverse-designed GaP photon extractors integrated with NV centers . . . 46
5.1 Introduction . . . 47
5.2 GaP photon extractors on diamond . . . 47
5.2.1 Inverse design and device optimization . . . 47
5.2.2 Fabrication of photon extractors . . . 48
5.3 Enhanced collection efficiency of NV photoluminescence . . . 51
5.3.1 Analysis of photon-autocorrelation measurements . . . 53
5.4 Charge-state and spectra stability of device-coupled NV centers . . . 56
5.4.1 Oxygen surface termination of devices . . . 58
5.5 Summary and outlook . . . 60

Chapter 6: Investigation of spectral stability of implanted NV centers in diamond . . . 61
6.1 Introduction . . . 62
6.2 Experimental details . . . 63
6.2.1 Samples . . . 63
6.2.2 Measurements . . . 65
6.3 Correlated ODMR and PLE spectroscopy . . . 67
6.4 Automated spectroscopy . . . 71
6.5 Summary and outlook . . . 73

Chapter 7: SiV centers coupled to GaP 1-D photonic crystal resonators . . . 75
7.1 Introduction . . . 76
7.2 1-D PhC design and fabrication . . . 76
7.2.1 Fabrication of 1-D PhC devices . . . 79
7.2.2 Stamp transfer on diamond . . . 80
7.3 Characterization of BGaP . . . 81
7.3.1 Photonic add-drop test chips . . . 82
7.3.2 Comparison of BGaP and Fariba GaP material . . . 87

7.4 Pre-transfer PhC measurements . . . 88
7.4.1 Suspended BGaP PhC devices . . . 88
7.4.2 Fariba GaP-on-oxide PhC devices . . . 90
7.4.3 Tuning PhC devices by thinning GaP layer . . . 90
7.5 Stamp transferred PhCs coupled to SiV centers in diamond . . . 93
7.5.1 Post-transfer PhC transmission measurements . . . 93
7.5.2 PhC cavity coupling to SiV centers . . . 93
7.6 Summary and outlook . . . 95

Chapter 8: Progress towards on-chip entanglement circuits . . . 97
8.1 (1)-Coherent spin-photon interface . . . 98
8.1.1 On-chip Hong-Ou-Mandel experiment . . . 98
8.1.2 Diamond surface passivation techniques . . . 99
8.1.3 On-chip acousto-optic frequency shifters . . . 99
8.2 (2)-Waveguide integrated on-chip superconducting single photon detectors . . . 100
8.3 (3)-Passive photonic components . . . 102
8.4 (4)-GaP ring resonators for on-chip frequency conversion . . . 103
8.5 Conclusion . . . 106

Appendix A: E-beam lithography . . . 107
A.1 E-beam system overview . . . 107
A.2 Beamer pattern processing . . . 109
A.3 Pre e-beam checklist . . . 115
A.4 Spin coating resist . . . 116
A.5 E-beam operation . . . 118
A.6 Post e-beam write . . . 121
A.7 Sample position on stage . . . 122
A.8 Using a carrier chip . . . 125
A.9 Advanced fracturing and exposure strategies . . . 126
A.10 More resources . . . 127

Appendix B: BGaP-on-Silicon device fabrication . . . 128
B.1 Material preparation . . . 128
B.2 Pattering with e-beam . . . 129
B.3 BGaP photonics etch and device release . . . 129

Appendix C: Fariba-GaP wet transfer and device fabrication 133
C.1 Material preparation 133
C.2 Patterning membranes 133
C.3 Membrane transfer 134
C.4 GaP photonics process 136

Appendix D: Reactive-ion-etching plasma processing 138
D.1 GaP photonics etch 138
D.2 Diamond implantation etch 140
D.3 Diamond photonics etch 142

Appendix E: AQM-HSQ processing 145
E.1 Preparing 6% solution of AQM-HSQ 145
E.2 Patterning with AQM-HSQ 146

Appendix F: Annealing diamond samples 147
F.1 Sample preparation 147
F.2 Vacuum high temperature annealing 148
F.3 Oxygen annealing 150
F.4 Additional notes 151

Appendix G: Miscellaneous process notes 152
G.1 E-beam charge dissipation layer 152

Bibliography 154

LIST OF FIGURES

Figure Number Page

2.1 **a.** The four orientations of an NV center in the diamond lattice. The two sets of optically distinguishable orientations for a <100> diamond sample are indicated by magenta and green. **b.** The electronic structure of the NV^- center within the band gap of diamond. A simplified excited state structure is shown. **c.** Room temperature PL spectra of an ensemble of NV centers under off-resonant excitation. The NV^0 and NV^- ZPLs are shown along with the large phonon side bands. The sharp line at 573 nm is the first order diamond Raman line due to the 532 nm excitation. 9

2.2 **a.** Illustration of total internal reflection limiting NV PL collection into free space. **b.** (adapted from Ref.[33]) The behavior of NV^- excited state structure as a function of the local transverse strain. This behavior is analogous to variation in transverse electric field, and is the primary cause of spectral diffusion. **b.1.** At high strain, the excited state manifold splits into two triplets. The allowed optical-transitions are shown as red arrows. **b.2.** Level-crossings in the lower branch (E_y) can enable spin-flip transitions. **c.** Low temperature (8 K) spectra under off-resonant excitation of a single implanted NV in a high strain environment exhibiting a 48 GHz E_x-E_y splitting. Inset: the E_x, E_y transitions show near-orthogonal excitation polarization dependence. 10

2.3 **a.** The structure of the SiV center in the diamond lattice. **b.** Energy level structure of the SiV center. Adapted from R. Evans et al.[53] **c.** SiV photoluminescence spectra showing the four transitions and their polarization dependence. Adapted from C. Hepp et al.[35]. 11

2.4 **a**. Simplified NV electronic structure for discussion of the remote entangle protocol. **b**. A four step approach for remote entanglement generation. 14

2.5 An illustration of the GaP membrane transfer process. The typical sacrificial AlGaP thickness is 300 nm and GaP membrane thickness is 125 to 250 nm (defined by the photonic design requirements). The membrane etch-via are defined by optical lithography and GaP plasma etching. 16

3.1 Illustration of the process flow involved in the fabrication of the NV-photonic integrated devices. The grey, pink and yellow represent diamond, GaP and gold layers respectively. Details of the fabrication process are provided in Appendix A.1-4 . . . 20

3.2 **a.** A schematic of the measurement configuration. The NVs coupled to either disk cavities or waveguides are excited by off-resonant 532 nm laser and the NV ZPL emission is collected at the output grating. **b.** Scanning electron micrograph (SEM) image of the fabricated devices. Inset: false color SEM image showing the diamond, GaP and gold (grey, pink, yellow) layers. **c.** By deposition of Xe gas (purple) on the disk cavities, the cavity resonance can be red-shifted. **d.** Left: Xe gas tuning of a disk resonator. The cavity mode is indicated by a dashed white line. The laser excitation spot is moved slightly between the two measurements at $t \sim 28$ minutes, resulting in the appearance of a second coupled NV center. At 50 minutes, the Xe gas flow is restored and the cavity tuned from resonance. Right: Stark tuning of the two coupled emission lines with the application of a square wave bias. 22

3.3 **a.** Linewidth of N= 15 device-coupled implanted NV centers (blue bars). Red line shows a normal distribution of mean 34.7 GHz, standard deviation 7.4 GHz. **b.** Tuning range of N= 30 device-coupled implanted NV centers. 24

3.4 **a.** Optical characterization of waveguide coupled NVs. **b.** The distribution of electric field intensity across the photonic devices for a 100V bias across the electrodes.**c.** Spectral trace of multiple waveguide coupled NVs showing variation in ZPL emission energy and bias response over time. **d.** Dynamic frequency stabilization of ZPL emission from an individual waveguide coupled NV by applying a PID-feedback biasing voltage. (a) PL from an unstabilized ZPL at a constant 45 V bias voltage. The maximum spectral diffusion is 7.2 GHz and the average absolute difference from the center wavelength is 2.7 GHz. (b) Stabilized ZPL PL from a waveguide-coupled NV center. The maximum spectral diffusion is 3.9 GHz and the average absolute difference from the center wavelength is 1.2 GHz. (c) Bias voltage applied during active Stark effect stabilization of the ZPL in (b). NV PL is collected at the excitation spot due to the temporal drift of the cavity resonance over the time required for these measurements. 26

3.5 NV frequency stabilization using proportional feedback. **a.** PL from an unstabilized ZPL at a constant 45 V bias voltage. The maximum spectral diffusion is 8.3 GHz and the average absolute difference from the center wavelength is 3.2 GHz. **b.** Stabilized ZPL PL from a waveguide-coupled NV center. The maximum spectral diffusion is 4.5 GHz and the average absolute difference from the center wavelength is 1.3 GHz. **c.** Bias voltage applied during active Stark effect stabilization of the ZPL in **b.**. Feedback is purely proportional to the error in peak position i.e. K_p=0.8, K_i= K_d=0. 28

3.6 PLE measurements of an individual implanted NV center (100 nm deep) at low temperature (8 K) exhibiting a ZPL linewidth of ∼200 MHz **a.** Intrinsic temporal variation in the ZPL emission frequency without any applied bias. **b.** Reduced temporal variation in the ZPL emission frequency with dynamic Stark tuning. 29

4.1 Schematic of the microscope setup for off-resonant excitation and NV photoluminescence measurement. The diamond sample is at room temperature (298K). 33

4.2 A single (50 µm × 50 µm) area scan data showing the increase in NV^- density from initial (no-anneals) state to post anneal #12 (maximum NV^- density) in the same region. The blue circles mark NVs retained through the anneals. The red square marks a persistent defect used for image registration. 34

4.3 (a) 350 µm × 350 µm stitched large-area scan after anneal #12 showing the MST graph. (b) A 50 µm × 50 µm scan showing NV^- position detection via CHT algorithm. 35

4.4 A sequence of subareas of the "large-area scan" confocal images showing NV^- changes. Green and magenta indicate the two sets of distinguishable NV^- orientations. Two examples each of appearances, disappearances and re-orientations are indicated by blue, grey and yellow circles, respectively. The red square marks a persistent defect used for image alignment. 38

4.5 Total NV^- density and observed changes obtained from the stitched confocal scans ($\approx 350 \times 350$ µm^2) after every anneal. Several anneals are combined due to an inability to accurately match a significant portion of the scan area in the intermediate scans. For combined anneals, comparisons are made before and after the first and last anneal. Error bars represent uncertainty due to automation errors and differences in scan area between datasets. Note the significant increase in annealing time which occurs at anneal 11. 40

4.6 (a,b) Confocal scan and spectra of 3 NVs in sample B taken with 450 nm excitation. (c,d) Confocal scan and spectra of same 3 NVs in sample B taken with 532 nm excitation. (e,f) Confocal scan and spectra of NV^0 from a reference sample taken with 532 nm excitation. 42

4.7 Log of the reorientation rate as a function of $\beta = (k_B T)^{-1}$ 44

5.1 **a.** Schematic of the photon extractor designed via topology optimization (TO). **b.** SEM image of an array of fabricated inverse design extractor structures.**c.** Colorized SEM of a device indicating the different layers; HSQ resist (blue), GaP (pink) and diamond (grey). The structure has an estimated $Q \approx 50$. 48

5.2 Change in collection flux enhancement for x/z polarized dipoles shifting from inverse design position. Coordinate origin is at the center of the bottom face of the device, inverse design position situated at $(0, 0, -100)$ nm. Enhancement factors are normalized to that at the inverse design position; dashed lines indicate contour where enhancement is 50% of that at inverse design position. There is an increase in enhancement factor as the dipole shifts closer to the surface. 49

5.3 **a.** Illustration of fabrication process. The key idea here is to avoid plasma etching of the diamond substrate. **b.** Design of the photon extractor. **c.** Top down SEM image of the photon extractor pattern (before GaP plasma etch) with annotated measurements (Sample B). **d.** SEM image of the photon extractors (after the GaP plasma etch) with annotated layer thicknesses and sidewall angle (Sample B). 50

5.4 **a.** Illustration of full microscope setup. **b.** Confocal image of NV PL from an implanted square outside the grid of photonics devices on sample B. **c.** Confocal image of PL from a grid of photonics devices on sample B. 51

5.5 **a.** Implanted NV centers coupled to grating devices are excited with off-resonant 532 nm (resonant 637nm) laser source and the ZPL at 637 nm (PSB emission from 650 to 800 nm) is collected for photon-antibunching (PLE) studies. **b.** Comparison of simulated (grey) and measured (blue) broadband enhancement for inverse extractor devices coupled to NV ensemble (Sample A). The red line indicates the average simulated spectrum and the red envelope is one standard deviation around the average. Variation in individual spectra for both simulation and measurement stems from randomness of NV positions relative to any given device on top of the ensemble sample. **c.** Spectra showing broadband NV PL enhancement for NV ensemble (Sample A) **d.** Spectra comparing ZPL emission of device-coupled and a non-device (bare) single NV (Sample B). **e.** Saturation counts from devices coupled to single NVs. Inset: Histogram of measured devices and the observed ZPL enhancement (Sample B). **f.** $g^2(\tau)$ measurement of device coupled to single NV under 532 nm 300 µW excitation (Sample B). 52

5.6 **a.** Energy levels and transitions of the NV^- and NV^0 charge states utilized for modelling the $g^{(2)}(\tau)$ data. **b.** $g^{(2)}(\tau)$ for 120 µW non-resonant excitation. **c.** $g^{(2)}(\tau)$ for 300 µW off-resonant excitation. **d.** $g^{(2)}(\tau)$ for 600 µW non-resonant excitation. Note the increase in bunching peaks with increase in excitation intensity. 54

5.7 (Sample B, T=8 K) **a.** The ratio of ZPL intensities of NV^- (637 nm) and NV^0 (575 nm) charge states for device-coupled and non-device NVs as a function of the 532 nm excitation intensity. **b.** The distribution of ZPL wavelength for device-coupled and non-device NVs. **c.** The distribution of observed average PLE linewidth for non-device NVs. **d.** PLE characterization of NVs; (d.i) Grown-in deep NV avg. linewidth = 44 MHz, (d.ii) Implanted NV pre-fabrication avg. linewidth = 66 MHz, (d.iii) Implanted NV post-fabrication after oxygen annealing avg. linewidth = 59 MHz, (d.iv) Device-coupled NV (device 3) post oxygen annealing avg. linewidth = 844 MHz. The green markers indicate 532 nm repump pulses that re-initialize the NV into the NV^- charge state. 57

5.8 **a.** Sample A NV PL spectra before and after oxygen annealing. **b.** Sample B device-coupled NV ZPL (device 1, shown in Fig.2 main text and SI.5) before and after oxygen annealing. 59

6.1 Diamond surface preparation and simulations of implantation conditions: **a.** Morphology of the diamond surface measured by atomic force microscopy. The RMS surface roughness for sample A (B) was measured to be 0.63 (0.43) nm before implantation and 0.56 (0.30) nm after implantation and annealing. **b.** A simulation of the implantation profile obtained by SRIM for sample A (red, 7°) and sample B (blue, 85°) showing the damage trails and final positions of implanted ^{15}N atoms. The green circle represents our excitation laser spot. Note that the implantation yield is low (<5%), hence within an excitation spot there is a small probability each trail results in a NV center upon annealing. **Inset i.** Illustration of the implantation geometry. **Inset ii.** A cross-section of the simulation showing the ion damage trails for the two implant angles. Total vacancies generated per ion is similar for both the implant angles. However on sample B, some ^{15}N atoms are lost due to ion scatter out of the surface. 64

6.2 Correlated NV ODMR (RT) and PLE (T<12K) measurements on sample A: **a.** Pulsed ODMR scheme utilized to identify the N isotope. Laser and radio-frequency (RF) pulses are generated by an acousto-optical-modulator and RF switch, respectively. (Laser power 0.8-1.0 mW, spot diameter ∼800 nm.) Pulses and photon collection are triggered by a programmable pulse generator. **b.** Confocal PL map of the implanted region with the measured NV centers indicated by their isotope (green ^{15}N, red ^{14}N). **c.** ODMR spectra for the marked NV incorporating implanted ^{15}N. **d.** ODMR spectra for the marked NV incorporating grown-in ^{14}N. **e.** Resonant excitation (PLE) scheme utilized for characterizing the optical coherence of the marked NV centers. Sidebands at 2.9 GHz are added (using an electro-optic modulator) to the scanning resonant laser to counteract optical spin pumping. Upon detection of an NV^- to NV^0 ionization event (indicated by lack of NV^- PL) a 50 ms off-resonant green re-pump is used to reset the NV charge state. **f.** Time traces of PLE scans measured at 10.5 K for three NV centers. Off-resonant re-pump between scans are indicated by green squares along the right column, this induces large spectral jumps in many ^{15}NV centers (e.g. NV 1). The '\\' markers along the scan axis indicate discarded scans where no NV PL is observed. The PLE traces for ^{15}NV centers typically show long periods of spectral stability between re-pump pulses. 66

6.3 Photoluminescence excitation characteristics of measured NV centers on samples A and B: **a.** The fitted Lorentzian FWHM distributions for each observed NV. The color box and black marker represent the interquartile range and median linewidth respectively. The total number of scans and measurement duration comprising each distribution is recorded in the accompanying table. The PLE traces for NV centers 1 to 3 are also shown in Fig. 6.2f. **b.** The distributions of the scan-to-scan change in the center frequency of the fits, representing spectral variation. Off-resonant re-pump pulses are only applied when NV ionization is detected. On average, there are six re-pump events over a measurement duration of 10 min. The blue markers indicate large spectral jumps after re-pump pulses. 68

6.4 Automated ODMR and PLE measurements are performed on four additional samples (C to F). We are not able to track the NV centers between ODMR and PLE with the automated protocol. ODMR ^{15}NV/^{14}NV ratio suggests predominance of ^{15}NVs across all implanted samples. Similar to the previous dataset (Fig. 6.3), the average linewidth for each individual NV is computed as the mean FWHM obtained by fitting each of the 30 frequency scans to a Lorentzian. Automated PLE scans performed on deep grown-in NVs (25 µm from surface, sample F) are used as a reference. 70

6.5 The NV ZPL inhomogeneous distribution. The histogram is generated by recording the center wavelength of all peaks observed with 532 nm excitation from locations within an implantation region (except the grown-in reference NV centers) on the respective samples. Note that no distinction is made of the different transitions associated with the NV excited state spin sublevels. The bin size is 0.025 nm, and the spectrometer resolution is 0.021 nm. The histogram data is fitted to a Gaussian to extract the full-width half max (FWHM) of the distribution. Sample B show an obvious deviation from other samples. 72

7.1 **a.** SEM image of a fabricated GaP 1-D PhC resonator coupled to input and output grating structures. A series of elliptical holes in GaP defines the PhC. **b.** Simulated dispersion diagram of TE-modes supported by a blank waveguide structure (no holes). The grey region marks non-guided modes within the diamond light-line. Inset shows the top and cross-sectional view of the unit cell (cell width=a_{mir}=140 nm) consisting of GaP-on-diamond structure. The GaP waveguide is 222 nm high and 360 nm wide. Simulations assume periodic boundary conditions along all directions. **c.** Dispersion diagram with the optimized elliptical air hole $(hx, hy) = (71, 183)$ nm in the unit cell. Now we see the appearance of a TE band gap (marked in green). . . 77

7.2 **a.** SEM image of a fabricated GaP 1-D PhC resonator with the mirror and taper regions annotated.**b.** The variation of the hole spacing across the PhC, distinguishing the mirror and taper regions. **c.** FDTD simulated scaling of the total Q-factor of the GaP-on-diamond PhC resonator with increasing number of mirror and taper holes. The left edge (M=0) of the plot describes the over-coupled cavity regime (dominated by Q_{c}) whereas at the right edge (M=20) we are operating in the under-coupled regime (dominated by Q_{i}). For maximum SiV photoluminescence extraction, we would like to operate in the critically coupled regime (Q_{c}=Q_{i}). 78

7.3 **a.** An illustration of the stamp transfer process. We begin with GaP PhCs on a carrier chip and finish with PhC integration with SiV on diamond. **b.** Optical image of suspended BGaP-on-Si PhC devices before stamp transfer. The yellow/blue regions represent suspended and anchored regions of the BGaP. The suspended regions are picked up by the polymer stamp and transferred to diamond. **c.** BGaP PhC devices after transfer on diamond. **d.** Laser scanning profilometry data on transferred PhC devices showing good adhesion to the diamond substrate. 81

7.4 **a.** Optical image of HSQ electron-beam patterns on BGaP (green) wet-transferred on Si_3N_4/Si substrate. **b.** Optical cross-polarized image of the devices after the GaP RIE plasma etch. **c.** SEM image of etched photonic disk resonator devices in the add-drop coupling configuration. Each waveguide is coupled to a set of three disk resonators. **d.** Measured TM spectra of 5 µm diameter disk resonators through the drop port as a function of the waveguide coupling distance (d_c). The spectra shown here corresponds to approximately four free-spectral range of the resonators (i.e. four distinct groups of resonances). Few resonances are observed for the three most undercoupled disks (d_c = 200, 190, 180). **e.** The resonances are fitted to a Lorentzian and their quality factors (Q) are estimated as a function of the coupling distance. The highest observed Q is $\approx$24k and below the spectrometer resolution limit (red line). 84

7.5 **a.** Optical image of BGaP-on-Si suspended disk resonator devices. The yellow regions are suspended. The 5 µm diameter disks are supported by a small ($\approx$ 1 µm dia.) Si pedestal at the center (grey). **b.** Angled SEM image of suspended devices in the add-drop coupling configuration. Each waveguide is coupled to a pair of disks. The undercut between BGaP and Si substrate is $\approx$ 2 µm. We suspect that the waveguides may be slightly bowed due internal stress within the BGaP, leading to variation in resonator coupling across devices. **c.** Measured TE spectra of the disk resonators through the drop port as a function of the waveguide coupling distance (d_c). The spectra corresponds to approximately four free-spectral range of the resonators. The increased background in the spectra can be attributed to scatted light due to the co-polarized nature of the input and output gratings (design limitation of suspended structures). **d.** The resonances are fitted to a Lorentzian and their quality factors (Q) are estimated as a function of the coupling distance. The highest observed Q is $\approx$24k and below the spectrometer resolution limit (red line). 85

7.6 **a.** Optical image of HSQ electron-beam patterns on Fariba-GaP (green) wet-transferred to Si_3N_4/Si substrate. **b.** Devices after the GaP RIE plasma etch. The blue and red square marks two different photonic patterns. The red region is identical to the BGaP-on-Si_3N_4 chip (Fig.7.4). **c.** Angled SEM image of etched photonic disk resonator devices in the blue region. **d.** Measured TM spectra of 5 µm diameter disk resonators (in the red region) through the drop port as a function of the waveguide coupling distance (d_c). Resonances are observed for even the most undercoupled disks (d_c = 200). **e.** The resonances are fitted to a Lorentzian and their quality factors (Q) are estimated as a function of the coupling distance. The highest observed Q is spectrometer resolution limited (red line). 86

7.7 High resolution drop-port spectra obtained on the Fariba-GaP on Si_3N_4 using a tunable laser (760 to 785 nm). Here 1 V laser piezo-voltage corresponds to 8.33 GHz. For the 5 µm dia. undercoupled disk resonator devices, we observe that most resonances are split, with a Lorentzian fit (orange) giving Q ~300k. 87

7.8 **a.** Angled SEM of suspended BGaP PhC devices. The devices are supported by a large frame structure. **b.** Zoomed-in angled SEM showing the PhC resonator. Inset, top-down SEM view of the holes defining the PhC cavity. The hole dimensions are within 5 nm of design. **c.** Transmission spectra of a set of PhC resonators under TE supercontinuum excitation. The bottom and top devices are blank waveguides (no holes). We can see a photonic band gap structure between 680 to 725 nm. There are two resonator modes visible towards the edge of the band gap. **d.** Higher resolution transmission spectra of the devices showing the first and second order PhC resonances, with the estimated Q-factor obtained by fitting to a Lorentzian. . . 89

7.9 **a.** Optical image of HSQ electron-beam patterns on GaP (green) wet-transferred on SiO_2/Si substrate. **b.** Devices after the GaP RIE plasma etch. **c.** SEM image of etched PhC devices. **d.** High-magnification SEM image of the etched PhC holes. **e.** Transmission spectra of a set of PhC resonators under TE supercontinuum excitation. **f.** Distribution of observed PhC resonances across the chip. Because the GaP thickness is higher than design (290 nm), the resonances are red shifted. **g.** Distribution of fitted Q-factors measured across the chip. 91

7.10 **a.** The transmission spectra of one specific PhC resonator tracked through multiple thinning etch cycles. The resonance is blue shifted as the GaP thickness is reduced. Additionally the PhC holes are gradually eroded, likely changing the coupling regime from overcoupled to undercoupled. **b.** Devices after the blanket GaP RIE plasma thinning etch. The resonances in the red region of the chip are tuned to match SiV^- emission. **c.** Distribution of observed PhC resonances within the red region. **d.** Distribution of fitted Q-factors measured within the red region. 92

7.11 **a.** The room-temperature transmission spectra of one PhC resonator under supercontinuum excitation compared to 532 nm excitation. We can see the high-Q SiV-coupled cavity mode at 743 nm. **b.** A SiV PL confocal image of a stamped PhC device under 532 nm excitation. The SiV PL appears suppressed at the center of the cavity. **c.** A SiV PL confocal image of a stamped blank waveguide device under 532 nm excitation. Here the collection is fixed at the output grating coupler (red circle) while the excitation laser is scanned across the image. Significant SiV PL is coupled into the waveguide and out through output coupler. 94

8.1 Illustration of a GaP-on-diamond photonic circuit for entanglement generation. . . . 97

8.2 **a.** Illustration of the SSPD loop (teal) on the GaP waveguide (pink). The incident photons are guided within the waveguide. **b.** Hotspot formation within the SSPD upon absorption of the incident photon. Each hotspot event triggers a voltage pulse. **c.** Colorized SEM image showing the NbN (blue) nanowire on GaP. **d.** A waveguide coupled SSPD device identifying the AlGaP (grey), GaP (pink), NbN (blue) and gold contact (yellow) layers. **e.** The detector response to normal attenuated laser excitation vs nanowire bias current for various nanowire widths. **f.** The dark count rate vs nanowire bias current for various nanowire widths. Optical measurements performed at 4.2K. 101

8.3 Schematic views with overlaid FDTD simulations and SEM images of integrated devices. **a.** Waveguide-coupled disk resonators, **b.** directional coupler, **c.** grating coupler (with schematic view halved for clarity). 102

8.4 **a.** SEM image of the fabricated GaP-on-Si_3N_4 resonator with accompanying grating couplers. The device is excited with telecom band tunable laser (red) and the SHG signal is measured out of the vis/NIR output grating (yellow). **b.** Simulated resonator $\vec{E}$-field profiles of the quasi-phase matched telecom and second-harmonic modes. **c.** Pre and post trimming optical images of a device. The ring was exposed with a donut pattern. The waveguide and grating structures were utilized for exposure alignment and thus were sometimes exposed. To reveal the exposed HSQ pattern during the trimming process, the post-trimmed optical image was acquired after developing the exposed HSQ in a 25% TMAH solution. Note that all optical characterizations were performed before the development. **d.** Relationship between HSQ exposure dose and observed wavelength shift of hybrid TE_{01}/TM_{00} resonances at the fundamental wavelength. **e, f.** A target trim-test showing the fundamental wavelength resonances for nine devices with identically designed resonator dimensions pre- and post-exposure, respectively. 105

A.1 **a.** Beamer flow. **b.** Fractured photonics pattern. **c.** Fully processed photonics pattern showing the field boundaries and fractured shapes colored by dose. The dense features near the center get a lower dose (blue), whereas the features near the edges get a higher dose (red). 113

A.2 **a.** Diamond sample with gallium phosphide membrane before spin-coating **b.** After spin coating HSQ. The large edge bead is because of the small sample size. **c.** After spin coating water soluble spacer. 118

B.1 a) Angled SEM image of an array of suspended BGaP photonic devices after the XeF_2 release step. The silicon substrate has been undercut releasing the photonic devices, however upon closer inspection, we can see silicon gossamer like material underneath the freestanding beams. b) A zoomed in SEM of the red box in (a). This gossamer material can be removed by the XeF_2 cleanup step. c) SiF_x residue on the BGaP after the vapor etch process. d) Optical bright field image of a successfully released BGaP structure. The freestanding BGaP is yellow and BGaP still bonded to the silicon substrate is purple. This variation in BGaP color can be utilized to determine the etch endpoint. . . . 132

D.1 a) Top down SEM view of a HSQ test pattern on GaP after plasma RIE-ICP etching with optimized parameters detailed in table.C1. The test pattern consists of arrays of ridges (1:1, 1:2 and 1:4 duty cycle) and dots (1:1 duty cycle) with feature dimensions of 62.5nm, 125nm and 250nm. b) SEM zoom-in of the 62.5nm dots, showing the etched region between has cleared. c)Angled SEM view of the 62.5nm dots (pattern transferred as cylindrical pillars) showing vertical sidewalls with high aspect-ratio. . 144

E.1 a) SEM images of dose test patterns for AQM-HSQ written on a silicon substrate. Spin speed 6k rpm for 45s produced a resist layer 150 nm thick. Per standard HSQ procedure, the resist was baked at 80C for 4 min. After exposure the resist was developed in 25% TMAH for 4 min. a) Dose of 1900 $\mu C/cm^2$, underexposed lines (37.5 nm). b)Dose of 2300 $\mu C/cm^2$, underexposed lines (41.8 nm). c)Dose of 2700 $\mu C/cm^2$, accurate exposure (50 nm). Features match design. d) Dose of 2700 $\mu C/cm^2$, accurately exposed array of dots (50nm dia. 100nm pitch). . . . 146

F.1 The vacuum annealing setup consisting of a turbo pump directly connected to a single ended quartz tube (via KF-25 vacuum fitting). The quartz tube sits inside a tube furnace that is controlled by a computer interface. . . . 148

F.2 Inside the tube furnace. The temperature is controlled externally (the control knob on the front panel is disconnected) by a PID algorithm. When placing the quartz tube inside the furnace, ensure the tube is supported at the ends (purple boxes) with quartz wool. The wool serves as insulation and dampens vibrations from the turbopump. . . . 149

F.3 The oxygen annealing setup consisting of a double ended quartz tube. One end is connected to the oxygen gas supply, whereas the other end is connected to a gas bubbler. . . . 150

LIST OF TABLES

Table Number | Page

4.1 Raw NV^- counting data used in Fig. 4.5. 37

4.2 Details of anneals conducted on the sample. 40

5.1 Rates for modelling NV dynamics 56

B.1 Silicon vapor etch parameters release of freestanding BGaP structures. Please keep in mind that the silicon undercut rate for a given recipe is highly dependent on sample geometry. 131

D.1 Plasma processing parameters for photonics GaP etch 140

D.2 Plasma processing parameters for pre-implantation etch of all diamond samples. . . 142

ACKNOWLEDGMENTS

I am very grateful that I had the opportunity to pursue my PhD at University of Washington. The work accomplished in this thesis would not have been possible without the unwavering support provided by a large group of people, and I would like to acknowledge them below.

First, I would like to thank my advisor **Kai-Mei Fu**. Your wide knowledge, enthusiasm and openness has been a driving force and a constant inspiration for me. I am always surprised by your ability to find new angles to approach problems and push experiments further. I feel very lucky to have had you as my advisor.

Arka Majumdar, Mo Li, David Masiello and Scott Dunham, thank you for being members of my committee and providing valuable feedback and interesting new ideas. Arka, your nanophotonics course was my introduction to the field and influenced design decisions throughout this thesis. Mo, I have learned much about acousto-optics from our collaboration discussions. I look forward to awesome device integration results from the close collaboration with your group.

I could not have asked for better hands-on postdoc mentors. Never having worked on experimental optics before, joining a quantum optics research group was quite intimidating. **Mike Gould**, thank you for teaching me everything about confocal microscopy and practical photonic design/fabrication. **Emma Schmidgall**, thank you for being patient with me and answering my incessant, mostly naive questions during the stark tuning experiments. I learned a great deal from our discussions and that work serves as the leading chapter in my thesis. I also greatly appreciate your help figuring out low-temperature measurements, particularly the sensitive resonant excitation NV spectroscopy. You have made a lasting impression on me with your penchant for detailed note-taking and data organization, skills that have served me very well through the years.

Fariba Hatami and group at Humboldt-Universität zu Berlin, thank you for the exceptional gallium phosphide epitaxial growth that served as the basis for all photonic fabrication during the course of this thesis.

Maria Huffman and all the clean-room staff, thank you for keeping the facility running all year round, notwithstanding the occasional snowstorm or pandemic. **Mark Morgan**, thank you for pointers on plasma processing and keeping the finicky chlorine plasma-etcher in its happy place. **Shane Patrick**, thank you for your extensive support with the electron-beam lithography system (the most complex, delicate and expensive piece of equipment that I have ever had the privilege of operating).

Oscar Vilches, your expertise in low temperature physics and constant encouragement was instrumental during my endeavor to build an immersion helium cryostat from scratch. I was very surprised to learn that ordinary materials and systems behave in entirely unexpected ways near absolute zero. Thank you for the hundreds of hours of hands-on apprenticeship, it provided the basis for my knowledge and passion for cryogenic and vacuum systems.

I would like to thank my best friends in Seattle, **Arushi Sonkhya** and **Owen Lawrence** for their support over the past few years. We have had many memorable adventures in the Pacific-Northwest and beyond. Backpacking and hiking has always been my escape from the rigors of graduate school and I look forward to many more adventures in the future.

Finally, I would like to thank my family for their love and support. Mom thank you for always believing in me!

DEDICATION

To my family, friends and fellow members of the quantum-defects team.

"To succeed, planning alone is insufficient.
One must improvise as well."
- *Isaac Asimov*

Chapter 1

Introduction

1.1 Background

Optically addressable defect qubits in materials like diamond[1,2], silicon carbide[3,4], ZnO[5] and rare-earth doped crystals[6,7] show tremendous potential for realization of a wide range of quantum technologies including single-photon generation, quantum metrology and quantum information science.

At the heart of the emerging field of quantum information science is the development of quantum networks[8] consisting of distant entangled qubit nodes[9]. Connecting spatially separated nodes via optical photons into a quantum network will enable distributed quantum computing[10] and long-range quantum communication[11]. In this quantum network approach, each node consists of a long lived quantum memory associated with several ancillary physical qubits[12]. Every node couples to a common optical channel via one or more physical qubits. Quantum information is transferred among stationary qubit nodes through flying qubits (photons) and multiple nodes can be entangled with high fidelity using heralded optical measurements[13]. The presence of several physical qubits at every node can also enable quantum error correction[14] supporting robust interconnections. Initial experiments on quantum dots[15], superconducting qubits[16], trapped atoms[17] and ions[18] as well as defects in diamond[19] have demonstrated entanglement between multiple nodes.

The nitrogen-vacancy (NV) center[1] in diamond is a promising platform for this networking architecture because it offers all the components for formation of qubit nodes. It has a stable electronic spin with long coherence time (>1 ms)[20,21] coupled to several nuclear spins that act as memory qubits[22], while also coupling to photons through its optical transitions[23]. NV centers can be

created on demand with high spatial precision by nitrogen ion-implantation and high-temperature vacuum annealing. However, this implantation process results in damage to the diamond lattice and results in concomitant creation of other defects. Full control over NV center formation thus requires a detailed understanding of all the underlying defect kinetics. Recently, there has been significant progress in understanding NV center energetics[24–27] and engineering NV center formation kinetics[28]. Here, we utilize a new tool, the tracking of thousands of individual NV centers, to provide insight into the formation, quenching, and orientation kinetics of a quantum defect in an ultra-pure diamond host.

On demand NV center formation allows for integration with nanophotonic structures. Photonic integration is particularly desirable as it provides a scalable architecture for photon routing, interaction and detection i.e. the building blocks of a quantum networking system. Optimizing nanophotonic structures for efficient defect integration is often nontrivial and bespoke to meet unique constraints imposed by the targeted application for a given defect system. For example, if we consider high-sensitivity quantum metrology with NV centers in diamond, photonic structures need to be optimized for efficient broad-band extraction of photons from NV centers located a few nm from the sensing surface. In contrast, for quantum information applications, we prefer to isolate the NV from any external influence and couple to the narrow-band zero-phonon line (ZPL) transition of deep NV centers ($\gtrsim 50\,\mathrm{nm}$ from the surface). At cryogenic temperatures, about $4\,\%$ of the NV photon emission is emitted into the ZPL transition[1]. Thus photonic device operation in the Purcell-enhanced[29], or high-cooperativity[30], regime is preferable.

Maintaining the optical coherence and homogeneity of engineered defect qubits while simultaneously coupling to photonic structures is a very difficult challenge. Every qubit is unique in that its quantum properties are a function of its local environment. This environmental sensitivity is a key issue we focus on throughout this thesis. To date, photonic integration of implanted defects with identical optical properties, essential for quantum information, has not been demonstrated. There are two approaches to solving this problem, bottom-up starting with the defect qubit and top-down starting with the photonic structures. The current state-of-the-art quantum information experiments utilize the bottom-up approach, involving exhaustive search for well-behaved grown-in deep single NV centers and fabricating micron-scale individual solid immersion lenses around the targeted defects[19,23]. While it is important to demonstrate that a certain coherence time, optical

behavior, quantum operation, etc. is possible in one device with favorable characteristics, it must also be possible to reproduce these characteristics. The top-down approach to photonic integration that we employ here utilizes semiconductor processing techniques to enable fabrication of thousands of photonic devices on diamond substrates hosting NV defects. The qubit-photonic coupling is stochastic in nature. Although the NV centers are characterized prior to integration, we cannot determine precisely which NV will couple to a given photonic device. While moving forward we can employ implantation-device alignment strategies to mitigate this stochastic coupling, here we show that with careful control of qubit density and design of photonic arrays, we can ensure a reasonable yield of qubit coupled photonics. The primary factor behind observed device-to-device variability is the high sensitivity of NV centers to their local charge environment[31–34]. This sensitivity is particularly problematic for quantum information schemes that rely on two-photon interference for qubit entanglement. Here, the indistinguishable nature of emitted photons is essential[13], requiring spectrally stable NV centers. Thus, the concept of scalability is not merely the ability to fabricate many physical devices using semiconductor processing techniques. In order to move beyond proof-of-principle experiments, the properties of the defect and coupled device must all be precisely controlled in a scalable approach to provide an efficient, reliable and reproducible system.

On account of the variability of NV centers, we also explore nanophotonic integration with a different point defect in diamond called the silicon-vacancy (SiV^-) center[35,36]. Owing to its inherent inversion symmetry within the diamond lattice, SiV^- centers exhibit reduced sensitivity to variations in their local charge environment. In addition, the SiV center also exhibits higher ZPL emission efficiency (70 %)[37]. Unlike the NV center, orbital relaxation through electron-phonon coupling[38] limits the SiV^- electron spin coherence time to 45 ns at 4 K[39]. However, freezing out phonons by cooling to milli-kelvin temperature in a dilution refrigerator allows the spin coherence time to recover to 13 ms at < 500 mK[40]. Thus SiV^- centers present a reasonable near-term compromise of reduced operation temperature for increased spectral stability, enabling realization of photonic integrated devices for quantum networking.

We demonstrate three different geometries for photonic integration, all of which utilize a thin ($\leq$250 nm) high index (n = 3.4) gallium phosphide (GaP) on diamond (n = 2.4) structure. The first design involves NV centers coupled to photonic disk-cavities demonstrating high Purcell enhancement. These devices exhibit high cavity quality factors and enhanced NV ZPL collection efficiency,

and employ fabrication techniques that etch into the diamond host. In these devices we utilize an external electric field applied by patterned electrodes to dynamically stabilize NV optical emission by Stark tuning[31,41,42]. A second design utilizes a novel inverse-design photonic optimization technique to design broadband photon-extractor devices. This design is constrained to only etch the GaP layer, preserving the integrity of the diamond host and minimizing perturbations experienced by coupled NV centers. Finally, in the third design, we further isolate the diamond qubit host from the fabrication process by fabricating 1-D photonic crystal cavities (PhC) on a separate carrier substrate. Using a gentle polymer stamp transfer technique, these PhC devices are stamped on diamond samples containing near-surface SiV^- centers.

Thus the important figures of merit for successful defect qubit nanophotonic integration are:

- Efficient photoluminescence collection from the defect qubit
- Enhanced photon emission rate into a desired optical mode which results in reducing the lifetime of the defect excited state
- Reduced inhomogeneous distribution and spectral stability of qubit transitions (including defect charge-state stability)
- Integrated mechanism for tuning defect qubit transition frequency

In summary, we demonstrate the ability to tailor defect qubits in diamond starting from the initial defect formation process through to nanophotonic integration. Extensive optical characterization of the defect centers performed both before and after fabrication provides insight into changes in the local environment and points to important fabrication/design considerations for future integration of defect qubits and nanophotonics.

1.2 Overview of this thesis

This thesis consists of five experimental projects that are each presented as a separate chapter in chronological order. We begin by discussing briefly some underlying theoretical concepts in

Chapter 2. A brief description of diamond as a qubit host material, with a focus on NV centers, and the recently investigated SiV center is provided. A simple photon-mediated quantum networking protocol is demonstrated to provide context for the overall idea of quantum information processing. This is followed by a discussion of gallium phosphide as a photonic device layer and the advantages of hybrid nanophotonic integration.

In chapter 3, we demonstrate coupling of single NV centers to GaP disk resonators. The NV centers are created at a depth of 20 nm by nitrogen ion-implantation and annealing (800°C, in inert Ar atmosphere). Significant enhancement of the NV ZPL photon collection efficiency (>25-fold Purcell-enhanced regime) is observed. Careful spectroscopic study provides insight into optical inhomogeneity and spectral diffusion of the coupled defects. We attempt to compensate for the spectra diffusion by utilizing dynamic Stark tuning feedback, obtaining linewidths of $\approx$3 GHz, two orders of magnitude higher than the NV lifetime limit ($\approx$15 MHz). We suspect that strain and charge-trap driven electric field fluctuations experienced by the NV centers due to implantation and etching into the diamond could be the major source of NV spectral diffusion.

In chapter 4, by performing repeated vacuum annealing of diamond samples and tracking thousands of individual NV centers between anneals via photoluminescence confocal microscopy, we study the formation dynamics of NV centers. Detailed analysis of the annealing data provides insight on optimal NV formation conditions and preferential orientation of NV centers within the diamond lattice.

In chapter 5, we fabricate and characterize a novel inverse-designed grating like structure optimized for photon extraction from near-surface NV centers. Based on results from the previous chapter, post-implantation we anneal the diamond at a higher temperature (1200°C, in vacuum) to heal the implantation damage and mitigate bulk defects. Further, we constrain the photonic design to etch just the GaP layer, leaving the underlying diamond defect host undisturbed. Significant enhancement (14-fold) of the NV ZPL photon collection efficiency is demonstrated. Spectroscopy of coupled NV centers shows reduced spectral diffusion, and linewidths of $\approx$800 MHz are observed. Although our design avoids etching into the diamond, the GaP photonics plasma etch likely modifies the surface termination of the diamond and introduces new surface charge traps. The observed spectral behavior is surprising as the NV centers are implanted 100 nm beneath the surface specifically to isolate against surface perturbations.

In chapter 6, we perform a detailed investigation of surface and laser-induced noise on the behavior of implanted near surface NV centers (100 nm to 20 nm deep). To pin down the likely source of spectral diffusion observed in chapters 3 and 5, linewidth statistics on a large number of implanted NV centers is collected and analyzed by an automated resonant spectroscopy technique. We observe that implanted NV centers 100 nm deep exhibit long periods of spectral stability, wherein their spectral characteristics can be akin to optically coherent grown-in NV centers. The implanted and grown-in centers exhibit comparable median optical linewidths. However, we do see distinct advantages for grown-in centers in terms of behavior under off-resonant green re-pump and inhomogeneous ZPL distribution. Further, we show that the optical stability rapidly degrades with increasing proximity to the diamond surface (depth < 100 nm).

In chapter 7, because of the high surface sensitivity of NV centers, we investigate photonic integration with the SiV center in diamond. Here, we utilize 1-D photonic crystal (PhC) waveguide cavities defined in GaP. Based on techniques developed with NV centers, we first create SiV centers at a depth of 20 nm by silicon ion-implantation and annealing (1200°C, in vacuum). We transition to independent fabrication of photonic PhC devices on a silicon oxide carrier chip (GaP-on-SiO_2) and subsequent integration with a diamond qubit host using a stamp-transfer technique. The stamping process avoids the plasma exposure of diamond, preserving the qubit environment. Additionally, stamping allows us to carefully characterize the cavity resonances of the PhC GaP-on-SiO_2 devices before transfer to diamond. Tuning of the PhC cavity resonance wavelength to match the SiV ZPL transition is demonstrated by controlled iterative thinning of the GaP photonic layer. This significantly increases the yield (80 %) of qubit coupled photonic devices. After transfer to diamond, we measure high SiV-coupled PhC cavity quality factors within 10 % of the design goal and show enhanced SiV ZPL collection efficiency (Purcell-enhanced regime).

We conclude in chapter 8 with a focus on the experimental realization of on-chip entanglement circuits. We begin with a discussion of current and future research directions to improve the performance of defect coupled photonic devices. Next, we present results on ancillary on-chip photonic components (single-photon detectors, passive devices, frequency-converters) necessary for implementation of on-chip entanglement generation and distribution using the GaP nanophotonic platform.

Chapter 2

Theory

2.1 Solid-state qubits in diamond

2.1.1 Diamond host material

Diamond is an electronic insulator with a wide band gap of 5.45 eV making it optically transparent in the visible regime. It can be synthesised with impurity concentrations below parts-per-billion scale and isotopically purified[43] to eliminate magnetic noise from nuclear spins. We utilize 2 mm $\times$ 2 mm ultra-pure (type-IIa) chemical vapor deposition (CVD) grown single-crystal diamond samples (electronic grade, ElementSix, N $<$ 5 ppb, B $<$ 1 ppb), with the surface oriented along the <100> crystal axis. The CVD diamond surface is typically polished to $\approx$1 nm RMS roughness. The as-grown diamond surface has dangling bonds that are hydrogen-terminated from the presence of hydrocarbon precursors in the growth environment. Exposing the diamond to oxygen plasma or oxygen gas at elevated temperatures can oxygen-terminate the surface[44]. Changing the surface-termination modifies the local Fermi-level and is an important consideration for the charge state stability of near-surface defects.

2.1.2 The NV center in diamond

Physical structure:

The NV center is a point defect in diamond consisting of a substitutional nitrogen atom and a vacancy occupying a nearest-neighbor lattice site. The NV defect axis is parallel to the <111> diamond crystal axis. Thus there are four possible orientations of the NV center in the diamond

lattice (eight orientations if the nitrogen and vacancy positions are interchanged). Exciting with a linearly polarized light source, the two sets of optically distinguishable NV orientations for a <100> diamond sample are indicated in Fig. 2.1a.

Electronic structure:

The electronic level-structure of the NV center lies deep within the diamond band gap (Fig. 2.1b) and is defined by the electron number, C_{3v} defect symmetry, spin-orbit and spin-spin interactions, as well as external electric and magnetic field perturbations. The NV center is observed to exist in the neutral (NV^0) and negative (NV^-) charge states. Rapid charge-state conversion can be observed between the NV^0 and NV^- states, mediated by two-photon absorption and subsequent electron recombination processes[45]. Thus every NV center has emission corresponding to both NV^0 and NV^- transitions, with the ratio of the average photoluminescence (PL) intensities determined by the local Fermi-level, excitation wavelength and excitation intensity. Under off-resonant excitation (532 nm, Fig. 2.1c), both the NV^0 and NV^- charge states exhibit a sharp zero-phonon transition (ZPL, at 575 nm and 637 nm respectively) with a broad phonon-mediated sideband (NV^0 PSB, 575 nm to 800 nm; NV^- PSB, 637 nm to 800 nm).

The NV^- state, consisting of five electrons from the dangling bonds of the three carbon atoms and a nitrogen plus an extra electron captured from the environment, forms a spin-1 system which in its ground state occupies an orbital-singlet spin-triplet state. The ms=0 and ms=±1 ground state spin triplets are separated by a 2.87 GHz zero-field splitting. The ground state spins can therefore be manipulated by the application of a RF microwave field. The ground state couples optically to an orbital-doublet spin-triplet excited state, which can decay back into the ground state either directly or via the spin-singlet states (inter-system crossing[46]) (Fig. 2.1b). An essential feature of the NV^- electron spin state is that it can be initialized, manipulated, and read out optically at room temperature. For both sensing and quantum information applications, the NV^- charge state is required. Thus, a critical consideration for device integration is the need to minimize ionization into the NV^0 charge state. Henceforth, all mentions of NV centers refer to the NV^- charge state, unless explicitly specified otherwise.

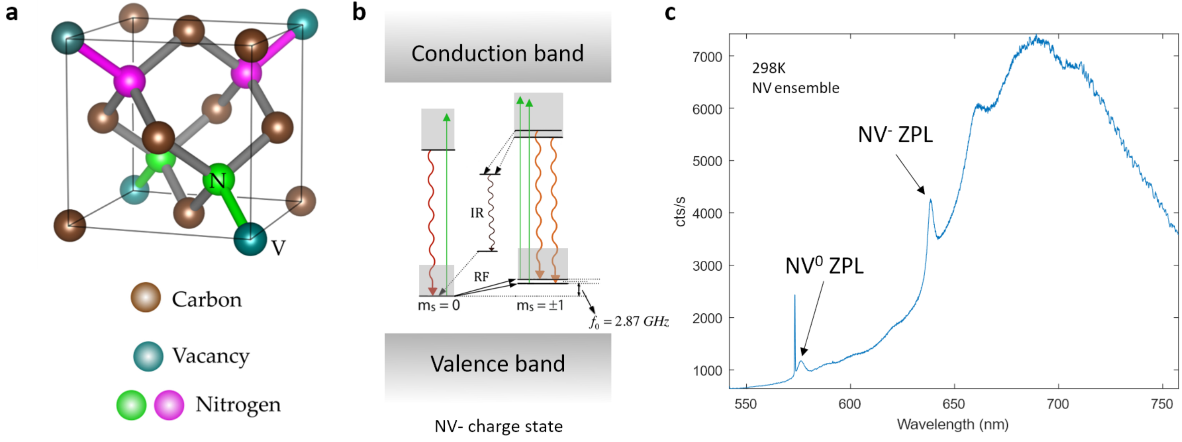

Figure 2.1: **a.** The four orientations of an NV center in the diamond lattice. The two sets of optically distinguishable orientations for a <100> diamond sample are indicated by magenta and green. **b.** The electronic structure of the NV^- center within the band gap of diamond. A simplified excited state structure is shown. **c.** Room temperature PL spectra of an ensemble of NV centers under off-resonant excitation. The NV^0 and NV^- ZPLs are shown along with the large phonon side bands. The sharp line at 573 nm is the first order diamond Raman line due to the 532 nm excitation.

Optical properties:

For NV centers in diamond, photoluminescence (PL) detection efficiency is intrinsically limited by the non-directional spatial emission of PL and total internal reflection between the high-index host material and its low-index environment (Fig. 2.2a). For a diamond-air interface, even with a high numerical-aperture objective (NA=0.95), less than 4 % of the emitted NV photons can be collected. To enable high PL collection efficiency, photonic structures such as solid-immersion lenses[47], waveguides [3,48] and nanophotonic cavities [34,49–51] have been utilized. Nanophotonic devices are particularly attractive for their small footprint and potential for scalable integration.

The NV center exhibits an overall radiative quantum efficiency of ∼80 % with 3 % of the photons emitted in the ZPL. This is dictated by the relatively large shift in nuclear coordinates between the NV center's ground and excited states, which results in decay from the excited state into phonon-coupled higher vibrational levels of the ground state. Only ZPL photons are usable for quantum information applications. The rate of ZPL photon emission can be selectively enhanced by coupling

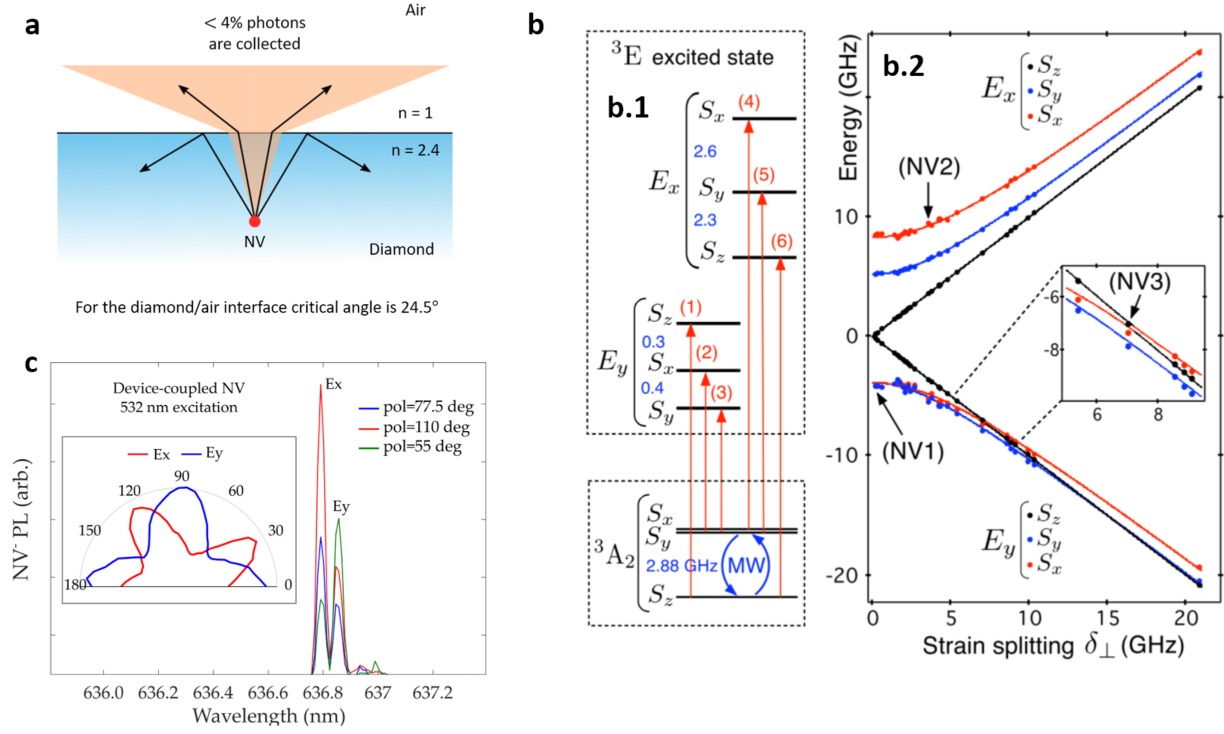

Figure 2.2: **a.** Illustration of total internal reflection limiting NV PL collection into free space. **b.** (adapted from Ref.[33]) The behavior of NV^- excited state structure as a function of the local transverse strain. This behavior is analogous to variation in transverse electric field, and is the primary cause of spectral diffusion. **b.1.** At high strain, the excited state manifold splits into two triplets. The allowed optical-transitions are shown as red arrows. **b.2.** Level-crossings in the lower branch (E_y) can enable spin-flip transitions. **c.** Low temperature (8 K) spectra under off-resonant excitation of a single implanted NV in a high strain environment exhibiting a 48 GHz E_x-E_y splitting. Inset: the E_x, E_y transitions show near-orthogonal excitation polarization dependence.

the NV ZPL to a high quality-factor (Q-factor) resonator. This is experimentally demonstrated in chapter 3.

At low temperature (T<4 K), the lifetime-limited linewidth of NV centers has been measured to be ∼13 MHz[41] corresponding to an excited state lifetime of 11.5 ns. It must be noted that lifetime limited linewidths have only been observed for spectrally stable grown-in deep NV centers. The excited state structure of the NV center is composed of an orbital doublet (e_x, e_y). Any perturbation of the local strain or charge environment breaks the orbital degeneracy and results in mixing of the e_x and e_y orbital branches[32,33]. In the limit of high transverse strain or electric field, the excited state

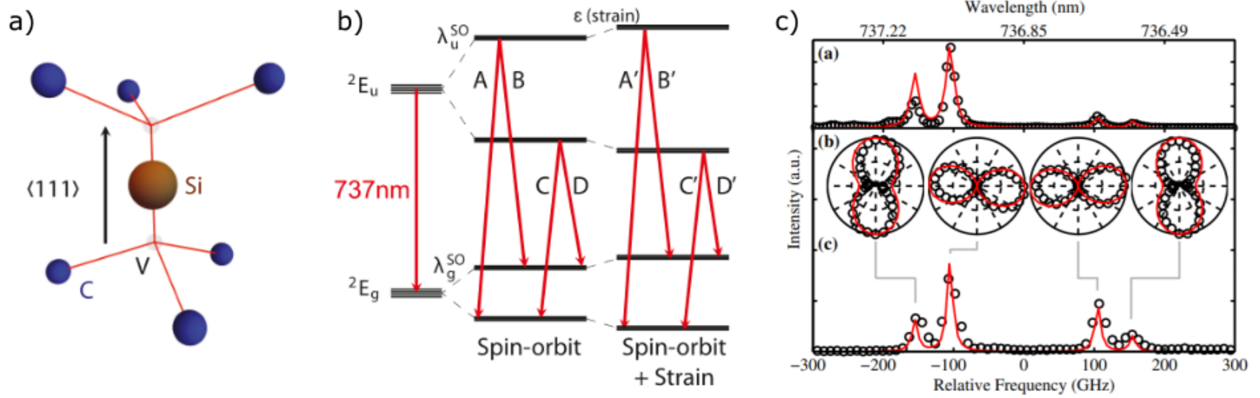

Figure 2.3: **a.** The structure of the SiV center in the diamond lattice. **b.** Energy level structure of the SiV center. Adapted from R. Evans et al.[53] **c.** SiV photoluminescence spectra showing the four transitions and their polarization dependence. Adapted from C. Hepp et al.[35].

manifold splits into two triplets (Fig. 2.2b). The strain (or electric field) component parallel to the NV axis results in the overall shift of the entire excited state manifold and further increases the static inhomogeneous variation of the ZPL emission energy (Fig. 2.2b, c). Thus, local charge fluctuations originating from interaction with other defect centers or surface-functionalization triggers spectral diffusion and dephasing of the NV center ZPL. On-demand creation of transform-limited NV centers by methods such as ion-implantation, laser-writing, etc. is an ongoing challenge faced by the defect qubit community[52].

2.1.3 The SiV center in diamond

Physical structure:

The SiV center is a point defect in diamond, consisting of a substitutional silicon atom and a split vacancy occupying the nearest-neighbor lattice sites i.e. the silicon atom is centered between two empty lattice sites (Fig.2.3a). Similar to the NV, the SiV symmetry axis is parallel to the <111> diamond crystal axis and there are four possible orientations[35] of the SiV center in the diamond lattice.

Electronic structure:

Utilizing photoluminescence measurements the SiV center has been observed to exist in two charge states; SiV^{-}[35] and SiV^{0}[54] with transitions near 737 nm (SiV^{-}) and 940 nm (SiV^{0}) respectively. It has been suggested that charge-state conversion occurs between the two states upon excitation[55], but unlike the NV charge state dynamics, much is still unknown about the SiV. Here, we focus on the well established SiV^{-} charge state. The center hosts a total number of eleven electrons: six electrons contributed by dangling bonds, four electrons from the Si atom and one electron trapped from nearby donors to account for the negative charge. It is a spin-1/2 systems that exhibits a D_{3d} symmetry in the diamond lattice, which renders the optical transitions insensitive to electric fields to first order in perturbation theory[35,56,57]. The ground and excited states each consist of a fourfold degeneracy (twofold orbital and a twofold spin degeneracy). At zero magnetic field, the excited and ground states have their orbital degeneracy partially lifted by the spin-orbit coupling, and the splittings are 260 GHz and 47 GHz respectively. In an external magnetic field, Zeeman interaction lifts the spin degeneracy.

Optical properties:

The four dipole allowed transitions are labeled A, B, C, and D in the order of decreasing energy in Fig.2.3b. Each excited state has dipole transitions to the two ground states forming an optical Λ system, resulting in the emission spectrum shown in Fig.2.3c. These four transitions comprise the zero-phonon line (ZPL), which contains more than 70 % of the total fluorescence. The SiV ZPL efficiency present a significant advantage of NV centers, however the overall radiative quantum efficiency is lower (0.1 for SiV vs 0.8 for NV) resulting in similar observed ZPL counts in experiments[56]. The polarization of the four transitions can be grouped into two subsets. The inner transitions are polarized parallel to each other and perpendicular to the outer ones[35].

At low temperature (T<4 K), the lifetime-limited linewidth of SiV centers has been measured to be $\approx$94 MHz[53], corresponding to an excited state lifetime of 1.7 ns. Typically SiV centers (even those formed by Si ion-implantation and annealing) exhibit optical linewidths within a factor of three of the lifetime limit (including the effects of phonon broadening and spectral diffusion). The SiV is sensitive to strain, which can both shift the average energy (for axial strain) and increase

the splitting (for transverse strain) in the ground and excited state manifolds. Transitions B and C within the ZPL are relatively insensitive to transverse strain because their ground and excited states shift in the same direction: both upward for transition B and both downward for transition C.

2.2 *Photon-mediated entanglement protocol*

Several protocols have been proposed for entangling distant spin qubits through photon detection. The process relies on state-dependent photon scattering from two qubits, followed by erasure of the which-path information, which serves to remove any information regarding the origin of the scattered photons, creating quantum indistinguishability. The photonic qubit can be encoded in either photon polarization, spatial modes or in the photon number state (photon number states 0 or 1). Either way, the quantum erasure step projects the quantum states of the spin qubits into a non-local quantum superposition. Various schemes for universal quantum computers based on this heralded entanglement technique have been proposed.

A brief description of a simple photon-mediated remote defect entanglement process follows (Fig.2.4b). Here we consider identical NV centers as our two target qubits, with each qubit emitting identical photons (i.e. having the same polarization, the same temporal mode and the same spatial mode) corresponding to their ZPL transitions. The two photon entanglement scheme[58] can be divided into four steps.

1. **Initialization:** The protocol starts by initializing each NV to the $|0\rangle$ ground state (Fig.2.4a). This is typically achieved by a short off-resonant (532 nm) excitation pulse. Due to decay channels involving excited state mixing and singlet inter-system crossing, the NV system has a very high spin-polarization fidelity into the $|0\rangle$ state of $>85\,\%$ ($>99.5\,\%$ with resonant initialization)[59].

2. **Spin superposition:** Next, a $\pi/2$ RF pulse (at frequency corresponding to the ground state energy splitting of ≈ 2.8 GHz) is applied to each NV (Fig.2.4b). This brings each qubit into a ground state superposition state (in this description, we ignore the normalization of the

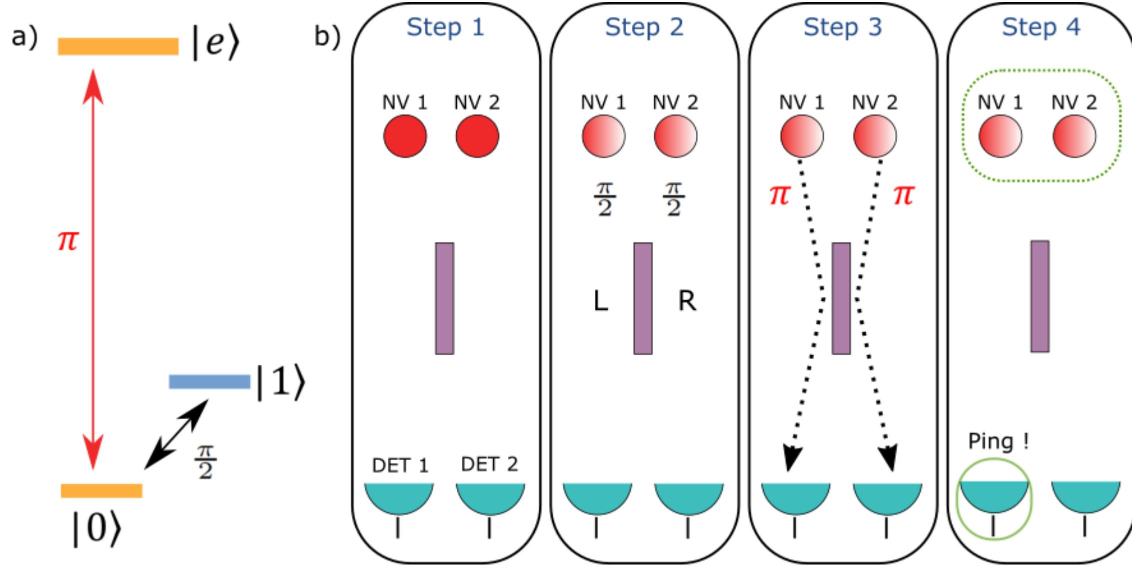

Figure 2.4: **a**. Simplified NV electronic structure for discussion of the remote entangle protocol. **b**. A four step approach for remote entanglement generation.

states for convenience)

$$|\psi\rangle_{NV-1/2} = |0\rangle + |1\rangle$$

3. **Photon emission:** A short optical π pulse is applied to each NV (resonantly exciting the NV ZPL transition $|0\rangle \rightarrow |e\rangle$) bringing the NV center to the optically excited state $|e\rangle$ only if it was in the $|0\rangle$ state; from there, it will spontaneously decay, emitting a photon. Each NV qubit is now entangled with the presence/absence of a photon

$$|\psi\rangle_{NV-1/2} = |0\rangle_e |1\rangle_c + |1\rangle_e |0\rangle_c$$

Here $|0/1\rangle_e$ represent the NV electronic spin states and $|0/1\rangle_c$ represent the photon number state.

4. **Photon interaction:** Collecting the NV photons in a common optical channel and interfering them on a 50/50 beam splitter, erases the which-path information. Detection of a single photon in the output channels, projects the system into an entangled state. e.g. if detector-1

clicks we obtain the total two NV state is given below:

$$|\Psi\rangle = \langle 1|_{c1/c2}\ (|0\rangle_{e1}|0\rangle_{e2}|1\rangle_{c1}|1\rangle_{c2} + |0\rangle_{e1}|1\rangle_{e2}|1\rangle_{c1}|0\rangle_{c2} + |1\rangle_{e1}|0\rangle_{e2}|0\rangle_{c1}|1\rangle_{c2} + |1\rangle_{e1}|1\rangle_{e2}|0\rangle_{c1}|0\rangle_{c2})$$

$$|\Psi\rangle = |0\rangle_{e1}|0\rangle_{e2} + |0\rangle_{e1}|1\rangle_{e2} + |1\rangle_{e1}|0\rangle_{e2}$$

Here, to get rid of the first term, step-3 can be repeated after application of a π RF pulse to the NV qubits. Now, we end up with the maximally entangled Bell state:

$$|\Psi\rangle = |0\rangle_{e1}|1\rangle_{e2} + |1\rangle_{e1}|0\rangle_{e2}$$

The entanglement success rate for such a protocol scales as the square of the overall photon detection efficiency (including all the optical losses along the path from the NV to the detector and the intrinsic probability of NV ZPL photon emission). For a real-world implementation of such a scheme with free-space optics (including experimental overheads), the overall success probability is of the order of 10^{-4} [19,23]. This illustrates the need to maximize both the ZPL emission rate and photon collection efficiency, and motivates the application of nanophotonic devices.

2.3 Gallium phosphide for hybrid nanophotonics

Nanophotonic coupling to defects in diamond can be achieved either by defining nanostructures directly in diamond or by utilizing a hybrid materials approach. In this thesis, we focus on the hybrid approach, involving transfer of a thin gallium phosphide (GaP) membrane (125 to 250 nm thick) on diamond. The GaP membrane is grown over an aluminium gallium phosphide (AlGaP, >80 %Al content) sacrificial substrate by a molecular beam epitaxy (MBE) process[60]. For photonic device fabrication, we undercut the sacrificial AlGaP and wet-transfer the thin GaP membrane either directly on the diamond qubit host (chapter 3, 5) or to a separate silicon oxide carrier wafer (chapter 7) for further processing (Fig.2.5). There are many advantages to utilizing a hybrid integration with GaP-on-diamond nanophotonics:

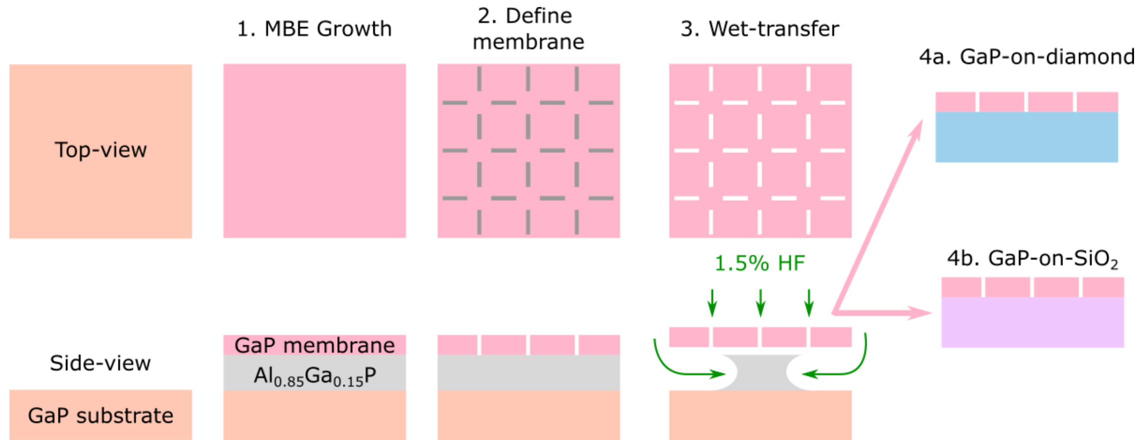

Figure 2.5: An illustration of the GaP membrane transfer process. The typical sacrificial AlGaP thickness is 300 nm and GaP membrane thickness is 125 to 250 nm (defined by the photonic design requirements). The membrane etch-via are defined by optical lithography and GaP plasma etching.

1. GaP with its large band gap (2.26 eV, 548 nm) is transparent in the visible band and exhibits a higher refractive index than diamond (3.25 vs 2.4 at 700 nm respectively). This index contrast enables guided optical modes primarily localized within the GaP layer. Defect emission is coupled to the evanescent field of the guided modes. We have demonstrated very high quality factors ($Q > 3e5$) in the visible range for small (5 µm diameter) GaP disk resonators, indicating very low intrinsic loss.

2. Being a non-centrosymmetric material, GaP exhibits a large second-order optical nonlinearity. GaP photonic devices have been used for second-harmonic[61] and sum-frequency generation[62]. This could enable on-chip frequency conversion of defect emission to the telecom band allowing remote-entanglement schemes across vast distances utilizing existing optical-fiber infrastructure.

3. GaP possesses sufficient stiffness and structural integrity for fabrication of narrow suspended photonic structures (≈150 nm wide) and subsequent transfer via physical stamp transfer. Such devices are discussed in detail in chapter 7.

4. The MBE-grown GaP surface typically exhibits sub-nm RMS roughness[60] suitable for the de-

velopment of on-chip superconducting nanowire single-photon detectors. Preliminary devices utilizing superconducting niobium-nitride on GaP detectors are demonstrated in chapter 8.

5. High-performance on-chip acousto-optical devices[63,64] could be fabricated in GaP with its combination of slow sound velocity (acoustic confinement), high refractive index (optical confinement), and large photoelastic constant[65,66]. Such devices could compensate for the inhomogeneous distribution of optical emission from defect qubits in diamond.

6. Making use of the piezoelectric properties of GaP, coherent transduction of microwave signals to optical frequencies has been recently demonstrated[64,67]. This could provide a route for coupling optically addressable defect centers in diamond with superconducting qubit circuits, enabling hybrid qubit architectures.

7. GaP is nearly lattice-matched to silicon (5.43 Å vs 5.45 Å respectively). Boron doped (2.7 % B) BGaP-on-silicon is commercially available in large 300 mm wafers. The optical properties of the BGaP material are characterized in chapter 7.

Chapter 3

Integration of NV centers with GaP disk resonators and dynamic stabilization

Generating entangled states of qubits requires efficient detection of indistinguishable photons from separate qubits. In this chapter, we demonstrate coupling of single NV centers to GaP disk resonators. The NV centers are created at a depth of 20 nm by nitrogen ion-implantation and annealing (800°C, Ar atmosphere). Large enhancement of the NV ZPL photon collection efficiency is observed, at the cost of increased optical inhomogeneity and spectral diffusion. We show that the NV inhomogeneity can be partially compensated by electric field tuning. These results address some of the challenges of chip-scale entanglement generation.

This chapter has been published as:

Schmidgall, E.R.*, **Chakravarthi, S.***, Gould, M., Christen, I.R., Hestroffer, K., Hatami, F. and Fu, K.M.C., 2018. **Frequency control of single quantum emitters in integrated photonic circuits**. Nano letters, 18(2), pp.1175-1179. Reprinted with permission, copyright 2018 American Chemical Society.
* Equally contributing authors

https://doi.org/10.1021/acs.nanolett.7b04717

3.1 Introduction

A quantum network, or entangled graph state of qubits[50,68–70], enables both quantum communication and universal quantum computation. Optically heralded entanglement[58] of defect qubits can be utilized to generate the graph state's entanglement edges between qubit nodes. However, to date, entanglement generation rates are too low to realize multi-qubit networks[23] due to photon emission into unwanted spatial and spectral modes. The integration of crystal defect-based qubits with photonic circuits offers an opportunity to significantly enhance photon collection efficiency[71], albeit at the cost of degrading the defect's optical properties, such as an increase in inhomogeneous ZPL emission energy and decreased spectral stability[44,72]. Since the entanglement protocols used for generating graph state edges require detection of multiple indistinguishable photons from separate emitters[58,73], compensating for the static and dynamic spread in emission energies is of critical importance for scalable on-chip graph state generation.

The dc Stark effect has been used previously to tune[42,74] and stabilize[31] the emission energy of quantum defects in bulk diamond. Here, in a series of experiments, we demonstrate the ability to tune the emission energy of photonic device-coupled near-surface NV centers over a large tuning range. Measurements on many single waveguide-coupled NV centers highlight the variability in response to an applied bias voltage, suggesting challenges in reaching the level of control necessary for chip-scale integration. Despite this variability, we are able to apply real-time voltage feedback control to partially stabilize the emission energy of a device-coupled NV center.

3.2 Hybrid GaP-on-diamond photonic resonators

In a GaP-on-diamond photonics platform,[75,76] we are able to efficiently couple single NV centers to disk resonators, enhancing the zero-phonon line (ZPL) emission rate via the Purcell effect[51].

3.2.1 Fabrication process and device yield

Near-surface NV centers were created in the single-crystal electronic grade diamond sample (ElementSix) by N^+ ion implantation (10 keV, 3×10^{10} cm^{-2}, CuttingEdge Ions), followed by a two-step anneal. A 2-hour, 800°C annealing step was performed under a 5%/95% H_2/Ar forming gas atmo-

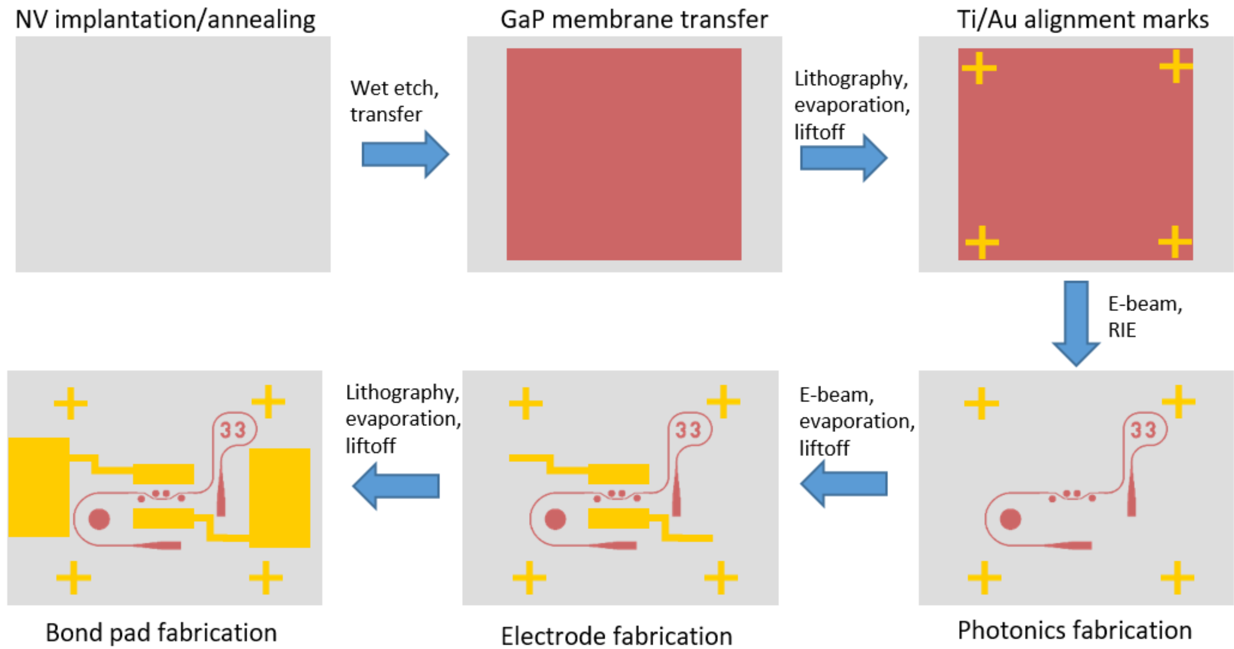

Figure 3.1: Illustration of the process flow involved in the fabrication of the NV-photonic integrated devices. The grey, pink and yellow represent diamond, GaP and gold layers respectively. Details of the fabrication process are provided in Appendix A.1-4

sphere in order to allow diffusion of vacancies to form NV centers. A subsequent 24-hour 460°C anneal was performed in air in order to oxygen-terminate the surface and improve stability of the negatively charged state of the near-surface NV centers[77]. A 125 nm thick GaP membrane was transferred to the diamond via epitaxial liftoff in hydrofluoric acid and van der Waals bonding[78]. Using negative-tone optical lithography (NR9-1000 resist, AD10:DI 3:1 developer), a set of 5 nm/50 nm Ti/Au alignment marks was fabricated on the GaP-on-diamond chip via evaporation and liftoff in acetone. These alignment marks were used for ensuring overlay between the electron beam lithography and reactive ion etching step that defined the photonic devices and the electron beam lithography and evaporation/liftoff step that defined the integrated Ti/Au electrodes and wires around the photonic devices.

Following definition of the alignment marks, hydrogen silsesquioxane (HSQ) was spin-coated to be used as the electron beam lithography resist. Photonic devices were patterned by electron-beam

lithography (JEOL 6300). Two reactive-ion etch (RIE) steps were then used to etch the devices. The first RIE step (3.0 mTorr, 1.0/6.0/3.0 sccm $Cl_2/Ar/N_2$, 235 V dc bias) was used to etch the GaP layer and the second (25.0 mTorr, 20 sccm O_2, 65 V dc bias) was used to etch the diamond. The diamond etch depth was $\sim$ 600 nm.

For the definition of metal electrodes, PMMA A8 495 was used as a positive resist for electron beam lithography. After development in 1:1 MIBK/IPA, 7 nm/70 nm Ti/Au was deposited via evaporation and liftoff in acetone. Thick 70 nm/700 nm Ti/Au bond pads for wirebonding were defined by negative-tone optical lithography (NR9-1000 resist, AD10:DI 3:1 developer), evaporation, and liftoff. The sample was then indium mounted on the sample holder, and ball/wedge ultrasonic wirebonding with Au wire was used to connect sample electrodes to the sample holder electroless nickel immersion gold PCB connections. Fig. 3.1 shows an overview of the fabrication process.

Due to variation in the local environment induced by ion-implantation and plasma processing, the NV centers experience local strain and electric field fluctuations. As a result of the static dipole moment of the NV's excited state, there is variation in ZPL emission energy both between different NVs and in the emission energy of a single NV over time (spectral diffusion). However, this dipole moment also enables electric field control of the defect's emission energy[13,41,42,74]. We provide this control through the addition of Ti/Au electrodes to this GaP-on-diamond photonics platform. Around each photonic device is a pair of Ti/Au electrodes with a $\sim 6\,\mu$m spacing. These electrodes allow application of an electric field transverse to the waveguides, with a simulated field strength inside the waveguide and disk resonators of a few MV/m (Fig. 3.4b), similar to values used in previous Stark effect tuning experiments[31]. Due to the <100> diamond surface, this externally applied field has components both parallel and perpendicular to the NV axis.

Of the 32 waveguides and 128 disk resonators fabricated on this sample, 12 waveguides had working electrodes such that a voltage-dependent response was observed from waveguide-coupled NV centers (38%). The remaining devices had either broken waveguides (10 devices, 31%), broken electrode leads (7 devices, 22%), or both (3 devices, 9%). In the intact waveguides, every waveguide had coupled NV centers whose emission could be observed via the grating coupler. Of the 128 disk resonators, 21 were located on intact waveguides with working electrodes and had cavity modes within Xe gas tuning range ($\sim$ 2nm) of the ZPL emission wavelength (16 % of the disk resonators). Xe gas tuning resulted in resonator-coupled NV centers in 8 of these 21 resonators. Thus, the overall

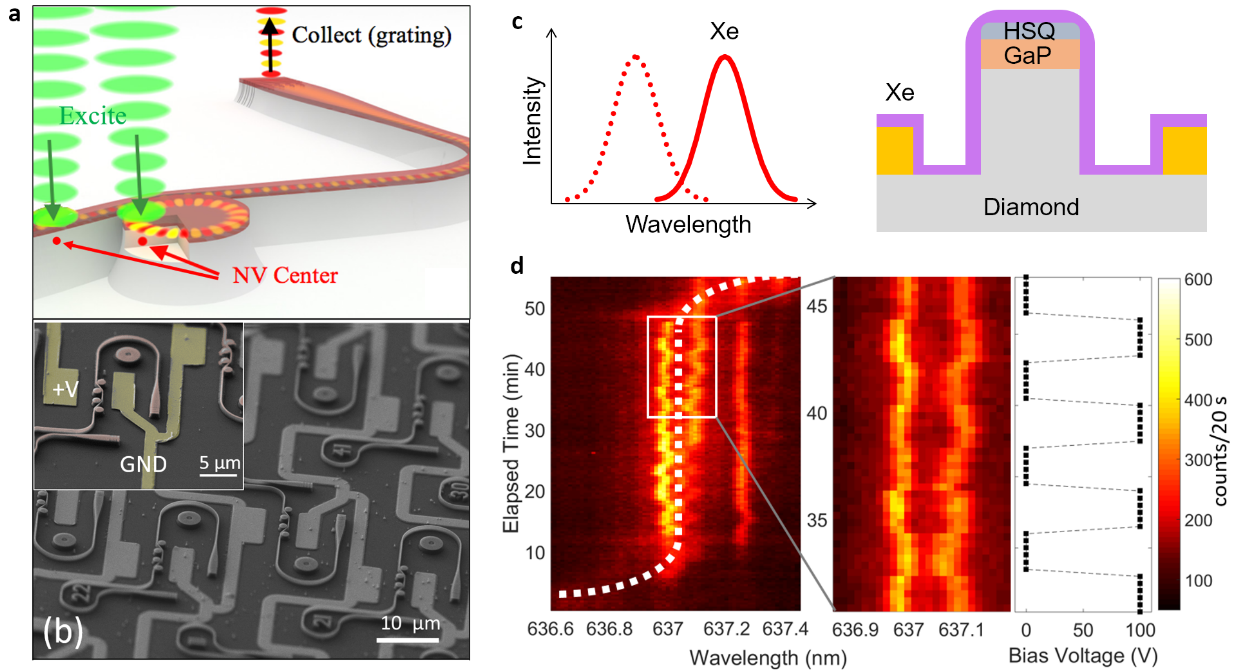

Figure 3.2: **a.** A schematic of the measurement configuration. The NVs coupled to either disk cavities or waveguides are excited by off-resonant 532 nm laser and the NV ZPL emission is collected at the output grating. **b.** Scanning electron micrograph (SEM) image of the fabricated devices. Inset: false color SEM image showing the diamond, GaP and gold (grey, pink, yellow) layers. **c.** By deposition of Xe gas (purple) on the disk cavities, the cavity resonance can be red-shifted. **d.** Left: Xe gas tuning of a disk resonator. The cavity mode is indicated by a dashed white line. The laser excitation spot is moved slightly between the two measurements at $t \sim 28$ minutes, resulting in the appearance of a second coupled NV center. At 50 minutes, the Xe gas flow is restored and the cavity tuned from resonance. Right: Stark tuning of the two coupled emission lines with the application of a square wave bias.

yield for resonator-coupled NV centers with working electrodes is 6 %. The photonic device yields are comparable with yields reported in previous GaP-on-diamond device fabrication attempts[76,79]. The addition of electrodes lowers the overall yield for the disk resonators, but increasing the number of disk resonators per waveguide from the 4 used here to 6 or more should offset this effect. The complete process flow is available in appendix 1-4.

3.2.2 Characterization of cavity-coupled NV centers

We first tune the cavity mode of a waveguide-coupled disk resonator onto NV ZPL resonance via Xe gas deposition, while monitoring the PL emission from the waveguide grating coupler. The Xe gas deposition results in a red-shift (Fig. 3.2c, d) of the resonator cavity mode. Coupled NV centers are bright when in resonance with the cavity mode and not visible otherwise[51]. The placement of NVs with respect to the optical mode is random; the ion-implantation fluence used to create the NV centers, was chosen such that probability of obtaining coupled cavities is high. Hence, several centers can be excited in a single laser spot (d ∼ 0.8 µm). In (Fig. 3.2d:left) there are several NV centers that couple to the cavity mode of this particular disk resonator.

In these devices, the average linewidth for a device NV center as measured in our standard grating spectrometer is 34.7 GHz with a standard deviation of 7.4 GHz (Figure 3.3a). This is based on fitting the observed linewidths of 15 waveguide-coupled NV centers. Using our high-resolution Echelle spectrometer we find a cavity NV linewidth of 6.3 ± 3.3 GHz from a set of 14 centers. We note that due to the higher resolution of this system, we are biased toward detecting NV centers with narrower linewidths. For comparison purposes, the standard spectrometer-limited and Echelle spectrometer-limited linewidths of a single deep as-grown NV center in this same sample is 16 GHz and 1.3 GHz (1 pixel), respectively. Thus the linewidths of the device-incorporated shallow implanted NV centers are overall larger than those of growth-incorporated deep NV centers.

3.3 Spectral behavior of cavity-coupled NV centers and stark tuning

With the cavity mode tuned to resonance with two individual NV centers, application of a square wave bias voltage to the integrated electrodes, results in repeatable shifting of the ZPL emission lines in response (Fig. 3.2d:right). This demonstrates our ability to reliably tune NV center emission energy even while coupled to a cavity mode, combining the enhanced emission rates from the cavity coupling with tunability from biasing the electrodes.

Measurements of the tuning range of many coupled NVs show substantial variation in voltage response (Figure 3.3b). In a set of 30 of the observed device-coupled implanted NV centers, no tuning was visible for 11 of the centers (37%) though this does not preclude tuning that we cannot

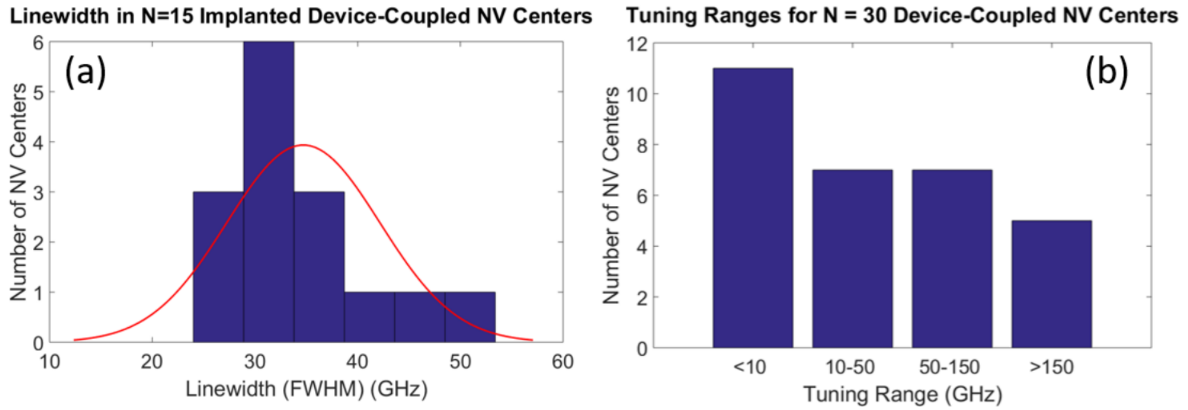

Figure 3.3: **a.** Linewidth of N= 15 device-coupled implanted NV centers (blue bars). Red line shows a normal distribution of mean 34.7 GHz, standard deviation 7.4 GHz. **b.** Tuning range of N= 30 device-coupled implanted NV centers.

observe with our spectrometer resolution. In 7 of the centers (23%), tuning was observed but the range was less than 50 GHz. In 5 of the NV centers (17%), the tuning range was between 50 and 100 GHz. In 7 of the centers (23%), the tuning range was larger than 100 GHz. In all centers where tuning was observed, hysteretic behavior was also observed. Fig. 3.4c shows the bias voltage response of an ensemble in a waveguide (Fig. 3.4a). One of the NV centers (red arrow), displays a large voltage-dependent tuning range of 190 GHz, while a nearby NV ZPL has a stable emission energy under the applied bias voltage (yellow arrow) and a third (green arrow) displays a large spectral diffusion ($\sim$ 70 GHz) uncorrelated with the applied bias voltage.

This variation in NV behavior can be attributed to several causes. The first factor is the center's relative orientation to the electric field. Longitudinal fields, parallel to the NV symmetry axis, will shift excited state energy levels linearly, while transverse fields will result in an excited state energy splitting that grows with increasing field[31,42].

The magnitude of these energy changes depends on the components of the NV dipole moment parallel to ($d_{||}$) and perpendicular to ($d_{\perp}$) the NV symmetry axis. The resulting energy shifts are thus:

$$\begin{cases} E_x = d_\perp F \approx 25 \text{ GHz} & \text{Case 1} \\ E_y = -d_\perp F \approx -25 \text{ GHz} & \text{Case 1} \\ E_x = d_{||}0.8F + d_\perp 0.6F \approx 31 \text{ GHz} & \text{Case 2} \\ E_y = d_{||}0.8F - d_\perp 0.6F \approx 1 \text{ GHz} & \text{Case 2} \end{cases} \tag{3.1}$$

where F is the magnitude of the electric field and the tuning ranges are calculated using literature-reported values for $d_{||}$ and $d_\perp$ of 4 GHz/MV/m and 5 GHz/MV/m respectively[80] and the previously simulated field magnitude of F =5 MV/m.

These values do not take into account the fact that observed Stark tuning coefficients are ~ 4 times larger under strong cw green excitation of the type used in our experiments[42,80], nor do they take into account photoinduced local fields. The total local field experienced by the NV centers are a combination of this local photoinduced field and the externally applied field. Additionally, the reported $d_{||}$, $d_\perp$ values are estimated to be correct only to within a factor of 2-3[80]. The fundamental mode of the waveguide is TE polarized (parallel to the applied external field), such that only NV transitions that emit in this polarization will be observed via the grating coupler. When accounting for these factors, the tuning ranges observed in our devices are consistent with what can be expected from the applied external field.

Previous work on Stark tuning of grown-in NV centers has shown similar variation in tuning ranges and voltage responses[31,41,42]. This variability in behavior even over small spatial scales presents a challenge to achieving the level of control required for chip-scale entanglement generation. In addition to spatial variability, we often observe temporal variability in the bias voltage response of these NV centers. The observed emission linewidths of these NV centers also suggest fast spectral diffusion of the ZPL energy.

3.4 Dynamic feedback stabilization of NV transitions

Chip scale entanglement generation will require addressing the spatial and temporal variations of implanted NV center energies so that multiple centers can be tuned to and maintained in resonance, despite the static and dynamic energy variation of these centers that results from implantation and

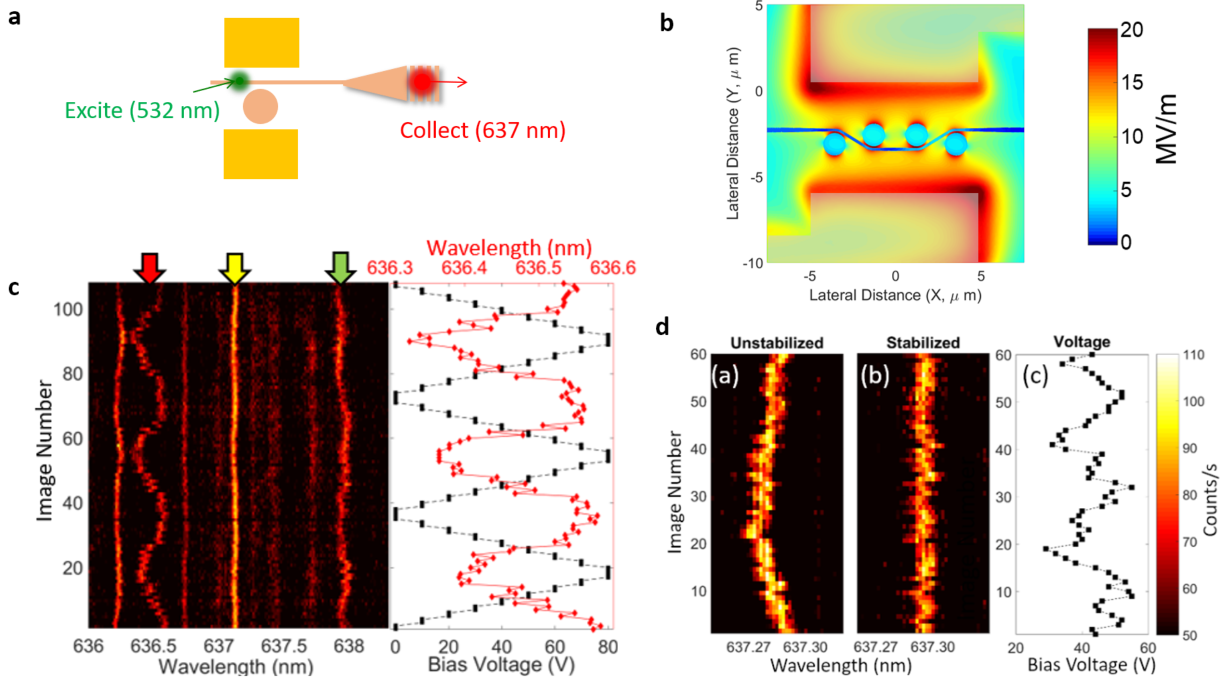

Figure 3.4: **a.** Optical characterization of waveguide coupled NVs. **b.** The distribution of electric field intensity across the photonic devices for a 100V bias across the electrodes.**c.** Spectral trace of multiple waveguide coupled NVs showing variation in ZPL emission energy and bias response over time. **d.** Dynamic frequency stabilization of ZPL emission from an individual waveguide coupled NV by applying a PID-feedback biasing voltage. (a) PL from an unstabilized ZPL at a constant 45 V bias voltage. The maximum spectral diffusion is 7.2 GHz and the average absolute difference from the center wavelength is 2.7 GHz. (b) Stabilized ZPL PL from a waveguide-coupled NV center. The maximum spectral diffusion is 3.9 GHz and the average absolute difference from the center wavelength is 1.2 GHz. (c) Bias voltage applied during active Stark effect stabilization of the ZPL in (b). NV PL is collected at the excitation spot due to the temporal drift of the cavity resonance over the time required for these measurements.

processing damage. Previous NV center emission energy stabilization experiments used photoluminescence excitation (PLE) measurements of grown-in NV centers for feedback control of the bias voltage[31], but the large dynamic energy variation of implanted NV centers annealed at 800°C makes PLE measurements difficult[44]. To obtain the necessary spectral resolution to demonstrate temporal stabilization, we thus utilized an Echelle spectrometer with 1.3 GHz resolution[31].

3.4.1 Voltage Feedback Algorithm

The applied bias voltage is updated per spectrum based on current peak position p. Due to the broad linewidths, a Gaussian of the form $y = a\exp\{[-(p-b)/c]^2\} + d$ is fit to a region around the desired ZPL emission line, where a is the intensity above background, b the center emission energy, c relates to the linewidth, and d is the background. The difference between the current emission line location and the initial line location Δp is then calculated and the bias voltage updated by a proportional integral derivative (PID) algorithm to correct for this error.

$$V_{new} = V_{prev} + (K_p\ \Delta p + K_i\ I + K_d\ D)\ V_{pix} \tag{3.2}$$

$$I = I + \Delta p\ \Delta V \tag{3.3}$$

$$D = (\Delta p - \Delta p_{old})/\Delta V \tag{3.4}$$

$$\Delta V = |V_{prev} - V_{old}| \tag{3.5}$$

where K_p, K_i and K_d are the PID parameters determined by a semi-supervised learning algorithm. For the data shown in Fig.3.4, K_p=0.8, K_i=K_p/500, K_d=K_p/10 and V_{pix}=4.17 V/pixel]. ΔV is the previous voltage step and Δp_{old} is the previous error in peak position. The PID algorithm delivers better stabilization than simple proportional feedback scheme which is shown in Fig. 3.5.

3.4.2 Stabilization results

To demonstrate feedback tuning, we identified a spectrally-diffusing NV center with a Stark tunability of $\sim$ 300 MHz/V over a range of 100 V. We measured the spectral diffusion of this NV center under a constant bias voltage of 45 V for 50 minutes (Fig. 3.4d.(a)). The measured linewidth was 4.5±1.2 GHz, a result of spectral diffusion of the ZPL emission during the integration time of the CCD camera. In the second measurement, the bias voltage was actively adjusted to stabilize the ZPL emission energy (Fig. 3.4d). After each 40s spectrum, the ZPL emission energy was determined and a correction to the bias voltage applied based on a PID algorithm. Under active stabilization, the NV exhibits a ZPL linewidth of 5.2±1.2 GHz.

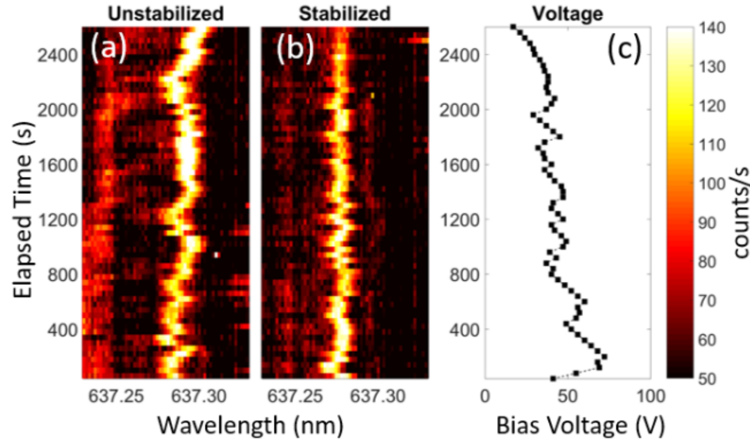

Figure 3.5: NV frequency stabilization using proportional feedback. **a.** PL from an unstabilized ZPL at a constant 45 V bias voltage. The maximum spectral diffusion is 8.3 GHz and the average absolute difference from the center wavelength is 3.2 GHz. **b.** Stabilized ZPL PL from a waveguide-coupled NV center. The maximum spectral diffusion is 4.5 GHz and the average absolute difference from the center wavelength is 1.3 GHz. **c.** Bias voltage applied during active Stark effect stabilization of the ZPL in **b.**. Feedback is purely proportional to the error in peak position i.e. K_p=0.8, K_i= K_d=0.

3.5 Summary and outlook

We have shown electric field control of the emission energy of photonic device-integrated implanted NV centers and feedback stabilization of this emission energy. Combined with the enhanced emission rates and collection efficiencies possible in photonic devices, these results are a necessary component of chip-scale entanglement generation. The performance of these devices can be improved by implementing the following:

1. Pre ion-implantation surface processing of the CVD diamond samples[81] can result in near-surface NV centers with narrower linewidths and smaller spectral diffusion. This will enable the use of PLE measurements for the requisite fast feedback stabilization and better enable the generation of indistinguishable photons from separate NV centers.

2. Post ion-implantation, annealing samples at a higher temperature (at $>1000\,^{\circ}$C vs $800\,^{\circ}$C used in this work) should result in dissociation of many non-NV defects (di-vacancies, NV_xH_y

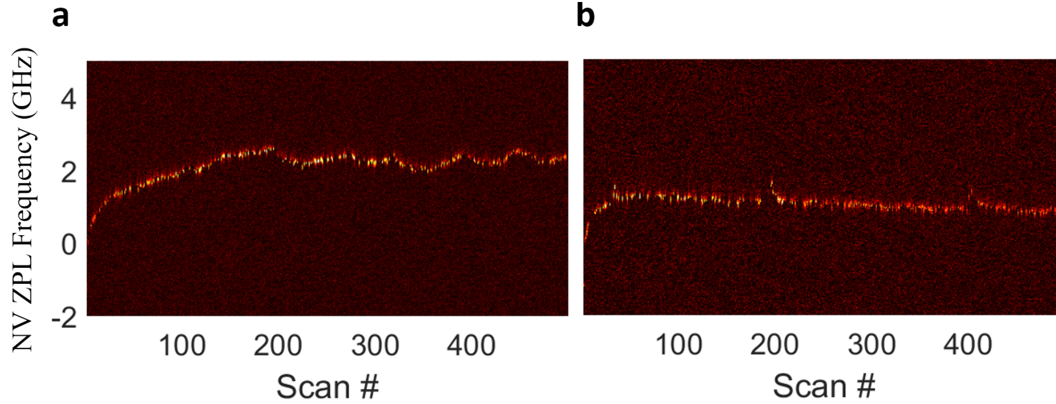

Figure 3.6: PLE measurements of an individual implanted NV center (100 nm deep) at low temperature (8 K) exhibiting a ZPL linewidth of ∼200 MHz **a.** Intrinsic temporal variation in the ZPL emission frequency without any applied bias. **b.** Reduced temporal variation in the ZPL emission frequency with dynamic Stark tuning.

complexes, etc.) resulting in better charge state stability and reduced perturbation of the NV environment under optical excitation. We explore this in detail in the next chapter.

3. Photonic devices optimized for coupling with deeper (∼100 nm) NV centers. Deeper NVs are screened from surface-chemistry related Fermi-level variations, surface-charge fluctuations and the near-surface layer of damage caused by ion-implantation and fabrication processing.

4. Photonic device design can be constrained from etching into the diamond, further reducing the strain and charge-trap driven electric field fluctuations experienced by the NVs.

5. Future device designs can incorporate both aligned ion-implantation and multi-axis Stark control to improve the yield of tunable NV centers.

With these improvements, it should be possible to perform on-chip generation of indistinguishable photons from multiple NV centers with the collection rates necessary for scalable entangled state generation. As a proof-of-concept, we implement improvements 1 thru 3 by patterning electrodes on an implanted bare CVD diamond (no photonic integration). On this test sample, NVs are formed ∼ 100 nm from the surface by N-implantation at a higher energy (85 keV vs 20 keV).

Dynamic Stark tuning of individual NVs show very promising ZPL linewidths ($<$200 MHz) and reduced temporal spectral variation (Fig. 3.6). Encouraged by these results, we incorporate improvements 1 thru 4 for NV-coupled inverse-designed photonic devices demonstrated in chapter 5.

Chapter 4

Formation of NV centers by annealing

To preserve the homogeneity of NV emission energy and minimize spectral diffusion, we have observed that it is necessary to maintain the integrity of the NV defect environment within the diamond lattice. Hence, knowledge of the NV center formation kinetics in diamond is critical to engineering quantum information devices based on this defect. Here we utilize the longitudinal tracking of single NV centers to elucidate NV defect kinetics during high-temperature vacuum annealing from 800-1100 °C in high-purity chemical-vapor-deposition diamond. We observe three phenomena which can coexist: NV formation, NV quenching, and NV orientation changes. Of relevance to NV-photonic integration, a 6 to 24-fold enhancement in the NV density, in the absence of sample irradiation, is observed by annealing at 980 °C, and NV orientation changes are observed at 1050 °C. With respect to the fundamental understanding of defect kinetics in ultra-pure diamond, our results indicate a significant vacancy source can be activated for NV creation between 950-980 °C and suggest that native hydrogen from NVH_y complexes plays a dominant role in NV quenching, supported by recent *ab initio* calculations. Finally, the direct observation of orientation changes allows us to estimate an NV diffusion barrier of 4.7 ± 0.9 eV.

This chapter has been published as:

Chakravarthi, S., Moore, C., Opsvig, A., Pederson, C., Hunt, E., Ivanov, A., Christen, I., Dunham, S. and Fu, K.M.C., 2020. **Window into NV center kinetics via repeated annealing and spatial tracking of thousands of individual NV centers**. Physical Review Materials, 4(2), p.023402. Copyright 2020 by the American Physical Society.

https://doi.org/10.1103/PhysRevMaterials.4.023402

4.1 Introduction

On-demand formation of NV centers is achieved by bombarding the diamond surface with high energy ions. The implantation process results in substantial damage to the diamond lattice. For example, a nitrogen ion accelerated to 50 keV will leave a trail of over 100 vacancies when it impacts the diamond surface. Post-implantation, annealing the diamond at high temperature (800 to 1200 °C) under vacuum (to prevent etching/graphitization of the diamond surface) heals the damaged lattice and provides energy required for defect formation. Here, NV centers can either be formed by vacancy recombination with native or implanted nitrogen. However, this process also results in the formation of vast number of undesirable defects (V_2NH, V_xH_y, N_xVH_y, etc.) that modify the local Fermi-level and introduce electric-field fluctuations under optical-excitation, resulting in NV^- charge-state instability and spectral diffusion. Of significant interest are methods to synthesize NV centers with minimal perturbation to the local environment, preserving the quantum and optical properties of the center. Additionally, we would like to tailor the NV orientation for optimum coupling to photonic structures. Preferential NV alignment has only been demonstrated for NVs incorporated during the diamond CVD growth process for <111> substrates. Post-growth, controlled re-orientation of NV centers would be a great asset to the NV community.

Full control over NV^- center formation requires a detailed understanding of all the underlying defect kinetics. By characterizing a pristine diamond sample and performing a series of annealing experiments (under different temperatures and durations), we can deduce details of defect formation and kinetics of native defects.

4.2 Confocal photoluminescence maps of NV centers

We perform repeated vacuum annealing of CVD diamond, and track individual NV centers between anneals via photoluminescence confocal microscopy of a large experimental volume ($350 \times 350 \times 25$ µm^3) 100 µm from the diamond surface.

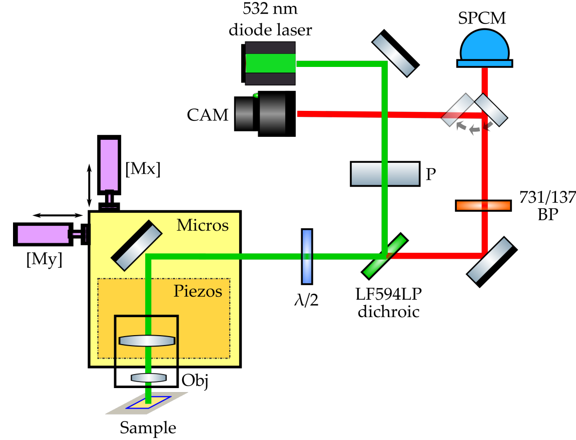

Figure 4.1: Schematic of the microscope setup for off-resonant excitation and NV photoluminescence measurement. The diamond sample is at room temperature (298K).

4.2.1 Optical measurement setup

To characterize NV centers, off-resonant optical measurements are performed using a home-built confocal microscope (Fig. 4.1) with a 0.75 NA, 40x objective (Nikon Fluor 40X). A piezo stage (MadCityLabs nano-positioner) was used for imaging 50x50 μm^2 area scans (see Fig. 4.2), while a micrometer stage comprised of two 25 mm actuators (Newport TRA25CC) was used to move to sequential scanning locations in steps of 40 µm. A 637 nm laser reflection signal was used between subsequent piezo scans to track the sample surface to maintain the experimental depth to within 2 µm.

The nitrogen-vacancies were optically excited with a 532 nm diode-pumped solid-state laser (RGBLase LLC FB-532-100-FS-FS-010-1N) at powers between 4-5 mW with a spot diameter of $\sim$1.6 µm. The spot size was chosen to increase the number of NV^- centers within the depth of focus. The microscope point spread function is an ellipsoid with axes 1.8 µm, 1.5 µm, and (10$\times$2.4) µm. A linear polarizer (ThorLabs LPVIS100) was used in the excitation path and a half-wave plate was used to preferentially excite a given NV^- orientation. NV^- phonon-sideband emission was filtered into the collection path by a combination of dichroic beam splitter (Semrock LF594LP) and a 660-800 nm bandpass filter (Semrock FF01-731/137-25). The NV^- photons were measured with an avalanche photodiode (Excelitas SPCM-AQ4C).

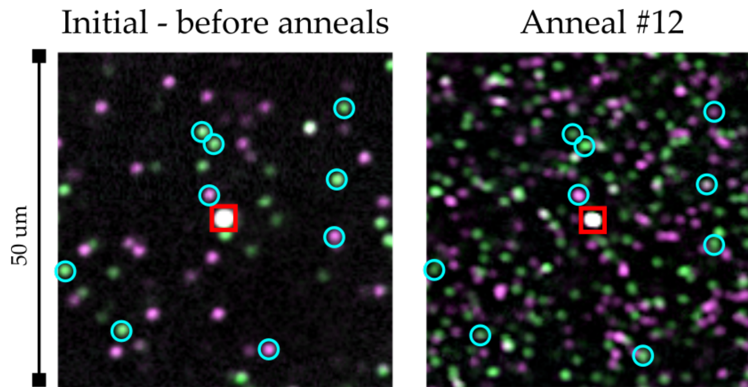

Figure 4.2: A single (50 µm × 50 µm) area scan data showing the increase in NV^- density from initial (no-anneals) state to post anneal #12 (maximum NV^- density) in the same region. The blue circles mark NVs retained through the anneals. The red square marks a persistent defect used for image registration.

4.2.2 Data analysis techniques

Large-area scan stitching: large-area scans, composed of 9 × 9 overlapping 50 µm × 50 µm scans for each of the two distinguishable orientations, were stitched into composite images with a custom tool. First, the tool performed normalization across all individual scans to ensure uniform appearance of NV intensities in the output images; then it calculated pairwise alignments (via digital image correlation with subsequent brute-force optimization) for all adjacent area scans along with corresponding misalignment scores. The final composite image was produced by selecting pairwise alignments forming a minimum spanning tree (MST, see Fig. 4.3(a)) with respect to the misalignment scores. This fully-automated process generally produced quality results; however, in order to compensate for possible imperfections, the tool also allowed manual adjustments of pairwise alignments in the MST. The tool is publicly available on github (https://github.com/optospinlab/lateral-scan-analysis).

Registration of large-area scans: Successive pairs of large-area scans were aligned using affine homography transformation (performed by *ImageJ*[82,83]). Essentially, this transformation amounted to a rotation and perspective transformation such that NV^- centers present in both scans overlapped, which compensated for discrepancies in the orientation and tilt of the sample under the microscope. The overlapping regions of aligned pairs of successive scans were then compared by

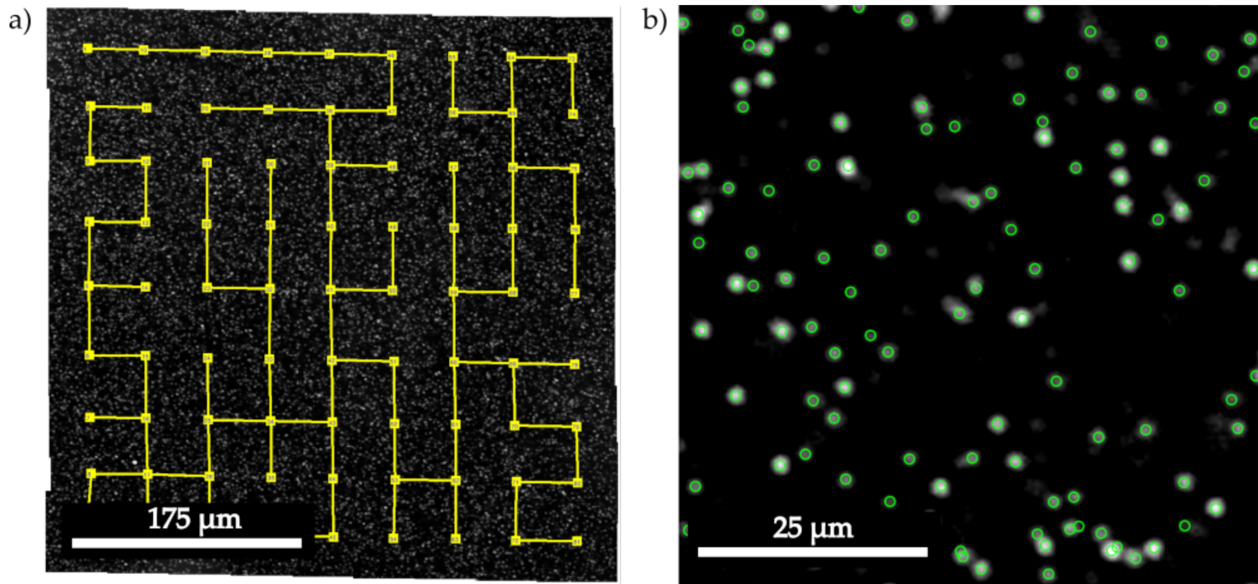

Figure 4.3: (a) 350 µm × 350 µm stitched large-area scan after anneal #12 showing the MST graph. (b) A 50 µm × 50 µm scan showing NV^- position detection via CHT algorithm.

means of image subtraction, which allowed manual and automated detection of the changes in the spatial maps of the NV^- centers.

Tracking NV^- changes: The registered large-area scan images from consecutive anneals (say anneal A & B) are processed through an image subtraction algorithm after normalization. First the data sets A & B are converted to 3D matrices, with the array indices indicating {position x , position y, orientation (1 or 2)} and the array values representing the intensity (measured photon counts). Each individual scan constituting matrices A & B were normalized prior to stitching, however excitation laser power and collection efficiency can vary slightly between anneals. Thus NV^- intensity histograms of the two data sets (A & B) are used for normalization (factor N) between anneals. This allows us to clearly identify and subtract the background during comparison. The following matrix algebra was performed to extract appearance, disappearance and orientation-

change information:

$$C = A(x, y, 1)/N - B(x, y, 1) \tag{4.1}$$

$$D = A(x, y, 2)/N - B(x, y, 2) \tag{4.2}$$

$$E = C + D \tag{4.3}$$

$$F = C - D \tag{4.4}$$

$$\text{Appearances}(x, y) = \begin{cases} -E & \text{if } E < 0 \\ 0 & \text{if } E \geq 0 \end{cases} \tag{4.5}$$

$$\text{Disappearances}(x, y) = \begin{cases} E & \text{if } E \geq 0 \\ 0 & \text{if } E < 0 \end{cases} \tag{4.6}$$

$$\text{Orientation changes}(x, y) = \text{abs}(\ \text{abs}(F) - \text{abs}(E) \times F) \tag{4.7}$$

For visualization of differences, the three matrices; Appearances, Disappearances and Orientation changes, represented by blue, grey and yellow colors respectively, are combined into a single RGB image to generate the difference image, shown in Fig. 4.4. The next step after the identification of differences is to map the spatial location (x,y) of every NV with the corresponding changes, if any. This allows us to track the evolution of every individual NV^- defect through all the anneals. This is performed by MATLAB code implementing the Circular Hough Transform (CHT) to detect NV^- centers and record their centroid (see Fig. 4.3(b)). This code also provides the total number of NV^- centers and differences reported in Fig. 3 of the main text. A similar code is used to process the depth scan data. The processing code and raw data are available here upon request.

Conversion from NV^- number/area to density: While each large-scan area was nominally $(360\ \mu m)^2$, due to an image offset, image rotation, or failed stitching, only a subset of this area could be reliably matched before and after each anneal. This cropped area was utilized, in addition to the 25 µm confocal depth of focus, to obtain the NV^- density used in Table I and Fig. 3 in the main text. Table 4.1 provides the NV^- counting data and crop areas for sample B.

Anneal #	1-3	4,5	6,7	8	9, 10	11	12	13	14	15	16
Area (μm)^2	$(282)^2$	$(287)^2$	$(285)^2$	$(299)^2$	$(307)^2$	$(298)^2$	$(291)^2$	$(339)^2$	$(331)^2$	$(303)^2$	$(311)^2$
Total NVs	2126	2822	3213	4635	5579	8772	9174	11511	10080	8225	8456
Appear.	732	1101	672	1014	664	3641	1266	543	122	56	70
Disappear.	145	602	47	41	19	80	157	618	1478	90	181
Reorient.	6	17	1	6	4	64	129	272	1163	1642	3093

Table 4.1: Raw NV^- counting data used in Fig. 4.5.

Uncertainty estimate in total NV^- density: For each anneal, this estimate consists of two components, E_1 and E_2, added in quadrature. E_1 represents error due to the automated image analysis. This error is estimated by comparing the change in the total NV's counted before and after each anneal to the difference in appearances and disappearances detected. E_1 ranges from 2-10%. The second uncertainty E_2 arises from the density variation across the scan area combined with the different comparison areas used. Assuming a random density variation with the magnitude given by Fig. S4 and the crop-areas given in Table S1, this density variation results in an estimated uncertainty of 4%.

4.3 Study of NV annealing dynamics

We observe a 6-fold increase in the overall concentration of NV centers due to annealing at 980 °C (Fig. 4.5, orange). This indicates there is a source of vacancies within CVD diamond at moderate temperatures that enables one to significantly increase NV density without introducing additional lattice damage via irradiation. Individual NV tracking allows us to go beyond measuring simple net increases and decreases. Coincident with appearances (Fig. 4.5, blue), we are able to observe significant NV disappearances, with peaks in disappearances near 960 °C and 1050 °C (Fig. 4.5, grey). The disappearances near 960 °C provides an essential clue regarding the quenching process at higher temperatures. At 1050 °C, we observe large-scale NV center orientation changes (Fig. 4.5, yellow). After the first 1050 °C anneal, orientation changes are observed in the absence of a significant number of disappearances or appearances. Thus, only partial N-V dissociation occurs at these temperatures. This lack of full dissociation indicates the observed disappearances at 960 °C

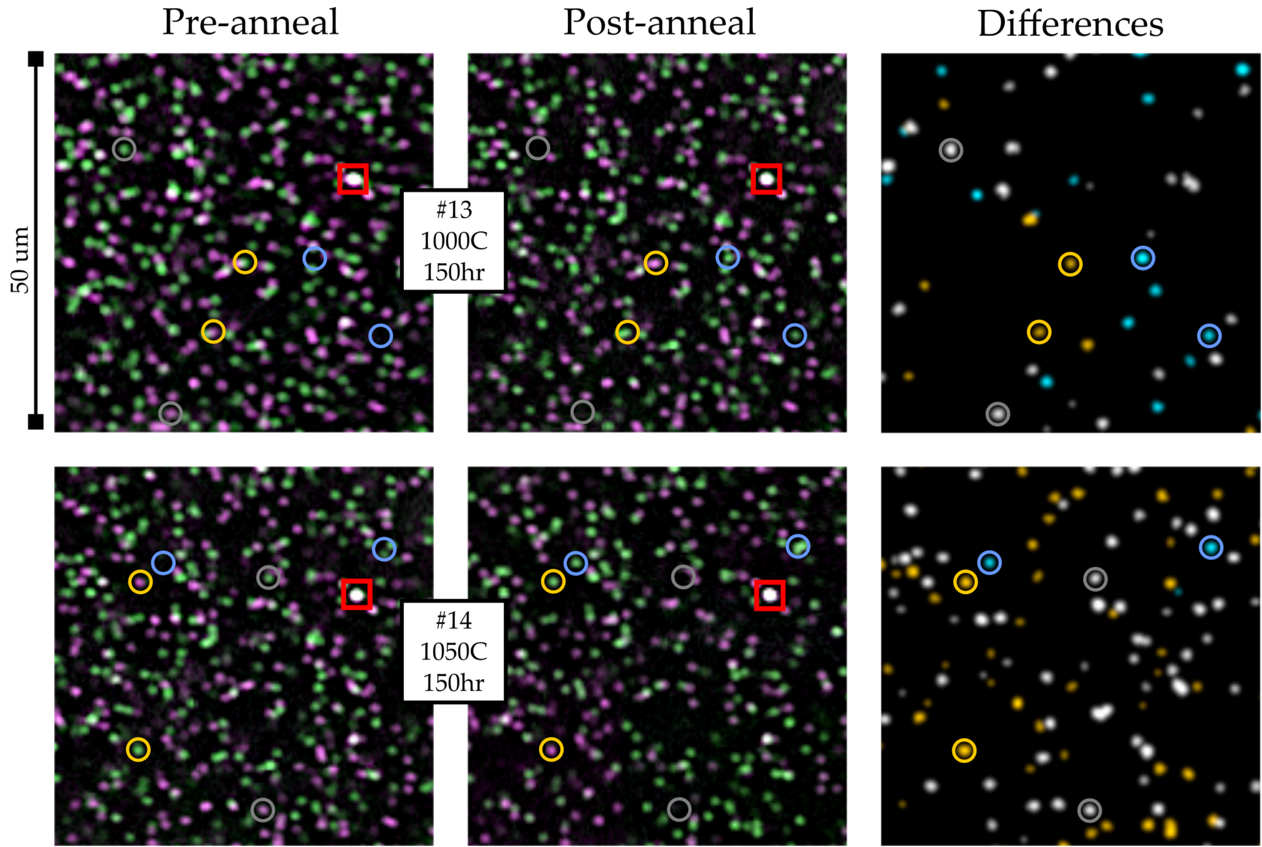

Figure 4.4: A sequence of subareas of the "large-area scan" confocal images showing NV^- changes. Green and magenta indicate the two sets of distinguishable NV^- orientations. Two examples each of appearances, disappearances and re-orientations are indicated by blue, grey and yellow circles, respectively. The red square marks a persistent defect used for image alignment.

and 1050 °C are not due to N-V-disassociation but due to a quenching source (e.g. H). Finally, beginning at temperatures above 1000 °C, we begin to observe almost complete NV quenching originating from the surface.

Based on the above results, we can deduce the kinetics of NV appearances, disappearances and orientation changes.

4.3.1 Appearances of NV centers

There are three candidate processes for NV center appearances: charge state conversion of $NV^0 \rightarrow NV^-$, direct dissociation of NVH $\rightarrow$ NV + H, and diffusion and capture of single vacancies, N+V

$\rightarrow$ NV.

- In high-purity type IIa diamond, both the neutral and negatively charged state of NV centers are stable under optical excitation. The ratio of the two populations at a given Fermi-level depends on the excitation wavelength and intensity[84,85]. In agreement with other groups studying high-purity CVD diamond with 532 nm excitation[86,87], we find NV^- is the dominant charge state in pre- and post-annealed samples.

- If NV is formed by the dissociation of a larger complex, the homogeneity and scale of NV^- appearances indicate this dissociating species should be uniform and abundant. In similar CVD samples, the NVH density is 10 times greater than the NV^- density[88], suggesting NVH as the NV source. However, the dissociation of NVH $\rightarrow$ (NV + H) can be ruled out as this complex is observed to be stable until 1400 °C[89,90].

- Single vacancies combining with native nitrogen is a third possible source. Single vacancies can exist in the neutral and negative (V^0 or V^-) charge states in diamond in which NV^- is the dominant NV charge state. It is generally accepted that vacancies are only mobile in their neutral charge (V^0) state at temperatures above 700 °C, with an activation energy of 2.3 eV[91]. However, it has been confirmed that the NV center forms as a unit during CVD growth[88,92] and not via vacancy capture. Thus during growth, all vacancies incorporated are either in the V^- state or trapped in complexes (V_2, NVH, VH, etc.). Divacancy (V_2) dissociation can be ruled out because it has been observed to anneal out at 800 °C[93] and other complexes have high (>1100 °C) dissociation temperatures. This leaves the negative vacancy (V^-). *Ab initio* calculations estimate a 3.4 eV migration energy for V^-[94]. Assuming a 30 THz attempt frequency, this migration energy corresponds to a diffusion length on the order of 100 nm for a 150 hour anneal at 980 °C. While there is uncertainty in both the migration energy and attempt frequency, direct migration and trapping of V^- appears to be a viable candidate for NV center formation.

NV formation in the absence of irradiation has previously been reported between 1500-1600 °C[95,96] in CVD diamond. The vacancy source in these reports could be similar to what we observe in our lower temperature, longer duration anneals, or could be due to dissociation of NVH[89,90] or VH[97].

Anneal #	1	2	3	4	5	6	7	8	9	10	11	12	13	14	15	16
Temp, °C	800	800	950	960	960	970	970	970	980	980	980	980	1000	1050	1050	1050
Time, h	2	10	10	10	10	2	10	20	2	10	150	150	150	150	150	150

Table 4.2: Details of anneals conducted on the sample.

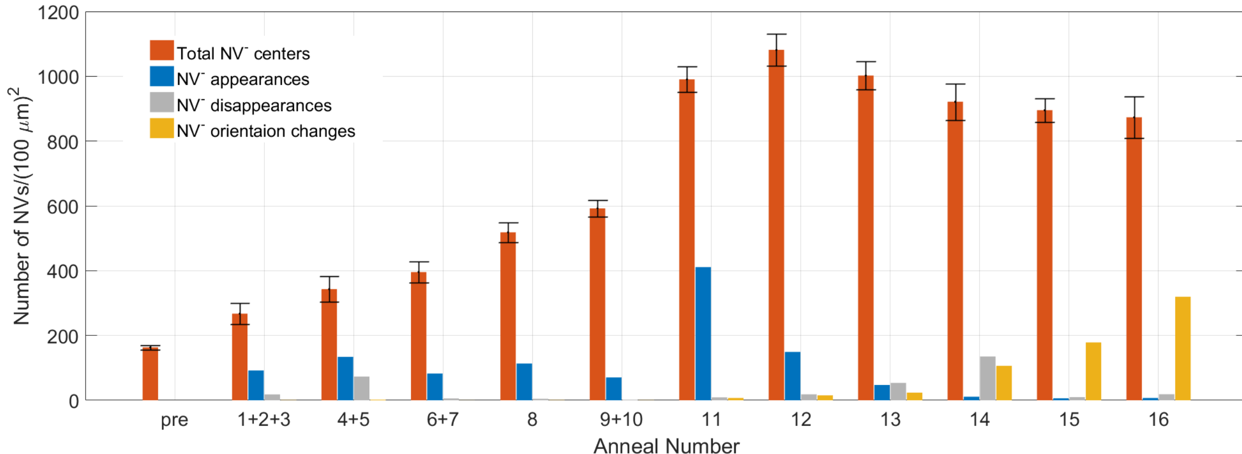

Figure 4.5: Total NV^- density and observed changes obtained from the stitched confocal scans ($\approx 350 \times 350\ \mu m^2$) after every anneal. Several anneals are combined due to an inability to accurately match a significant portion of the scan area in the intermediate scans. For combined anneals, comparisons are made before and after the first and last anneal. Error bars represent uncertainty due to automation errors and differences in scan area between datasets. Note the significant increase in annealing time which occurs at anneal 11.

4.3.2 Disappearances of NV centers

The spatially homogeneous disappearances occur at temperatures below the full NV^- dissociation temperature (which our data show must be above 1050 °C), strongly suggesting another impurity is being trapped at the NV site. Hydrogen is the most likely candidate. Given the abundance of C, N, H, and vacancies in our samples, complexes either in the form of CH[98,99], NH[99], V_xH_y[90,100,101] or N_xVH_y[90,97,102] are potential spatially homogeneous hydrogen sources.

A comparison of our experimental results and recent *ab initio* calculations indicate the NVH_y complex, in which $y \in \{1, 2, 3\}$ is a plausible H source for the observed NV^- quenching near 960 °C and 1050 °C. Salustro *et al.*[101] calculated the dissociation energies, E_H, for the following reaction path,

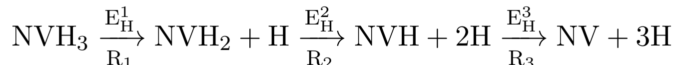

$$\mathrm{NVH_3} \xrightarrow[\mathrm{R_1}]{\mathrm{E_H^1}} \mathrm{NVH_2} + \mathrm{H} \xrightarrow[\mathrm{R_2}]{\mathrm{E_H^2}} \mathrm{NVH} + 2\mathrm{H} \xrightarrow[\mathrm{R_3}]{\mathrm{E_H^3}} \mathrm{NV} + 3\mathrm{H}$$

finding $E_H^1 = 2.83$ eV, $E_H^2 = 3.17$ eV, and $E_H^3 = 3.68$ eV. The dissociation rate for a given reaction is given by $R_i(T) = \nu_i \exp\big(-(E_H^i + E_D)/k_B T\big)$, in which T is the annealing temperature (in K), E_D is the dissociation barrier, and ν_i is the rate for capture of the H by the NVH complex. The ν_i primarily depend on the hopping rate for interstitial H and can be expected to be nearly the same for all the complexes. If we assume R_1 (the rate at which $NVH_3 \rightarrow NVH_2 + H$) becomes discernible at 960 °C (the temperature at which we first observe disappearances), we can estimate when R_2 become discernible using $R_2(T_2) \approx R_1(960\ °C)$, finding $T_2 \approx 1110$ °C. While this is higher than our observed second peak in disappearances at 1050 °C, we note that the 1050 °C anneal was more than 7 times longer than the 960 °C anneal. Extrapolating further to the dissociation of NVH, we obtain that $R_3(1330\ °C) \approx R_1(960\ °C)$. $T_3 = 1330$ °C is consistent with the experimental observation of NVH disappearance beginning near 1400 °C during shorter, 4 hour anneals[89,90]. We cannot use these annealing times to quantitatively predict when the ratios between R_1, R_2, and R_3 will become equal as disappearances typically saturate during each anneal. This saturation suggests a depletion of the H source. Qualitatively, however, the larger magnitude of disappearances at 1050 °C is consistent with a larger expected density $[NVH_2]$ relative to $[NVH_3]$.

Additionally, near-total NV depletion near the surfaces was observed starting at 980 °C, with the depletion layer growing in subsequent anneals. The surface dependence suggests a second, inhomogeneous, surface-driven hydrogen source. The observation of a surface-driven depletion suggests it may be desirable to protect the diamond surface to preserve near-surface NV centers during annealing.

NV PL quenching has been reported in the literature over a wide range of temperatures from 1100-1500°C[103–106], with higher temperature quenching often attributed to NV migration to form larger complexes[106,107]. Due to the short N_s diffusion length, complex formation with multiple N atoms (e.g. N_xVH_y, N_xV) can only explain quenching in high-N_s samples[95]. Our results indicate the following factors could contribute to the observed variance in NV quenching reported in the literature: (1) Compositional sample variance with respect to hydrogen traps, (2) Simultaneous creation and quenching events with the specific annealing temperatures and times determining a net outcome in either direction and (3) the hydrogen content in the annealing furnace, suggested by our observed surface dependence of the depletion layer.

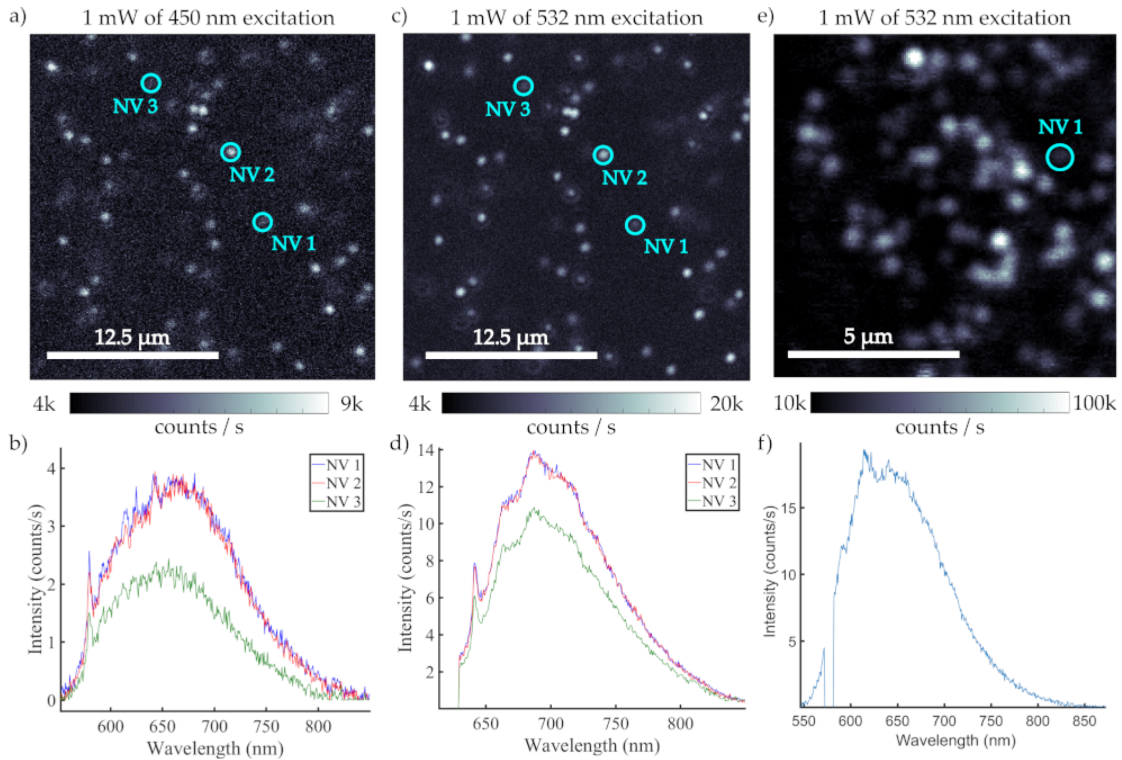

Figure 4.6: (a,b) Confocal scan and spectra of 3 NVs in sample B taken with 450 nm excitation. (c,d) Confocal scan and spectra of same 3 NVs in sample B taken with 532 nm excitation. (e,f) Confocal scan and spectra of NV^0 from a reference sample taken with 532 nm excitation.

NV charge state identification

We consider charge state conversion from the bright NV^- charge state into the dark NV^0 as a possible explanation for NV disappearances in our scans by investigating the depletion region of sample B. 4.6(a,c) show confocal scans taken of the same region with 1 mW of 450 nm and 532 nm excitation respectively. Collection in 4.6(a) includes wavelengths greater than 539 nm while 4.6(c) includes only collection above 600 nm. 532 nm excitation is commonly used to detect NV centers, however the relatively bright first (575 nm) and second (611 nm) order diamond Raman lines occur in the NV^0 PL band, which could obscure the weak PL from a single NV^0. We utilize 450 nm excitation to solve this issue since the first order (479 nm) and second order (511 nm) Raman lines are no longer collected. If charge state conversion were to be responsible for the disappearances,

we would expect to see defects in the 450 nm confocal scan that did not appear in the 532 nm confocal scan, but this is not observed. 4.6(d) shows characteristic, background subtracted spectra of 3 NVs in the scan region under 532 nm excitation, resulting from the NVs existing in the ratio of NV^0 to NV^- as 1:3. NV-3 is dimmer than the other NVs due to the orthogonal polarization. In 4.6(b) we only observe NV^0 PL from the same 3 defects under 450 nm excitation, indicating that NV^- ionizes without contributing to the PL. We are thus able to observe single NV^0. On these grounds we exclude charge state conversion as a cause for disappearances. For reference, spectra from a sample containing predominantly NV^0 is shown in 4.6(e,f).

4.3.3 Orientation changes of NV centers

Recently, a loss of preferential orientation was observed in ensembles of oriented NV centers[105] also at 1050 °C. The mechanism for this orientation change was believed to involve the full dissociation of the NV center with subsequent recombination with either the original N or another N in the lattice. Our single defect tracking shows that full dissociation does not occur at 1050 °C. If the vacancy is able to migrate, we would expect to observe orientation changes accompanied by NV disappearances. Additionally, if the vacancy diffusion length is comparable to the N_s-N_s spacing (∼1 µm in sample B), we would also expect to see new NV^- appearances. However, after an initial round of disappearances in the first 1050 °C anneal, we primarily only observe orientation changes. This suggests there is an attractive force, extending to at least the 3rd nearest neighbor (the minimum separation required for NV re-orientation), between the vacancy and the nitrogen[107]. While practical implementation may be challenging, this result opens a path toward preferential orientation by annealing under strain[108].

If many re-orientation cycles occur during a single anneal, we would statistically expect 50 % of the NV centers will undergo a detectable orientation change. The maximum fraction of orientation changes we observe is 37 % during anneal 16, suggesting that NV centers do not undergo multiple re-orientation cycles during each anneal. Thus, we can utilize the fractional rate from anneals 11-16 to estimate the orientation-change barrier E_b using the re-orientation rate $R = \nu \exp(-E_b/kT)$. A fit to the data gives $E_b = 4.7 \pm 0.9$ eV. This value is comparable to the theoretical value of 4.85 eV[107] determined by density functional theory calculations. With a larger dataset and annealing times in

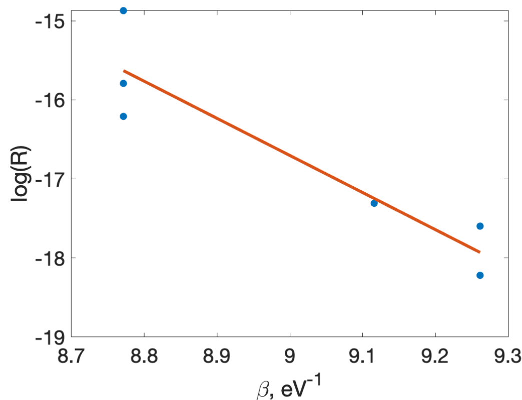

Figure 4.7: Log of the reorientation rate as a function of $\beta = (k_B T)^{-1}$

which thermal equilibrium is reached for all processes, this method of observing orientation changes could be used to provide benchmarks for theoretical estimates of ν and E_b.

Estimation of NV reorientation barrier

The reorientation rate was calculated for anneals 11-16 using the data in Table 4.1 and the 150 hour anneal time. We neglect the effect of appearances and disappearances and the possibility of multiple reorientation cycles in a single anneal. The fractional change between two distinct orientations, e.g. orientations 1 changing to 2, is $F_{12} = \Delta N_{12}/N_1$ in which ΔN_{12} is the number of changes from orientation 1 to 2 and N_1 is the population of orientation 1. We can approximate $F_{12} = \Delta N_{12}/N_1 = \Delta N_{\text{total, exp}}/(N_{\text{total}})$, in which $N_{\text{total, exp}}$ is the total number of reorientations experimentally detected and N_{total} is the total number of NV^- centers. This approximation assumes all orientations are equally populated and all orientation changes are equally probable. In calculating the fractional change, we utilized the population of the NV^- centers before the anneal. To calculate the rate, we divide the fractional change by the annealing time.

The rate for a single orientation change, *e.g.* R_{12} from orientation 1 (green) to 2 (purple), will be given by $R_{12} = F_{12}/t = \nu \exp(-E_{b,12}/kT)$ where t is the anneal duration and T is the anneal temperature in K. In Fig. 4.7, $\log(R_{12})$ is plotted as a function of $\beta = (k_B T)^{-1}$ and is fit to a line. The absolute value of the slope determines the re-orientation barrier E_b and the

x-intercept determines log(ν), which ν is an effective attempt frequency. A least square fit gives $E_b = 4.7 \pm 0.9eV$ and $\nu = \exp(26 \pm 9)$ s^{-1}. Both the calculated value of E_b (4.85 eV[109] and a typically used attempt frequency of 30 THz lie in the uncertainty range.

4.4 Summary and outlook

The formation and dissociation of observable defects has long been used to probe defect kinetics in crystals. For example, a model for vacancy diffusion in diamond was facilitated by correlating V^0 (GR1) emission, V^- (ND1) absorption, and NV^- emission in ensembles of defects[91]. However, ensemble measurements such as photoluminescence, visible and infrared absorption spectroscopy, and electron-spin resonance techniques, do not provide sufficient resolution and lack the sensitivity to probe competing mechanisms driving point defect kinetics (appearances vs disappearances; individual orientation changes). Nor do they typically have the sensitivity to probe ultra-pure diamond samples with very low defect density (< parts-per-trillion) such as those now utilized for quantum information applications. Here we extend this ensemble technique using confocal microscopy, a tool capable of detecting single defects in bulk crystals. Three results relevant to engineering NV centers for photonic integration are obtained:

1. The observation of NV^- density enhancement in the absence of sample irradiation at 950-980 °C. This suggests that for the highest implantation to NV yield, we should pick a anneal temperature higher than 980°C.

2. NV^- re-orientation in the absence of full NV dissociation at 1050 °C and NV quenching (likely from NVH_x complexing) below 1050 °C. This points to an ideal annealing temperature of around 1050 to 1200 °C, where NV centers are energetically stable but many concomitant bulk defects in diamond are removed by dissociation and recombination.

3. A near-surface NV^- depletion region is observed for long anneals (> 1-week). This could be the result of gradual hydrogen-diffusion into the diamond and NVH_x complexing/Fermi-level pinning at the diamond surface. Further studies are required to confirm the exact mechanism.

Chapter 5

Inverse-designed GaP photon extractors integrated with NV centers

Inverse-design optimization of photonic devices enables unprecedented flexibility in tailoring critical parameters of a spin-photon interface including spectral response, photon polarization and collection mode. Further, the design process can incorporate additional constraints, such as material processing limitations. Based on results from the previous chapters, we constrain our photonic design to couple to NV centers implanted deeper (100 nm below surface) in the diamond, with the device defined by an etch only through the GaP layer, leaving the underlying diamond defect host undisturbed. Post-implantation we anneal the diamond at a higher temperature (1200°C, in vacuum) to heal the implantation damage and mitigate bulk defects. Large enhancement (14-fold) of the NV ZPL photon collection efficiency is observed. Spectroscopy of coupled NV centers shows reduced spectral diffusion, and linewidths of ≈ 800 MHz are observed. This is a significant step forward from the disk-resonator coupled NV centers discussed in chapter 3. We expect that such inverse-designed devices will enable realization of scalable arrays of single-photon emitters, rapid characterization of new quantum emitters, efficient sensing and heralded entanglement schemes.

This chapter has been published as:

Chakravarthi, S.*, Chao, P.*, Pederson, C., Molesky, S., Hestroffer, K., Hatami, F., Rodriguez, A.W. and Fu, K.M.C., 2020. **Inverse-designed photon extractors for optically addressable defect qubits.** Optica, 7(12), pp.1805-1811. © 2020 Optica Publishing Group.
* Equally contributing authors

https://doi.org/10.1364/OPTICA.408611

5.1 Introduction

We demonstrate a flexible inverse-design optimization framework that can reconcile a wide range of design constraints and generate planar dielectric gallium phosphide(GaP)-on-diamond photonic structures. For a dipole located 100 nm from the surface and oriented perpendicular to the NV axis, an optimized 1.5 µm × 1.5 µm device is calculated to provide a 17-fold average PL enhancement of the free-space PL collection. Recent work[110] suggests that the performance of such an inverse-designed extractor is close to the theoretical limit. Orders of magnitude larger enhancement factors are found for defects positioned closer to the surface. Additionally, during optimization, we constrain patterning to the dielectric layer in order to minimize perturbations of the defect environment.

Experimentally, we fabricate the optimized GaP-on-diamond photon extractors and observe efficient PL collection from shallow (≈ 100 nm deep) single NV centers created by nitrogen ion implantation and vacuum annealing. These versatile devices exhibit a broadband PL enhancement for wavelengths in the measured range of 575 nm to 750 nm. We observe up to 14-fold enhancement of free-space PL collection for device-coupled single NVs. Extensive optical characterization of the NV centers performed both before and after fabrication provides insight into changes in the local NV environment. Post-fabrication sample treatment substantially improves device NV stability and points to important fabrication/design considerations for future defect qubit-photonics integration.

5.2 GaP photon extractors on diamond

The photon extractors are designed for robust enhancement of ZPL photon collection from near-surface NV centers, and modeled via a 3D finite-difference frequency-domain (FDFD) solver, with the frequency set at the negatively-charged NV^- ZPL of 637 nm.

5.2.1 Inverse design and device optimization

Topology optimization[111] was used to design the device within a design region situated directly on top of the diamond substrate (Fig. 5.1a) with dimensions 1.5 µm × 1.5 µm × 0.25 µm. For the simulations, a harmonic dipole source representing the NV center is situated 100 nm below

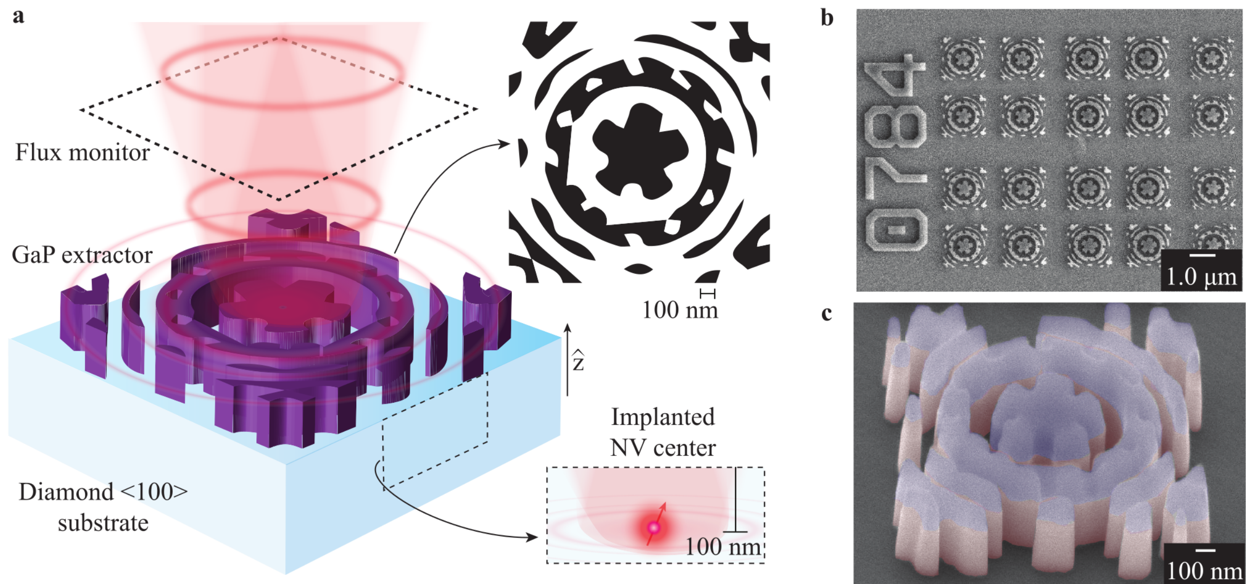

Figure 5.1: **a.** Schematic of the photon extractor designed via topology optimization (TO). **b.** SEM image of an array of fabricated inverse design extractor structures.**c.** Colorized SEM of a device indicating the different layers; HSQ resist (blue), GaP (pink) and diamond (grey). The structure has an estimated $Q \approx 50$.

the diamond-GaP interface. Device performance is robust against spatial displacement of the NV center; the enhancement factor decreases by less than 50% for spatial displacements smaller than 70 nm from the original location of the NV center (Fig. 5.2). While the optimized extractor leads to large enhancements in the collected flux, it does not significantly increase the net radiation from the NV center, quantified by the local density of states (LDOS); hence, most of the observed improvement comes from a higher collection efficiency as opposed to fluorescence rate enhancement via the Purcell effect.

5.2.2 Fabrication of photon extractors

We fabricate photon extractors (Fig. 5.3) on two samples, one for ensemble-averaged measurements (Sample A) and the other for single-emitter characterization (Sample B). Sample A is a high pressure high temperature synthesised diamond (Element Six, N < 200 ppm, B < 0.1 ppm) implanted with ^{14}N accelerated to 20 keV and vacuum annealed at 800 °C. Here, annealing forms NVs primarily

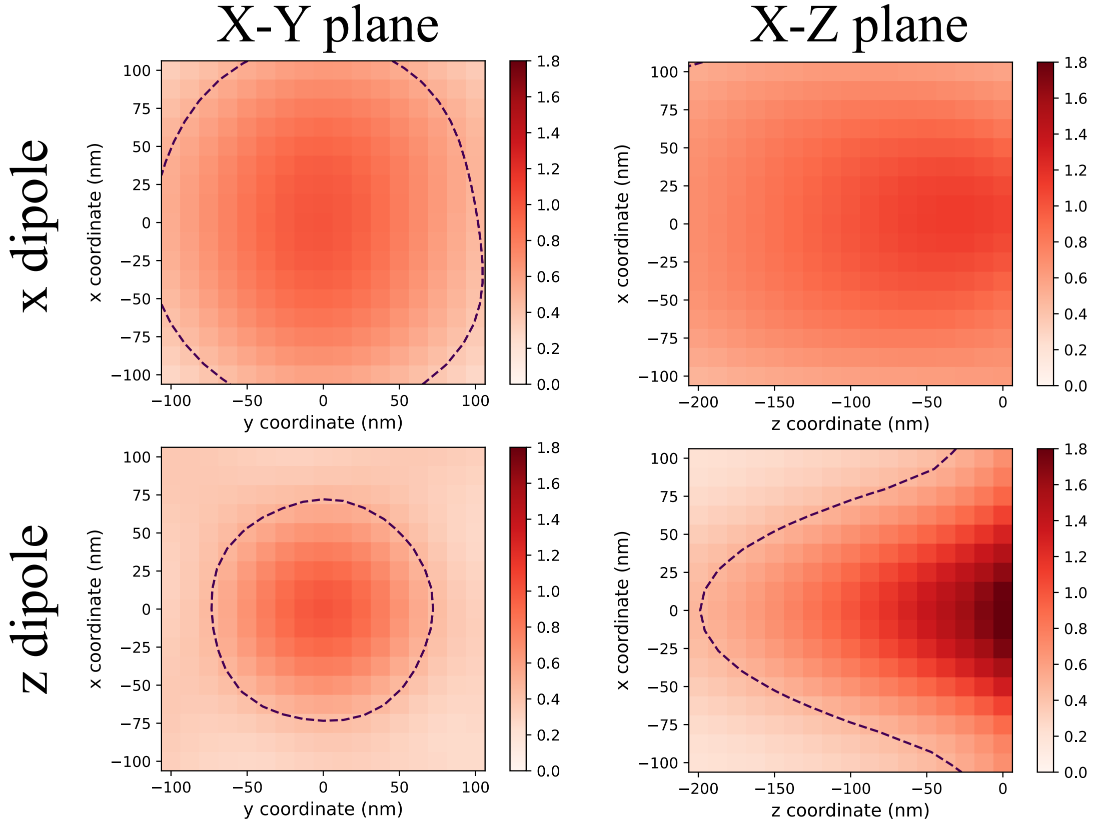

Figure 5.2: Change in collection flux enhancement for x/z polarized dipoles shifting from inverse design position. Coordinate origin is at the center of the bottom face of the device, inverse design position situated at $(0, 0, -100)$ nm. Enhancement factors are normalized to that at the inverse design position; dashed lines indicate contour where enhancement is 50% of that at inverse design position. There is an increase in enhancement factor as the dipole shifts closer to the surface.

by vacancy recombination with native nitrogen. The resulting NV distribution is dictated by the vacancy diffusion profile[112], yielding a dense layer ($\approx$100 NVs per 800 nm excitation spot diameter) of NV centers $\leq$100 nm below the diamond surface.

Sample B is a chemical vapor deposition diamond (Element Six, electronic grade, N $<$ 5 ppb, B $<$ 1 ppb) implanted with ^{15}N accelerated to 85 keV and vacuum annealed at 1200 °C. During annealing, NV centers are formed primarily by vacancy recombination with the implanted nitrogen, yielding a thin layer ($\approx$ 3 NVs per excitation spot) of single NVs 100 nm $\pm$ 20 nm from the surface.

After NV-formation, a 250 nm thick gallium phosphide (GaP) membrane is transferred to each

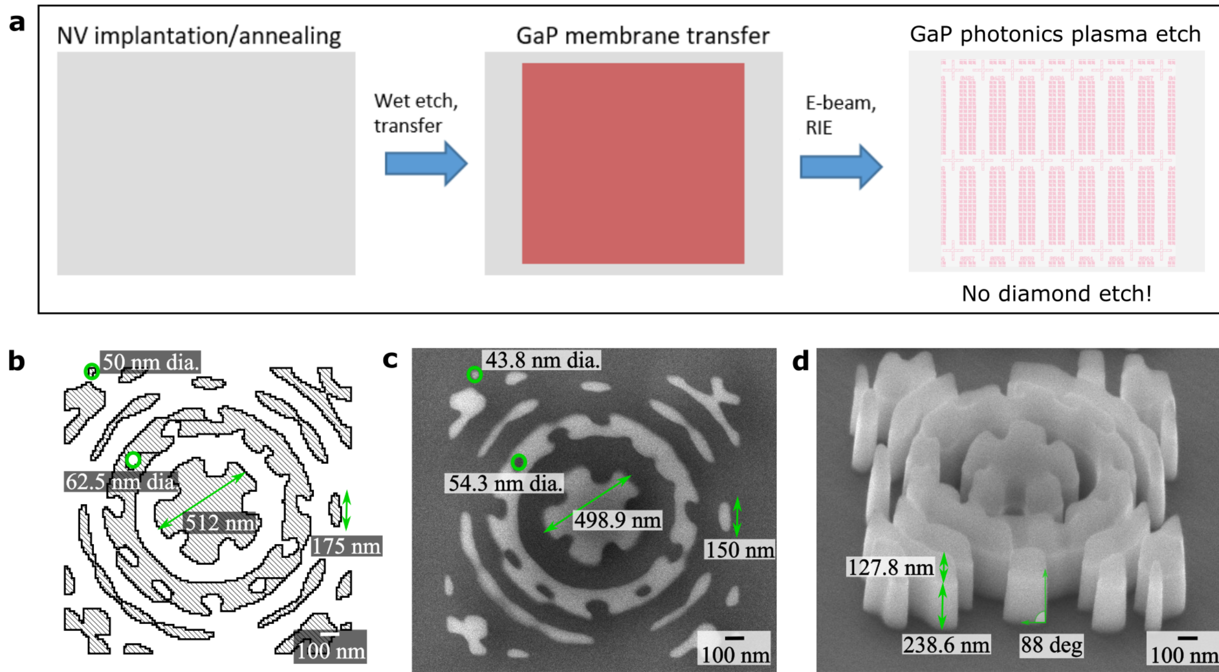

Figure 5.3: **a.** Illustration of fabrication process. The key idea here is to avoid plasma etching of the diamond substrate. **b.** Design of the photon extractor. **c.** Top down SEM image of the photon extractor pattern (before GaP plasma etch) with annotated measurements (Sample B). **d.** SEM image of the photon extractors (after the GaP plasma etch) with annotated layer thicknesses and sidewall angle (Sample B).

sample via a wet lift-off process[34,51,113]. Electron beam lithography and subsequent plasma RIE etching of the GaP layer forms the 1.5 µm × 1.5 µm photon extractors. The small footprint was chosen for compatibility with on-chip electrodes enabling optical frequency tuning[31,34]. Over 100 000 devices are fabricated in multiple arrays on the 2 mm × 2 mm diamond substrate. An array of fabricated devices and a false color SEM image highlighting the material stack is shown in Fig. 5.1c. On average, each feature is measured to be within 10% of the design, with near vertical ($\theta = 88^\circ$) GaP sidewalls.

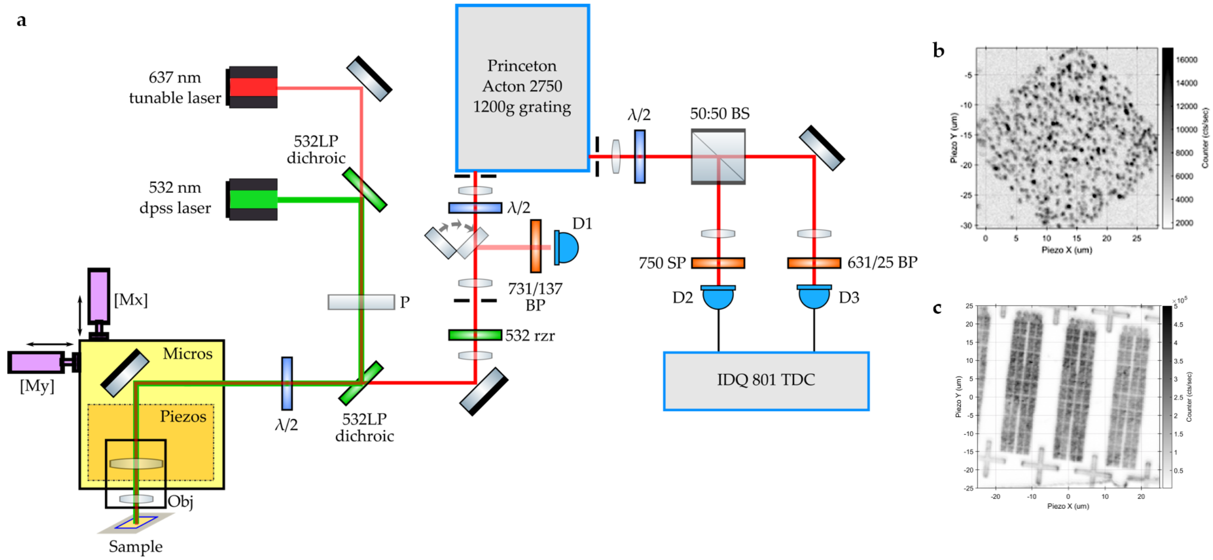

Figure 5.4: **a.** Illustration of full microscope setup. **b.** Confocal image of NV PL from an implanted square outside the grid of photonics devices on sample B. **c.** Confocal image of PL from a grid of photonics devices on sample B.

5.3 Enhanced collection efficiency of NV photoluminescence

To study NV PL enhancement from the fabricated devices, we use spatially-resolved photoluminescence spectroscopy under off-resonant 532 nm excitation (Fig. 5.4). The measurement setup is based on the microscope discussed in chapter 4.

First, sample A is utilized for broadband characterization of ensemble-averaged enhancement over the entire NV spectrum. The room temperature spectra from devices are normalized to a non-device ensemble on the same sample. We observe an average six-fold enhancement that is relatively flat over 575 to 750 nm and matches well to the theoretical spectrum-averaged four-fold enhancement (Fig. 5.5b, c).

Having demonstrated broadband NV PL enhancement, we move on to single-NV coupled devices on sample B and characterize the enhancement of the NV zero-phonon line (ZPL) emission. Identification of single-NV coupled devices is performed by comparing the low temperature (8 K) NV^- ZPL spectra under 532 nm excitation of devices to nearby non-device NVs (Fig. 5.5c). Enhanced ZPL collection rates (Fig. 5.5d) were exhibited in 74 of 480 tested devices. The distribution

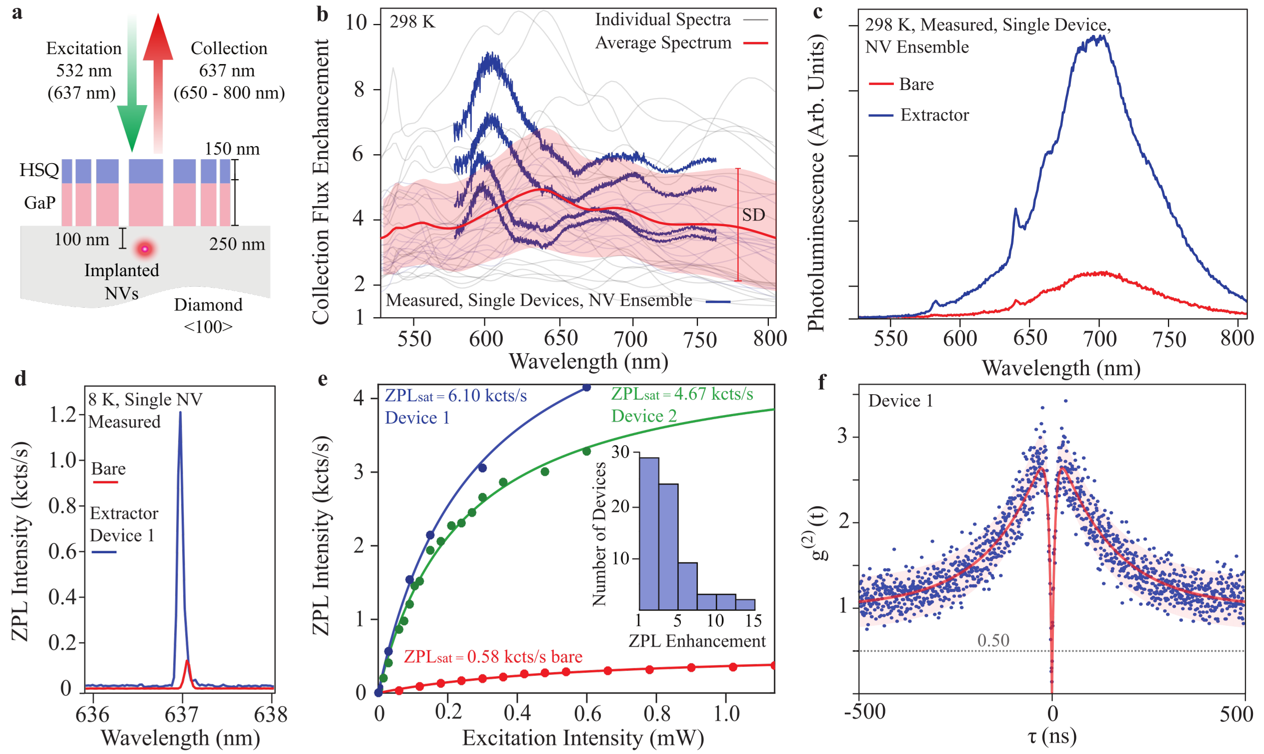

Figure 5.5: **a.** Implanted NV centers coupled to grating devices are excited with off-resonant 532 nm (resonant 637nm) laser source and the ZPL at 637 nm (PSB emission from 650 to 800 nm) is collected for photon-antibunching (PLE) studies. **b.** Comparison of simulated (grey) and measured (blue) broadband enhancement for inverse extractor devices coupled to NV ensemble (Sample A). The red line indicates the average simulated spectrum and the red envelope is one standard deviation around the average. Variation in individual spectra for both simulation and measurement stems from randomness of NV positions relative to any given device on top of the ensemble sample. **c.** Spectra showing broadband NV PL enhancement for NV ensemble (Sample A) **d.** Spectra comparing ZPL emission of device-coupled and a non-device (bare) single NV (Sample B). **e.** Saturation counts from devices coupled to single NVs. Inset: Histogram of measured devices and the observed ZPL enhancement (Sample B). **f.** $g^2(\tau)$ measurement of device coupled to single NV under 532 nm 300 µW excitation (Sample B).

of observed enhancement can be seen in Fig. 5.5e. For devices on sample B, the placement of NVs with respect to the optical mode is random; coupled device yield can be significantly improved by targeted implantation or pattern alignment to registered defect centers[114] during fabrication.

We verify that the observed enhanced PL emission corresponds to a single-emitter using an autocorrelation measurement on the NV^- ZPL at 637 nm. When a stream of single photons are

incident on a 50/50 beam splitter, the normalized correlation of recorded photon arrival time at the two beam splitter output ports will be <0.5 at zero time delay (τ). Fig. 5.5f shows the normalized coincidences under continuous off-resonant excitation for a device-coupled NV. The dip in coincidences at $\tau = 0\,\text{ns}$ is $0.12 < 0.5$ and verifies single-photon emission. Autocorrelation measurements on the eight brightest devices confirm single-NV coupling in six of the devices. In addition to the dip at zero time delay, significant bunching is observed in all devices on the 100 ns timescale.

5.3.1 Analysis of photon-autocorrelation measurements

In modeling the autocorrelation curve (red line, Fig. 5.5f), we find it is necessary to include both the NV^- singlet state and the NV^0 charge state to reproduce the magnitude and timescale of the bunching for a series of power-dependent measurements. Consideration of charge state dynamics is a critical for NV device performance as discussed further below. Consistent with theoretical expectations, excited state lifetime reduction (due to an increased LDOS) is not necessary to obtain good agreement between the experimental data and model.

The normalized autocorrelation measurements on the NV^- ZPL photons emitted shown in Fig. 5.6(b-d) provide definitive evidence that we are observing enhancement from a single quantum emitter, yet also reveal significant photon bunching. Power dependent photon bunching is a well-documented effect in NV centers, however the number of coincidences we observed at delays around 20 ns for the $300\,\mu W$ and $600\,\mu W$ data is larger than typically observed in literature. We observe similar bunching in implanted, bare-diamond coupled NV centers in the same sample, but under higher excitation intensity. This similarity suggests that the devices enhance the excitation field at the defect, but are not responsible for the presence of the bunching. Photon bunching is detrimental for many applications since it arises from non-cycling transitions shelving the NV center into inaccessible, or dark, states.

The connection between the photon statistics and the NV center's state is given by the following equation,

$$g^{(2)}(\tau) = \frac{p(e,\tau|g,0)}{p(e,\infty)}, \tag{5.1}$$

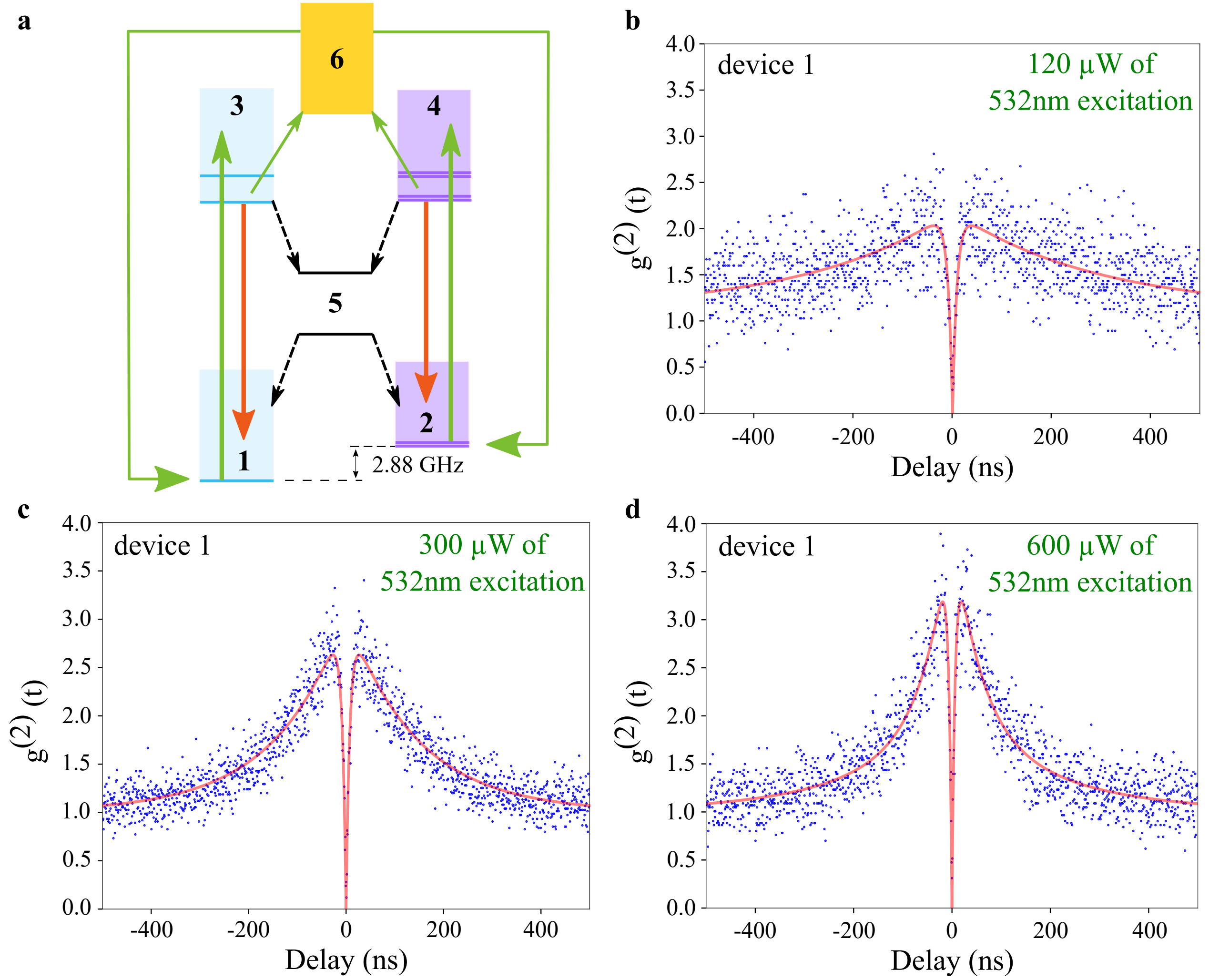

Figure 5.6: **a.** Energy levels and transitions of the NV^- and NV^0 charge states utilized for modelling the $g^{(2)}(\tau)$ data. **b.** $g^{(2)}(\tau)$ for 120 µW non-resonant excitation. **c.** $g^{(2)}(\tau)$ for 300 µW off-resonant excitation. **d.** $g^{(2)}(\tau)$ for 600 µW non-resonant excitation. Note the increase in bunching peaks with increase in excitation intensity.

where $p(e,\tau|g,0)$ is the probability of finding the NV center in the excited state at time delay τ given that it was in the ground state at 0 time delay, and $p(e,\infty)$ is the steady state population in the excited state under continuous excitation.

We model the NV center as a 6 level system in order to account for the NV^- ground states, excited states, singlet states, and NV^0 states as shown in Fig. 5.6(a). In our labelling scheme,

manifolds 1 and 3 corresponds to the $m_s = 0$ ground and excited states respectively. Manifolds 2 and 4 correspond to the $m_s = \pm 1$ ground and excited states. Manifold 5 contains the singlet states, and manifold 6 consists of the NV^0 states. The probability of being in level i is p_i and the rate from level i to j is given by k_{ij}, and P is the optical excitation power. Coherences between the different energy levels are assumed to decay on time scales faster than the excitation/relaxation rates due to the non-resonant pumping, which simplifies the model to following set of 6 rate equations.

$$\begin{bmatrix} \dot{p}_1 \\ \dot{p}_2 \\ \dot{p}_3 \\ \dot{p}_4 \\ \dot{p}_5 \\ \dot{p}_6 \end{bmatrix} = \begin{bmatrix} -k_{13}(P) & 0 & k_{31} & 0 & k_{51} & k_{61}(P^2) \\ 0 & -k_{13}(P) & 0 & k_{31} & k_{52} & 2k_{61}(P^2) \\ k_{13}(P) & 0 & -(k_{31}+k_{36}(P)+k_{35}) & 0 & 0 & 0 \\ 0 & k_{13}(P) & 0 & -(k_{31}+k_{36}(P)+k_{45}) & 0 & 0 \\ 0 & 0 & k_{35} & k_{45} & -(k_{51}+k_{52}) & 0 \\ 0 & 0 & k_{36}(P) & k_{36}(P) & 0 & -3k_{61}(P^2) \end{bmatrix} \begin{bmatrix} p_1 \\ p_2 \\ p_3 \\ p_4 \\ p_5 \\ p_6 \end{bmatrix} \tag{5.2}$$

One subtlety is that each level of our model corresponds with a manifold of NV states. This has implications in our treatment of off-resonant excitation into the excited state, the multiplicity of the $m_s = \pm 1$ level, and the NV^0 internal dynamics. We address the issue of off-resonant excitation by taking the excitation rate to depend linearly on power, while the photon emission rate is power independent. We account for the multiplicity of the $m_s = \pm 1$ states by properly normalizing the branching ratios. For example, the recombination from the NV^0 manifold into $m_s = \pm 1$ is taken to be twice the recombination into $m_s = 0$. Lastly, we ignore the internal dynamics of NV^0, and treat recombination as a two-photon process that in the weak excitation limit should scale as the power squared.

The initial condition is determined by the spin polarization, $p_1/(p_1 + p_2)$, and is determined by forcing our solution to be self consistent. In other words $p_1(0)/(p_1(0) + p_2(0)) = p_1(\infty)/(p_1(\infty) + p_2(\infty))$. We find that the equilibrium spin polarization approaches a maximum value of 0.8 at low power and decreases with power.

Older models of NV dynamics ignore ionization and recombination, and focus on the role of the NV$^-$ singlet state and spin non-conserving transitions[115]. We are unable to reproduce the power dependent bunching we observe with the rates from these models. Our model is more similar to recent literature models which account for both the long-lived NV$^-$ singlet state, as well as the NV^0

Rate (μs^{-1})	**Model 1 NV 1** [116]	**Model 1 NV 2** [116]	**Model 2** [115]	**Model 3** [117]	**This Model**
k_{13} (1 mW)	10	10	NA	59	82
k_{31}	77	66	77	75	89
k_{35}	0	7.9	0	11	17
k_{45}	30	53	30	80	17
k_{51}	5	1.7	3.3	2.6	1.7
k_{52}	0	1	0	2.3	0.50
k_{36} (1 mW)	852	852	0	2.2	24
k_{61} (1 mW)	45	45	0	47	11

Table 5.1: Rates for modelling NV dynamics

charge state, but we ignore internal dynamics within the singlet and neutral states[116,117] as we are able to obtain satisfactory agreement simulataneously fitting the three power-dependent $g^{(2)}$ curves with the simplified model (Fig. 5.6. We begin the optimization with rates taken directly from these models and optimize over each parameter. This is necessary, since the rates can vary significantly between different NV centers (Table 5.1). We find the final optimized rates are in reasonable agreement with reported values, with the only disagreement being in lower shelving rates into the singlet state, and lower deshelving rates out of the singlet states. Nevertheless, it is clear that ionization and recombination are important factors in the emission properties of an NV center, and should be considered in a variety of applications.

5.4 Charge-state and spectra stability of device-coupled NV centers

As discussed in the previous sections, single defect qubit devices have requirements beyond photon collection efficiency including charge state stability and spectral homogeneity and stability. These

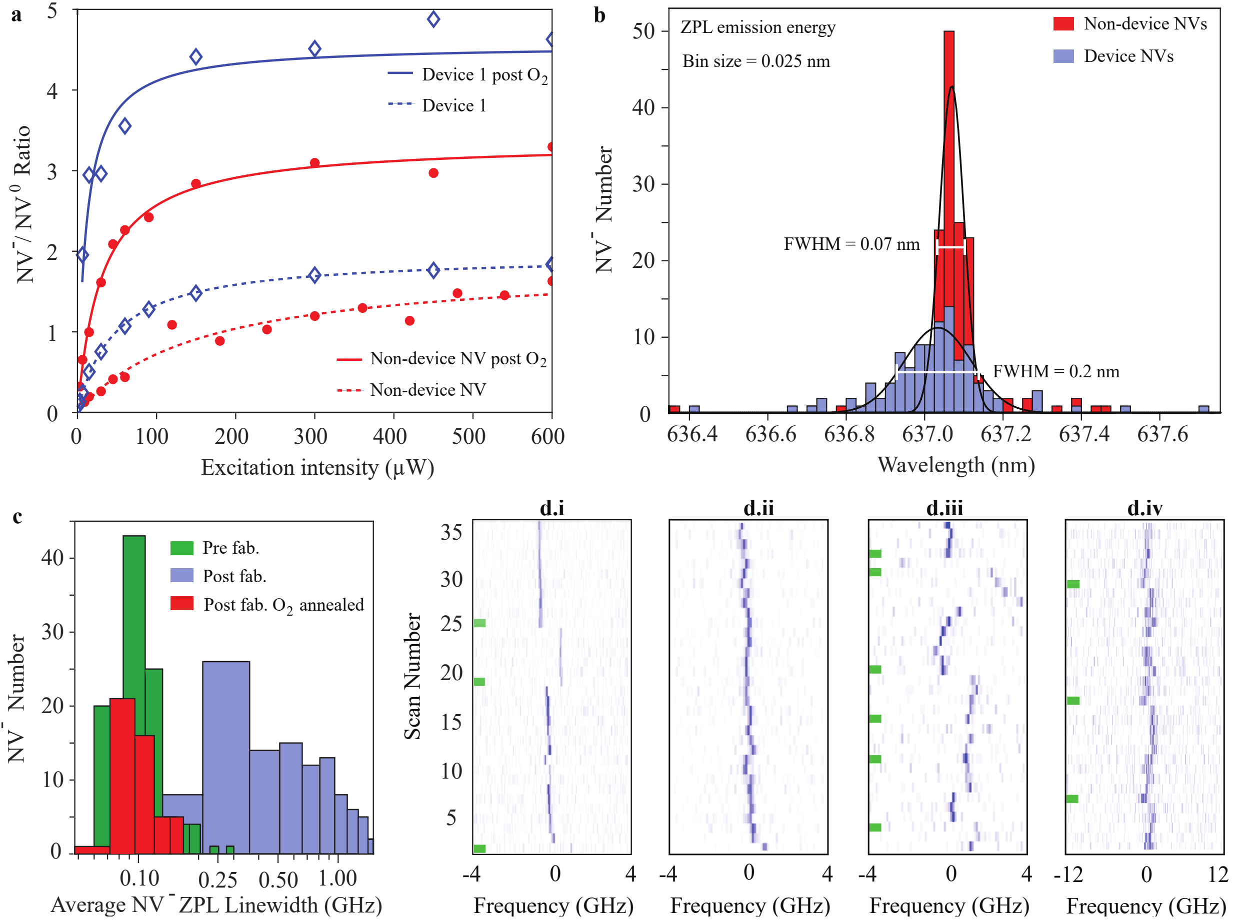

Figure 5.7: (Sample B, T=8 K) **a.** The ratio of ZPL intensities of NV^- (637 nm) and NV^0 (575 nm) charge states for device-coupled and non-device NVs as a function of the 532 nm excitation intensity. **b.** The distribution of ZPL wavelength for device-coupled and non-device NVs. **c.** The distribution of observed average PLE linewidth for non-device NVs. **d.** PLE characterization of NVs; (d.i) Grown-in deep NV avg. linewidth = 44 MHz, (d.ii) Implanted NV pre-fabrication avg. linewidth = 66 MHz, (d.iii) Implanted NV post-fabrication after oxygen annealing avg. linewidth = 59 MHz, (d.iv) Device-coupled NV (device 3) post oxygen annealing avg. linewidth = 844 MHz. The green markers indicate 532 nm repump pulses that re-initialize the NV into the NV^- charge state.

properties should be preserved during device integration. Our autocorrelation model suggests that rapid charge-state conversion occurs between the neutral (NV^0) and negatively-charged (NV^-) states. For both sensing and quantum information applications, the NV^- charge state is required, hence we need to minimize ionization into the NV^0 charge state. Every NV center, device or non-device, has emission at both NV^0 and NV^- ZPL transitions, with the ratio of the ZPL intensities

(Fig. 5.7a) determined by the local Fermi-level[44,118] and excitation intensity[119]. We also observe a broadening in the inhomogeneous NV^- ZPL distribution (Fig. 5.7b) for device-coupled NVs vs nearby non-device NVs. This static inhomogeneous broadening may be due to local variation in the strain environment[33,120]. Identical photon emission from different coupled defects are essential for photon-mediated defect qubit entanglement schemes[13,23]. The observed static inhomogeneity can be bridged by Stark tuning[31,34] or quantum frequency conversion techniques[121,122].

High resolution photoluminescence excitation (PLE) spectroscopy gives us further insight into the temporal spectral stability of individual defects. In PLE measurements, a narrow-band tunable laser is scanned across the NV^- ZPL while collecting the NV^- phonon-sideband PL (650 nm to 800 nm). From the PLE spectra we obtain the average NV^- optical linewidth as well as the scan-to-scan variation in the ZPL frequency, indicating NV spectral diffusion. During PLE we can observe a loss of the NV^- PL signal due to ionization to the NV^0 state. When PL is lost, we apply a short 532 nm repump pulse (0.1 s) between scans to reinitialize into the NV^- charge state. Hence, the interval between repump pulses is another indicator of the NV^- charge state stability.

For a deep, single NV center incorporated during growth, NV^- is the preferred charge state at low excitation power (NV^-/NV^0 =3.4 at 60 µW of 532 nm excitation). An average linewidth of 44 MHz is observed (Fig. 5.7d.i). Minimal spectral diffusion is observed between repump pulses, with the NV^- ZPL frequency exhibiting a standard deviation of 48 MHz, It is a challenge to demonstrate this level of optical stability with device-coupled implanted near-surface NVs. Pre-fabrication, the implanted single NV centers exhibit an average optical linewidth of < 100 MHz (Fig. 5.7c, green). Between repump pulses, the standard deviation of the NV^- ZPL frequency is $\sim$100 MHz, indicating low spectral diffusion. (Fig. 5.7d.ii). The NV^- charge state remains stable, no ionization is observed for multiple scans over ten minutes of measurement time. This data compares favourably with the grown-in NVs.

5.4.1 Oxygen surface termination of devices

Post-fabrication, for both device and non-device implanted NV centers, the preferred charge state at low excitation power is NV^0. In addition to the low NV^-/NV^0 ratio (Fig. 5.7a dashed lines), we observe broadening of the average single NV^- linewidth (Fig. 5.7c, blue), rapid ionization and

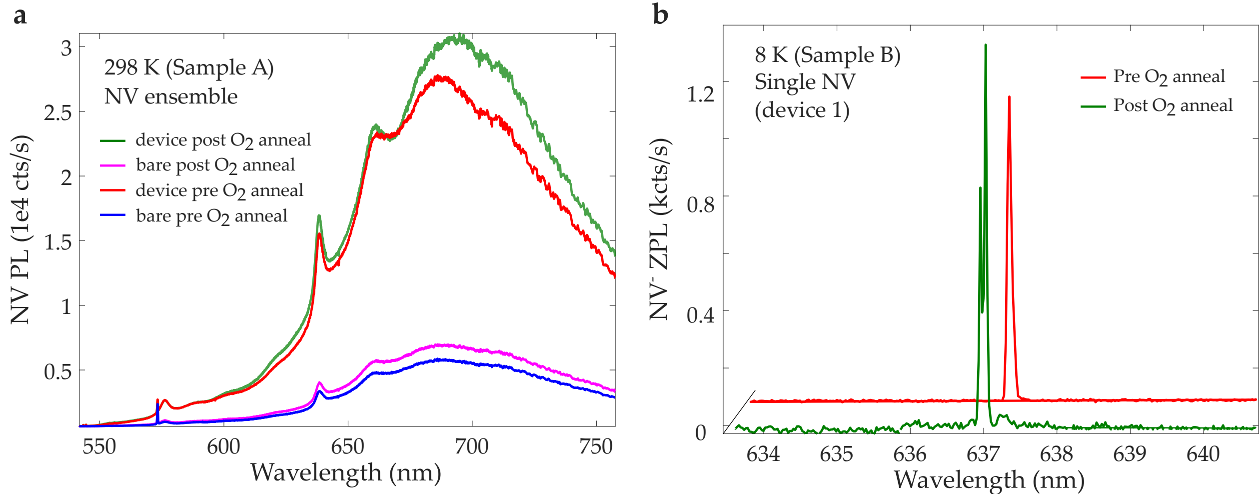

Figure 5.8: **a.** Sample A NV PL spectra before and after oxygen annealing. **b.** Sample B device-coupled NV ZPL (device 1, shown in Fig.2 main text and SI.5) before and after oxygen annealing.

large spectral diffusion. We suspect that although our design avoids etching into the diamond, the GaP photonics plasma etch ($Ar/Cl_2/N_2$) modifies the surface termination[123,124] of the diamond and introduces new surface charge traps. Encouraged by prior studies[44,125], we performed a post-fabrication oxygen anneal of the sample at 400 °C. From Fig. 5.7a (solid lines), we see that the surface treatment more than doubles the NV^-/NV^0 ratio. For the non-device NV centers, we recover the pre-fabrication average NV^- linewidth (Fig. 5.7c, red), but the NVs retain the larger spectral diffusion (Fig. 5.7d.iii). Post-oxygen annealing, for device-coupled NV centers (Fig. 5.7d.iV), we measure an average device-coupled NV linewidth of 844 MHz (1.5 GHz pre-O_2 annealing). This linewidth is $\approx$ 8 times larger than non-device NVs. Further studies are needed to determine if this fast spectral diffusion can be attributed to the GaP-diamond interface (*charge traps*) or laser-induced due to modification of the excitation intensity profile. One promising avenue for further reduction in fabrication-induced NV instability is to perform the GaP device transfer post-fabrication via a stamping process[126]. Our inverse-design optimization framework can accommodate additional constraints such as interconnected support structures required by the stamp-transfer fabrication technique.

5.5 Summary and outlook

Compared with related devices in the literature such as solid immersion lenses[47, 127], diamond nanowires[128], bullseye gratings[129], diamond metalenses[130] and parabolic reflectors[131], our approach enables compact devices and avoids directly etching the diamond via harsh processes that degrade the optical properties of the coupled defect qubits. Other designs based on hybrid metal-dielectric gratings / plasmonic resonances may achieve Purcell enhancement along with high directivity, but they require the NV to be either very close (few nm) to the surface[132] or embedded in the device within a nanodiamond[133–135], both extremely challenging environments for the realization of high charge stability and spectral purity required for quantum information applications. Our design addresses efficient photon extraction given the constraint of an NV, formed by implantation, embedded in a low-perturbation environment within a bulk diamond sample. As near-surface defect qubit engineering advances, our inverse-design platform can readily be used for even higher enhancement of photon emission from shallower defects and provides the design flexibility for integration with emerging technologies such as stamp-transferred devices[126].

With the inverse-designed photonic devices, we have shown that the coupled-NV spectral linewidths can be improved by about an order of magnitude over disk-resonator coupling geometry (840 MHz vs 5 GHz). Further, we observe that even NV centers 100 nm below the surface are significantly perturbed by the diamond surface characteristics. To determine the best strategy to overcome this issue, in the next chapter, we study this surface dependence of the NV optical properties using automated PLE linewidth studies on thousands of NV centers.

Chapter 6

Investigation of spectral stability of implanted NV centers in diamond

Scalable realizations of quantum network technologies utilizing the nitrogen vacancy center in diamond require creation of optically coherent NV centers in close proximity to a surface for coupling to photonic structures. In this chapter, we create single NV centers by ^{15}N ion implantation and high-temperature vacuum annealing. Origin of the NV centers is established by optically detected magnetic resonance spectroscopy for nitrogen isotope identification. Near lifetime-limited optical linewidths ($<60\,$MHz) are observed for the majority of the normal-implant ($7°$, $\approx 100\,$nm deep) ^{15}NV centers. Long-term stability of the NV$^-$ charge state and emission frequency is demonstrated. The effect of NV-surface interaction is investigated by varying the implantation angle for a fixed ion-energy, and thus lattice damage profile. In contrast to the normal implant condition, NVs from an oblique-implant ($85°$, $\approx 20\,$nm deep) exhibit substantially reduced optical coherence. Our results imply that the surface is a larger source of perturbation than implantation damage for shallow implanted NVs. This work supports the viability of ion implantation for formation of optically stable NV centers. However, careful surface preparation will be necessary for scalable defect engineering.

This chapter has been published as:

Chakravarthi, S., Pederson, C., Kazi, Z., Ivanov, A. and Fu, K.M.C., 2021. **Impact of surface and laser-induced noise on the spectral stability of implanted nitrogen-vacancy centers in diamond.** Physical Review B, 104(8), p.085425. Copyright 2021 by the American Physical Society.

https://doi.org/10.1103/PhysRevB.104.085425

6.1 Introduction

Nitrogen-vacancy (NV) point defects in diamond combine optical addressability[1,59,136] with long spin coherence times[137], making them promising candidates for quantum networking[11,138]. NV centers in diamond have been used to demonstrate essential ingredients for quantum networks in recent experiments, including on-demand remote entanglement generation[19,23], coherent control of multiple nearby nuclear spin memories[139] and memory-enhanced quantum communication[19,140]. For networking schemes, optical coherence and photon collection efficiency are key figures of merit. Nanophotonic integration of NV centers has demonstrated potential for high collection efficiency and scalable integration[51,141–143] and thus should enable the scaling of quantum entanglement networks. The small mode volume needed for significant photonic coupling requires localization of NV centers to within tens of nanometers from diamond surfaces. Hybrid materials platforms[34,51], which minimize diamond fabrication, utilize evanescent coupling require NV centers in even closer surface proximity. Nitrogen ion (N^+) implantation followed by high-temperature annealing is a commonly utilized process for targeted spatial localization of NV centers for device integration. However, recent published results by van Dam *et al.*[144] and Kasperczyk*et al.*[145] determined that centers with high optical coherence created by N^+ implantation and annealing are predominantly formed by implantation-induced vacancies diffusing and combining with native nitrogen. As vacancies are relatively mobile at annealing temperatures[91,112,146,147], this result implies loss of localization and precludes deterministic photonic device integration.

The optical coherence of shallow NV centers can suffer degradation from two sources; (1) charge traps formed in the bulk from the implantation and annealing process and (2) charge traps associated with the surface or sub-surface of diamond. Ionization of charge traps produces a dynamically changing electric field which couples to the different dipole moments of the ground and excited states of the NV centers[31,34,148,149]. This effect manifests as linewidth broadening and spectral diffusion of the NV optical transitions. Since the prescription for each possible source is quite different, it is important to identify the relevant culprit. Here we show that for ≈ 100 nm implant depth, it is possible to create ^{15}NV centers with typical optical transition linewidths <60 MHz. Additionally, the long-term spectral stability of the NV transitions to within 200 MHz is demonstrated. For this implant condition, given the average NV-surface distance, we expect bulk sources to dominate

optical decoherence. The observed spectral stability implies bulk sources can be overcome.

Encouraged by the 100 nm implantation results, we explore the possibility of implanting coherent centers closer to the surface. Shallower centers allow for enhanced optical coupling[51] for hybrid materials devices. We create NV centers at ≈ 20 nm by changing the angle of implantation as opposed to varying the energy of implantation. Hence, the local damage profile around an NV center is similar to the 100 nm implantation condition, merely rotated relative to the surface. Here we find that the optical linewidths are orders of magnitude larger and are accompanied by decreased spectral stability.

Combined, these observations strongly imply that the proximity to the diamond surface is the dominant source of optical decoherence, and that the bulk implantation damage profile is not the limiting factor for shallow implanted NV centers.

6.2 Experimental details

6.2.1 Samples

In our primary study, to elucidate the effect of the surface on the optical properties of implanted NV centers, we utilize two identical chemical vapor deposition diamonds samples A and B (Element Six, electronic grade, N $<$ 1 ppb, B $<$ 1 ppb), with $\langle 100 \rangle$ surfaces. As purchased, the diamond surfaces are polished to less than 1 nm RMS surface roughness. Both samples are processed identically unless stated otherwise. First, we etch away $\approx$5 µm from the surface using plasma reactive-ion etching to remove polishing damage[148]. We take the following precautions to avoid micro-masking that is a common occurrence during diamond etching: At each step the diamonds are cleaned in a boiling 1:1:1 mixture of H_2SO_4, H_2NO_3 and $HClO_4$ at 260 °C for one hour to remove organic contaminants and graphitic carbon[148]. A sapphire carrier wafer is utilized to prevent silicon contamination of the diamond surface during the etch[150]. We utilize a two step Ar/Cl plasma (physical etching via sputtering) followed by O_2 plasma (chemical etching via oxidation) process to remove any deposited material that may result in micro-masking (process details are provided in Appendix A). The total etch duration is 45 min of Ar/Cl_2 and 20 min of O_2 etching. Post processing, both diamonds have nearly identical surface morphology with sample A (B) exhibiting 0.63 (0.43) nm RMS roughness

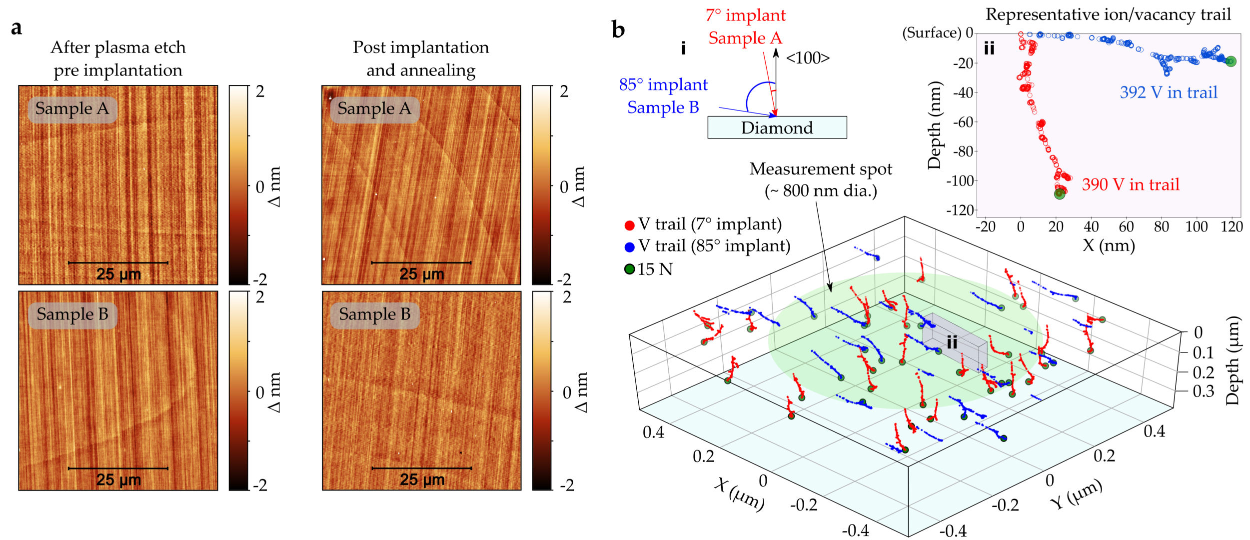

Figure 6.1: Diamond surface preparation and simulations of implantation conditions: **a.** Morphology of the diamond surface measured by atomic force microscopy. The RMS surface roughness for sample A (B) was measured to be 0.63 (0.43) nm before implantation and 0.56 (0.30) nm after implantation and annealing. **b.** A simulation of the implantation profile obtained by SRIM for sample A (red, 7°) and sample B (blue, 85°) showing the damage trails and final positions of implanted ^{15}N atoms. The green circle represents our excitation laser spot. Note that the implantation yield is low (<5%), hence within an excitation spot there is a small probability each trail results in a NV center upon annealing. **Inset i.** Illustration of the implantation geometry. **Inset ii.** A cross-section of the simulation showing the ion damage trails for the two implant angles. Total vacancies generated per ion is similar for both the implant angles. However on sample B, some ^{15}N atoms are lost due to ion scatter out of the surface.

(Fig. 6.1a).

We implant both samples A (B) with ^{15}N at identical energies and effective beam dosages of 85 keV and 3e9 ions/cm^2. The implantation angle for samples A and B are 7° and 85° respectively. We model the effect of the different ion incidence angles on the implantation profile using the Stopping and Range of Ions in Matter (SRIM) code[151]. For sample A (B), the average depth of the ^{15}N atoms is 100±20 (21±13) nm below the surface. Although the effective beam dosage is the identical for both samples, approximately 41% of the incident ions are back-scattered for sample B. This back-scattering is a geometric consequence of rotating the damage profile relative to the surface, such that some of the scattered ions escape the diamond surface. Hence the final ^{15}N

density in sample B is predicted to have 60% the density of sample A.

The samples are vacuum annealed at $< 1.4\times10^{-7}$ mbar, 1100 °C for two hours with long ramp times as described in Ref. [144,148]. This is followed by a short two hour anneal at 435 °C under O_2 flow to oxygen terminate the surface and stabilize the negative charge state[44,125] of the near-surface NV centers.

In addition, we characterize four supplemental diamond NV implantation samples (C-F) to support the reproducibility of the primary study. These diamond substrates have identical specifications (Element Six, electronic grade) but are sourced from different growth runs. Pre-implantation, all samples are processed as detailed in this section. The specifics of implantation/annealing conditions for each sample are provided in the table accompanying Fig. 6.4.

6.2.2 Measurements

A confocal microscope comprising a 532 nm DPSS laser and 60X (NA=0.7) objective lens is used to scan over 80x80 μm^2 areas using a piezo stage. A polarizing beamsplitter with an automated half-wave plate is used in the excitation path to preferentially excite a given NV orientation.

To identify the nitrogen isotope associated with each NV center, we use optically-detected magnetic resonance (ODMR) spectroscopy. For an NV in the $ms = \pm1$ ground spin-sublevel, reduced photoluminescence (PL) is observed upon off-resonant excitation due to a small likelihood ($\approx$ 20%) of relaxation through the dark inter-system crossing transition[46,152] (dotted line, Fig. 6.2a). The samples are placed in a weak magnetic field ($\approx$ 5 G) that splits the $ms = \pm1$ ground spin-sublevels. RF excitation is delivered via a small copper loop (radius 0.3 mm) suspended $\approx$50µm above the diamond sample. A short (5 µs) off-resonant 532 nm laser pulse initializes the NV into the $ms = 0$ spin state. Next, a radio-frequency (RF) π-pulse (0.8 µs) rotates the NV spin state before time resolved NV PL is recorded during the subsequent short (5 µs) readout laser pulse. The π-pulse area is initially calibrated by performing a Rabi experiment. The pulse sequence is repeated while sweeping the RF driving frequency over all the NV ground state spin transitions. The resulting two (three) dip PL intensity spectrum corresponds to the ^{15}N (^{14}N) NV-N ground state hyperfine interaction[1,153], indicating that the NV incorporates an implanted or grown-in nitrogen atom (Fig. 6.2c,d). ODMR spectra are measured at room-temperature for randomly sampled NV

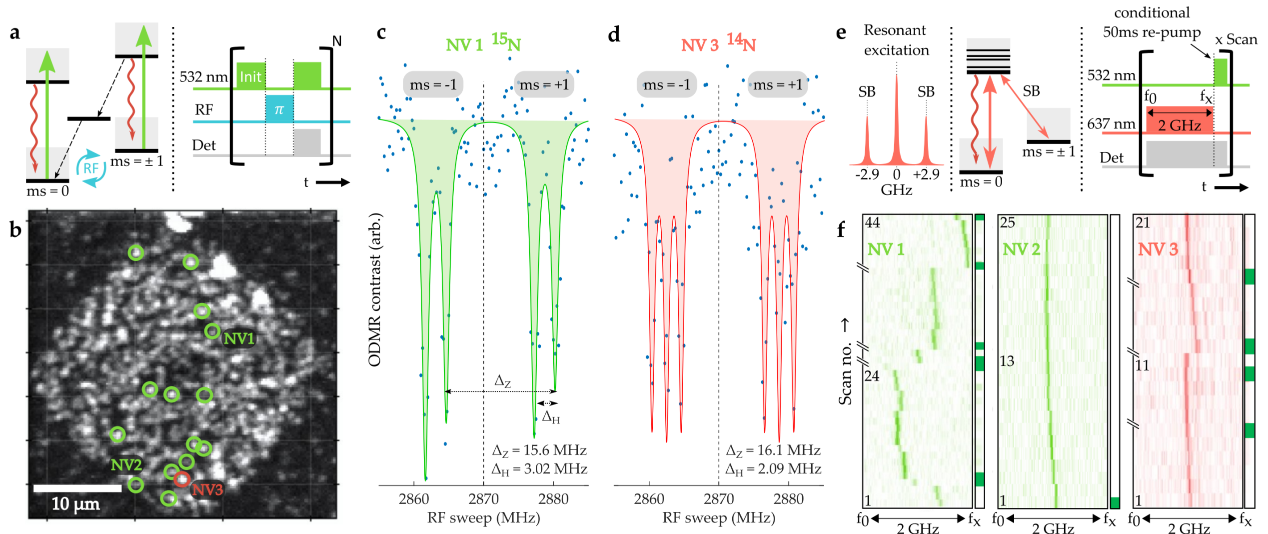

Figure 6.2: Correlated NV ODMR (RT) and PLE (T<12K) measurements on sample A: **a.** Pulsed ODMR scheme utilized to identify the N isotope. Laser and radio-frequency (RF) pulses are generated by an acousto-optical-modulator and RF switch, respectively. (Laser power 0.8-1.0 mW, spot diameter ∼800 nm.) Pulses and photon collection are triggered by a programmable pulse generator. **b.** Confocal PL map of the implanted region with the measured NV centers indicated by their isotope (green ^{15}N, red ^{14}N). **c.** ODMR spectra for the marked NV incorporating implanted ^{15}N. **d.** ODMR spectra for the marked NV incorporating grown-in ^{14}N. **e.** Resonant excitation (PLE) scheme utilized for characterizing the optical coherence of the marked NV centers. Sidebands at 2.9 GHz are added (using an electro-optic modulator) to the scanning resonant laser to counteract optical spin pumping. Upon detection of an NV$^-$ to NV^0 ionization event (indicated by lack of NV$^-$ PL) a 50 ms off-resonant green re-pump is used to reset the NV charge state. **f.** Time traces of PLE scans measured at 10.5 K for three NV centers. Off-resonant re-pump between scans are indicated by green squares along the right column, this induces large spectral jumps in many ^{15}NV centers (e.g. NV 1). The '\\' markers along the scan axis indicate discarded scans where no NV PL is observed. The PLE traces for ^{15}NV centers typically show long periods of spectral stability between re-pump pulses.

centers in the implantation region (Fig. 6.2b) and fit to a three (^{14}NV) or two (^{15}NV) dip Lorentzian. The positions of the sampled NV centers are recorded. The samples are then cooled to <12 K in a close cycle cryostat for spectral characterization of the selected NV centers.

Low-temperature NV$^-$ PL spectra under CW 532 nm excitation provides the inhomogeneous distribution of the ZPL transition (Fig. 6.3) arising from variations in the local strain and electric field environment of individual centers. The NV charge state ratio (NV$^-$/NV^0) is also recorded as

a function of the excitation intensity for a subset of centers (Appendix C). Additionally, high resolution photoluminescence excitation (PLE) spectroscopy provides insight into the optical coherence and temporal spectral stability of individual NV centers. In PLE measurements, a narrow-band tunable laser is scanned across the NV^- ZPL while collecting the NV^- phonon-sideband PL (650 nm to 800 nm) (Fig. 6.2e). The resonant laser and accompanying 2.9 GHz sidebands simultaneously drive the {ms=0, ms=±1} → {Ex, Ey} transitions[32,154,155].

From the PLE spectra we collect statistics on the ZPL single-scan linewidth as well as the scan-to-scan variation in the ZPL frequency. During PLE we can sometimes observe a loss of the NV^- PL signal due to ionization to the NV^0 state; to reinitialize into the NV^- charge state we apply a short low power 532 nm repump pulse (50 ms) between scans (as indicated by the green markers in Fig. 6.2f). The interval between repump pulses is an additional indicator of the stability of NV^- charge state.

6.3 Correlated ODMR and PLE spectroscopy

On sample A, ODMR was performed on 32 NV centers with 26 centers identified as ^{15}NV, one as ^{14}NV; remaining five NVs could not be conclusively identified. Similarly, on sample B, ODMR was performed on 38 NV centers with 27 centers identified as ^{15}NV, two as ^{14}NV; the remaining nine NVs could not be identified. The observed total NV density for sample A (B) is 1.2/ μm^2 (0.3/ μm^2) corresponds to an implantation conversion yield of 4 % (1 %). For both these samples, no grown-in NVs were observed in a 80 μm × 80 μm area at a depth of 50 μm implying very low native N_s density[88]. Considering the natural abundance of ^{15}N (0.4 %) and the ^{15}NV/^{14}NV ratio r for both samples ($r_A = 26$, $r_B = 13.5$), it is clear that for our diamond substrates and implantation conditions that NV formation incorporating implanted nitrogen is favored.

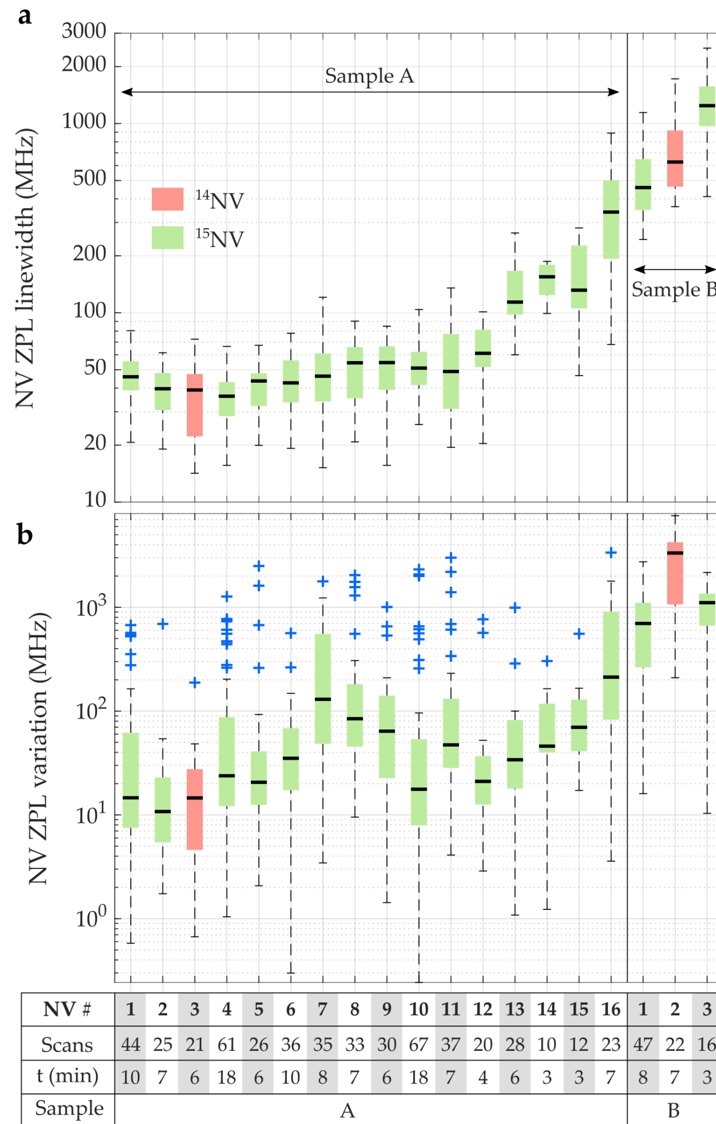

NV #	1	2	3	4	5	6	7	8	9	10	11	12	13	14	15	16	1	2	3
Scans	44	25	21	61	26	36	35	33	30	67	37	20	28	10	12	23	47	22	16
t (min)	10	7	6	18	6	10	8	7	6	18	7	4	6	3	3	7	8	7	3
Sample	A																B		

Figure 6.3: Photoluminescence excitation characteristics of measured NV centers on samples A and B: **a.** The fitted Lorentzian FWHM distributions for each observed NV. The color box and black marker represent the interquartile range and median linewidth respectively. The total number of scans and measurement duration comprising each distribution is recorded in the accompanying table. The PLE traces for NV centers 1 to 3 are also shown in Fig. 6.2f. **b.** The distributions of the scan-to-scan change in the center frequency of the fits, representing spectral variation. Off-resonant re-pump pulses are only applied when NV ionization is detected. On average, there are six re-pump events over a measurement duration of 10 min. The blue markers indicate large spectral jumps after re-pump pulses.

First let us consider sample A. The single NV low-temperature ZPL spectra under off-resonant 532 nm excitation is typically spectrometer resolution limited ($\Delta\lambda = 0.021$ nm). PLE spectroscopy reveals that both ^{15}N and ^{14}N centers typically exhibit near lifetime-limited linewidths. A sequence of laser scans over a span of ≈ 10 minutes (each scan is 4 to 8 s in duration) gives us a median linewidth of < 60 MHz for 12 out of 16 centers (Fig.6.3a). This linewidth is computed by individually fitting each scan to a Lorentzian. The laser intensity is set between 30 to 60 nW with a scan rate of 1 to 2.5 GHz/s. A linewidth power dependence measurement was performed on two centers to ensure that the observed linewidths are not significantly power-broadened in our intensity range. The PLE results are summarized in Fig. 6.3a; the solid boxes mark the fitted linewidths between first and third quartile. This interquartile range is an indicator of spectral diffusion ($\Delta\,\nu$) of the NV ZPL during a single resonant laser scan (on the timescale of ms).

Additionally, by tracking the ZPL frequency between scans, we can characterize the long term spectral stability (on the timescale of s). We calculate this spectral variation ($\Delta\,\omega$) by recording the change in ZPL frequency between subsequent scans (Fig.6.3b). Here, we emphasize that an off-resonant re-pump pulse is only applied when no NV PL is detected (i.e. NV$^-$ has ionized to NV^0) emulating emerging NV quantum networking protocols[19,23]. The median spectral variation is typically < 100 MHz, for long periods (60 to 300 s) between re-pumps. We observe that most ^{15}NV centers experience large spectral jumps (≈ 500 MHz) after an off-resonant re-pump pulse. These jumps occur in 95% of the re-pump events. In Fig.6.3b, the blue markers indicate re-pump triggered spectral jumps. This is the only metric where we see a clear advantage for the ^{14}NV also observed on sample A (Fig. 6.3, red). It is unclear at this time if the re-pump triggered perturbation originates at the surface (with the single ^{14}NV lying deeper within the sample) or from local implantation damage. Nevertheless, it may still be mitigated with the use of a low-power resonant NV^0 re-pump pulse[119].

Sample B reveals a different story, the low-temperature ZPL spectra under off-resonant 532 nm excitation for individual NV centers is much broader (0.02 to 0.25 nm;). Given that the lattice damage profile is similar to sample A, this spectral broadening could be attributed to rapid fluctuations of surface charges effectively Stark-tuning the NV centers within the exposure duration of the spectra. Such rapid ZPL fluctuations make resonant 637 nm PLE measurements very challenging. Of the six NV centers randomly sampled, only three showed PLE signal. All three NV centers (two

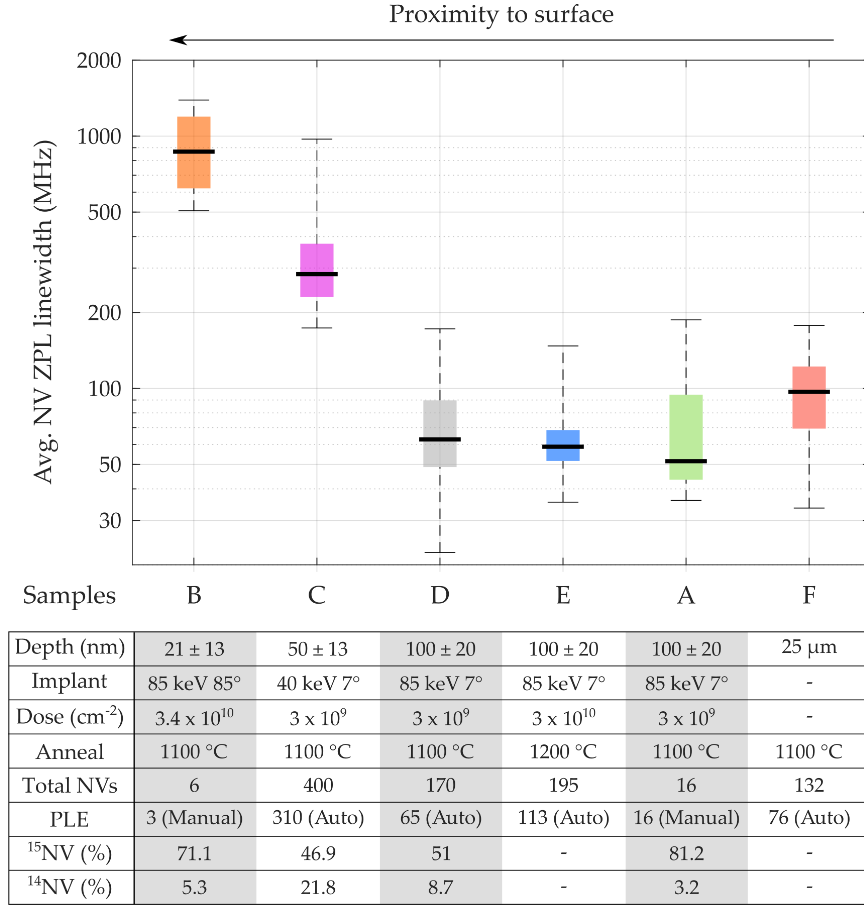

Samples	B	C	D	E	A	F
Depth (nm)	21 ± 13	50 ± 13	100 ± 20	100 ± 20	100 ± 20	25 µm
Implant	85 keV 85°	40 keV 7°	85 keV 7°	85 keV 7°	85 keV 7°	-
Dose (cm^{-2})	3.4×10^{10}	3×10^{9}	3×10^{9}	3×10^{10}	3×10^{9}	-
Anneal	1100 °C	1100 °C	1100 °C	1200 °C	1100 °C	1100 °C
Total NVs	6	400	170	195	16	132
PLE	3 (Manual)	310 (Auto)	65 (Auto)	113 (Auto)	16 (Manual)	76 (Auto)
^{15}NV (%)	71.1	46.9	51	-	81.2	-
^{14}NV (%)	5.3	21.8	8.7	-	3.2	-

Figure 6.4: Automated ODMR and PLE measurements are performed on four additional samples (C to F). We are not able to track the NV centers between ODMR and PLE with the automated protocol. ODMR ^{15}NV/^{14}NV ratio suggests predominance of ^{15}NVs across all implanted samples. Similar to the previous dataset (Fig. 6.3), the average linewidth for each individual NV is computed as the mean FWHM obtained by fitting each of the 30 frequency scans to a Lorentzian. Automated PLE scans performed on deep grown-in NVs (25 µm from surface, sample F) are used as a reference.

^{15}N and one ^{14}N) exhibit broad median linewidths (0.5 GHz to 1.2 GHz) and increased spectral variability (Fig. 6.3).

Finally, we confirm that the NV^{-} charge state is preferred across the full range of optical powers (15 to 600 µW of 532 nm excitation) for both samples A and B (Appendix C).

6.4 Automated spectroscopy

To corroborate the data from our primary samples (A, B), we present automated ODMR, PLE and low-temperature off-resonant PL spectroscopy datasets on four other samples (C to F). Our automation procedure allows us to sample hundreds of NV centers, however we are unable to track individual NV centers between PL, PLE and ODMR datasets. Details of the automated measurement protocol are provided in Appendix B.

First, let us consider samples D and E with similar implant conditions (^{15}N, 85 keV 7°) to sample A. Uncorrelated ODMR measurements on sample D show most centers are ^{15}N. The measured average ZPL linewidth distribution (Fig. 6.4) of hundreds of NV centers, tracks well with the dataset from sample A, indicating reproducibility of narrow-linewidth ^{15}NV centers. In the ideal case, the linewidth of NV centers created through ion implantation and annealing would be equal to the linewidth observed in background NV centers distributed throughout the sample. No background NV centers could be identified in either samples (A, B) and a low density prohibited automated measurements in samples (C, D, E). Automated PLE measurements on native NV centers 25 µm within sample F, a similar electronic-grade sample that has undergone high-temperature annealing (with no implantation), serve as our reference. From the data presented in Fig. 6.4, the average NV linewidth distribution of all the 85 keV, 7° implant samples are in agreement with the reference sample.

Next, we examine the shallow implantation samples. The average ZPL linewidth distribution in Fig. 6.4, shows that both the shallow NV samples C (40 keV 7°) and B (85 keV 85°) exhibit decreased optical coherence. This is despite the fact that initial implantation damage for sample C is significantly lower compared to samples A, D and E (85 keV 7°). We can use the average number of vacancies (V) generated per implanted ion trail as an analogue for local lattice damage. From SRIM[151] simulations, sample C incorporates 203 V/ion whereas samples A, B, D and E incorporate 390 V/ion. This provides further evidence that the broadening seen for the shallow implants is unrelated to the implantation damage at these energies and dosages and instead is a result of charge traps associated with the surface.

In addition, low-temperature PL spectra (off-resonant excitation) from a large number of NV centers provides the inhomogeneous ZPL distribution (Fig. 6.5). Regardless of the variations in the

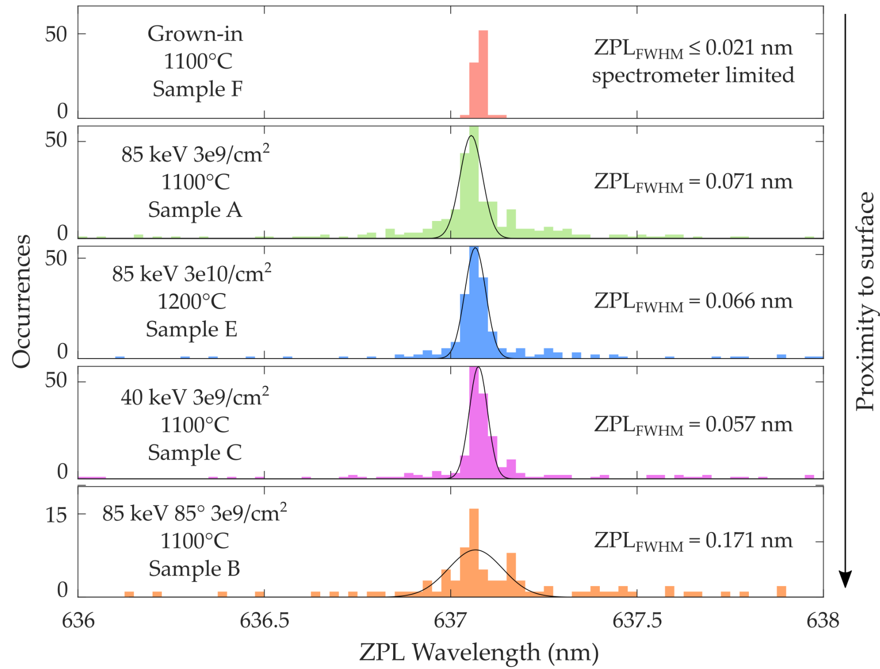

Figure 6.5: The NV ZPL inhomogeneous distribution. The histogram is generated by recording the center wavelength of all peaks observed with 532 nm excitation from locations within an implantation region (except the grown-in reference NV centers) on the respective samples. Note that no distinction is made of the different transitions associated with the NV excited state spin sublevels. The bin size is 0.025 nm, and the spectrometer resolution is 0.021 nm. The histogram data is fitted to a Gaussian to extract the full-width half max (FWHM) of the distribution. Sample B show an obvious deviation from other samples.

total implant damage ($V/\mu m^3$), the inhomogeneous NV ZPL distributions are similar for samples A, C and E (Gaussian fit FWHM = 52.5 GHz, 42.1 GHz and 48.8 GHz respectively). The grown-in NV centers exhibit a narrower ZPL spread (FWHM ≤ 15.4 GHz, spectrometer resolution limited). Finally, the ZPL distribution for sample B is much broader (FWHM = 126 GHz) than any of our other samples. A comparison suggests that there is still a small amount of residual strain remaining in the implantation samples.

6.5 Summary and outlook

Lattice damage from the ion-implantation process introduces localized perturbations of the defect environment. Our result with the 85 keV 7° implant samples indicates much of this damage can be annealed out for an ^{15}NV created directly from an implanted nitrogen. We observe that ^{15}NV centers exhibit long periods of spectral stability, wherein their spectral characteristics are akin to optically coherent grown-in NV centers. The implanted ^{15}NV and grown-in centers exhibit comparable median optical linewidths. However, we do see distinct advantages for grown-in centers in terms of behavior under off-resonant green re-pump and inhomogeneous ZPL distribution. For ^{15}NV centers, green re-pump pulses used to reinitialize the NV charge state introduce large spectral variation ($\approx$500 MHz). This behavior hints at why our ^{15}NV linewidths are qualitatively different from van Dam *et al.*[144] and Kasperczyk *et al.*[145]. They utilize re-pump pulses every scan, which we can see would cause linewidth broadening into GHz. In fact, an analysis considering only the PLE scans immediately after the repump pulse indicates our results in Sample A are consistent with the 400 nm 400 keV ^{15}N implanted sample in van Dam *et al.* Further studies are necessary to pin down the source of the re-pump triggered variation. Nevertheless, for the ^{15}NV centers, observation of long periods of spectral stability between re-pumps shows promise for implementation of quantum networks with integrated photonic devices.

Further, we show that this optical stability rapidly degrades with increasing proximity to the diamond surface, corroborating measurements by Ref. [149] of NV centers in thin diamond membranes which showed strong correlation of reduced NV spectral stability with decreasing membrane thickness, not accompanied by a change in the NV strain environment. Ref. [149] suggests that the additional NV dephasing may be attributed the Ar/Cl_2 plasma etch process even for micron-scale thick samples. Our past work has seen a similar effect on implanted centers[143]. Indeed, Ref. [156] show that $\approx$1 µm thin diamond membranes with improved diamond surface quality (etched by a soft graded O_2 plasma) can host NV centers with narrow linewidths.

Our conclusions fit into a larger narrative regarding the source of degradation of other properties near surfaces as well, such as NV T_2. Recent work by Ref. [157] correlating the reduction of NV T_2 within 20 nm of the surface has shown that the T_2 for NV center within 10 nm of the surface can be enhanced an order of magnitude by preparing diamonds with smoother surfaces and well-ordered

oxygen termination. Further work would need to be done to determine whether the spin-bath responsible for T_2 degradation is related to the charge traps we infer in our optical measurements, however both suggest that solving the surface interaction problem is more important than fixing residual implantation damage.

Chapter 7

SiV centers coupled to GaP 1-D photonic crystal resonators

Due to the high surface sensitivity of NV centers observed in the previous chapters, here we investigate photonic integration with the SiV center in diamond utilizing 1-D photonic crystal (PhC) waveguide cavities defined in GaP. Based on techniques developed with NV centers, we first create SiV centers at a depth of 20 nm by silicon ion-implantation and annealing (1200°C, in vacuum). We transition to independent fabrication of photonic PhC devices on a silicon oxide carrier chip (GaP-on-SiO_2) and subsequent integration with a diamond qubit host using a stamp-transfer technique. The stamping process avoids the plasma exposure of diamond, preserving the qubit environment. Additionally, stamping allows us to carefully characterize the cavity resonances of the PhC GaP-on-SiO_2 devices before transfer to diamond. Tuning of the PhC cavity resonance wavelength to match the SiV ZPL transition is demonstrated by controlled iterative thinning of the GaP photonic layer. This significantly increases the yield of qubit coupled photonic devices. After transfer to diamond, we measure SiV-coupled PhC cavity quality factors ($Q \approx 9$k) remarkably close to the design goal ($Q \approx 10$k) and show enhanced SiV ZPL collection efficiency (Purcell-enhanced regime).

This chapter is being prepared for publication. Follow-up optical measurements are currently in progress.

7.1 Introduction

SiV centers in high-quality diamond crystals show nearly lifetime-limited optical transitions with a narrow inhomogeneous distribution[53]. These properties arise from the inversion symmetry of the SiV center which protects the optical transitions from electric field noise in the environment[35,56]. This makes the SiV centers much more favourable for integration with nanophotonic structures than NV centers. Here we demonstrate coupling of waveguide integrated 1-D photonic crystal (PhC) cavities to single SiV centers. In order to minimize the perturbation to the environment of the SiV centers, the PhC cavities are fabricated on an independent gallium phosphide (GaP) chip. The PhC cavities are then transferred to a pre-characterized SiV^- diamond sample via a gentle polymer stamping process adapted from the 2-D materials community[158]. The PhC consists of a thin GaP beam patterned with elliptical holes, providing a wavelength scale confinement of the cavity mode ($V \leq \lambda^3$)[159–161]. The SiV centers are coupled to the evanescent field of the cavity mode. The presence of a cavity with physical dimensions comparable to the wavelength of the atomic transition modifies the optical density of states dramatically[57,162–164]. The objective of this experiment is to reach the high-cooperativity regime[30,165] of cavity QED where near-deterministic spin-photon interfaces can be realized.

7.2 1-D PhC design and fabrication

The PhC device consists of a 1-D array of elliptical holes etched into the GaP. The designed GaP layer is constrained to 222 nm thick (selected to match the BGaP thickness of commercial BGaP-on-Si wafer). Consider a unit cell of the PhC consisting of a single elliptical hole with major-axis hy and minor-axis hx, GaP width wz and a lattice constant a_{mir} (that also defines the horizontal extent of the unit cell). The PhC parameters are optimized to maximize the photonic band gap shown in the dispersion diagram Fig.7.1a,b (TE-modes). The software packages MPB[166] and MEEP[167] are utilized to simulate and extract the mode solutions. The solver computes the energies of the eigen-modes depending on the k-vector. Full details of the PhC optimization can be found in Ref. [168, 169]. The light-line separates the energies of the modes that are guided ($\omega < ck$) from the modes leaking into air ($\omega > ck$). The target frequency (SiV^- zero-phonon transition at 737 nm,

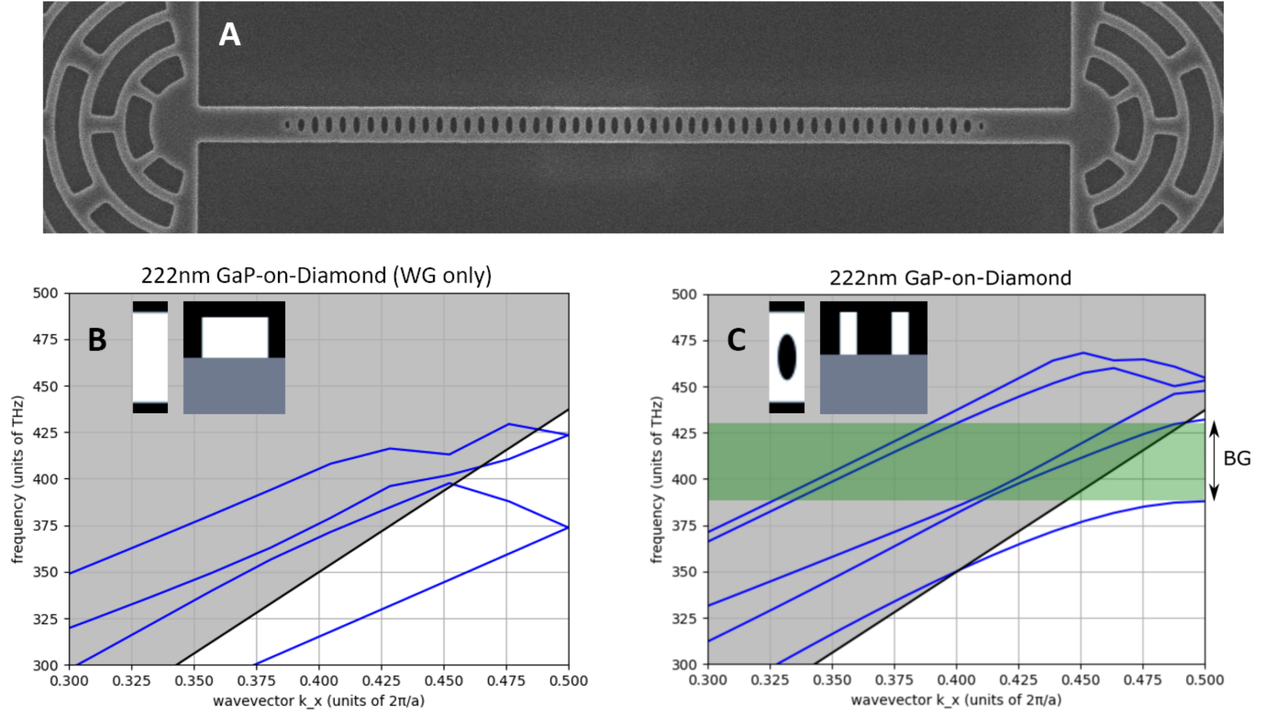

Figure 7.1: **a.** SEM image of a fabricated GaP 1-D PhC resonator coupled to input and output grating structures. A series of elliptical holes in GaP defines the PhC. **b.** Simulated dispersion diagram of TE-modes supported by a blank waveguide structure (no holes). The grey region marks non-guided modes within the diamond light-line. Inset shows the top and cross-sectional view of the unit cell (cell width=a_{mir}=140 nm) consisting of GaP-on-diamond structure. The GaP waveguide is 222 nm high and 360 nm wide. Simulations assume periodic boundary conditions along all directions. **c.** Dispersion diagram with the optimized elliptical air hole $(hx, hy) = (71, 183)$ nm in the unit cell. Now we see the appearance of a TE band gap (marked in green).

407 THz) is designed to be within the band gap, with the fundamental TE-mode at the edge of the band gap. Now, by introducing local perturbations in the periodic array of holes we can create a defect, thus forming the PhC resonator.

The symmetric design of the PhC resonator can be divided into two regions; the taper (T) and mirror (M) sections (Fig.7.2a). Within the taper region, the hole periodicity a_{cav} is adiabatically reduced from the a_{mir} value (Fig.7.2b). This serves two purposes, the decreased spacing between holes reduces the effective-index and draws the fundamental TE mode at the edge of the band gap towards the light-line and into the band gap forming the PhC cavity TE mode. The taper also

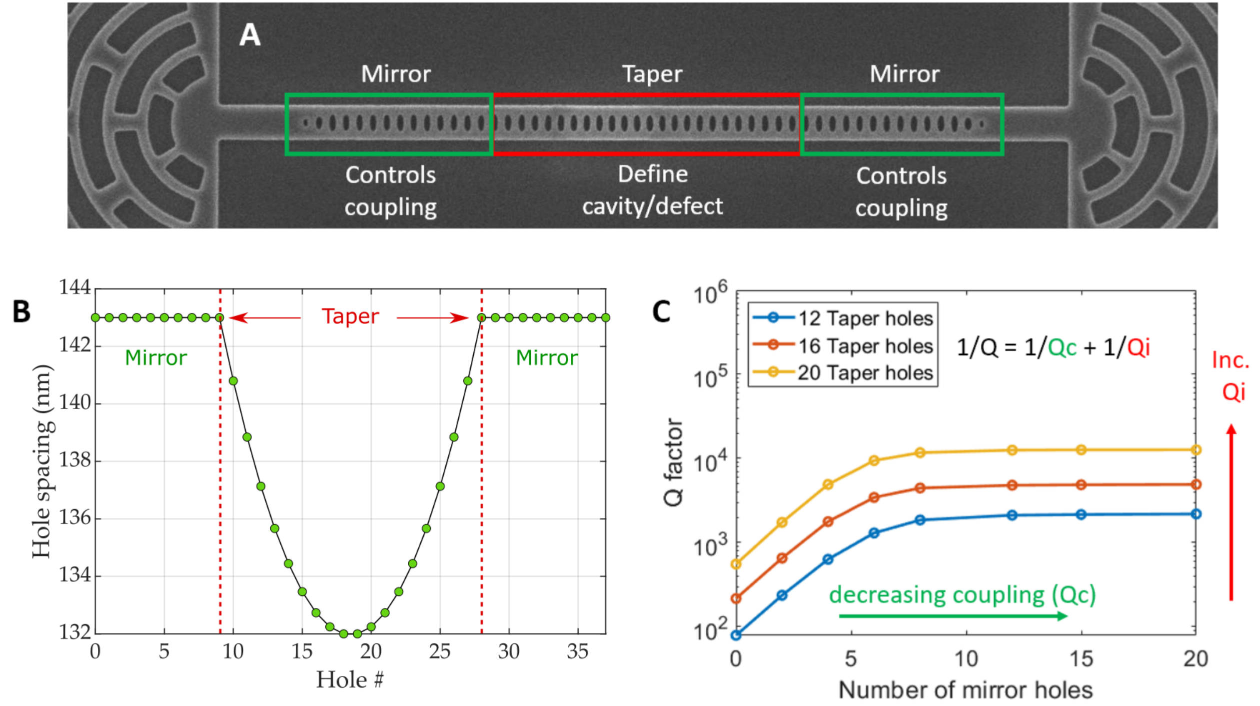

Figure 7.2: **a.** SEM image of a fabricated GaP 1-D PhC resonator with the mirror and taper regions annotated.**b.** The variation of the hole spacing across the PhC, distinguishing the mirror and taper regions. **c.** FDTD simulated scaling of the total Q-factor of the GaP-on-diamond PhC resonator with increasing number of mirror and taper holes. The left edge (M=0) of the plot describes the over-coupled cavity regime (dominated by Q_c) whereas at the right edge (M=20) we are operating in the under-coupled regime (dominated by Q_i). For maximum SiV photoluminescence extraction, we would like to operate in the critically coupled regime (Q_c=Q_i).

reduces scattering losses in the cavity thus increasing the intrinsic quality factor (Q_i). The mirror section consists of additional holes with the a_{mir} periodicity allowing tuning of the coupling quality factor (Q_c). Similar to disk-resonator structures discussed in chapter 3, the overall quality factor of the device is determined by the combination of Q_i and Q_c, $Q = 1/Q_i + 1/Q_c$. Here, we assume Q_i includes losses from absorption, scattering and leakage into the substrate. The presence of the high index diamond substrate underneath the GaP introduces design challenges towards achieving high Q because the substrate effectively expands the light-line such that photons can couple to the continuum of radiation and leaky modes and leak out of the resonator.

The optimized design, with (a_{mir}, a_{cav}, hx, hy, w) = (140, 133, 171, 183, 360) is simulated

in Lumerical finite-difference-time-domain (FDTD). With a dipole source (representing the SiV) placed within the cavity field, the time-decay of the electric-field components within the PhC structure is utilized to estimate the resonator quality factor. A parameter sweep of the number of mirror and taper holes is then performed to arrive at the Q-scaling shown in Fig.7.2c. Similar to disk-resonator device discussed in chapter 3, we can vary the device operation from undercoupled, critically coupled thru to overcoupled regimes by changing the number of mirror holes. Typically, the fabricated pattern consists of arrays of devices with a sweep of mirror and taper holes. We aim for critically coupled devices to collect maximum SiV ZPL emission.

The FDTD simulation provides the distribution of the evanescent cavity field within diamond substrate. Using the electric field amplitude and characteristics of the SiV, we can estimate the cavity-defect coupling regime. The cooperativity of the SiV-cavity system is given by $C = 4g^2/\kappa\gamma$, where g is the single-photon Rabi frequency, κ is the cavity intensity decay rate and γ is the total decay rate of the emitter (SiV optical linewidth). The single photon Rabi frequency is related to the cavity field by $g = (\mu_{\mathrm{ge}}/\hbar)|\vec{E}(\vec{r})|$, where μ_{ge} is the electric dipole moment for the ground-to-excited state optical transition (SiV ZPL) and $|\vec{E}(\vec{r})|$ is the electric field of a single photon in the cavity mode at position $\vec{r}$ within the diamond (position of the SiV). Given the (100) diamond surface orientation, the TE cavity mode matches the transition dipole moment of two (out of four possible) orientations of the SiV center (to a factor of 0.8; cos(35°)). The cavity decay rate κ can be estimated as $\kappa{=}\omega/Q$. At a depth of 25 nm $|\vec{E}(\vec{r})| \approx$10% of maximum cavity field. Assuming we can obtain a $Q \approx 5$k on diamond, $C > 1$ should be achievable.

7.2.1 Fabrication of 1-D PhC devices

The PhC structures are fabricated with two different substrates:

1. **BGaP-on-Si:** This material is appealing because it commercially available as large 300 mm wafers. The BGaP layer thickness is 222 nm, with a boron doping (2.7% B) required for lattice matching to the silicon substrate. The refractive index of BGaP is very close to GaP ($\Delta n \approx 0.02$), however suitability of this novel BGaP material with regards to nanophotonic devices is unknown. Hence, in the next section we fabricate test photonic structures (disk resonators, PhC devices, etc.) to quantify its optical properties.

2. **GaP-on-AlGaP:** This is similar to the material that we previously utilized in chapters 3 and 5. The 290 nm GaP layer was released from a GaP substrate by etching an intermediate $Al_{0.8}Ga_{0.2}P$ sacrificial layer with dilute HF. The GaP was then transferred to the SiO_2/Si substrate using a wet-transfer process[34,113].

After substrate preparation, electron-beam lithography is performed with a JEOL-6300 EBL system using HSQ resist to pattern the PhC devices. Extra care has to be taken during lithography because of the sensitivity of the PhC structure to small variations in the hx, hy dimensions. Typically, a test PhC pattern is written on the day of the device patterning to verify the electron-beam condition. For details on the lithography process, see Appendix-A.

Subsequent inductively-coupled plasma reactive-ion-etching (ICP-RIE) of the BGaP/GaP layer forms the photonic devices. For the BGaP-on-Si devices, the Si substrate is undercut with a XeF_2 vapor etch process. For details on the BGaP/GaP process, see Appendix-B/C respectively. The devices are now ready for pre-transfer optical characterization and eventual stamp transfer to diamond.

7.2.2 Stamp transfer on diamond

A stamping procedure adapted from the stacking of 2-D Van der Waals materials, as shown in Fig.7.3. This technique is described in detail in Ref. [168, 169]. The process is carried out in a flip-chip wafer-bonder (Tresky T-3000-FC3-HF), which controls the pressure, heating and allows precise sample alignment. The process uses a PDMS mesa stamp and a intermediate polypropylene carbonate (PPC) film. The PDMS/PCC stack is brought in contact with the PhC devices and heated to 60° C to promote adhesion. Now, the PDMS/PCC/PhC stack is gently lifted-off the carrier substrate. Next, the diamond substrate, hosting pre-characterized implanted SiV centers is cleaned in a fuming sulphuric acid bath. It is critical that the diamond surface is clean and smooth (roughness $\approx$ 1 nm RMS) for good adhesion to the PhC devices. The PDMS/PCC/PhC stack is aligned and pressed down on the diamond substrate. The stamp and diamond are heated to 130° C, which softens the PPC layer to release the PPC film (with the PhCs) from the PDMS stamp. Finally, we dissolve the PPC in chloroform and rinse the diamond with acetone and IPA, leaving the PhCs in place on the diamond substrate.

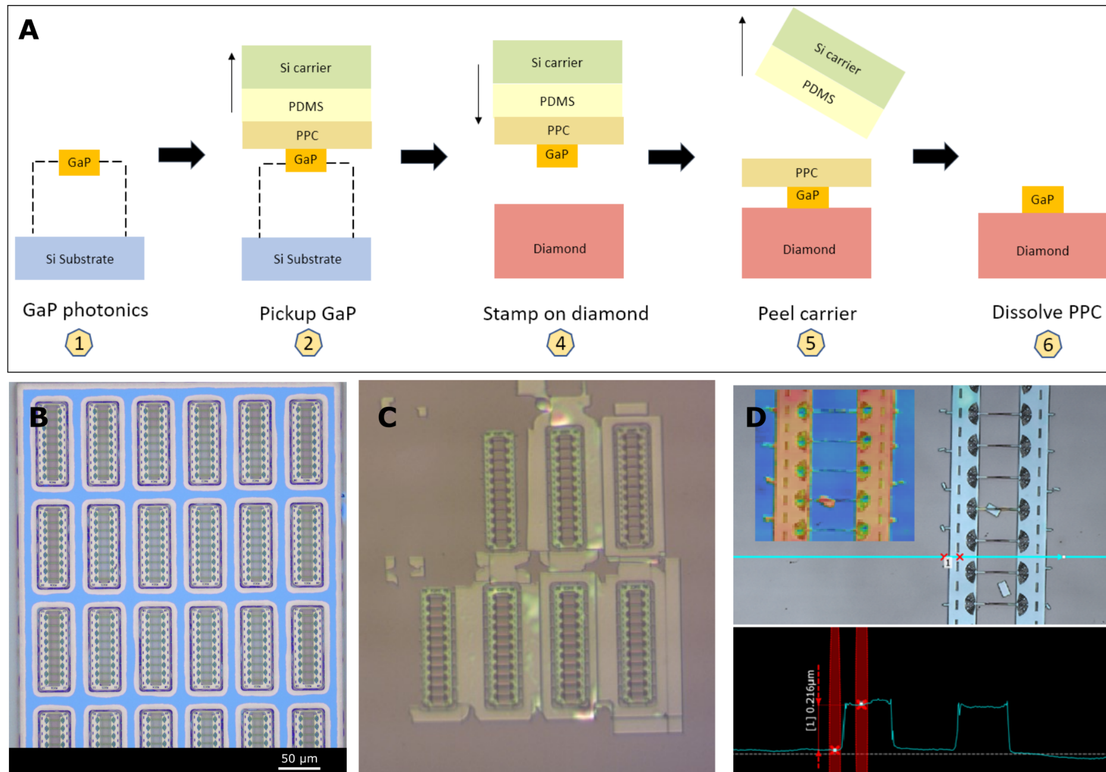

Figure 7.3: **a.** An illustration of the stamp transfer process. We begin with GaP PhCs on a carrier chip and finish with PhC integration with SiV on diamond. **b.** Optical image of suspended BGaP-on-Si PhC devices before stamp transfer. The yellow/blue regions represent suspended and anchored regions of the BGaP. The suspended regions are picked up by the polymer stamp and transferred to diamond. **c.** BGaP PhC devices after transfer on diamond. **d.** Laser scanning profilometry data on transferred PhC devices showing good adhesion to the diamond substrate.

7.3 *Characterization of BGaP*

Before moving forward with fabrication of the novel PhC devices, we need to verify the optical properties of the untested BGaP material. In order to characterize the intrinsic optical quality of the BGaP, we design and fabricate disk-resonator devices in BGaP. Here, we borrow photonic design and fabrication ideas detailed in chapter 3.

The intrinsic quality factor (Q_i) of a nanophotonic disk resonator is related to the losses caused by scattering, absorption and radiative process, and can be estimated from the resonance peak full width half maximum (FWHM or $\Delta\lambda$). We realize an add-drop configuration with multiple disks evanescently coupled to a pair of waveguides. The in and out coupling regions are symmetric

(characterized by coupling quality factor Q_c). The waveguides terminate at free-space grating couplers. The input and drop (output) gratings are placed along orthogonal orientations, thus the input and output light are cross-polarized. The resonances of individual devices are identified by using a supercontinuum laser (650 to 800 nm) for excitation and detecting the output at the drop port with a grating spectrometer. The excitation is linearly polarized, and set to excite either TE or TM resonator modes. Scattered excitation light was filtered out of the collection path via polarization and spatial filtering.

In our system, $\Delta\lambda$ is linked to the loaded or total quality factor ($Q_t = \lambda/\Delta\lambda$). In our add-drop configuration, it is related to Q_i and the coupling quality factor Q_c by $Q_t = Q_i^{-1} + 2Q_c^{-1}$. As the coupling is strength is increased, the light tends to leave the cavity sooner via the waveguide, thus increasing the losses due to the coupling and decreasing Q_c. Depending on the dominating loss processes, the coupling regime can be identified as undercoupled ($Q_i < Q_c$), critically coupled ($Q_i = 2\,Q_c = 2\,Q_t$) or overcoupled ($Q_i > Q_c$). In the deep undercoupled regime, Q_t is dominated by Q_i. In our fabricated devices, we vary Q_c by progressively increasing the waveguide disk coupling distance from 100 nm to 200 nm in steps of 10 nm. Thus, we sweep the entire parameter space from overcoupled to undercoupled regime and expect to see the measured Q_t as a function of the coupling distance (d_c) saturate at Q_i for large d_c.

7.3.1 Photonic add-drop test chips

We fabricate and optically characterize three test chips, each with hundreds of disk resonator devices. Each device array contains disks of varying sizes (2, 3 and 5 µm diameter). We focus our measurements on the 5 µm disks because they are expected to exhibit the highest Q_i (the radiative bending loss decreases with increasing disk diameter). Multiple disks are coupled to the bus waveguides, the diameters (d) of the disks are varied by 10 nm to make the individual disk resonances distinguishable in the drop port spectra (free spectral range = $\lambda^2/(\pi n d) \approx 12$ nm).

1. **Chip-1 BGaP-on-Si_3N_4:** The BGaP (222 nm) is released from the Si substrate by XeF_2 vapor-etch process and then wet-transferred to the Si_3N_4 substrate (Fig.7.4a). Here we choose a Si_3N_4 substrate because its refractive index is close to diamond (2.0 vs 2.4, respectively). HSQ e-beam lithography and RIE etch, as described in section 7.2.1 defines the photonic

structures (Fig.7.4b,c). The results from the TM-mode drop-port measurements (Fig.7.4d,e) reveal that the average Q_t for undercoupled disks is $\approx$ 15k, with the maximum observed Q_t of 24k. This is an order of magnitude lower than expected for GaP[61,170,171]. Some nanometer scale residue (perhaps from the wet-transfer process) can be observed both in optical and SEM images near the devices. One can hypothesise that such residue could limit the observed Q. To verify this claim, next we use a simplified/cleaner process to fabricate suspended disk resonator structures with the BGaP-on-Si material.

2. **Chip-2 Suspended BGaP-on-Si:** We begin with BGaP-on-Si samples and move directly to HSQ e-beam lithography and RIE etching, as described in section 7.2.1 to define the photonic structures. We clean the etched samples in hydrofluoric-acid (remove HSQ resist) and use a vapor phase etch (XeF_2) to undercut the disks and release them from the Si substrate (Fig.7.5a,b). The grating orientation and geometry (optimized for TE mode) are different because of the suspended architecture. Given that the disks are suspended (highest possible index contrast), we expect to see $Q_t > 100$k. However, just as seen on the previous BGaP chip, the results from the TE-mode drop-port measurements (Fig.7.5c,d) reveal the average Q_t for undercoupled disks to be $\approx$ 15k, with the maximum observed Q_t of 24k. The results suggest Q_i is limited by intrinsic loss within the BGaP.

3. **Chip-3 Fariba-GaP wet-transferred to Si_3N_4:** For reference, we also make photonic devices with the GaP-on-AlGaP material utilized in chapters 3, 5. The GaP (290 nm) is lifted-off by wet etching the AlGaP and wet-transferred to 250 nm Si_3N_4-on-Si substrate (Fig.7.6a). We make identical devices to Chip-1 using the same exact fabrication process (Fig.7.6b,c). The results from the TM-mode drop-port measurements (Fig.7.6d,e) reveal that the average Q_t for critically coupled disks is spectrometer limited (Q_t >33k).

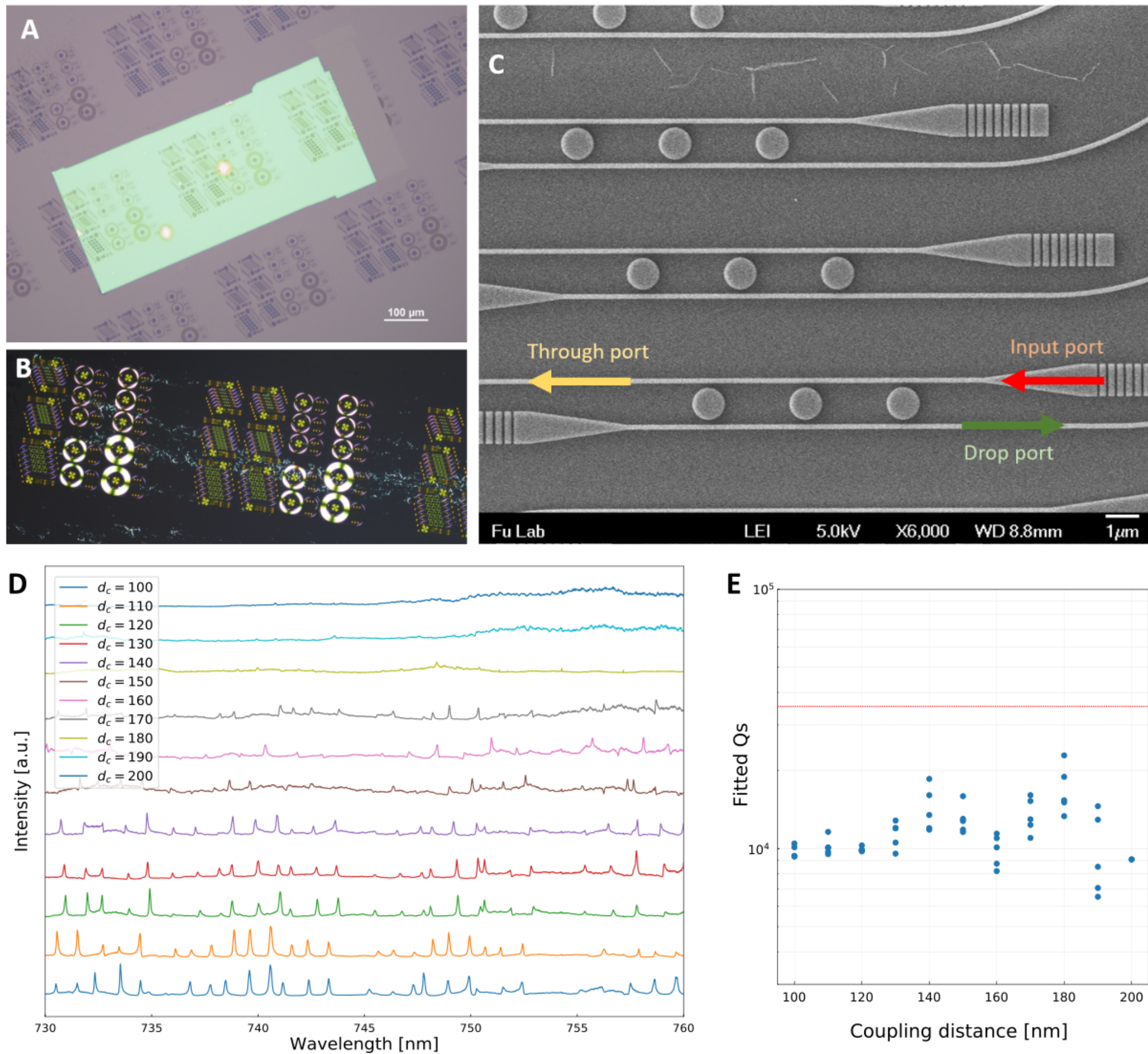

Figure 7.4: **a.** Optical image of HSQ electron-beam patterns on BGaP (green) wet-transferred on Si_3N_4/Si substrate. **b.** Optical cross-polarized image of the devices after the GaP RIE plasma etch. **c.** SEM image of etched photonic disk resonator devices in the add-drop coupling configuration. Each waveguide is coupled to a set of three disk resonators. **d.** Measured TM spectra of 5 µm diameter disk resonators through the drop port as a function of the waveguide coupling distance (d_c). The spectra shown here corresponds to approximately four free-spectral range of the resonators (i.e. four distinct groups of resonances). Few resonances are observed for the three most undercoupled disks (d_c = 200, 190, 180). **e.** The resonances are fitted to a Lorentzian and their quality factors (Q) are estimated as a function of the coupling distance. The highest observed Q is $\approx$24k and below the spectrometer resolution limit (red line).

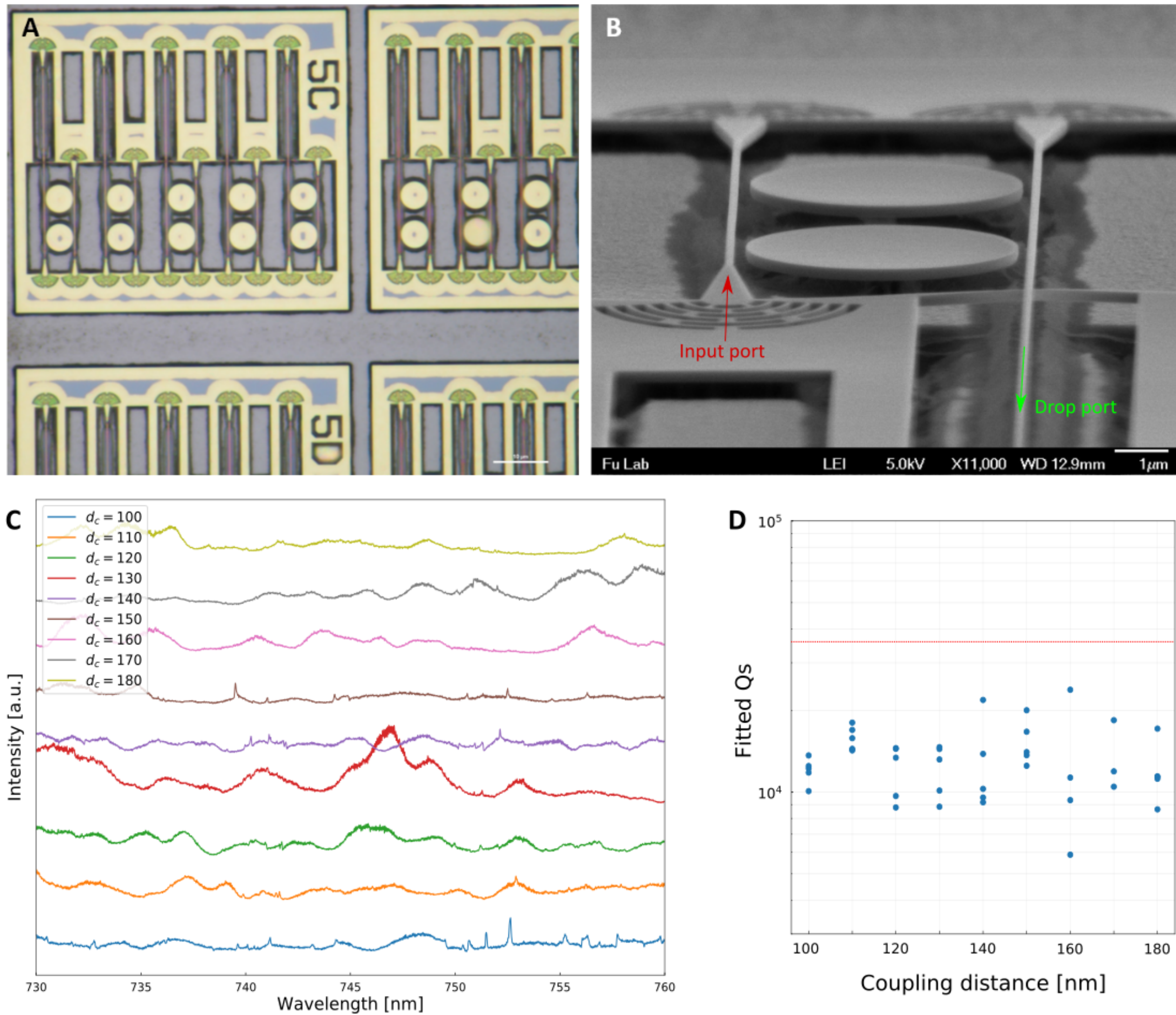

Figure 7.5: **a.** Optical image of BGaP-on-Si suspended disk resonator devices. The yellow regions are suspended. The 5 µm diameter disks are supported by a small (≈ 1 µm dia.) Si pedestal at the center (grey). **b.** Angled SEM image of suspended devices in the add-drop coupling configuration. Each waveguide is coupled to a pair of disks. The undercut between BGaP and Si substrate is ≈ 2 µm. We suspect that the waveguides may be slightly bowed due internal stress within the BGaP, leading to variation in resonator coupling across devices. **c.** Measured TE spectra of the disk resonators through the drop port as a function of the waveguide coupling distance (d_c). The spectra corresponds to approximately four free-spectral range of the resonators. The increased background in the spectra can be attributed to scatted light due to the co-polarized nature of the input and output gratings (design limitation of suspended structures). **d.** The resonances are fitted to a Lorentzian and their quality factors (Q) are estimated as a function of the coupling distance. The highest observed Q is ≈ 24k and below the spectrometer resolution limit (red line).

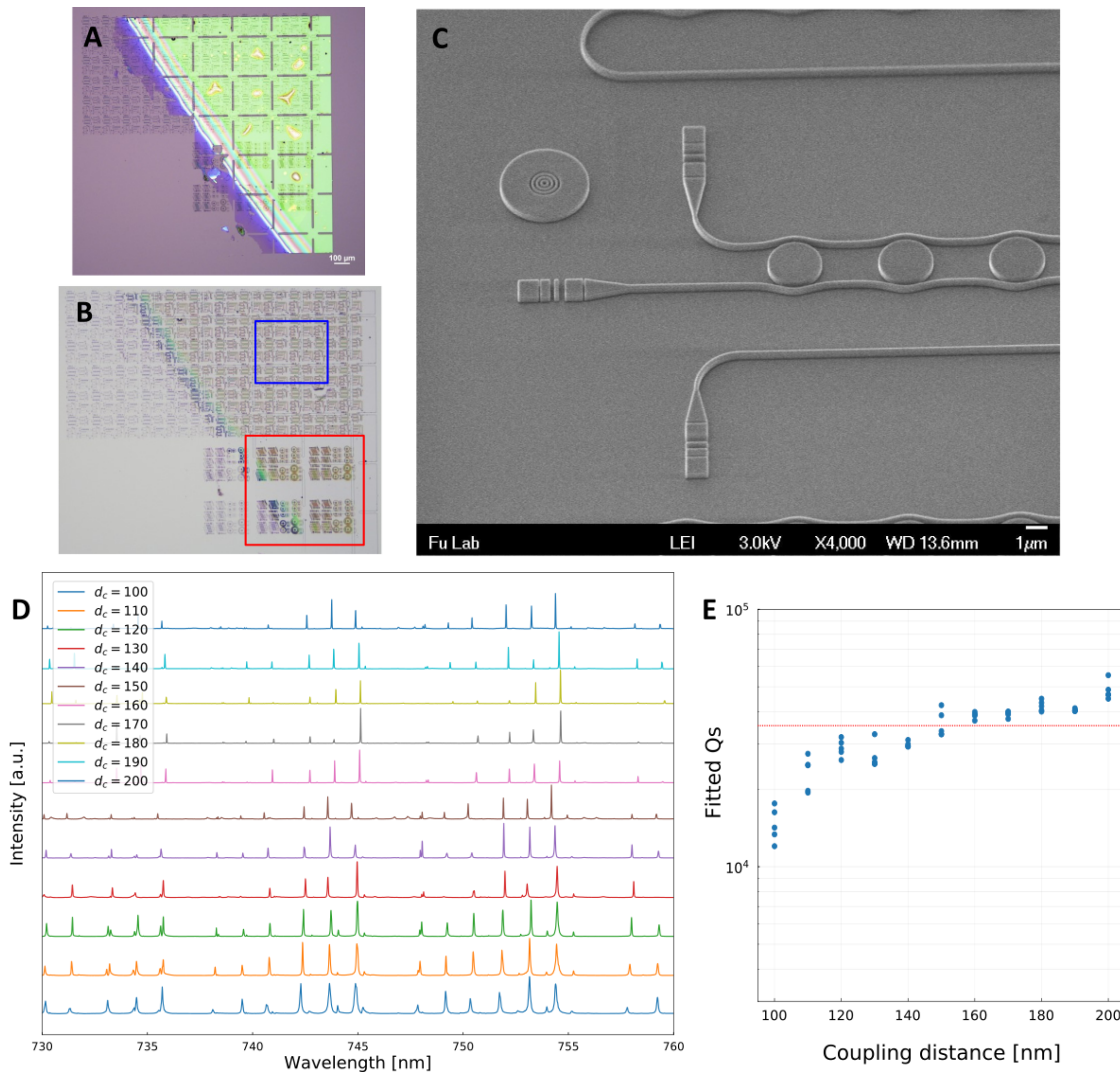

Figure 7.6: **a.** Optical image of HSQ electron-beam patterns on Fariba-GaP (green) wet-transferred to Si_3N_4/Si substrate. **b.** Devices after the GaP RIE plasma etch. The blue and red square marks two different photonic patterns. The red region is identical to the BGaP-on-Si_3N_4 chip (Fig.7.4). **c.** Angled SEM image of etched photonic disk resonator devices in the blue region. **d.** Measured TM spectra of 5 µm diameter disk resonators (in the red region) through the drop port as a function of the waveguide coupling distance (d_c). Resonances are observed for even the most undercoupled disks (d_c = 200). **e.** The resonances are fitted to a Lorentzian and their quality factors (Q) are estimated as a function of the coupling distance. The highest observed Q is spectrometer resolution limited (red line).

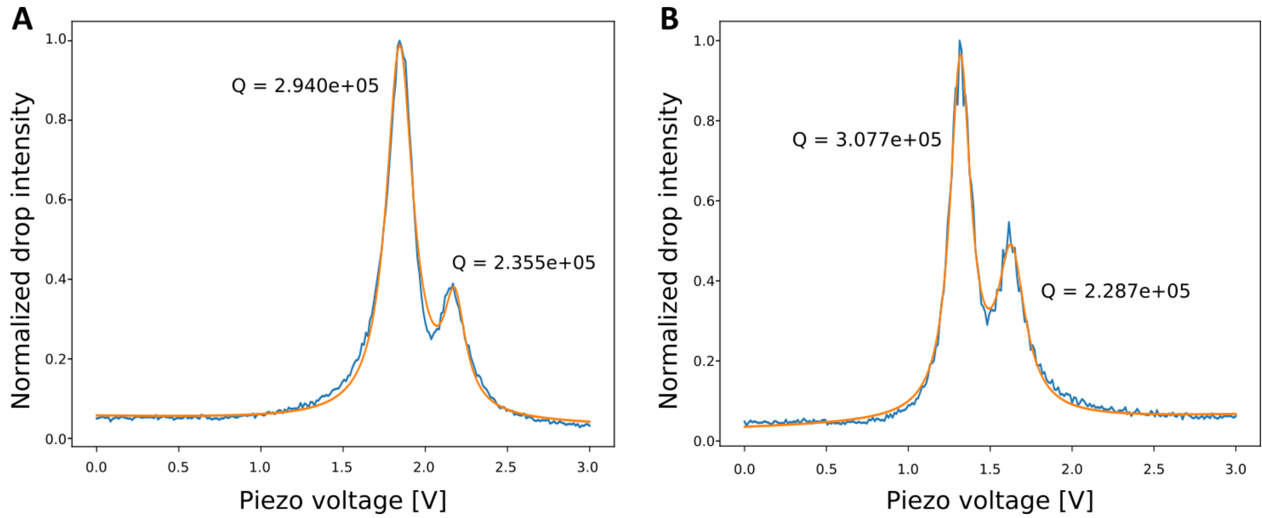

Figure 7.7: High resolution drop-port spectra obtained on the Fariba-GaP on Si_3N_4 using a tunable laser (760 to 785 nm). Here 1 V laser piezo-voltage corresponds to 8.33 GHz. For the 5 µm dia. undercoupled disk resonator devices, we observe that most resonances are split, with a Lorentzian fit (orange) giving Q ~300k.

7.3.2 Comparison of BGaP and Fariba GaP material

The spectrometer measurements for the three chips, suggests that the Fariba GaP-on-AlGaP material has significantly lower intrinsic optical loss compared to the BGaP-on-Si material. To verify, we perform high-resolution scanning laser spectroscopy on spectrometer-limited resonances of chip-3 (Fig.7.7). We measure average Q-factors >200k, with the max Q of ≈ 310k at 760 nm.

Based on these measurements, we select the Fariba GaP-on-AlGaP material for the final PhC device fabrication. However, it can be argued that we have not explored the absolute limits of the BGaP material here because both the BGaP chips-(1,2) exhibited certain fabrication irregularities; chip-1 had some residue near the devices area, chip-2 exhibited irregular coupling because of bowed suspended waveguides (due to internal BGaP stress). Although the average and max Q-factor data from chips 1 & 2 agree well, for conclusive proof of BGaP capabilities further studies are necessary.

7.4 Pre-transfer PhC measurements

The PhC devices are characterized prior to stamp transfer to diamond. Each device consists of a PhC cavity ending with a free-space grating coupler at either end. One grating is utilized for excitation while the cavity transmission is measured at the other grating. The resonances of individual devices are identified by using a supercontinuum laser (600 to 800 nm) for excitation and detecting the output with a grating spectrometer. The excitation is linearly polarized, and set to excite the TE resonator mode. Scattered excitation light was filtered out of the collection path via spatial filtering. The PhC devices are sensitive to nm scale changes in the structure. Hence, we vary the hole dimensions across the device arrays to compensate for fabrication variations. Additionally, we sweep the number of mirror $M \in \{2, 14\}$ and taper $T \in \{12, 20\}$ holes to gather information on the coupling and Q scaling. Each array also consists of black waveguides to characterize the in/out grating coupling efficiency.

7.4.1 Suspended BGaP PhC devices

First we look at suspended BGaP PhC devices (Fig.7.8a). The PhC beams are attached to a large frame support structure. The frame is held in place by narrow pinch points. With careful e-beam lithography calibration and fabrication process control, PhC hole dimensions within 5% of design can be achieved (Fig.7.8b).

Initially we perform a survey of the chip measuring the transmission spectra (Fig.7.8c) with a wide-range low-resolution grating (300g). We observe a pseudo-band gap for the PhCs extending from 680 to 725 nm. The pseudo-band gap refers to the fact that additional guided modes are revealed within the band gap due to a change in the slope of the light-line because the substrate is now air and not diamond (Fig.7.1c). Two resonance modes can be observed close to the edge of the pseudo-band gap. We then zoom-in on the resonances (Fig.7.8d) using a high-resolution grating (1800g). The resonances are close to the design wavelength (721 nm) and exhibit Q-factors ranging from 2k to 8.5k across the chip. Because these PhC devices are suspended, the simulated Q-factors are three orders of magnitude higher than shown in Fig.7.2c.

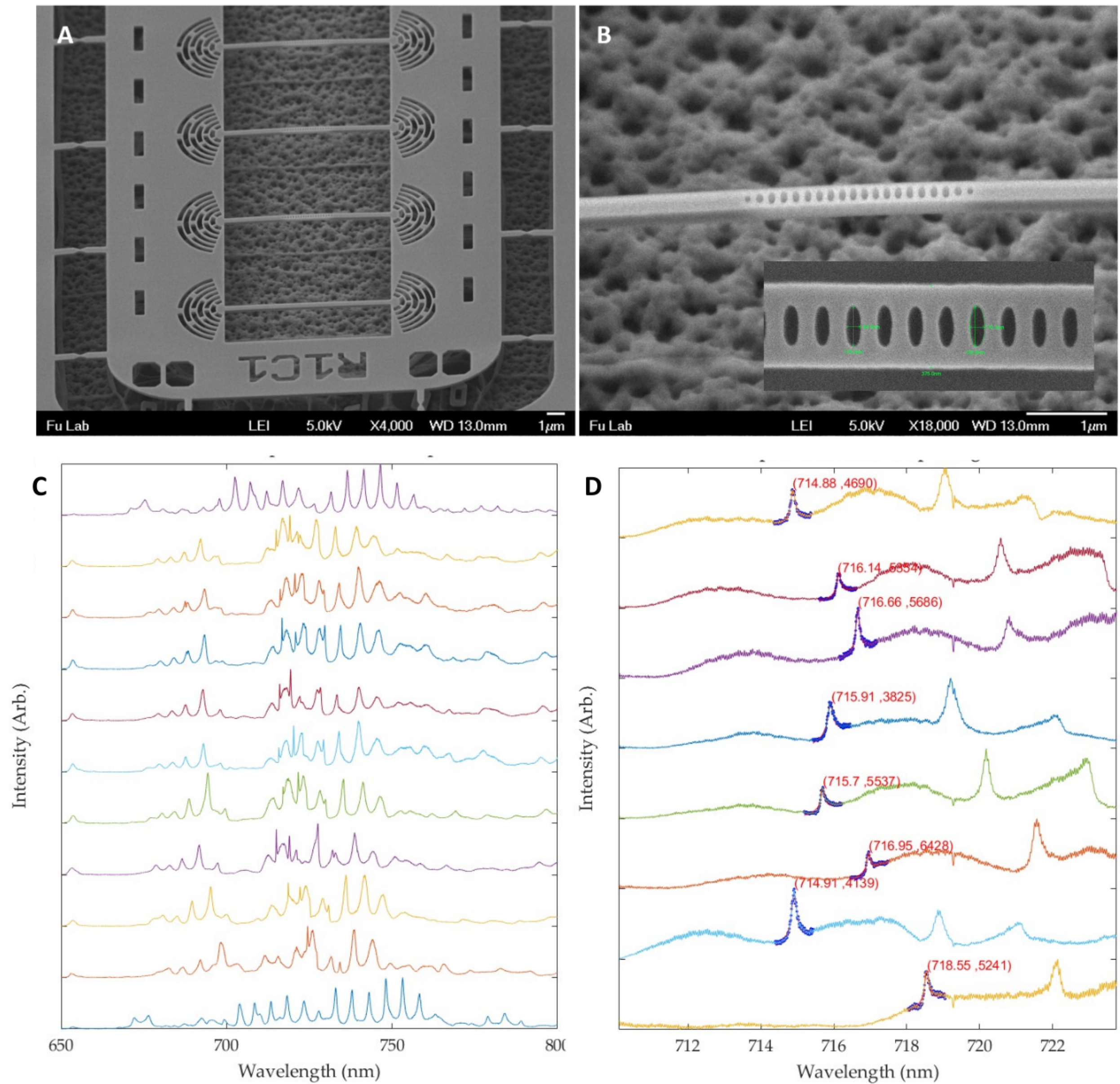

Figure 7.8: **a.** Angled SEM of suspended BGaP PhC devices. The devices are supported by a large frame structure. **b.** Zoomed-in angled SEM showing the PhC resonator. Inset, top-down SEM view of the holes defining the PhC cavity. The hole dimensions are within 5 nm of design. **c.** Transmission spectra of a set of PhC resonators under TE supercontinuum excitation. The bottom and top devices are blank waveguides (no holes). We can see a photonic band gap structure between 680 to 725 nm. There are two resonator modes visible towards the edge of the band gap. **d.** Higher resolution transmission spectra of the devices showing the first and second order PhC resonances, with the estimated Q-factor obtained by fitting to a Lorentzian.

7.4.2 Fariba GaP-on-oxide PhC devices

An identical PhC pattern is fabricated on GaP wet-transferred to SiO_2 substrate (Fig.7.9a-d). As before, we perform a survey of the chip measuring the transmission spectra (Fig.7.9e) with a wide-range low-resolution grating (300g). No band gap is observed, but we find resonances near 770 nm that exhibit a wide range of Q-factors from 1k to 10k across the chip (Fig.7.9f,g). Here we need to note that the GaP thickness of 290 nm is much larger than the design specification of 222 nm. Thus, the PhC resonances are strongly red-shifted. However the fact that Q-factors for devices on an oxide substrate are similar to the previous suspended BGaP chip is very promising (reduced Q is expected from decreased index contrast and introduction of additional optical loss mechanisms when PhC are in contact with substrate).

7.4.3 Tuning PhC devices by thinning GaP layer

To couple the Fariba-GaP devices to SiV^- emitters, the resonances need to be centered around 737 nm. We can blue-shift the PhC resonances by iterative thinning of the GaP layer (Fig.7.10a). The thinning process involves a short ($<$15 s) blanket GaP RIE plasma etch. After each etch cycle, the PhC transmission is measured to track the resonance blue-shift. We selectively tune one section of the PhC array to match SiV^- (Fig.7.10b). Here we target 731 nm (Fig.7.10c) as stamp transfer to higher index diamond substrate is expected to red-shift the resonances by $\approx$7 nm. In addition to resonance shift, we observe that the cavity Q increase by a factor of five (Fig.7.10d). Many PhCs exhibit Q-factors at the spectrometer limit ($\approx$30k). We suspect that the thinning process gradually erodes the holes, increasing their diameters. This is supported by the observation of increasing Q with decreasing resonance transmission intensity (Fig.7.10a) through the thinning cycles. It appears that the PhC are likely changing their coupling regime from overcoupled to undercoupled. Next, these promising devices are stamped on diamond substrate hosting SiV centers.

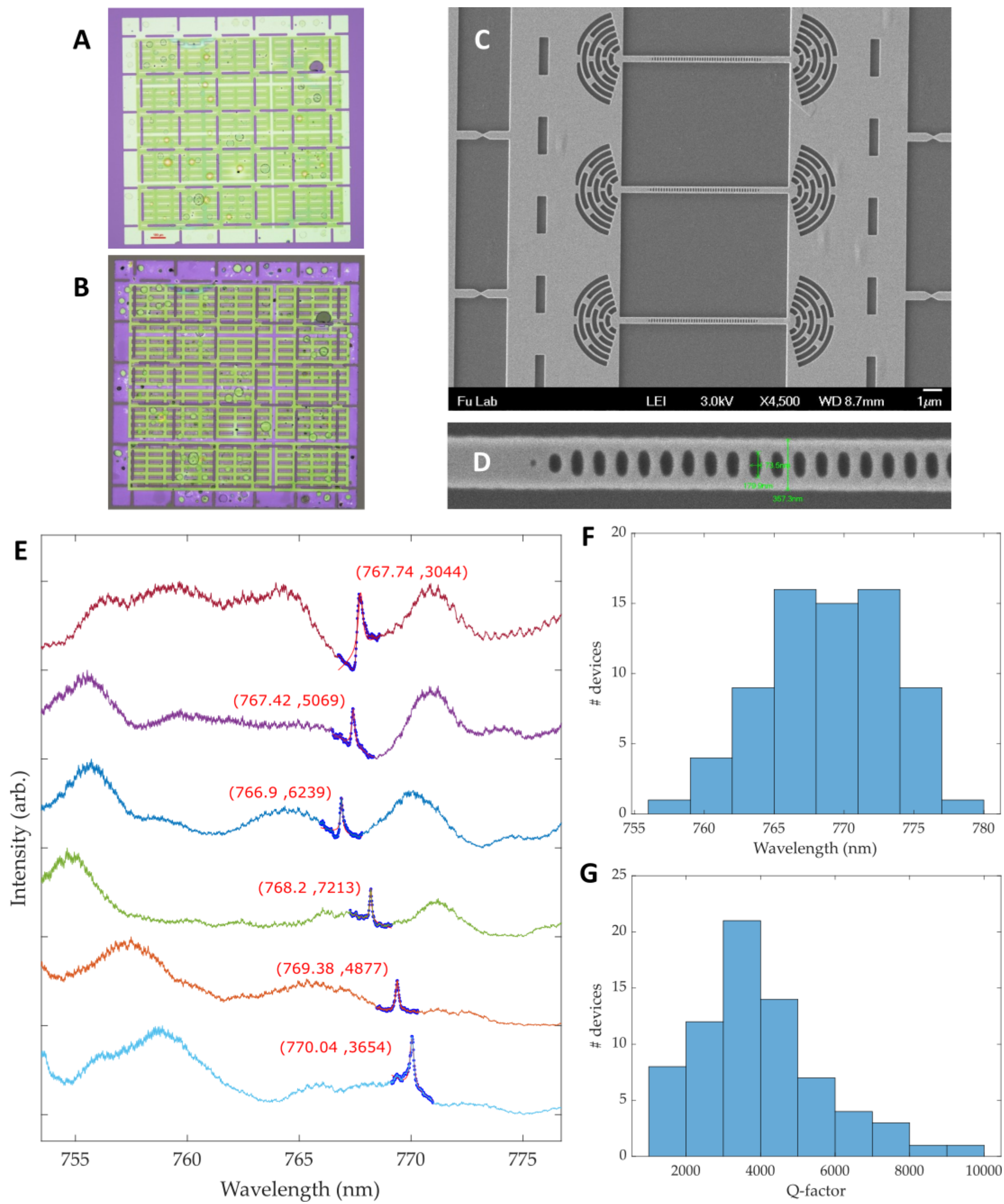

Figure 7.9: **a.** Optical image of HSQ electron-beam patterns on GaP (green) wet-transferred on SiO_2/Si substrate. **b.** Devices after the GaP RIE plasma etch. **c.** SEM image of etched PhC devices. **d.** High-magnification SEM image of the etched PhC holes. **e.** Transmission spectra of a set of PhC resonators under TE supercontinuum excitation. **f.** Distribution of observed PhC resonances across the chip. Because the GaP thickness is higher than design (290 nm), the resonances are red shifted. **g.** Distribution of fitted Q-factors measured across the chip.

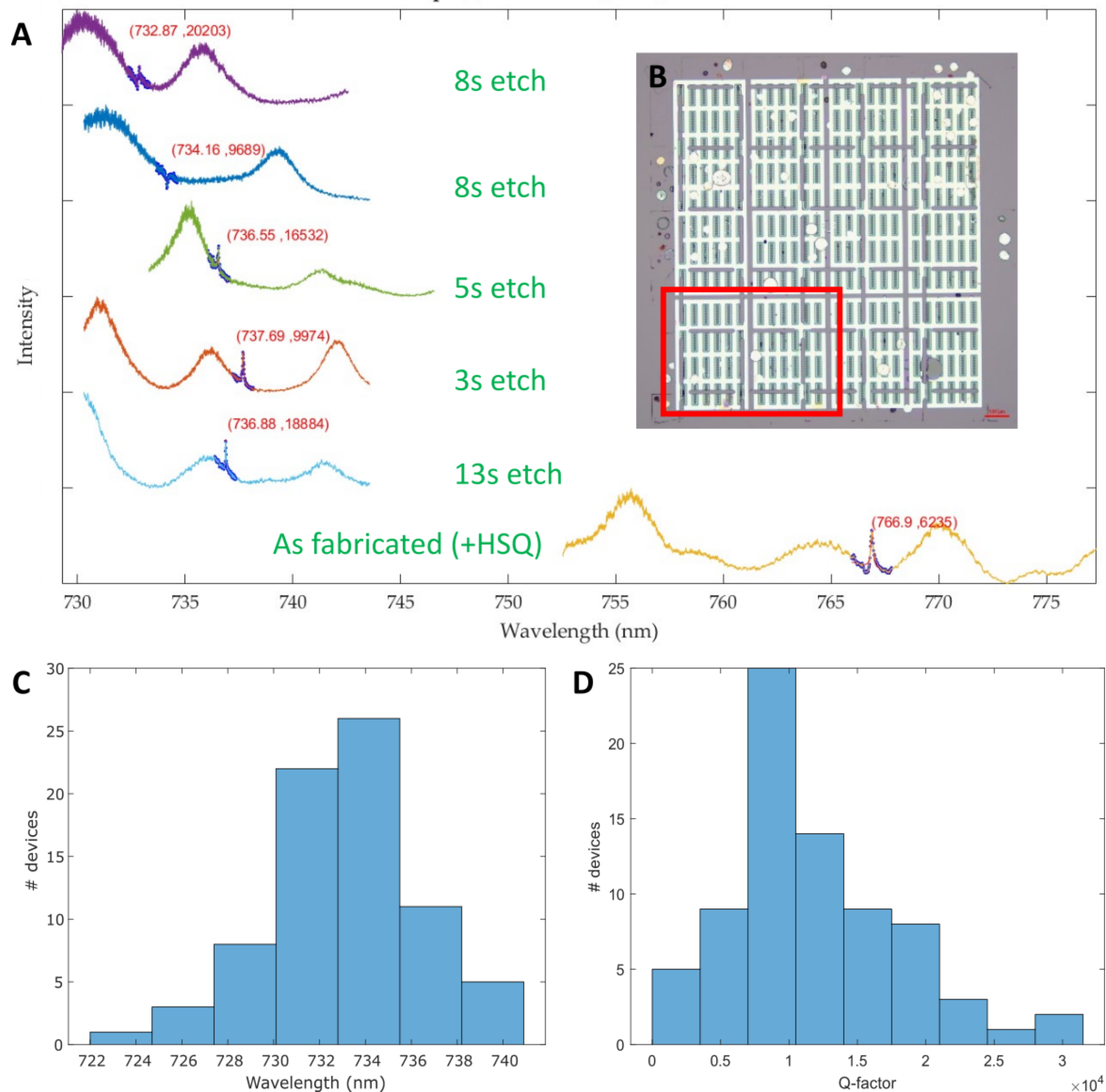

Figure 7.10: **a.** The transmission spectra of one specific PhC resonator tracked through multiple thinning etch cycles. The resonance is blue shifted as the GaP thickness is reduced. Additionally the PhC holes are gradually eroded, likely changing the coupling regime from overcoupled to undercoupled. **b.** Devices after the blanket GaP RIE plasma thinning etch. The resonances in the red region of the chip are tuned to match SiV^- emission. **c.** Distribution of observed PhC resonances within the red region. **d.** Distribution of fitted Q-factors measured within the red region.

7.5 Stamp transferred PhCs coupled to SiV centers in diamond

Based on the pre-transfer PhC optical measurements, we select the Fariba GaP-on-oxide PhCs for stamp transfer to diamond. We use a chemical vapor deposition diamond (Element Six, electronic grade, N $<$ 5 ppb, B $<$ 1 ppb) implanted with Si accelerated to 26 keV (5e11/cm^2 dose, 7° angle) and vacuum annealed at 1200 °C. During annealing, SiV centers are formed by vacancy diffusion and recombination with the implanted silicon (concentration of silicon atoms incorporated during diamond growth is negligible), yielding a thin layer of SiVs 20 nm from the surface ($\approx$ 10 SiV centers per excitation spot). Because this SiV layer is sampled by the small mode volume of our PhC devices, we expect to observe coupling to single SiV centers. Stamp transfer is performed by the technique described in section-7.2.2. The stamping yield is low (5%) due to surprisingly strong adhesion of the fabricated GaP devices to the oxide carrier substrate, i.e. few devices are picked-up by the polymer stamp. In the future, we can mitigate this issue by suspending the GaP photonics layer with a vapor-HF oxide-undercut etch.

7.5.1 Post-transfer PhC transmission measurements

Following the pre-transfer characterization, we first perform transmission measurements on the transferred GaP-on-diamond PhCs. The resonances of individual devices are identified by using a supercontinuum laser (600 to 800 nm) for excitation and detecting the output with a spectrometer. For devices with both coupling gratings intact, the excitation and collection is performed at the input and output gratings respectively. However, if the gratings are missing (lost during stamping), we excite at the break in the waveguide or directly at the center of the cavity. Enough light can be coupled into the structure even without gratings to allow detailed characterization of the cavity resonances. We observe cavity resonances for all intact PhCs, with resonance wavelengths in the range of 730 to 755 nm. Remarkably, many stamped devices show high-Q resonances to within 20 % of the design $Q \approx 10$k (Fig.7.11a).

7.5.2 PhC cavity coupling to SiV centers

Next, we perform room-temperature measurements to study SiV coupling to the stamped GaP photonic devices. Here we excite with an off-resonant 532 nm laser and collect SiV PL both at

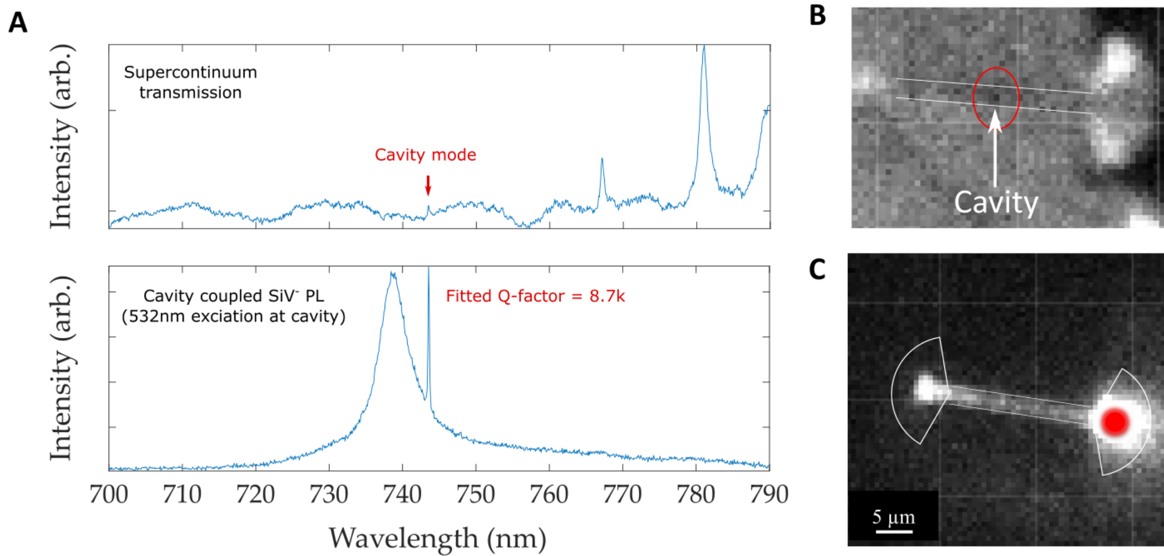

Figure 7.11: **a.** The room-temperature transmission spectra of one PhC resonator under supercontinuum excitation compared to 532 nm excitation. We can see the high-Q SiV-coupled cavity mode at 743 nm. **b.** A SiV PL confocal image of a stamped PhC device under 532 nm excitation. The SiV PL appears suppressed at the center of the cavity. **c.** A SiV PL confocal image of a stamped blank waveguide device under 532 nm excitation. Here the collection is fixed at the output grating coupler (red circle) while the excitation laser is scanned across the image. Significant SiV PL is coupled into the waveguide and out through output coupler.

the excitation position and from the waveguide at the output grating. When exciting PhCs at the cavity mode maxima, we see enhanced SiV PL emission within the cavity resonance (Fig.7.11a). Further, when we perform confocal scanning across the PhC devices, we see what appears to be suppressed SiV PL at the center of the cavity (Fig.7.11b). This could indicate that only the SiV PL component resonant with the narrow cavity mode is enhanced (higher optical density of states), while all other PL components are suppressed due to the PhC band gap (lower optical density of states)[164]. To verify SiV-GaP photonic coupling, we can look at blank waveguide devices (no PhC holes). Here, we spatially filter out the SiV PL collection from the output grating coupler, while scanning the off-resonant excitation laser across the waveguide (Fig.7.11c). We observe that a significant fraction of SiV PL is coupled into the waveguide and measured at the output coupler. These results confirm that a good optical interface can be established between the diamond and the stamped GaP photonic layer.

7.6 Summary and outlook

In this chapter, we have shown that GaP PhC cavities can be fabricated on a separate carrier chip and successfully integrated with a diamond SiV qubit host by stamp transfer. Before integration the cavities can be characterized and tuned to the specific target resonance wavelength (737 nm for SiV ZPL). This ensures that we maximize SiV-cavity coupling yield, while preserving the qubit environment within the diamond. For the transferred GaP-on-diamond PhC cavities, we measure quality factors close to the design target. The maximum SiV-coupled quality factor observed was $Q = 8.7$k (target $Q = 10$k). We see an enhancement of the SiV PL coupled to the cavity resonance, laying the foundation for several follow-up experiments necessary to fully characterize the SiV-cavity spin-photon interface:

1. The optical measurements detailed in this chapter are performed at room-temperature, where the SiV ZPL is significantly temperature broadened (linewidth at 300 K is typically 3 THz or about 5.5 nm)[38]. This allows us to easily identify SiV-cavity coupling, however, for quantum information applications we have to operate at low temperature (< 10 K). And at low temperature, the narrow SiV ZPL are revealed with their four-line fine-structure (linewidth at 10 K is typically < 200 MHz)[38]. Additionally, due to the GaP index dependence on temperature[172] the cavity resonances are expected to blue-shift by about 7.8 nm. Thus fine-tuning of the cavity mode by gas deposition (as shown in chapter 3 with disk-resonators) will be necessary for achieving coupling to the SiV ZPL transitions. This will also allow us to characterize the coupled SiV Purcell-enhancement and estimate the SiV-cavity coupling strength.

2. Next, we need to carefully study the spectral properties of cavity coupled SiV centers by resonant excitation spectroscopy (as demonstrated for NV centers in chapter 5). Given the inherent immunity of the SiV centers to charge noise and the fact that we do not disturb the SiV diamond environment, we expect to observe near lifetime-limited SiV linewidth ($\approx$100 MHz at 4 K)[38, 56]. Here, it is also important to demonstrate long-term stability of the coupled-SiV ZPL transition energy.

A new commercially available boron doped GaP (BGaP-on-Si) material is considered for photonic device fabrication. Initial results with disk-resonator devices show more than an order of

magnitude lower quality factors when compared to the Fariba-GaP (disk-resonator $Q \approx$15k for BGaP vs $Q \approx$300k for Fariba-GaP). Hence, we utilize the Fariba-GaP material for the stamped GaP-on-diamond PhCs. However, we are working with the BGaP manufacturer to figure out the factors limiting the optical quality of the material. Having a high-quality commercial source of GaP material (300mm wafers) would be a great advantage for future scalable realizations of the GaP-on-diamond photonics platform.

Chapter 8

Progress towards on-chip entanglement circuits

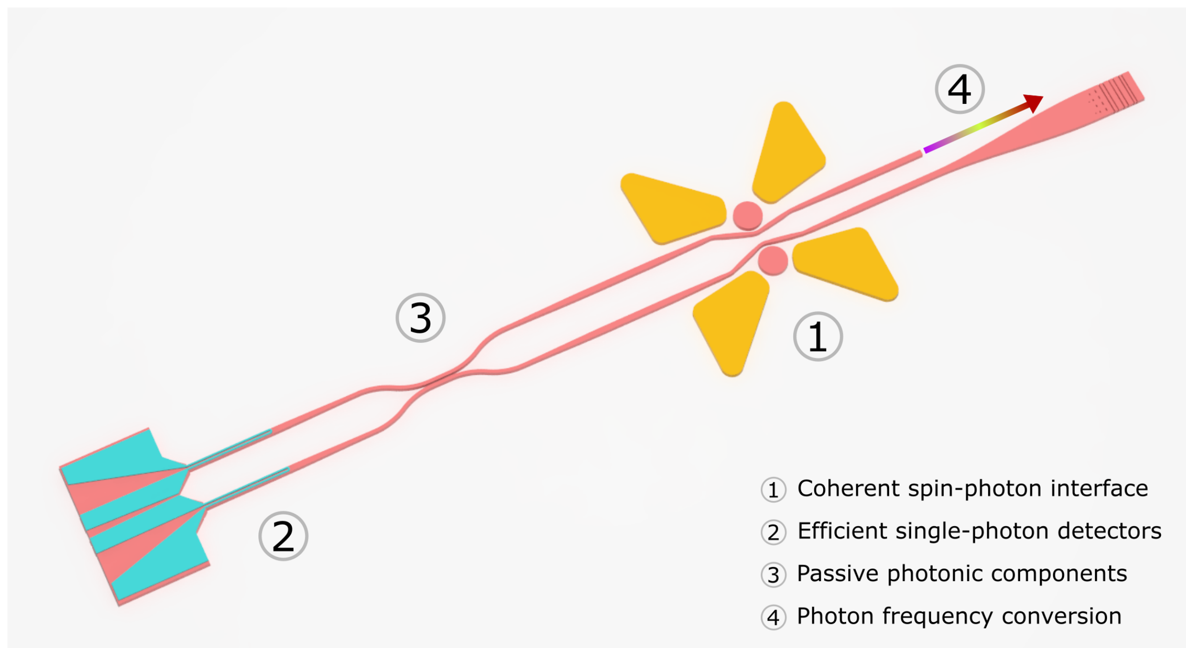

Figure 8.1: Illustration of a GaP-on-diamond photonic circuit for entanglement generation.

The goal of this thesis is to demonstrate that optically addressable defect qubits in diamond can be utilized to build a scalable photonic architecture for quantum information applications. Ultimately, we envision a compact integrated GaP-on-diamond on-chip photonic entanglement generation circuit as illustrated above. In this chapter, we discuss our progress towards realization of the different components of such a circuit and ideas for robust/flexible operation that we are currently exploring.

8.1 (1)-Coherent spin-photon interface

The primary component of an integrated entanglement generation circuit is the coherent spin-photon interface, wherein the electron spin-states of defect qubits in diamond are coupled to optical modes in the photonic GaP layer. We devote the bulk of this thesis to fabricating and characterizing different approaches to optical coupling of spins in diamond. Various geometries of photonic devices such as disk-resonators (chapter 3), inverse-designed grating-like photon extractors (chapter 5) and 1-D photonic crystal cavities (chapter 7) are investigated in order to build a robust spin-photon interface.

One of the main challenges we faced when performing the NV-photonic coupled experiments of chapters 3 and 5 was the significant spectral instability of the implanted NV centers. To quantify and mitigate the NV behaviour we performed extensive confocal and spectroscopic studies in chapter 4 and 6. A major ongoing effort in quantum information science is to develop a solid-state qubit node with optical and spin transitions that are robust against sources of decoherence. SiV centers in diamond have recently emerged as a promising qubit candidate due to their inherent optical stability[56, 57]. In chapter 7, we create SiV centers by ion-implantation and demonstrate coupling of the implanted SiV centers to stamp transferred 1-D GaP photonic crystal cavities. There are several promising future directions we are pursuing following the results presented in this thesis.

8.1.1 On-chip Hong-Ou-Mandel experiment

To generate entanglement between distant optically addressable defect centers, the defect spins must each be entangled with photons that are indistinguishable and thus capable of coherently interfering on a beam splitter. When two identical photons, which are bosonic particles, enter a beam-splitter simultaneously with one photon in each input port, they bunch together at either of the two output ports. The corresponding disappearance of the coincidence count is the Hong–Ou–Mandel[173] (HOM) effect. The HOM measurement is a precursor for remote-entanglement based protocols and the visibility of the HOM dip is a figure-of-merit for a viable quantum information platform. In solid-state defect qubits, this effect has been demonstrated for deep grown-in NV centers[174] and implanted SiV centers in diamond[56]. Successful HOM can demonstrated two things; (1) that a single defect can produce identical photons (using delayed photons from a single defect center) and

(2) that multiple defect centers can produce identical photons. As discussed previously, because of the issues with charge state stability, spectral diffusion and spectral variation, it is a challenge to demonstrate HOM with implanted device coupled NV centers. We hope to achieve this milestone by refining our photonic integration process and exploring other defects such as SiV^0 centers in diamond.

8.1.2 Diamond surface passivation techniques

For integration with photonic structures, defect centers have to be relatively close to the diamond surface. In chapter 5 and 6, we have discussed the important role played by the surface on the charge-state stability and coherence properties of near-surface NV centers. A careful investigation of the diamond surface as a function of the surface termination needs to be performed to determine mitigation strategies. Various approaches such as plasma exposure[175], chemical treatment[157], functionalization with organic molecules[176, 177] and atomic-layer deposition[178] of thin films have been explored in literature.

8.1.3 On-chip acousto-optic frequency shifters

For high-fidelity entanglement schemes, we require spectrally indistinguishable photons emitted from defect qubits. Although defects such as SiV centers exhibit enhanced spectral stability, the problem of spectral inhomogeneity remains. SiV centers are susceptible to local variations in the strain environment, hence typically a broad distribution of optical transitions can be observed for defects created by implantation. We can compensate for the spectral inhomogeneity by frequency shifting[179, 180] emitted photons using integrated acousto-optic modulators (AOM). A similar scheme has recently been demonstrated for distinguishable cavity-integrated SiV centers using commercial electro-optic modulators[181]. Integrated nanophotonic AOM devices have been demonstrated with material platforms such as lithium niobate[182] and aluminium nitride[183]. Alternatively, on-chip frequency conversion schemes could be utilized to convert the distinguishable defect photon emission to a common output frequency. This is discussed in section-8.4 below.

8.2 (2)-Waveguide integrated on-chip superconducting single photon detectors

For photon-mediated quantum information processing with defect centers, high-efficiency on-chip photon detection is very important. Waveguide-integrated superconducting single photon detectors (SSPD) provide the highest possible performance with respect to dark-count rates (milli-Hz)[184], visible light detection efficiencies (>80%)[185], speed (>200 MHz)[186], and total system efficiency (detection is on-chip). The SSPD consists of a thin nanowire (∼80 nm wide) patterned from a few nm thick (∼8 nm) niobium nitride (NbN) superconducting film deposited on top of the GaP photonics layer (Fig. 8.2a).

The nanowire devices are operated below the superconducting critical temperature (<16 K) and are biased close to but below their critical current (Ic, at I > Ic the superconducting nanowire switches to normal ohmic behavior). The nanowire couples to the evanescent field of the waveguide. When a photon is absorbed by the nanowire, it creates a resistive hotspot region. This hotspot grows to encompass the entire cross-section of the nanowire, increasing resistance of the nanowire and causing a measurable voltage pulse i.e. each voltage pulse is a single-photon detection event (Fig. 8.2b).

Proof-of-concept device fabrication and testing was performed on the original GaP-on-AlGaP substrate (i.e. not transferred to diamond). Prior to fabrication, the thin superconducting NbN films exhibit a Tc ∼13 to 16 K and room temperature sheet resistance of 450-500 Ωcm^{-2}. We fabricated single wire detectors (36 devices) with the form-factor needed for waveguide integration (Fig. 8.2c, d). Characterization was performed under 637 nm normal incidence illumination. The order-of-magnitude estimated intrinsic efficiency of these devices was ≈ 10 %. The low photon detection efficiency and yield can be attributed to non-uniform etching of the NbN film and poor surface quality of the underlying GaP. Maximum count rates of 18 MHz were obtained (Fig. 8.2e), limited by the maximum data rate of ID-Quantique counting board. With a measured detector dead time of ∼5 ns, we can estimate the max count rate of the detector to be about 200 MHz. Dark count rates of less than <0.1 Hz were obtained (Fig. 8.2f) for bias currents I_b <0.8 I_c.

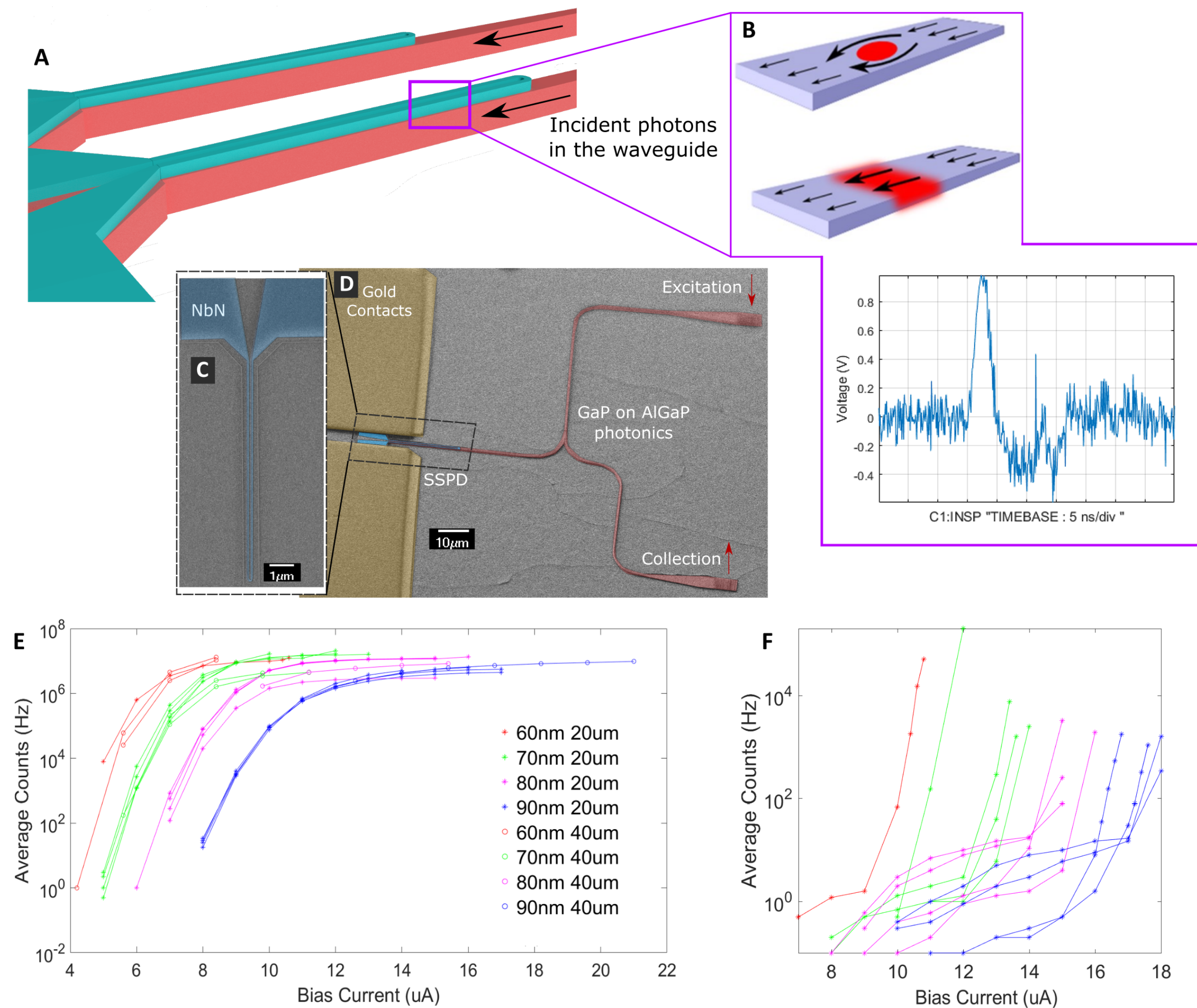

Figure 8.2: **a.** Illustration of the SSPD loop (teal) on the GaP waveguide (pink). The incident photons are guided within the waveguide. **b.** Hotspot formation within the SSPD upon absorption of the incident photon. Each hotspot event triggers a voltage pulse. **c.** Colorized SEM image showing the NbN (blue) nanowire on GaP. **d.** A waveguide coupled SSPD device identifying the AlGaP (grey), GaP (pink), NbN (blue) and gold contact (yellow) layers. **e.** The detector response to normal attenuated laser excitation vs nanowire bias current for various nanowire widths. **f.** The dark count rate vs nanowire bias current for various nanowire widths. Optical measurements performed at 4.2K.

8.3 (3)-Passive photonic components

In addition to a spin-photon interface (such as disk-resonator coupled NV centers) and detectors, other passive photonic components such directional couplers and grating couplers (Fig. 8.3) are necessary for on-chip entanglement generation. This is motivated not only by the potential for large improvements in entanglement efficiency/fidelity, but also by the inherent scalability advantages of integrated systems. Chip-scale transmission measurements of the passive components fabricated using the GaP-on-diamond platform were realized to characterize and optimize the device yield and performance of integrated passive optical components. While the primary goal here is to set a benchmark for large-scale integration in the GaP-on-diamond material platform, the demonstrated device performance suggests there are already areas where the platform should provide large advantages relative to free-space techniques.

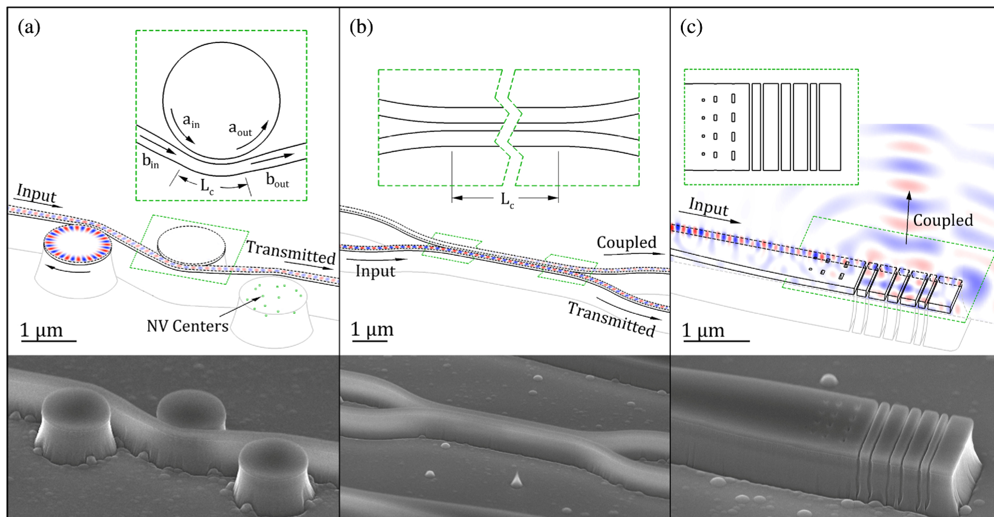

Figure 8.3: Schematic views with overlaid FDTD simulations and SEM images of integrated devices. **a.** Waveguide-coupled disk resonators, **b.** directional coupler, **c.** grating coupler (with schematic view halved for clarity).

The work presented in this section 8.3 is published as:

Gould, M., **Chakravarthi, S.**, Christen, I.R., Thomas, N., Dadgostar, S., Song, Y., Lee, M.L., Hatami, F. and Fu, K.M.C., 2016. **Large-scale GaP-on-diamond integrated photonics platform for NV center-based quantum information. JOSA B, 33(3), pp.B35-B42**. © 2016 Optica Publishing Group.

https://doi.org/10.1364/JOSAB.33.000B35

The measured quality factors of the waveguide-coupled disk-resonators, along with relatively strong output coupling, allows for total quantum efficiency into useful waveguide modes of around 33 %. Further, the combined yields and device performance of the demonstrated passive components are sufficient to allow the integration of elements for a spin-entanglement protocol, with significant total quantum efficiency advantages and reasonable yield. This represents a potential improvement by a factor of more than 200 over what has been demonstrated with free-space optics. This work was instrumental to the design, fabrication and characterization of devices presented in chapter 3.

8.4 (4)-GaP ring resonators for on-chip frequency conversion

Efficient frequency conversion of single photons from optically accessible qubits is essential for enabling long-range remote-entanglement schemes utilizing fiber transmission[187–191]. Further, distinguishable defect photon emission can be converted to a single target frequency enabling photon-interference based remote-entanglement. Photon mode shaping can also enable coupling of dissimilar quantum memories. For these applications, absolute frequency control of one or more interacting fields is required. Multi-resonant frequency conversion of photons to/from the telecom band has been demonstrated in nanophotonic structures fabricated from non-linear materials such as gallium phosphide (GaP) [61], aluminum nitride[192], lithium niobate[193,194] and silicon nitride[195,196]. However, tight fabrication tolerances for such devices typically cause resonant wavelengths to differ significantly from their designed values, presenting a challenge for practical device implementation.

We demonstrate post-fabrication target-wavelength trimming with a gallium phosphide on silicon nitride integrated photonic platform using controlled electron-beam exposure of hydrogen-silsesquioxane (HSQ) cladding. A linear relationship between the electron-beam exposure dose and red-shift of ring-resonator mode enables deterministic, individual trimming of multiple devices on the same chip to within 30 pm of a single target wavelength. This enables demonstration of sec-

The work presented in this section 8.4 is published as:

Thiel, L., Logan, A.D., **Chakravarthi, S.**, Shree, S., Hestroffer, K., Hatami, F. and Fu, K.M.C., 2021. **Precise electron beam-based target-wavelength trimming for frequency conversion in integrated photonic resonators. Optics Express, 30(5), pp.6921-6933**. © 2021 Optica Publishing Group.

https://doi.org/10.1364/OE.446244

ond harmonic generation from telecom to near-infrared at a specific target wavelength in multiple devices with quality factors on the order of 10^4.

Ultimately, a single-photon difference frequency generation (DFG) scheme will be required for down-conversion of NV (637 nm) and SiV (737 nm) ZPL emission to the telecom-band (1550 nm). This involves a single ring-resonator simultaneously supporting three different interacting modes; (1) single-photons from defect qubits in visible-band, (2) pump source in near-infrared and (3) target telecom output at 1550 nm. For a realistic DFG scheme, we require independent tuning capability for each individual ring-resonator mode. Temperature based mode shift[61] can be one of the tuning mechanisms. The HSQ exposure technique presented here provides an additional tuning mechanism. We are currently working on implementing the DFG scheme with GaP-on-oxide ring-resonator devices, initial results are very promising[62].

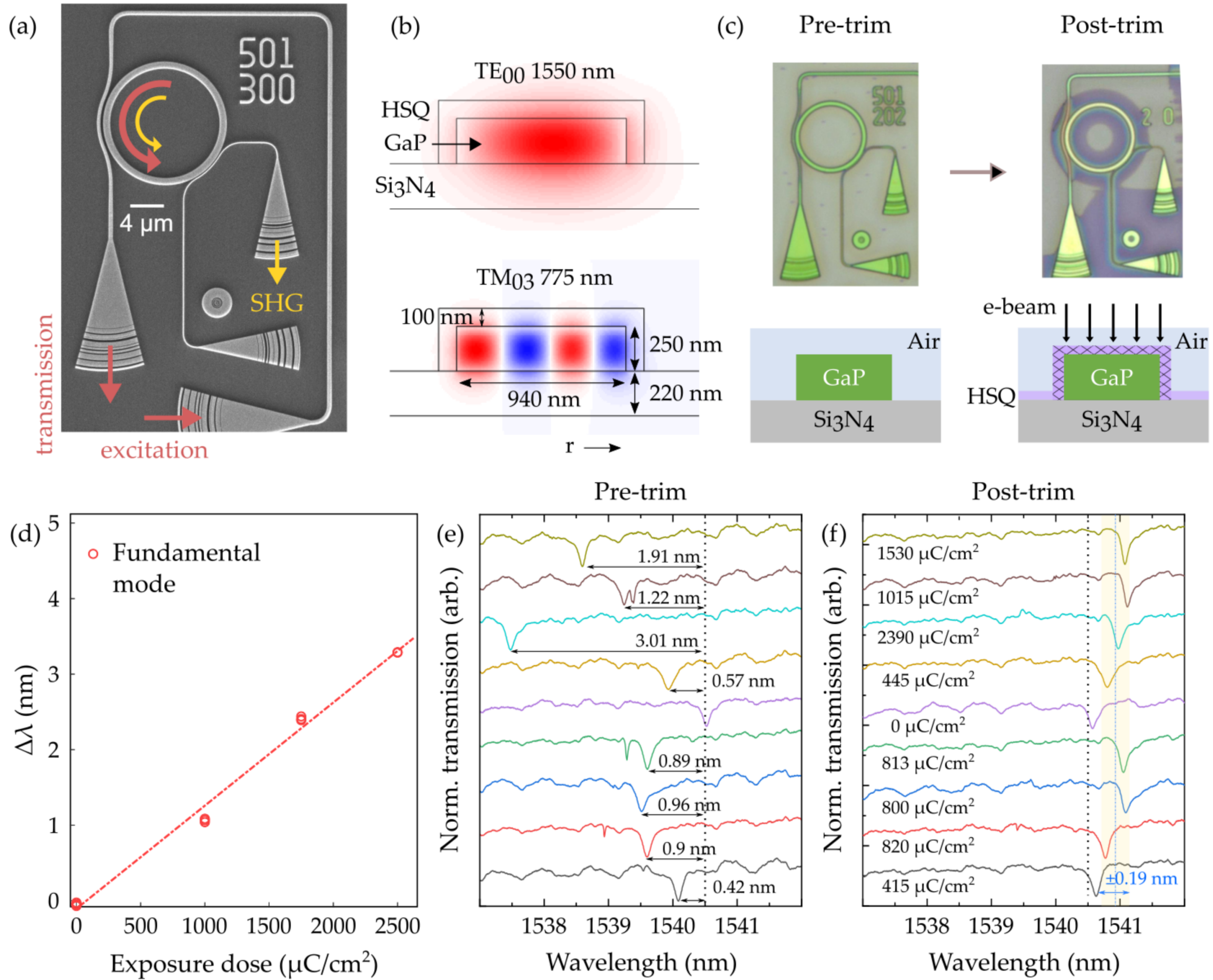

Figure 8.4: **a.** SEM image of the fabricated GaP-on-Si_3N_4 resonator with accompanying grating couplers. The device is excited with telecom band tunable laser (red) and the SHG signal is measured out of the vis/NIR output grating (yellow). **b.** Simulated resonator $\vec{E}$-field profiles of the quasi-phase matched telecom and second-harmonic modes. **c.** Pre and post trimming optical images of a device. The ring was exposed with a donut pattern. The waveguide and grating structures were utilized for exposure alignment and thus were sometimes exposed. To reveal the exposed HSQ pattern during the trimming process, the post-trimmed optical image was acquired after developing the exposed HSQ in a 25% TMAH solution. Note that all optical characterizations were performed before the development. **d.** Relationship between HSQ exposure dose and observed wavelength shift of hybrid TE_{01}/TM_{00} resonances at the fundamental wavelength. **e, f.** A target trim-test showing the fundamental wavelength resonances for nine devices with identically designed resonator dimensions pre- and post-exposure, respectively.

8.5 Conclusion

The key elements for a single chip photonic entanglement generation architecture such as spin-photon interfaces, single photon detectors, passive components and frequency-conversion utilizing GaP photonic layer are demonstrated. Three different nanophotonic geometries for optical coupling to NV and SiV defects in diamond are fabricated and characterized, with all three devices showing significant enhancement of defect photon collection. Stability of the defect optical transitions and homogeneity of the transition energy are critical requirements for photon-interference based quantum entanglement. Hence, we perform extensive optical coherence studies of photonics coupled NV centers, and determine the primary source of perturbation and implement mitigation mechanisms. Further, SiV centers in diamond are considered as an alternative, with SiV-photonic integration performed by stamp-transfer to prevent loss of optical coherence. Together, these results establish GaP-on-diamond as a viable platform for scalable on-chip entanglement network generation.

Appendix A

E-beam lithography

This is a compilation of my procedures, checklists, tips, tricks and gotchas. Consider this an addendum to the official e-beam documentation: https://ebeam.wnf.uw.edu/ebeamweb/index.html.

A.1 E-beam system overview

1. All features on the pattern must be on a grid (only polygons). No closed features are allowed. The pattern should be prepared in GDS2 format (database grid size ≤ 0.125 nm; note that this is equal to or smaller than the machine grid and much smaller than the actual exposure grid).

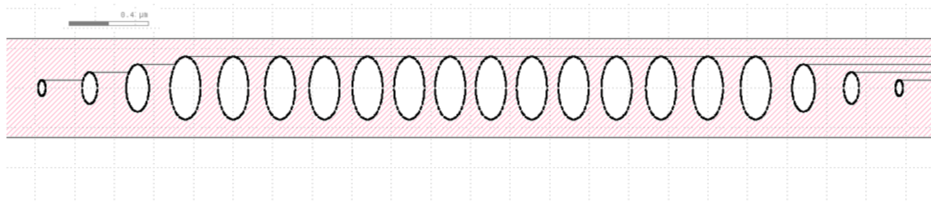

Increasing grid size

1. Database grid = min spacing on pattern gds
2. Machine grid = min spacing on tool (stage DAC limit) for 5th lens mode = 0.125 nm
3. Exposure grid
4. Fracturing grid
5. Isodose grid

Usually database grid = machine grid = 0.125 nm

2. The pattern to be exposed is approximated by a sequence of gaussian spots (also called shots). The spot size is determined by the e-beam condition (lens mode and beam current). The highest resolution (smallest spot size) can be obtained by using the 5th lens 500pA condition file. However be aware that the smaller the spot size, the longer it will take to expose large features. Although the beam diameter may typically be as small as 5 nm (at the highest resolution mode), the practical resolution is limited by electron back scatter.

   When the e-beam is incident on the resist, as the primary electrons slow down, much of their energy is dissipated in the form of secondary electrons with energies from 2 to 50 eV. They are responsible for the bulk of the actual resist exposure process. The net result can be considered to be an effective widening of the beam diameter by roughly 10 nm. This largely accounts for the minimum practical resolution of 20 nm.

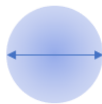

5 nm

The e-beam is a gaussian spot. This is also called a ‘shot’. The size of the beam and electron flux is dependent on lens mode and beam current.

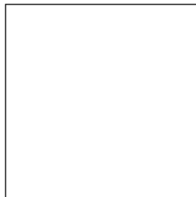

pattern

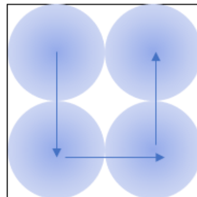

Exposing the pattern

The beam dwell at each shot determines the ‘dose’. The beam is blanked when moving from one location to another.

The required dose (base dose) is determined by the resist polymer chemistry.

3. For a given pattern file (GDS), start by selecting an acceptable exposure grid (i.e. shot pitch). Then select the beam current and lens mode that gives you a reasonable total exposure run time ($\leq$3 hrs).

4. Always double check that the machine grid is a multiple of the GDS layout database grid size

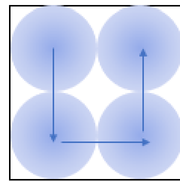

Exposing the pattern
grid = beam dia.

As we can see, this distorts the original shape of the pattern.

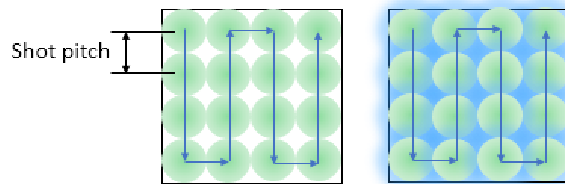

Exposing the pattern
grid < beam dia.

To better approximate the pattern, the system can reduce the dwell time and the exposure grid. The overall dose received is the same as above, but resolution is higher now.

Smaller shot pitch = better resist edge profile = smoother sidewalls. Limited by min dwell time = 1/(50MHz).

Smallest possible shot pitch = machine grid = 0.125nm

Smaller shot pitch = longer to write!

A.2 Beamer pattern processing

This should be completed the day before the scheduled write slot.

Log into the e-beam pattern server (putty + tightvnc). Start beamer by opening a terminal window ('Applications → system tools → XTerm') and typing 'beamer&'.

A standard beamer flow is shown in Fig. A.1.a. The different steps are as follows:

1. In GDSII: Import the GDS2 pattern file.
2. Extract: Extract the relevant layers for processing.
3. Transform: Change the coordinate system so that (0,0) lies at the center of the pattern. This is particularly important when aligning the write field to features on the sample (i.e. GaP membrane). Anisotropic global pattern scaling is also available but not recommended.
4. Grid: Change the pattern database grid. Default database grid = 0.125 nm.
5. Heal: Fix any minor errors (remove overlaps, etc.) in the GDS pattern.

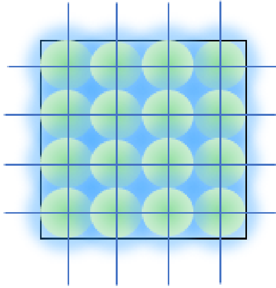

Exposure grid = shot pitch * machine grid = shot pitch * 0.125nm

Higher base dose resist -> smaller shot pitch is possible

HSQ resist has the highest base dose (2500 uC/cm2)

On our tool with HSQ, at 500pA beam current
Min shot pitch = 5 (exposure grid = **0.625nm** !)

Usually, we use 2000pA at shot pitch = 12 or lower

6. Fracture: Break the pattern into smaller rectangles. Each rectangle will receive a specific electron dose (based on the steps below). Fracture grid is usually set to the exposure grid (shot pitch $\times$ 0.125 nm). Processing large pattern files can take a long time (few hours). For patterns with lots of curved features (such as ring resonators), use curved + shot pitch fracturing option. There are many options available here, and the results are highly dependent on the input GDS. Good fracturing is critical, take the time to experiment and find the settings that work for your GDS. For complex structures such as photonic crystals, bordering sleeving is very useful.

7. PEC: Proximity error correction. This step applies varying electron beam dose to the fractured structures based on the feature density and material stack. The 1/e scattering length of 100 kV electrons in silicon is 26 µm, i.e. if two features on your chip are closer than 26 µm, the actual exposure dose for those features needs to be lower than the resist base dose (accounting for exposure from e- scattering). Choose the correct PEC profile for your material stack (for GaP-on-diamond go to 'global archive → no.7 diamond-200nm GaP'). Other parameters under the advanced tab that are important:

   i Accuracy: 0.2

   ii Classes: 256 (number of different doses utilized)

   iii Min dose: 0.5 (Dense features receive lower dose to account for over exposure by electron scattering from adjacent features)

iv Max dose: 3.0 (Sparse features receive larger dose to account for under-exposure from lack of scattered electrons)

v Do not enable short range correction !! If you enable short range correction, double check the final doses (after PEC) very carefully. Beamer has a tendency to assign very high doses to random pixels, this will distort your devices!

Check that the pattern is correctly processed by selecting view pattern in the PEC field (Fig. A.1b). In the viewer click on 'view → color by → dose' to display the different dose classes. You can control the range of doses by going to 'properties → dose range'. The dose data is contained in the '.jdi' file.

8. OutJeol52: This creates the .v30 binary file utilized by the e-beam tool. Important parameters are as follows:

i Machine type: JBX-6300FS

ii EOS mode: 6 (100keV 5th lens mode)

iii Fracturing: Should be identical to the initial fracturing step.

iv Under the 'advanced' tab: Field ordering (fixed, floating or manual). This parameter decides how the pattern is split into write fields. For the 5th lens mode the write field is 62.5 µm × 62.5 µm. Floating is the best option for photonics patterns where we would like to avoid field boundaries at critical devices (resonant cavities, grating couplers, etc.). Here centering features to the field can be another useful option. Always verify the processed pattern before committing to the write! See below.

v Feature sorting in field: This parameter decides how the order in which the features within a field are scheduled to be written. 'Array compaction' is the default and optimizes the write time. 'Follow geometry' can be useful for critical features like disk resonators, the entire fractured circular resonator can be written in one continuous pass. 'Follow geometry' requires a flag to be set in the jdf file.

9. Verification: After the execution of the beamer flow is finished, right click on OutJeol52 and

select 'view layout'. In the layout window check the following: (Always verify, never assume things are going to turn out okay!)

i Check the assigned exposure doses. Click on 'color by dose' in the toolbar and then normalize the color bar by going to 'properties→dose range' then select 'get limits automatically'. Verify that dense features get a lower dose, and isolated features get a higher dose. Zoom into your critical features e.g. resonator waveguide coupling, and check the uniformity of dose. There should be a smooth gradient, with no abrupt changes in the dose. You can check the actual dose of every fractured polygon by selecting 'properties→show dose annotations' when zoomed in. Here dose 1.0 is your resist base dose (set in the .jdf job file).

ii Check the shot shape and feature order (Fig. A.1c). To view the shot shape go to 'e-beam → Show shots'. You need to manually configure the shot parameters for the display, this is done by going to 'e-beam → shot-size settings' and display the grid 'properties → grid' (**this should have parameters for your exposure grid not database grid!**). The write order can be confirmed by clicking on the play button ('write representation') in the toolbar (a good simulation speed is 8x).

iii Finally, check that none of your critical features fall on the field boundaries. You can view the individual write fields by going to the fourth viewer tab 'Cell selection' and selecting a specific field from the drop down list (here in addition to a specific field you also need to select the last item which should have the same name as the output .v30 file). You can always set the field boundaries manually in OutJeol52.

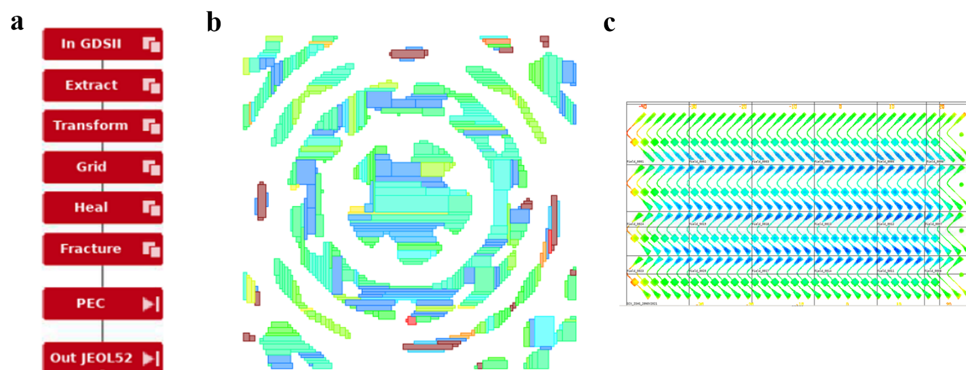

Figure A.1: **a.** Beamer flow. **b.** Fractured photonics pattern. **c.** Fully processed photonics pattern showing the field boundaries and fractured shapes colored by dose. The dense features near the center get a lower dose (blue), whereas the features near the edges get a higher dose (red).

Run the write parameters through the online e-beam runtime estimator. Schedule the e-beam appropriately. For a high-resolution photonics write at $\leq 2\,\mathrm{nA}$ beam current, the calculator output should look something like this:

```
Exposure Time Estimate
Inputs:
EOS Mode:                5th  Lens
Beam Current:            2000 pA
Shot Pitch:              14   pixels
Dose:                    2600 uC/cm^2
Area Per Die:            440  um^2
Fields Per Die:          2
Die Count in Job:        1427
Field Shift/Overlap:     1
Global Align Time:       0 secs/wafer
Die Align Time:          0 secs/die
Load/Unload/Calibrate?:  1
Results:
Machine Grid:            0.125 nm
```

Exposure Grid:	1.75 nm		
Clock Rate:	25.12 MHz		
Beam On Time:	8,162 sec	136.0 min	2.3 hr
Stage Move Time	1,427 sec	23.8 min	0.4 hr
Alignment Time:	0 sec	0.0 min	0.0 hr
Load/Unload/Calib Time:	1,200 sec	20.0 min	0.3 hr
Total Time:	10,789 sec	179.8 min	3.0 hr

A.3 Pre e-beam checklist

Check e-beam condition and write mode. At this point the design (.gds) should have been successfully run through Beamer software.

1. The samples need a 5 nm SiO_2 adhesion layer. I prefer deposition by e-beam evaporation (evap-1). If you have samples that are can be exposed to plasma (i.e. not diamond) PECVD-2 can also be used. If required verify by contact angle test (SiO_2 surface has smaller contact angle i.e. water does not form a bead, surface is hydrophilic).

2. Check HSQ pour date (ideally should be < 3 weeks old). Resist is usually stored in the e-beam resist cabinet. If preparing a new batch of 6% AQM-dry HSQ, see Appendix.E.

3. Before processing samples (spin-coating), check the e-beam status.

   i Password for ebeam system: 'Jeoleb' (case-sensitive)

   ii Put Calib window into operation mode [check the title bar to verify].

   iii Eosset double click to get parameters.

   iv Check 5th lens mode; condition file (eos mode).

   v Set condition file. Always save then cancel.

   vi After eos mode change wait ~ 1 hr. If within same lens mode; wait ~ 20 min is acceptable.

A.4 Spin coating resist

Use spin-3 EBL to coat samples. Enable spin-3 in coral. The 6% HSQ vial is stored in the refrigerator freezer in the wet processing chase. There will be older vials, only use the newest vial. Double check the pour date, it should be $\leq$ 2 weeks old. If the vial is older, please immediately notify Shane. Restocks can take up to a week, so keep track of the pour date and always be proactive.

1. Set the Thermo-Fisher hotplate to 150 °C. Set the VWR hot plate to 80 °C. Wait for the plate to reach set point. Place sample on plate for 4 min on the Thermo-Fisher plate (at 150 °C) to dehydrate immediately prior to spin-coating. Use ceramic or metal tweezers only on hot plate!

2. While waiting for dehydration bake, set the spin parameters on the spinner. Modify recipe-3 (do not change recipe-1 or recipe-2). Spin parameters are based on sample size and **6% HSQ** (for better uniformity and to minimize edge bead), see below:

   i **For large samples (> 10 mm square) :**

   1 s ramp to 500 rpm, hold 1 s

   1 s ramp to 6000 rpm hold 45 s

   3 s ramp to 0 rpm

   This gives **150 nm** thick resist (measured with alphastep).

   ii **For small samples (< 10 mm square) :**

   1 s ramp to 500 rpm, hold 1 s

   1 s ramp to 7500 rpm hold 45 s

   3 s ramp to 0 rpm

   This gives **100 to 150 nm** thick resist (measured with alphastep at the center). Note that for small diamond samples (2 mm × 2 mm) the edge-bead will be significant (∼ 50% of sample surface, resist thickness measured at the center), this is okay!

3. Use the appropriately sized sample chuck. The small chuck for diamond samples is stored in the e-beam room. Clean chuck with acetone both before and after use. Do not get acetone inside the chuck attachment point (o-ring can be damaged).

4. Remove dehydrated sample from the hot plate and let it cool before spinning. Blow with N2 just before placing on the chuck.

5. Use a small 1 ml pipette (stored in a rack inside spin bay 1 or 2) to dispense a small amount of HSQ on the sample. Be careful to not introduce any bubbles in the HSQ bottle or on the sample and please do not waste resist!

6. Visually inspect the coated samples for uniformity. If ok, place on the VWR hotplate (at 80 °C) for 4 min for the soft bake. If the HSQ does not cover the entire sample, clean with the 25% TMAH, DI rinse and restart. When in doubt, do not hesitate to clean the sample and retry!

7. Inspect the coat under optical microscope (Nikon). Remember to save images! (even if everything looks good).

8. For non-conductive substrates (Diamond, GaP-on-diamond, Gap-on-AlGaP) charging is an issue! Use 18% PSS solution diluted to 4.5% with added 1% tritonX surfactant as a water soluble spacer layer. Follow the same spin-parameters and soft bake as mentioned above. This will give ~1 µm layer. Then sputter 4 nm of Au-Pd (Quorum sputter coater, 1 min deposition recipe). This will allow for charge dissipation. Note: PSS can become crosslinked during ebeam exposure; this does not affect the write quality. It will lift off in DI (briefly sonicate in DI prior to development if required).

Clean all work surfaces, clean spin coater with acetone (Do not use acetone on the lid). Turn off the hot plates. Put unused resist back in the refrigerator. Disable spin-3 in coral.

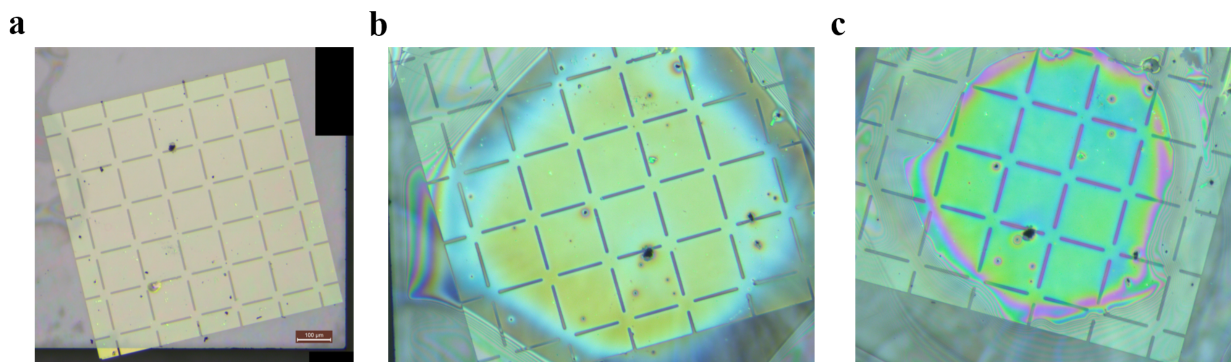

Figure A.2: **a.** Diamond sample with gallium phosphide membrane before spin-coating **b.** After spin coating HSQ. The large edge bead is because of the small sample size. **c.** After spin coating water soluble spacer.

A.5 E-beam operation

Sample mounting and loading

Mount sample to Si carrier using silver paste (can be found in the SEM bay). Use the 2" wafer holders with slots. I prefer holder-W slot 2D (8 mm slot height). Do not use holder 2C, there is a considerable z-offset that will smear <100 nm features. It is important to keep in mind that there is no mechanism to compensate for the z-offset in the tool. The e-beam focus plane is fixed and depth of field is small (≤20 µm). For writes where alignment is critical, consider using holder S (trapezoidal slot 2H) which has an inbuilt micrometer sample rotation stage.

Use the pre-alignment microscope to get rough coordinates of the sample. This will be converted to sample coordinates (use the online pre-alignment calculator to get stage coordinates for a particular holder, then in the stage operation window convert to sample coordinates) and used as the write offset in the .sdf file. There is no pre-alignment coordinate calculator for holder S, see appendix A for details.

Small samples (such as a 2x2 mm diamond) will require mounting on a silicon carrier chip. The carrier chip has to be designed to exactly match (to within 10 µm) the sample height, use the drop gauge to check the carrier height. See appendix B for details.

Always use a backing Si wafer (there are spare wafers in the e-beam room). Be careful to never touch the top surface of the holder!

Careful when loading sample. Follow the standard loading procedure. Don't touch loading rod. Change gloves immediately if you do get any vacuum grease on them.

Enable tool in Coral.

Manual calibration sequence

These notes are in addition to the standard operating sequence.

1. HEIMAP : double click; 5x5 points; check holder; pitch; and offset. All output numbers should be <20 µm. Note: if the sample is mounted close to the edge of the holder, HEIMAP will fail. If HEIMAP fails, unload and remount, do not force a write!

2. Drift : double click; update BE mark (acquisition of BE mark); execute; acquisition of last execution position then save and cancel.

3. Current : single click [check the current].

4. InitBE : single click [ok if it finds mark; no useful info].

5. InitAE : double click; does not auto update. Needs manual execute; update; save; cancel.

   i If it does not find mark [only bottom plane mark position used], go to setting and change scan width to 8 µm.

   ii Apply, Try again.

   iii If it works put back old numbers (4 µm) and execute then update then save and cancel.

6. SFOCUS : single click; check if stig is close to zero. Also check beam size [should be in range of 30 to 50 nm]

7. Only if everything is nominal, run BATCH calib. If something fails contact Shane immediately (call from the landline in the e-beam room).

Expose pattern

Transfer the e-beam job files (.v30, .jdi, .jdf and .sdf) to the e-beam exposure pc (use ebsend).

1. Compile your code schd 'XXX.sdf'.

2. Run array check: achk& and verify pattern. You can check the pattern by selecting a 'chip' in the 'chip array diagram' and going to 'view → show shot shape display'.

3. Switch to display mode. Open exposure window and start exposure process. Open 'Chip Array Diagram' to monitor the exposure process.

Additional notes:

- If using drift-correction on non-aligned write use mask write path [UWMW9X]. This is useful for long write sequences.

- STDCUR → only seen by the compiler. Max current during write is set 2% higher than condition file for safety

- If height map fails, change the acceptance % to ≤10% and try again.

- Calculation of offset in .sdf file: Offset = measured value (sample coordinates) - GDS value.

A.6 Post e-beam write

1. Unload the samples. Follow standard operating procedure.

2. Disable the tool in coral.

3. Unmount the sample from the Si carrier. Remove any silver paste from the backside by sliding sample on a cleanroom wipe soaked with acetone. (Use the solvent hood in the litho bay.)

4. Soak the sample in DI for 4 min to lift-off the PSS + metallized layer. (If required a short burst of sonication *approx* 1 min can be used.). N2 blow dry and inspect under Nikon. Ensure that the surface if free of any debris.

5. Develop pattern in 25% TMAH for 4 min. Gentle agitation at the 2 min mark.

6. Rinse the sample under running DI for 10s. This is critical to prevent HSQ residue.

7. Move to the solvent bench while keeping the sample immersed in DI (do not let the sample surface dry). Rinse in IPA to remove any HSQ solvent residue. N_2 blow dry.

8. Inspect developed pattern under Nikon, and use the profilometer (DektakXT) to measure the HSQ thickness. The thickness should be 150nm.

9. Inspect pattern under SEM.

A.7 Sample position on stage

This procedure is holder and sample window agnostic:

Microscope coordinates → stage coordinates → substrate coordinates → sdf offset

1. Load the sample into the holder. I recommend loading the sample roughly centered on the slot, this will make things easier.

2. Mark the corner of your sample with tweezers. This is shown below as a green cross. This will be your reference position (useful to confirm your position inside the tool and required for aligning writes from multiple beam conditions). If you are aligning to a membrane, record the position of the corners of the membrane.

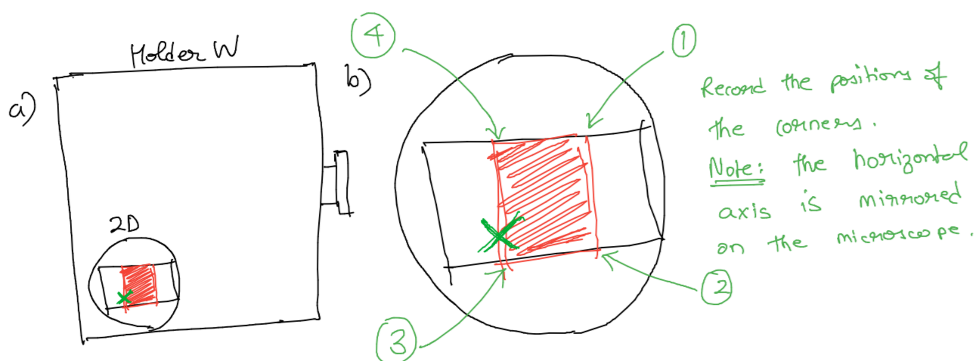

3. Put the holder on the pre-alignment microscope. Record the X, Y positions of the corners and the reference mark. Load the holder into the ebeam chamber per SOP.

4. First perform a HEIMAP (use a rough initial sample offset of X=0; Y=1000 µm) to verify that the sample surface is within the e-beam focal plane. If measured z-offset is ≥20 µm, unload the holder, remove the sample and try again.

5. Once HEIMAP is satisfactory, calculate the stage coordinates of one of the sample corners. Use the online calculator (https://ebeam.wnf.uw.edu/ebeamweb/ref/calculators/calc/prealign.html) and select holder 0. Convert the microscope coordinates to the e-beam stage reference.

6. In the e-beam stage control window, select stage coordinates (7), substrate/slot# (8) [this is 2D, 2H, etc.] and move to one of the corners of the sample by using (10) and click 'Movement'.

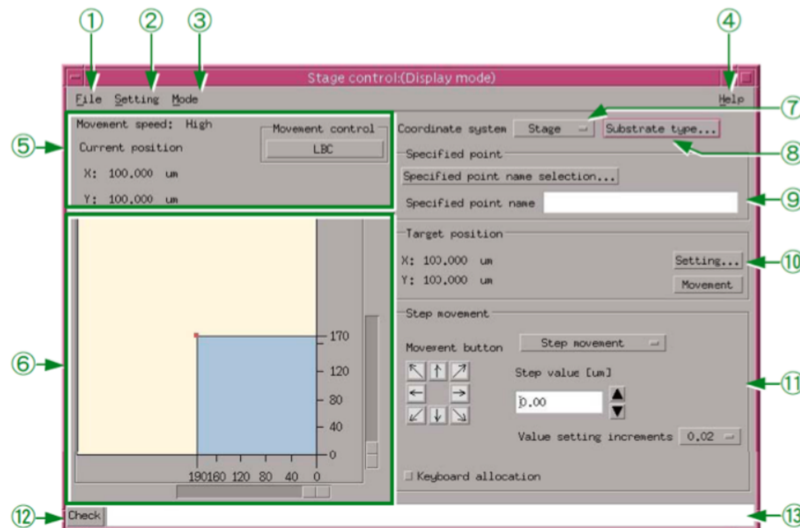

7. Switch to the SEM mode in the 'SSPVIDEO' window by going to 'Change → SEM'. Do not use the BE SEM mode. You can change the scan width (i.e. window size) and integration time in the 'Settings' tab. Enable the SEM by selecting 'SEM start'. You can adjust the brightness and the contrast under the 'Adjustment' tab. Note that SEM will expose your resist, be confident that you are away from the write area before enabling. Always disable SEM before moving large distances on the sample!

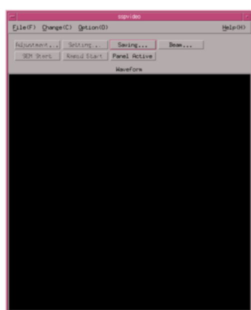

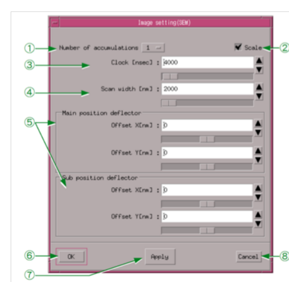

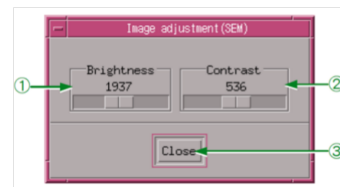

8. With the SEM on, move in small steps (10 µm) to find the corner. The step size can be set in the stage control window (11). The corner can be as far away as ±500 µm, be patient.

9. The final pattern offset in the sdf job file has to be set in terms of the substrate coordinates. To convert from stage to substrate coordinate system, go to the required stage position and then in stage control window (7), select substrate coordinates. Convert all your reference positions to the substrate coordinates before computing the offset. Never compute the offset with the stage coordinate system, substrate coordinates (and hence the offset) are depended on specific holder and sample window!

10. Once you have the corner, calculate the sample offset as [Measured coordinate on the tool - microscope coordinate, both in substrate system].

11. Using the calculated offset, look for the reference mark. Record position of the reference mark in substrate coordinates.

12. If aligning to a membrane, go to a membrane corner (with the calculated offset) and SEM to confirm. If required, adjust the offset. Be very careful not to expose regions on your membrane.

A.8 Using a carrier chip

The carrier chip is designed to hold a small sample at the focal plane of the e-beam with minimal drift.

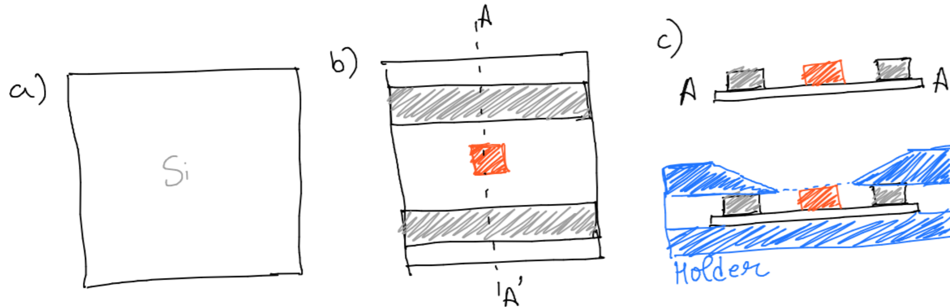

1. Start with a small piece of silicon (20x20 mm)

2. Place two supports as shown in (b). These supports need to be the same exact height as the sample, you can confirm this with the drop gauge. Glue the supports in place with silver paste (can be found in the SEM room).

3. Glue the sample to the carrier with silver paste.

4. Use the silver paste very sparingly, it is extremely critical that we do not get any silver particles in the e-beam system!. Just use enough to temporarily hold the parts in place. Silver paste does not have a lot of mechanical strength, so the glued parts can come apart easily.

5. Do not use carbon tape! It is highly porous and outgassing will cause massive sample drift issues when loaded into the e-beam high-vac chamber.

6. The 2x2 mm ppb diamond samples are approximately the same thickness as silicon wafers ($\approx$ 500 µm).

7. The 2x2 mm ppm diamond samples are typically 300 µm thick. We have a carrier that uses a few discarded ppm samples as the supports.

A.9 Advanced fracturing and exposure strategies

Below you can see the beamer flow for a suspended photonic crystal cavity chip. It is using two strategies to get functional devices:

1. We want the hole structure within the photonic crystal cavity to not have any rough/sharp edges during fracturing. Hence, the holes are extracted from the pattern by using a filter by area function. Then a sleeve is created for the holes, a feature bias based on prior writes is also incorporated to get accurate device dimensions. The sleeve is fractured independent of the main layout with curved shot pitch fracturing ensuring smooth edges.

2. Since we use negative resist (HSQ, only the exposed resist remains), writing large area structures such as supports for the suspended cavities can be very expensive. Hence, the support structures are created on a specific layer that can be extracted in the final step to be written with the low-resolution 4th lens mode.

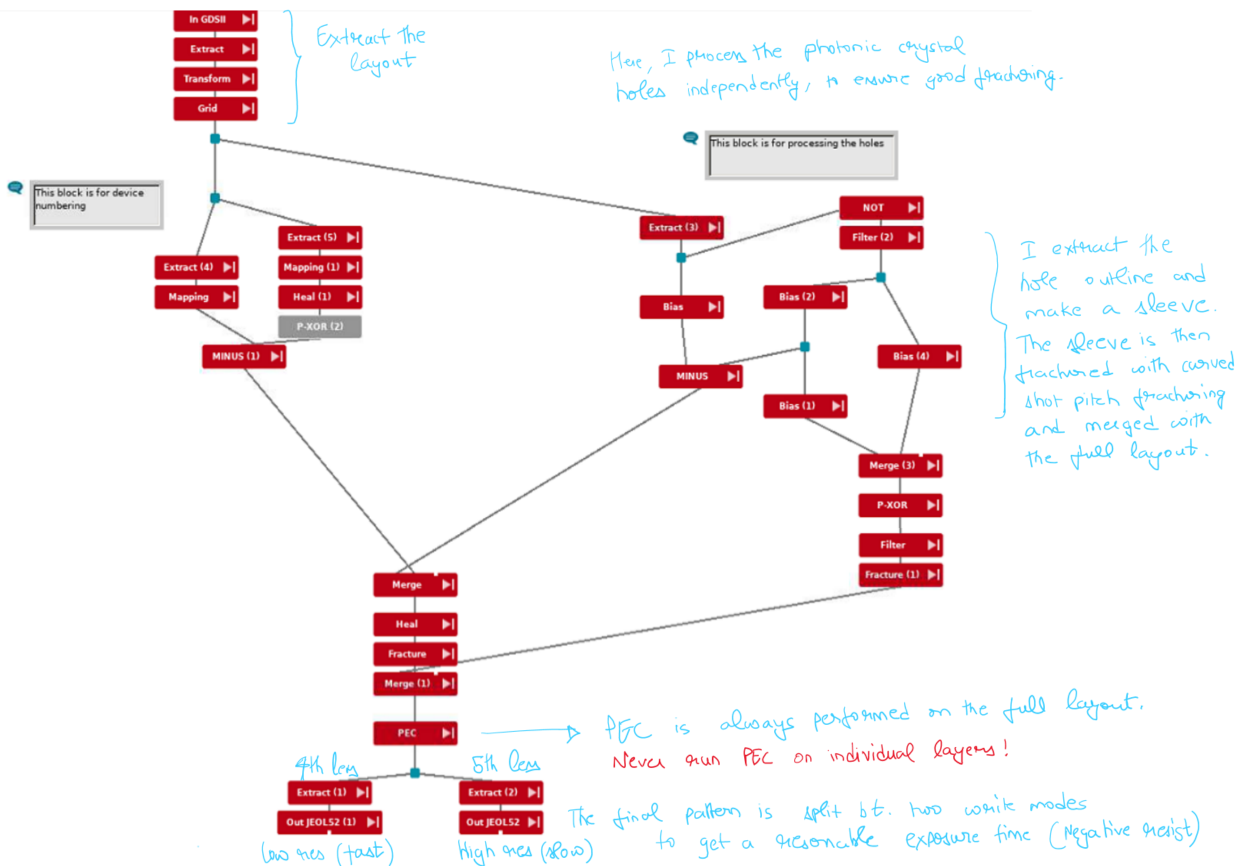

Note that switching between lens modes causes a large beam offset ≈ Δx=160; Δy=-140 µm. Use the reference mark position to calculate the offset for every write (this will be slightly different every time based on the tool condition and environment). Pattern registration to within 200 nm can be achieved. If higher accuracy is desired, use predefined alignment marks (usually Au marks on the sample) and SETWFR subroutine.

A.10 More resources

1. Jeol JBX-6300FS at University of Michigan
   https://lnf-wiki.eecs.umich.edu/wiki/JEOL_JBX-6300FS_Electron_Beam_Lithography_System

2. Jeol JBX-6300FS at Stanford
   https://snsf.stanford.edu/facilities/fab/npc/jeol

3. Jeol JBX-6300FS at Cornell
   https://www.cnfusers.cornell.edu/node/74

4. https://nano.yale.edu/manuals-documentation

5. More info on how to avoid charging effects:
   http://apps.mnc.umn.edu/archive/ebpgwiki/Charging.html

Appendix B

BGaP-on-Silicon device fabrication

The BGaP-on-Si material is commercially available in 300mm wafers from NAsP-III/V GmbH. The material consists of a boron doped gallium phosphide (BGaP) layer (2.8% boron content) epitaxially grown on a 40 nm thick undoped gallium phosphide (GaP) template layer on a 750µm thick silicon substrate. The boron doping is necessary to compensate for the small lattice mismatch between GaP and silicon (5.45 Å vs 5.43 Å respectively) [197–199]. The large 300mm wafer was diced into 1cm square chips prior to device fabrication.

B.1 Material preparation

1. The 1cm square BGaP chips are covered in Az-1512 positive photoresist for long-term storage. The first step is removal of this protective photoresist film.

2. Soak the resist covered sample in acteone for 10 min.

3. Rinse with IPA and DI water. Check the sample under optical microscope to verify removal of all photoresist. In some cases, if the photoresist is old or crosslinked it can become very hard to remove. EKC resist strip (at 80 °C) followed by a DI water rinse can be used for stubborn resist removal.

4. If any resist residue is observed, the sample can be cleaned in oxygen plasma (Barrel etch, 125W for 10 min).

5. Store the clean sample in a polypropylene 1" dia. sample holder. Do not use gel-pak as it can lead to residue.

B.2 Pattering with e-beam

1. Clean the sample by sonicating in either DI or IPA for 10 min. This should remove any macroscopic debris that could leave streaks during spin coating.

2. Follow the instructions for HSQ spin coat and e-beam exposure detailed in Appendix.A.

3. Since HSQ is a negative tone resist, the pattern files for suspended devices are usually distributed into two successive e-beam writes: the first write at high resolution (typically 1nA_A3_M6) for critical features and the second write at low resolution (8nA_A7_M3) for support structures. To maintain good alignment between the two writes, measure the reference mark position immediately after the first write. Take care to not disturb the cassette in the e-beam tool between writes. After switching to the second beam condition, include pattern offsets between e-beam condition files for rough reference mark position and measure the reference mark again. Use the measured offset in your pattern placement coordinate calculations. Typically pattern registration precision of <0.5µm can be achieved with a single reference mark.

B.3 BGaP photonics etch and device release

1. The HSQ e-beam patterns are transferred to BGaP by plasma ICP-RIE etching. Follow the instructions for GaP photonics etch in Appendix.D.1. For 220 nm thick BGaP, four etch cycles (total plasma duration of 2 min) should be sufficient to punch through to the silicon substrate. SEM the etched pattern to verify the etch depth and faithful pattern transfer before proceeding.

2. Remove the HSQ resist by dipping the chip in 0.5%HF solution for 4 min. Rinse in DI and N_2 dry.

3. A clean silicon carrier wafer is required for the XeF_2 silicon vapor etch process. Remove the native oxide from the carrier wafer with a 0.5%HF dip. Rinse in DI and N_2 dry.

4. Dehydrate both the sample and the carrier wafer by placing on a hotplate at 150 °C for 10 min. This step is critical to the prevention of SiF_x residue formation during the vapor etch process. The SiF_x residue can only be removed by a HF solution.

5. The vapor etch is performed in a 'SPTS-e2' tabletop etcher. Place the sample (without the carrier) in the tool for the release etch. Use the recipe 'Fulab_bgap_release'. For a given XeF_2 input gas volume, the silicon etch rate is proportional to the volume of exposed silicon. The first release step involves few cycles of rapid etching to release the freestanding photonics structures. However, residual silicon gossamer can typically be observed along the bottom surface of the free standing BGaP layer. It is likely the etch rate underneath structures is mass-transport/diffusion limited.

6. Remove the sample from the process chamber and verify with an optical microscope. Released regions of BGaP show up as lighter regions under bright-field microscopy. If required run additional cycles to clear all free standing structures. Take care to not over-etch.

7. Next, to obtain a clean bottom BGaP surface, the sample has to be exposed to many etch cycles. This requires reduction of XeF_2 etch rate to prevent collapse of free standing structure by silicon over-etching. For the the cleanup step, place the sample on the silicon carrier wafer and load the chamber. Use the recipe 'Fulab_bgap_cleanup'. The exposed silicon carrier consumes the majority of XeF_2 vapor in the chamber reducing the etch rate to few tens of nm per cycle.

8. Unload the sample and verify the undercut with angled SEM imaging.

Parameter	Release	Cleanup
XeF_2 (mT)	1	3
N_2 (mT)	5	5
Cycle duration (s)	120	120
No. of cycles	4	20
Total duration (min)	15	45

Table B.1: Silicon vapor etch parameters release of freestanding BGaP structures. Please keep in mind that the silicon undercut rate for a given recipe is highly dependent on sample geometry.

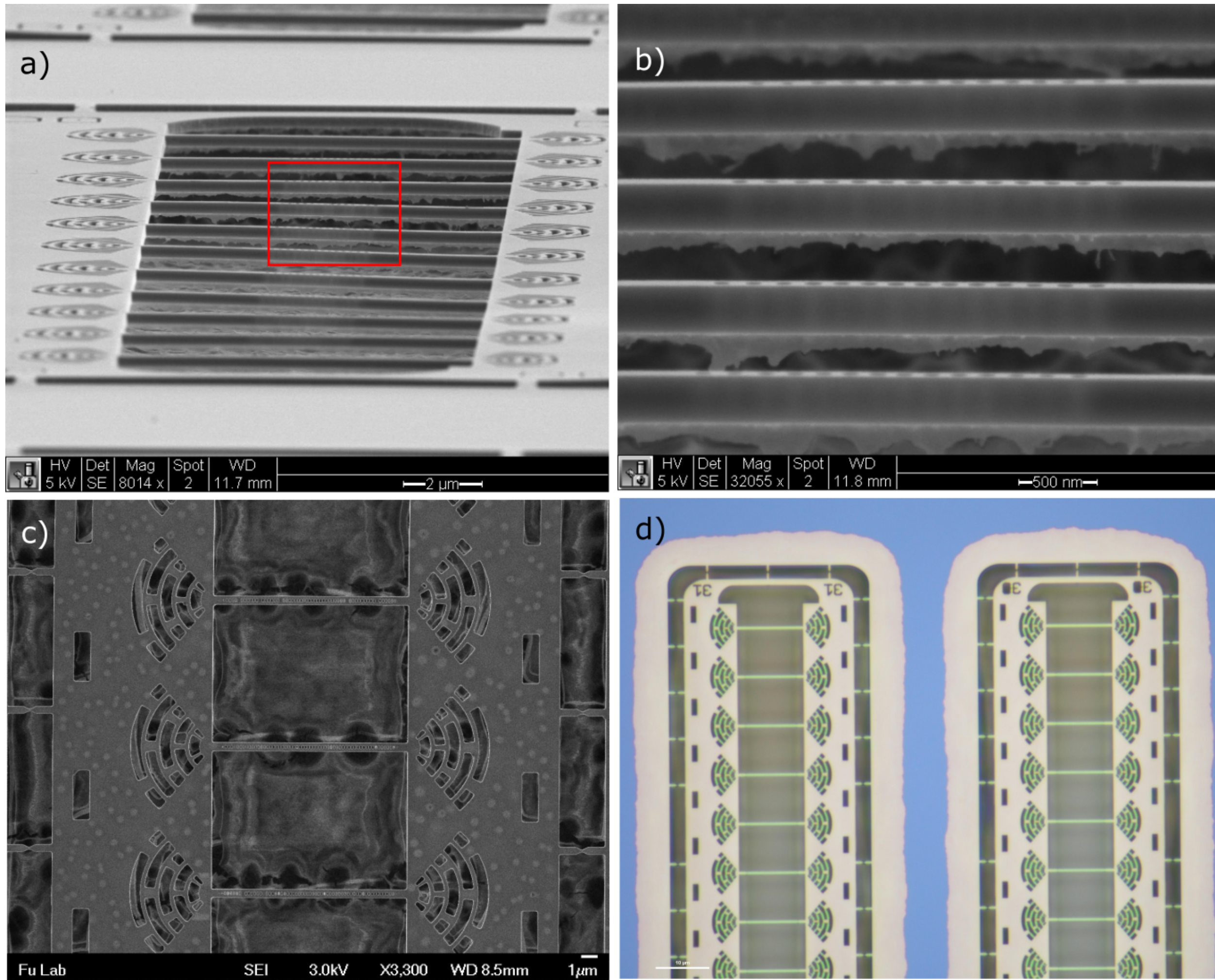

Figure B.1: a) Angled SEM image of an array of suspended BGaP photonic devices after the XeF_2 release step. The silicon substrate has been undercut releasing the photonic devices, however upon closer inspection, we can see silicon gossamer like material underneath the freestanding beams. b) A zoomed in SEM of the red box in (a). This gossamer material can be removed by the XeF_2 cleanup step. c) SiF_x residue on the BGaP after the vapor etch process. d) Optical bright field image of a successfully released BGaP structure. The freestanding BGaP is yellow and BGaP still bonded to the silicon substrate is purple. This variation in BGaP color can be utilized to determine the etch endpoint.

Appendix C

Fariba-GaP wet transfer and device fabrication

C.1 Material preparation

The GaP-on-AlGaP(80% Al) is epitaxially grown on a GaP substrate. GaP is very fragile and shatters readily, take care when handling the sample.

1. The GaP-on-AlGaP samples are covered in AZ-1512 positive photoresist for long-term storage. The first step is removal of this protective photoresist film.

2. Soak the resist covered sample in acteone for 10 min.

3. Rinse with IPA and DI water. Check the sample under optical microscope to verify removal of all photoresist. In some cases, if the photoresist is old or crosslinked it can become very hard to remove. EKC resist strip (at 80 °C) followed by a DI water rinse can be used for stubborn resist removal.

4. If any resist residue is observed, the sample can be cleaned in oxygen plasma (Barrel etch, 125W for 10 min).

5. Store the clean sample in a polypropylene 1” dia. sample holder. Do not use gel-pak as it can lead to residue.

C.2 Patterning membranes

1. Clean the sample by sonicating in either DI or IPA for 10 min. This should remove any macroscopic debris that could leave streaks during spin coating.

2. Dehydrate the sample by baking on hotplate at 110 °C for 5 min.

3. Spin coat AZ-1512 resist
   (2s ramp to 500 rpm and hold for 5s; 3s ramp to 5500 rpm and hold for 40s).

4. Softbake on hotplate 1min 110 °C for 60s.

5. Use membrane mask and ABM aligner to expose the resist. Align the corners of the chip in the big liftoff vias and adjust angle to maximize number of membranes. For devices that require precise alignment to crystal axis (i.e. second-harmonic generation) remember to align the membrane mask pattern to the edge of the cleaved sample. The cleave edge is typically (100). Do not use contact vacuum. Instead, chip is close enough to mask when mask moves out of focus as chip is raised. Si backing wafer under the GaP chip is essential. Expose for 4s.

6. Develop in 1:4 AZ340:DI (60s). Rinse with DI and blow dry.

7. Inspect under microscope. Measure the resist thickness with a profilometer (DektakXT). Typical thickness is 1µm.

8. Cleave the sample into individual pieces of membrane patterns. Each membrane is 1.5mm × 1.5mm, with etch vias spaced 0.2mm apart.

9. The membrane patterns are transferred to GaP by plasma ICP-RIE etching. Follow the instructions for GaP photonics etch in Appendix.D.1. For 220 nm thick GaP, four etch cycles (total plasma duration of 2 min) should be sufficient to punch through to the AlGaP substrate.

10. Measure the etch depth with a profilometer (DektakXT).

C.3 Membrane transfer

The GaP membranes are released from the AlGaP substrate and transferred to another substrate suitable for photonics (diamond, SiO_2, Si_3N_4).

C.3.1 Membrane release

1. Place the membrane face-up in 1.5% HF to etch the AlGaP and release the GaP membrane.

2. Release typically takes 1 hour (for AlGaP with 80% Al content). When the membrane is close to release, you can observe the GaP shimmer due to thin film interference. At this point grab the sample by the edge (without disturbing the membrane) with an acid safe tweezers and gently lift it to the liquid surface and re-submerge (dunk it) back in. The liquid flow should release the membrane with the hydrophobic resist and surface tension acting to neatly suspend the released membrane face-up at the liquid surface. If the membrane is released while inside the liquid, there is a risk of membrane curling up due to residual film stress from the growth process.

3. Allow membrane to float at surface of HF solution for 5 min to remove any remaining AlGaP.

4. Use the PTFE bucket tool to capture membrane with a small amount of HF solution, and transfer to a DI container.

5. Rinse the membrane again by using the PTFE bucket to transfer to a new DI container.

C.3.2 Substrate preparation

1. Clean the sample by sonicating in either DI or IPA for 10 min. This should remove any macroscopic debris that could leave streaks during spin coating.

2. For non-diamond substrates, perform a oxygen plasma clean (Barrel etch, 125W for 10 min).

3. If using a diamond substrate, do not perform the oxygen plasma clean. Instead perform a fuming sulphuric acid clean (96% H_2SO_4 + KNO_3 at 225 °C for 30 min).

4. Deposit a HMDS-mono layer on the clean substrate using the automated oven. This improves membrane adhesion.

C.3.3 Membrane transfer

1. Clamp the substrate into the bottom of the aluminium bucket tool. Dip it in DI and ensure that it has no air trapped in the drainage channels. There should be no air bubbles in the bucket when immersed.

2. Use the bucket to capture membrane from DI container and carefully drain as much water from tool by removing it from DI dish.

3. Use cleanroom wipes to slowly wick away remaining water and remove substrate chip from bucket tool.

4. Place the substrate with the transferred membrane under microscope with the lowest illumination power to dry the membrane (5 min). It is critical to use the lowest illumination possible to avoid bubble formation. Typically, you can see the liquid dissipate from the membrane substrate interface.

5. Let the sample dry on a hotplate at 80 °C overnight. Cover with a clean glass container and leave a note so it is not disturbed.

C.4 GaP photonics process

1. Remove AZ1512 resist from GaP. An EKC resist strip (at 80 °C) followed by a DI water dip can be used for resist removal. Use a small dish of EKC (not the communal tub in the solvent bench). If the membranes are not well bonded to the substrate, they can detach from the substrate. Be very gentle, take extra care to avoid agitating the sample during processing.

2. Let the sample dry on a hotplate at 80 °C overnight. Cover with a clean glass container and leave a note so it is not disturbed.

3. Any resist residue on the sample can be cleaned in oxygen plasma (Barrel etch, 125W for 10 min).

4. Follow the instructions for HSQ spin coat and e-beam exposure detailed in Appendix.A.

5. The HSQ e-beam patterns are transferred to GaP by plasma ICP-RIE etching. Follow the instructions for GaP photonics etch in Appendix.D.1. For 220 nm thick GaP, four etch cycles (total plasma duration of 2 min) should be sufficient to punch through to the substrate.

6. SEM the etched pattern to verify the etch depth and the transferred pattern.

Appendix D

Reactive-ion-etching plasma processing

We utilize an Oxford Plasmalab-100/ICP-180 etcher for all plasma processing. It provides highly anisotropic Inductively Coupled Plasma (ICP) etching using chlorine-based etch chemistries for etching silicon, III-V semiconductors, aluminum and chrome. The following process gases available on the tool: BCl3, Cl2, H2, N2, O2, CH4, SF6, and Ar.

D.1 GaP photonics etch

The GaP etch relies on N2/Cl2/Ar gas mixture to produce smooth vertical sidewalls by deposition of a passivating layer during the etch process. Be aware that the etch rate is dependent on the geometry of the devices. Small holes can have reduced etch rates and hence require longer etch duration to punch through. Additionally, the correct DC bias is critical for achieving vertical sidewall profile. The GaP plasma etch involves a careful balance of deposition (passivation) vs sputtering (etching). A low DC bias can result in a positive taper (top is smaller than bottom, passivation dominates). On the other hand, a high DC bias can result in a negative taper (the top is slightly larger than bottom, RF sputtering is dominating). Always perform a test etch of your device pattern on bare GaP test samples before committing.

For high-Q photonic devices, the sidewall roughness has to be kept to the minimum. Hence, the recipe operates at the lowest chamber pressure (3 mT) supported by the tool.

D.1.1 Pre-etch procedure

Check coral, ensure everything is in order (tool status, gas-availability, etc.). Enable the tool in coral.

1. Verify that the ICP-Cl chiller is set to 16 C.

2. Check the base pressure of the chamber (on the pumping screen). Note this down for reference. It should be <1e-5 mbar.

3. Check that ICP-Cl gas line is set to O_2. If not, then follow tool SOP to pump out line and set to O_2.

4. Go through the initial steps in the SOP.

5. Start a 1 hr BCl_3 chamber clean on a clean Si wafer. Note down the color of plasma (it should be bright white). This is critical to performance of the GaP etch. Always run the BCl3 clean just before processing your samples (and after switch to N2 gas). Any residual oxygen in the chamber will destabilize the GaP etch plasma. BCl_3 will scavenge all available oxygen (within the process chamber and adsorbed on the chamber walls). This is followed by a Cl2 chamber conditioning for 15 min. Both steps can be performed with a single recipe 'MM-conditioning-BCl_3/Cl_2-60/15'.

6. **If the Si wafer comes out clean (no macroscopic debris)** then load a pristine Si wafer into the chamber and start the actual recipe 'Fulab GaP etch loop2'. **Note down the plasma color and DC-bias**. Run the recipe for 15 mins as chamber conditioning. The bias should be 235V during the etch, if not adjust the RF setpoint (typically 41W) and repeat.

D.1.2 Sample etch

1. The samples are attached to the carrier wafer (Si) with a tiny droplet of fomblin PFPE oil.

Parameter	Value
RF power (W)	41
ICP power (W)	60
DC bias (V)	235
Chamber Pressure (mTorr)	3
Ar flow (sccm)	6
Cl_2 flow (sccm)	1
N_2 flow (sccm)	1
Chuck temperature (°C)	16
Total duration (min)	2

Table D.1: Plasma processing parameters for photonics GaP etch

2. Run the samples. The etch rate is typically 100nm/min. Each etch cycle is 30s long. Adjust number of cycles based on GaP layer thickness and device geometry. It is usually a good ideal to slightly over-etch devices. Recipe selectivity to HSQ (SiO2) is high (¿1:100).

3. Unload sample. Load dummy Si wafer. Start 30 min Cl_2 chamber clean.

D.2 Diamond implantation etch

The samples are sandwiched between two sapphire slides held in place with a drop of Crystalbond-509 (applied as a solution in acetone) on a 100 mm sapphire carrier wafer. Take care to not have any crystalbond exposed to the plasma. The total etch duration is broken up into multiple etch cycles involving 5 min of plasma processing followed by a 3 min no plasma cooldown phase. This ensures the diamond sample is maintained near the processing temperature. The samples remain in the etcher through the entire two step process. Detailed processing notes below:

D.2.1 Before plasma etch

Before enabling the ICP-Cl tool in coral:

1. Start the fuming sulphuric diamond clean in hood-2 (wet bench area).

2. Set the ICP-Cl chiller to 10 C.

D.2.2 Pre-etch procedure

Check coral, ensure everything is in order (tool status, gas-availability, etc.). Enable the tool in coral.

1. Check the base pressure of the chamber (on the pumping screen). Note this down for reference. It should be $<$1e-5 mbar.

2. Check that ICP-Cl gas line is set to O_2. If not, then follow tool SOP to pump out line and set to O_2.

3. Go through the initial steps in the SOP.

4. Start a 30 min Cl_2 chamber clean on a clean Si wafer. Note down the color of plasma (it should be light blue).

5. **If the Si wafer comes out clean (no macroscopic debris)** then load a pristine Si wafer into the chamber and start the actual recipe 'FuLab diamond etch combo loop' with 1-step each for Ar/Cl and O_2 loops. **Note down the plasma color and DC-bias**. This should take $\sim$17 min. [Meanwhile, add KNO_3 to the diamond clean].

6. N2-blow the sapphire carrier and load into tool. Run the same 1-step process as above. Note down the plasma color. If the plasma does not strike in any of the steps, repeat this step (and recipe) again until it does.

D.2.3 Sample etch

1. Remove sample from acid and drop it into a DI water container. Close the container and clean up the acid bench.

Parameter	Ar/Cl_2	O_2
RF power (W)	240	50
ICP power (W)	320	1500
DC bias (V)	530	150
Chamber Pressure (mTorr)	9	25
Ar flow (sccm)	32	0
Cl_2 flow (sccm)	20	0
O_2 flow (sccm)	0	20
Chuck temperature (°C)	15	15
Total duration (min)	45	20

Table D.2: Plasma processing parameters for pre-implantation etch of all diamond samples.

2. In the solvent hood (lithography area), prepare a container of IPA. Transfer the sample to IPA, gently agitate and the remove and N2 blow dry. Store sample in clean gel-pack (careful not to apply pressure on sample, else it will stick to the gel and rip it out).

3. Load the diamond sample onto the carrier and start the etch recipe. The estimated runtime is 1hr 45min. Actual runtime is 2hr 15min (accounting for pumpdown time). Note down the plasma color, He flow rate, chamber pressure.

4. Wait for process to finish.

5. Unload sample. Load dummy Si wafer. Reset chiller to 18 C. Start 30 min Cl_2 chamber clean. [Also check the SOP for any additional conditioning required after O_2 etch.]

D.3 Diamond photonics etch

D.3.1 Pre-etch procedure

Check coral, ensure everything is in order (tool status, gas-availability, etc.). Enable the tool in coral.

1. Set the ICP-Cl chiller to 10 C.

2. Check the base pressure of the chamber (on the pumping screen). Note this down for reference. It should be <1e-5 mbar.

3. Check that ICP-Cl gas line is set to O_2. If not, then follow tool SOP to pump out line and set to O_2.

4. Go through the initial steps in the SOP.

5. Start a 30 min Cl_2 chamber clean on a clean Si wafer. Note down the color of plasma (it should be light blue).

6. **If the Si wafer comes out clean (no macroscopic debris)** then load a pristine Si wafer into the chamber and start the actual recipe 'NT-Diamond-Etch'. **Note down the plasma color and DC-bias**. The bias should be 65V during the etch.

D.3.2 Sample etch

1. The diamond samples are attached to the carrier wafer (SiNx) with a tiny droplet of fomblin PFPE oil.

2. Run the samples using original recipe time.

3. Unload sample. Load dummy Si wafer. Reset chiller to 18 C. Start 30 min Cl_2 chamber clean. [Also check the SOP for any additional conditioning required after O_2 etch.]

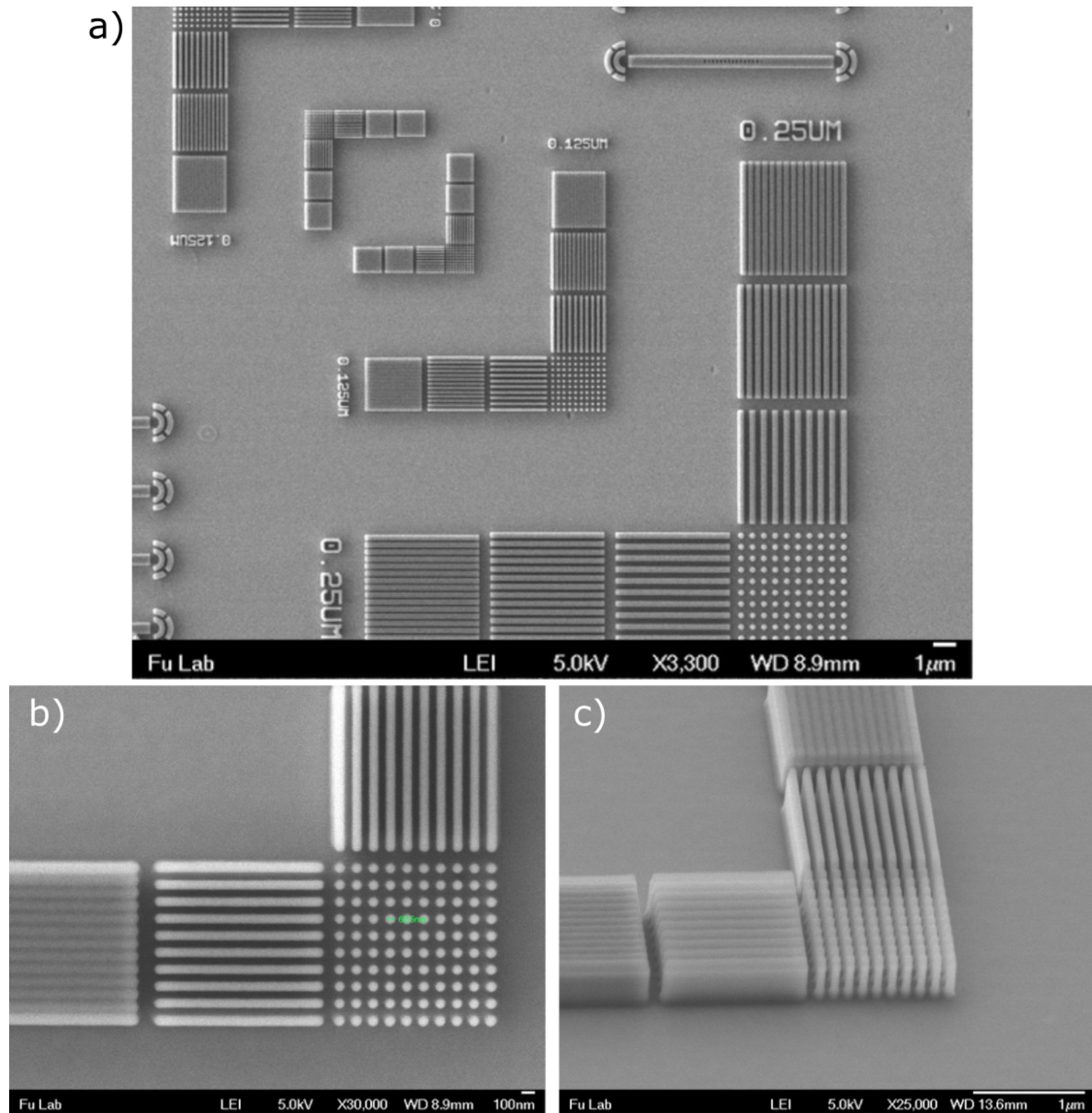

Figure D.1: a) Top down SEM view of a HSQ test pattern on GaP after plasma RIE-ICP etching with optimized parameters detailed in table.C1. The test pattern consists of arrays of ridges (1:1, 1:2 and 1:4 duty cycle) and dots (1:1 duty cycle) with feature dimensions of 62.5nm, 125nm and 250nm. b) SEM zoom-in of the 62.5nm dots, showing the etched region between has cleared. c)Angled SEM view of the 62.5nm dots (pattern transferred as cylindrical pillars) showing vertical sidewalls with high aspect-ratio.

Appendix E

AQM-HSQ processing

Applied Quantum Materials (AQM) HSQ is an alternative to Dow-Corning XR-1541 (Fox-16) HSQ e-beam negative resist. It is commercially available in dry-powder form (1 gram vials, www.aqmaterials.com) and has a long shelf life when stored in a sealed environment (i.e. vacuum jar). AQM-HSQ can be dissolved in MIBK (Methyl Iso Butyl Ketone) solvent at the required ratio to match the capabilities of Fox-16. The details of the process are provided below.

E.1 Preparing 6% solution of AQM-HSQ

This is equivalent to 6% XR-1541 (Dow-Corning)

1. Rinsed an empty poly-bottle with IPA, dry with N_2.

2. Rinse and dry (on hot plate) a beaker for mixing.

3. Measure 0.25 grams of AQM-dry HSQ into a dry beaker.

4. Added 5 ml of MIBK via a clean transfer syringe.

5. Mix by gentle agitation till there are no observable particulates ($\approx$ 5min) [avoid bubble formation].

6. Filter out the solution into the clean poly-bottle with a 0.2 µm membrane filter on a leur-lock syringe.

7. Store at 5C, and equilibrate to room temp before use.

E.2 Patterning with AQM-HSQ

Follow the same spin and bake procedure as XR-1541. The exposure dose for AQM-HSQ has been observed to be slightly higher than XR-1541. Please perform a dose test pattern exposure (consisting of 50 nm wide (100 nm pitch) 1:1 duty cycle lines) before committing to final devices.

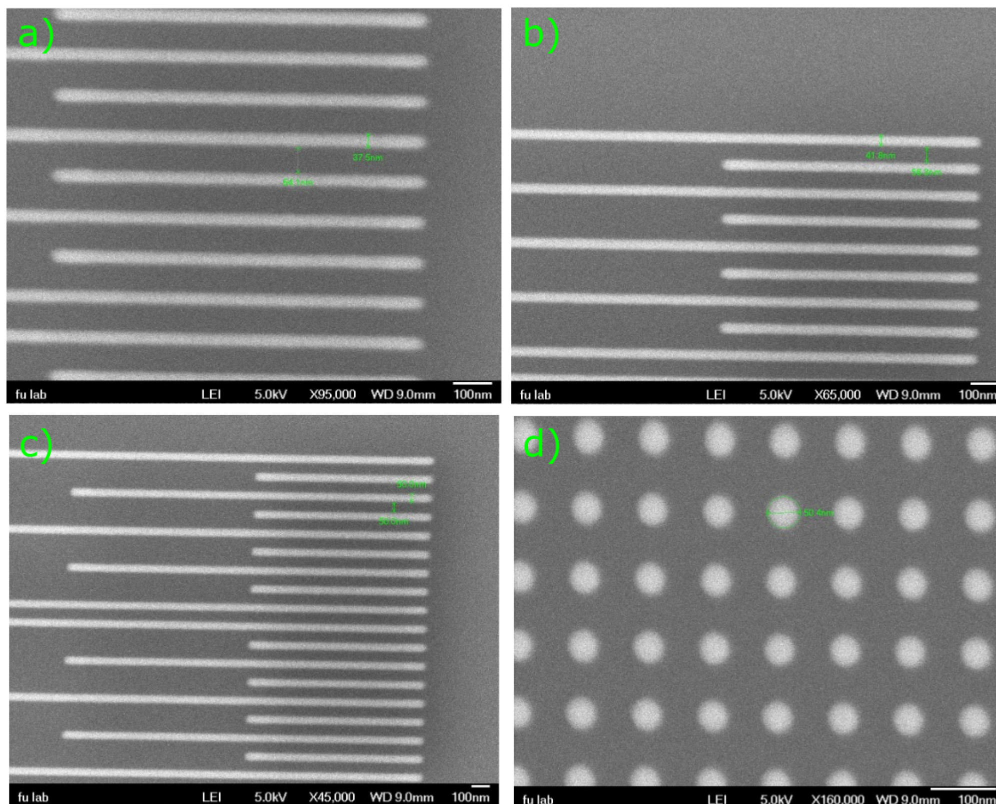

Figure E.1: a) SEM images of dose test patterns for AQM-HSQ written on a silicon substrate. Spin speed 6k rpm for 45s produced a resist layer 150 nm thick. Per standard HSQ procedure, the resist was baked at 80C for 4 min. After exposure the resist was developed in 25% TMAH for 4 min. a) Dose of 1900 μC/cm^2, underexposed lines (37.5 nm). b)Dose of 2300 μC/cm^2, underexposed lines (41.8 nm). c)Dose of 2700 μC/cm^2, accurate exposure (50 nm). Features match design. d) Dose of 2700 μC/cm^2, accurately exposed array of dots (50nm dia. 100nm pitch).

Appendix F

Annealing diamond samples

We use an old Lindberg tube furnace refitted with digital PID temperature control (Fig.F.1) for annealing diamond samples. The temperature sensor and heater coil are connected to an arduino micro-controller. The temperature control is achieved by comparing the set-point to measured temperature and modifying the duty cycle of the heater current input (MOSFET pulse-width-modulation) to match the set-point. The arduino is connected to a MATLAB GUI script (serial communication by USB) allowing programmed temperature ramps. Note that once the anneal start command has been issued to the arduino, it can operate independent of the MATLAB GUI (i.e. anneal proceeds even if the anneal-PC is turned off). The anneal can be aborted by issuing an abort command through the GUI or unplugging/resetting the arduino. The furnace and control software has been calibrated to 1200° C using an external temperature sensor placed inside the annealing tube. The temperature sensor is designed for high-temperature operation and is not accurate below 200° C. After completion of the anneal, the pressure/temperature plots and raw serial communication logs are saved in the anneal directory.

F.1 Sample preparation

1. First, we remove any macroscopic debris from the diamond sample. Wipe the diamond surface with a swab soaked in IPA. If the surface still looks visibly dirty, sonicate the sample in IPA for 10 min.

2. Now prepare a small beaker of sulphuric acid in the fume hood. Place the sample face-up in the beaker. Heat the sulphuric acid to 225° C. When it begins fuming, add KNO_3. Let the

sample soak in fuming acid for ≈1 hour.

3. Turn off the heat and allow the beaker of acid to cool down to ambient. Then remove the sample and rinse in two separate beakers of DI water and N_2 blow dry. Check the sample surface under the microscope.

F.2 Vacuum high temperature annealing

Figure F.1: The vacuum annealing setup consisting of a turbo pump directly connected to a single ended quartz tube (via KF-25 vacuum fitting). The quartz tube sits inside a tube furnace that is controlled by a computer interface.

1. Place the samples in the alumina boat face-down. We have observed that during long high temperature anneals (>1000° C; >24 hrs), a depletion region is formed near the exposed surface where no NV centers can be detected. We suspect this may be hydrogen diffusion and complexing with our defect centers. Hence, the implanted samples are placed face-down.

2. Carefully slide the boat into the quartz tube. Ensure that the sample is positioned right above the temperature sensor (Fig.F.2). Close and latch the furnace shut.

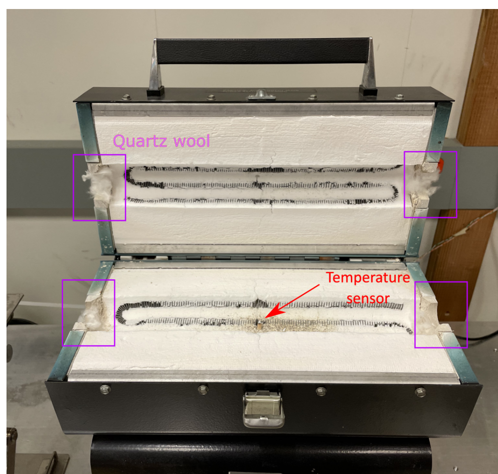

Figure F.2: Inside the tube furnace. The temperature is controlled externally (the control knob on the front panel is disconnected) by a PID algorithm. When placing the quartz tube inside the furnace, ensure the tube is supported at the ends (purple boxes) with quartz wool. The wool serves as insulation and dampens vibrations from the turbopump.

3. Connect the turbopump to the quartz tube with the KF-25 fitting (wipe all sealing surfaces with a kimwipe). Start the turbopump. The pump pressure readout should quickly go down to 1e-5mbar. If the pressure remains high, then there is a leak. Undo the vacuum seal and repeat the process.

4. Allow the turbo to pump on the tube overnight. Depending on the sample and tube condition, the pumpdown time can be longer (up to two days).

5. When the pressure has reached 5e-8 mbar. You can start annealing. All recipes are saved on the anneal-PC. Keep the temperature ramp rate to $<3^\circ$ C per minute.

6. After the anneal is done, the furnace will automatically power down. Let the furnace cool down to $<200^\circ$ C before opening.

7. Remove the boat carefully with the hooked steel rod.

8. Close the furnace and software. Clean up the work area.

F.3 Oxygen annealing

Typically the vacuum anneal is followed by a oxygen anneal. The oxygen anneal serves two purposes; (1) Selective removal of sp2 bonded carbon (graphite) from the surface and (2) Oxygen termination of the surface, stabilizing the charge state of near surface NV^- centers. We use the same furnace as before but with a different tube.

Figure F.3: The oxygen annealing setup consisting of a double ended quartz tube. One end is connected to the oxygen gas supply, whereas the other end is connected to a gas bubbler.

1. Place the samples on the alumina boat face-up. The implanted surface has to be exposed to the hot oxygen flow. We use separate boats for vacuum and oxygen annealing to prevent contamination.

2. Carefully slide the boat into the quartz tube. Ensure that the sample is positioned right above the temperature sensor (Fig.F.2). Close and latch the furnace shut.

3. Connect the narrow right end of the tube to the oxygen regulator using a 1/2" swagelok ultratorr fitting. Don't over tighten, finger tight is good enough. The narrow 1/2" quartz

input tube is very fragile.

4. Connect the left end with the KF-25 fitting to a gas bubbler (a copper tube going into a container of clean water). The bubbler allows estimation of the oxygen gas flow rate and prevents atmosphere from entering the tube.

5. Open the oxygen cylinder and adjust the regulator by observing the bubbler. A steady flow rate of 5 bubbles/sec is sufficient. Because the oxygen is exhausted into the ambient, please follow all safety protocols regarding handling of pure oxygen (no naked flame in the vicinity, etc.).

6. You can start annealing. All recipes are saved on the anneal-PC. Keep the temperature ramp rate to $<3^\circ$ C per minute.

7. After the anneal is done, the furnace will automatically power down. Turn off the oxygen cylinder. Let the furnace cool down to $<200^\circ$ C before opening.

8. Remove the boat carefully with the hooked steel rod.

9. Close the furnace and software. Clean up the work area.

F.4 Additional notes

Parts for building a new annealing tube:

```
https://technicalglass.com/product/fused_quartz_to_pyrex_graded_seal_22x25/ (Qty: 2) $93
https://technicalglass.com/product/fused_quartz_tubing_22x25/ (Qty: 1x4 ft) $37
https://www.idealvac.com/Adapter-KF-25-to-95percent-Pyrex/pp/P101975 (Qty: 1) $130
https://www.mtixtl.com/aluminacrucibleshighpurity100x20x20mmminicombustionboat-ca-l50w5h5.aspx (Qty: 1) $14
```

Appendix G

Miscellaneous process notes

G.1 E-beam charge dissipation layer

For non-conductive substrates (i.e. diamond, GaP-on-SiO_2, etc.), a significant issue with e-beam lithography is pattern distortion due to charging of the device substrate. To overcome this problem, a water soluble polymer (pss) layer is deposited on the sample followed by sputter coating a 5nm metal layer (gold + palladium). This metal layer allow dissipation of charge during e-beam exposure.

Before resist development, the metal layer can be lifted-off by rinsing the sample in water (the polymer spacer layer is dissolved). Note that for high e-beam doses (>1800 µC/cm^2) the polymer spacer layer will become cross-linked and be more resilient to liftoff. However, this does not affect the device pattern because any residual polymer is easily removed upon development (i.e. in 25%TMAH for HSQ). Briefly sonicate in DI prior to development if required.

G.1.1 Making a new batch of spacer polymer

The polymer is a dilution of PSS (poly-4-styrenesulfonic acid) 18 wt. % in H_2O, purchased from Sigma-Aldrich; part number 561223-100G).

1. Rinsed an empty poly-bottle with IPA, dry with N_2.

2. Rinse a beaker for mixing.

3. Make a 4.5% dilution of PSS in DI water. A lower dilution can be utilized for thinner polymer layers.

4. To obtain a smooth spin coat of polymer and to prevent adhesion issues, it is important to add a surfactant. Triton X-100 is a commercially available cleanroom certified surfactant suitable for this purpose (Sigma-Aldrich; part number 9036-19-05)

5. Add ≈1 ml of Triton-X for every 100 ml of 4.5% PSS solution. Take care, excess surfactant can result in residue formation during development.

6. Store the new pss+triton spacer solution at ambient away from bright light sources.

7. Dispose remaining solution after a year and make a new batch.

G.1.2 Spacer polymer application

Follow the spin-parameters and soft bake as mentioned below. This will give ∼1 µm spacer layer thickness. Then sputter 5 nm of Au-Pd (Quorum sputter coater, 1 min deposition recipe). This will allow for charge dissipation.

1. **For large samples (> 10 mm square) :**

   1 s ramp to 500 rpm, hold 1 s
   1 s ramp to 6000 rpm hold 45 s
   3 s ramp to 0 rpm

2. **For small samples (< 10 mm square) :**

   1 s ramp to 500 rpm, hold 1 s
   1 s ramp to 7500 rpm hold 45 s
   3 s ramp to 0 rpm

3. Visually inspect the coated samples for uniformity. If ok, transfer to hotplate (at 80 °C) for 4 min for the soft bake.

BIBLIOGRAPHY

[1] Marcus W. Doherty, Neil B. Manson, Paul Delaney, Fedor Jelezko, Jörg Wrachtrup, and Lloyd C.L. Hollenberg. The nitrogen-vacancy colour centre in diamond. *Physics Reports*, 528(1):1–45, July 2013.

[2] Carlo Bradac, Weibo Gao, Jacopo Forneris, Matthew E. Trusheim, and Igor Aharonovich. Quantum nanophotonics with group IV defects in diamond. *Nature Communications*, 10(1):5625, December 2019.

[3] Marina Radulaski, Matthias Widmann, Matthias Niethammer, Jingyuan Linda Zhang, Sang-Yun Lee, Torsten Rendler, Konstantinos G. Lagoudakis, Nguyen Tien Son, Erik Janzén, Takeshi Ohshima, Jörg Wrachtrup, and Jelena Vučković. Scalable Quantum Photonics with Single Color Centers in Silicon Carbide. *Nano Letters*, 17(3):1782–1786, March 2017.

[4] Kevin C Miao, Joseph P Blanton, Christopher P Anderson, Alexandre Bourassa, Alexander L Crook, Gary Wolfowicz, Hiroshi Abe, Takeshi Ohshima, and David D Awschalom. Universal coherence protection in a solid-state spin qubit. *arXiv preprint arXiv:2005.06082*, 2020.

[5] Xiayu Linpeng, Maria LK Viitaniemi, Aswin Vishnuradhan, Y Kozuka, Cameron Johnson, M Kawasaki, and Kai-Mei C Fu. Coherence properties of shallow donor qubits in zn o. *Physical Review Applied*, 10(6):064061, 2018.

[6] Tian Zhong, Jonathan M. Kindem, John G. Bartholomew, Jake Rochman, Ioana Craiciu, Evan Miyazono, Marco Bettinelli, Enrico Cavalli, Varun Verma, Sae Woo Nam, Francesco Marsili, Matthew D. Shaw, Andrew D. Beyer, and Andrei Faraon. Nanophotonic rare-earth quantum memory with optically controlled retrieval. *Science*, 357(6358):1392–1395, September 2017.

[7] Mouktik Raha, Songtao Chen, Christopher M Phenicie, Salim Ourari, Alan M Dibos, and Jeff D Thompson. Optical quantum nondemolition measurement of a single rare earth ion qubit. *Nature communications*, 11(1):1–6, 2020.

[8] H. J. Kimble. The quantum internet. *Nature*, 453:1023–1030, 2008.

[9] J. I. Cirac, P. Zoller, H. J. Kimble, and H. Mabuchi. Quantum state transfer and entanglement distribution among distant nodes in a quantum network. *Physical review letters*, 78(16):3221–3224, Apr 1997.

[10] D. Kielpinski, C. Monroe, and D. J. Wineland. Architecture for a large-scale ion-trap quantum computer. *Nature*, 417:709, 2002.

[11] Stephanie Wehner, David Elkouss, and Ronald Hanson. Quantum internet: A vision for the road ahead. *Science*, 362(6412), 2018.

[12] L. Jiang, J. S. Hodges, J. R. Maze, P. Maurer, J. M. Taylor, D. G. Cory, P. R. Hemmer, R. L. Walsworth, A. Yacoby, A. S. Zibrov, and M. D. Lukin. Repetitive readout of a single electronic spin via quantum logic with nuclear spin ancillae. *Science*, 326(5950):267–272, 2009.

[13] Hannes Bernien, Lilian Childress, Lucio Robledo, Matthew Markham, Daniel Twitchen, and Ronald Hanson. Two-Photon Quantum Interference from Separate Nitrogen Vacancy Centers in Diamond. *Physical Review Letters*, 108(4):043604, January 2012.

[14] C Monroe, R Raussendorf, A Ruthven, KR Brown, P Maunz, L-M Duan, and J Kim. Large-scale modular quantum-computer architecture with atomic memory and photonic interconnects. *Physical Review A*, 89(2):022317, 2014.

[15] Felix Borjans, XG Croot, Xiao Mi, MJ Gullans, and JR Petta. Resonant microwave-mediated interactions between distant electron spins. *Nature*, 577(7789):195–198, 2020.

[16] Anirudh Narla, Shyam Shankar, Michael Hatridge, Zaki Leghtas, Katrina M Sliwa, Evan Zalys-Geller, Shantanu O Mundhada, Wolfgang Pfaff, Luigi Frunzio, Robert J Schoelkopf, et al. Robust concurrent remote entanglement between two superconducting qubits. *Physical Review X*, 6(3):031036, 2016.

[17] Julian Hofmann, Michael Krug, Norbert Ortegel, Lea Gérard, Markus Weber, Wenjamin Rosenfeld, and Harald Weinfurter. Heralded entanglement between widely separated atoms. *Science*, 337(6090):72–75, 2012.

[18] Jan Benhelm, Gerhard Kirchmair, Christian F Roos, and Rainer Blatt. Towards fault-tolerant quantum computing with trapped ions. *Nature Physics*, 4(6):463–466, 2008.

[19] Matteo Pompili, Sophie LN Hermans, Simon Baier, Hans KC Beukers, Peter C Humphreys, Raymond N Schouten, Raymond FL Vermeulen, Marijn J Tiggelman, Laura dos Santos Martins, Bas Dirkse, et al. Realization of a multinode quantum network of remote solid-state qubits. *Science*, 372(6539):259–264, 2021.

[20] Gopalakrishnan Balasubramanian, Philipp Neumann, Daniel Twitchen, Matthew Markham, Roman Kolesov, Norikazu Mizuochi, Junichi Isoya, Jocelyn Achard, Johannes Beck, Julia Tissler, Vincent Jacques, Philip R. Hemmer, Fedor Jelezko, and Jörg Wrachtrup. Ultralong spin coherence time in isotopically engineered diamond. *Nature Materials*, 8(5):383–387, May 2009.

[21] ED Herbschleb, H Kato, Y Maruyama, T Danjo, T Makino, S Yamasaki, I Ohki, K Hayashi, H Morishita, M Fujiwara, et al. Ultra-long coherence times amongst room-temperature solid-state spins. *Nature communications*, 10(1):1–6, 2019.

[22] C. E. Bradley, J. Randall, M. H. Abobeih, R. C. Berrevoets, M. J. Degen, M. A. Bakker, M. Markham, D. J. Twitchen, and T. H. Taminiau. A ten-qubit solid-state spin register with quantum memory up to one minute. *Phys. Rev. X*, 9:031045, Sep 2019.

[23] Peter C. Humphreys, Norbert Kalb, Jaco P. J. Morits, Raymond N. Schouten, Raymond F. L. Vermeulen, Daniel J. Twitchen, Matthew Markham, and Ronald Hanson. Deterministic delivery of remote entanglement on a quantum network. *Nature*, 558(7709):268–273, June 2018.

[24] Alison Mainwood. Nitrogen and nitrogen-vacancy complexes and their formation in diamond. *Physical Review B*, 49(12):7934–7940, March 1994.

[25] J. P. Goss, P. R. Briddon, M. J. Rayson, S. J. Sque, and R. Jones. Vacancy-impurity complexes and limitations for implantation doping of diamond. *Physical Review B*, 72(3):035214, July 2005.

[26] Peter Deák, Bálint Aradi, Moloud Kaviani, Thomas Frauenheim, and Adam Gali. Formation of NV centers in diamond: A theoretical study based on calculated transitions and migration of nitrogen and vacancy related defects. *Physical Review B*, 89(7):075203, February 2014.

[27] D. Antonov, T. Häußermann, A. Aird, J. Roth, H.-R. Trebin, C. Müller, L. McGuinness, F. Jelezko, T. Yamamoto, J. Isoya, S. Pezzagna, J. Meijer, and J. Wrachtrup. Statistical investigations on nitrogen-vacancy center creation. *Applied Physics Letters*, 104(1):012105, January 2014.

[28] Felipe Fávaro de Oliveira, Denis Antonov, Ya Wang, Philipp Neumann, Seyed Ali Momenzadeh, Timo Häußermann, Alberto Pasquarelli, Andrej Denisenko, and Jörg Wrachtrup. Tailoring spin defects in diamond by lattice charging. *Nature Communications*, 8:15409, May 2017.

[29] Edward Mills Purcell. Spontaneous emission probabilities at radio frequencies. In *Confined electrons and photons*, pages 839–839. Springer, 1995.

[30] Lukas Greuter, Sebastian Starosielec, Andreas V Kuhlmann, and Richard J Warburton. Towards high-cooperativity strong coupling of a quantum dot in a tunable microcavity. *Physical Review B*, 92(4):045302, 2015.

[31] V. M. Acosta, C. Santori, A. Faraon, Z. Huang, K.-M. C. Fu, A. Stacey, D. A. Simpson, K. Ganesan, S. Tomljenovic-Hanic, A. D. Greentree, S. Prawer, and R. G. Beausoleil. Dynamic Stabilization of the Optical Resonances of Single Nitrogen-Vacancy Centers in Diamond. *Physical Review Letters*, 108(20):206401, May 2012.

[32] Ph Tamarat, N B Manson, J P Harrison, R L McMurtrie, A Nizovtsev, C Santori, R G Beausoleil, P Neumann, T Gaebel, F Jelezko, P Hemmer, and J Wrachtrup. Spin-flip and

spin-conserving optical transitions of the nitrogen-vacancy centre in diamond. *New Journal of Physics*, 10(4):045004, April 2008.

[33] A. Batalov, V. Jacques, F. Kaiser, P. Siyushev, P. Neumann, L. J. Rogers, R. L. McMurtrie, N. B. Manson, F. Jelezko, and J. Wrachtrup. Low Temperature Studies of the Excited-State Structure of Negatively Charged Nitrogen-Vacancy Color Centers in Diamond. *Physical Review Letters*, 102(19):195506, May 2009.

[34] Emma R. Schmidgall, Srivatsa Chakravarthi, Michael Gould, Ian R. Christen, Karine Hestroffer, Fariba Hatami, and Kai-Mei C. Fu. Frequency Control of Single Quantum Emitters in Integrated Photonic Circuits. *Nano Letters*, 18(2):1175–1179, February 2018.

[35] Christian Hepp, Tina Müller, Victor Waselowski, Jonas N Becker, Benjamin Pingault, Hadwig Sternschulte, Doris Steinmüller-Nethl, Adam Gali, Jeronimo R Maze, Mete Atatüre, et al. Electronic structure of the silicon vacancy color center in diamond. *Physical Review Letters*, 112(3):036405, 2014.

[36] Lachlan J Rogers, Kay D Jahnke, Marcus W Doherty, Andreas Dietrich, Liam P McGuinness, Christoph Müller, Tokuyuki Teraji, Hitoshi Sumiya, Junichi Isoya, Neil B Manson, et al. Electronic structure of the negatively charged silicon-vacancy center in diamond. *Physical Review B*, 89(23):235101, 2014.

[37] Lachlan J Rogers, Kay D Jahnke, Mathias H Metsch, Alp Sipahigil, Jan M Binder, Tokuyuki Teraji, Hitoshi Sumiya, Junichi Isoya, Mikhail D Lukin, Philip Hemmer, et al. All-optical initialization, readout, and coherent preparation of single silicon-vacancy spins in diamond. *Physical review letters*, 113(26):263602, 2014.

[38] Kay D Jahnke, Alp Sipahigil, Jan M Binder, Marcus W Doherty, Mathias Metsch, Lachlan J Rogers, Neil B Manson, Mikhail D Lukin, and Fedor Jelezko. Electron–phonon processes of the silicon-vacancy centre in diamond. *New Journal of Physics*, 17(4):043011, 2015.

[39] Benjamin Pingault, Jonas N. Becker, Carsten H. H. Schulte, Carsten Arend, Christian Hepp, Tillmann Godde, Alexander I. Tartakovskii, Matthew Markham, Christoph Becher, and Mete Atature. All-optical formation of coherent dark states of silicon-vacancy spins in diamond. *Phys. Rev. Lett.*, 113:263601, 2014.

[40] Denis D Sukachev, Alp Sipahigil, Christian T Nguyen, Mihir K Bhaskar, Ruffin E Evans, Fedor Jelezko, and Mikhail D Lukin. Silicon-vacancy spin qubit in diamond: a quantum memory exceeding 10 ms with single-shot state readout. *Physical review letters*, 119(22):223602, 2017.

[41] Ph Tamarat, T Gaebel, JR Rabeau, M Khan, AD Greentree, H Wilson, LCL Hollenberg, S Prawer, P Hemmer, F Jelezko, et al. Stark shift control of single optical centers in diamond. *Physical review letters*, 97(8):083002, 2006.

[42] L. C. Bassett, F. J. Heremans, C. G. Yale, B. B. Buckley, and D. D. Awschalom. Electrical tuning of single nitrogen-vacancy center optical transitions enhanced by photoinduced fields. *Phys. Rev. Lett.*, 107:266403, 2011.

[43] Toyofumi Ishikawa, Kai-Mei C. Fu, Charles Santori, Victor M. Acosta, Raymond G. Beausoleil, Hideyuki Watanabe, Shinichi Shikata, and Kohei M. Itoh. Optical and spin coherence properties of nitrogen-vacancy centers pace in a 100 nm thic isotopically purified diamond layer. *Nano Lett.*, 12:2083, 2012.

[44] K.-M. C. Fu, C. Santori, P. E. Barclay, and R. G. Beausoleil. Conversion of neutral nitrogen-vacancy centers to negatively charged nitrogen-vacancy centers through selective oxidation. *Applied Physics Letters*, 96(12):121907, March 2010.

[45] Nabeel Aslam, Gerhald Waldherr, Philipp Neumann, Fedor Jelezko, and Joerg Wrachtrup. Photo-induced ionization dynamics of the nitrogen vacancy defect in diamond investigated by single-shot charge state detection. *New Journal of Physics*, 15(1):013064, 2013.

[46] M. L. Goldman, M. W. Doherty, A. Sipahigil, N. Y. Yao, S. D. Bennett, N. B. Manson, A. Kubanek, and M. D. Lukin. State-selective intersystem crossing in nitrogen-vacancy centers. *Physical Review B*, 91(16):165201, April 2015.

[47] Mohammad Jamali, Ilja Gerhardt, Mohammad Rezai, Karsten Frenner, Helmut Fedder, and Jörg Wrachtrup. Microscopic diamond solid-immersion-lenses fabricated around single defect centers by focused ion beam milling. *Review of Scientific Instruments*, 85(12):123703, December 2014.

[48] S. Ali Momenzadeh, Rainer J. Stöhr, Felipe Favaro de Oliveira, Andreas Brunner, Andrej Denisenko, Sen Yang, Friedemann Reinhard, and Jörg Wrachtrup. Nanoengineered Diamond Waveguide as a Robust Bright Platform for Nanomagnetometry Using Shallow Nitrogen Vacancy Centers. *Nano Letters*, 15(1):165–169, January 2015.

[49] Luozhou Li, Tim Schröder, Edward H. Chen, Michael Walsh, Igal Bayn, Jordan Goldstein, Ophir Gaathon, Matthew E. Trusheim, Ming Lu, Jacob Mower, Mircea Cotlet, Matthew L. Markham, Daniel J. Twitchen, and Dirk Englund. Coherent spin control of a nanocavity-enhanced qubit in diamond. *Nature Communications*, 6(1):6173, May 2015.

[50] C Santori, P E Barclay, K-M C Fu, R G Beausoleil, S Spillane, and M Fisch. Nanophotonics for quantum optics using nitrogen-vacancy centers in diamond. *Nanotechnology*, 21(27):274008, July 2010.

[51] Michael Gould, Emma R. Schmidgall, Shabnam Dadgostar, Fariba Hatami, and Kai-Mei C. Fu. Efficient Extraction of Zero-Phonon-Line Photons from Single Nitrogen-Vacancy Centers in an Integrated GaP-on-Diamond Platform. *Physical Review Applied*, 6(1):011001, July 2016.

[52] Jason M Smith, Simon A Meynell, Ania C Bleszynski Jayich, and Jan Meijer. Colour centre generation in diamond for quantum technologies. *Nanophotonics*, 8(11):1889–1906, 2019.

[53] Ruffin E Evans, Alp Sipahigil, Denis D Sukachev, Alexander S Zibrov, and Mikhail D Lukin. Narrow-linewidth homogeneous optical emitters in diamond nanostructures via silicon ion implantation. *Physical Review Applied*, 5(4):044010, 2016.

[54] Brendon C. Rose, Ding Huang, Zi-Huai Zhang, Paul Stevenson, Alexei M. Tyryshkin, Sorawis Sangtawesin, Srikanth Srinivasan, Lorne Loudin, Matthew L. Markham, Andrew M. Edmonds, Daniel J. Twitchen, Stephen A. Lyon, and Nathalie P. de Leon. Observation of an environmentally insensitive solid-state spin defect in diamond. *Science*, 361(6397):60–63, 2018.

[55] Artur Lozovoi, Gyorgy Vizkelethy, Edward Bielejec, and Carlos A Meriles. Imaging dark charge emitters in diamond via carrier-to-photon conversion. *Science advances*, 8(1):eabl9402, 2022.

[56] A. Sipahigil, K. D. Jahnke, L. J. Rogers, T. Teraji, J. Isoya, A. S. Zibrov, F. Jelezko, and M. D. Lukin. Indistinguishable Photons from Separated Silicon-Vacancy Centers in Diamond. *Physical Review Letters*, 113(11):113602, September 2014.

[57] Alp Sipahigil, Ruffin E Evans, Denis D Sukachev, Michael J Burek, Johannes Borregaard, Mihir K Bhaskar, Christian T Nguyen, Jose L Pacheco, Haig A Atikian, Charles Meuwly, et al. An integrated diamond nanophotonics platform for quantum-optical networks. *Science*, 354(6314):847–850, 2016.

[58] S. D. Barrett and P. Kok. Efficient high-fidelity quantum computation using matter qubits and linear optics. *Phys. Rev. A*, 71:060310(R), 2005.

[59] Lucio Robledo, Lilian Childress, Hannes Bernien, Bas Hensen, Paul FA Alkemade, and Ronald Hanson. High-fidelity projective read-out of a solid-state spin quantum register. *Nature*, 477(7366):574–578, 2011.

[60] S Dadgostar, EH Hussein, J Schmidtbauer, T Boeck, F Hatami, and WT Masselink. Structural properties of algap films on gap grown by gas-source molecular-beam epitaxy. *Journal of Crystal Growth*, 425:94–98, 2015.

[61] Alan D Logan, Michael Gould, Emma R Schmidgall, Karine Hestroffer, Zin Lin, Weiliang Jin, Arka Majumdar, Fariba Hatami, Alejandro W Rodriguez, and Kai-Mei C Fu. 400%/w second harmonic conversion efficiency in 14 μm-diameter gallium phosphide-on-oxide resonators. *Optics express*, 26(26):33687–33699, 2018.

[62] Alan D Logan, Shivangi Shree, Karine Hestroffer, Fariba Hatami, and Kai-Mei C Fu. Triply-resonant sum-frequency generation in 10 μm gallium phosphide photonic ring resonators. In *Frontiers in Optics*, pages FM1B–8. Optical Society of America, 2021.

[63] Katharina Schneider, Yannick Baumgartner, Simon Hönl, Pol Welter, Herwig Hahn, Dalziel J Wilson, Lukas Czornomaz, and Paul Seidler. Optomechanics with one-dimensional gallium phosphide photonic crystal cavities. *Optica*, 6(5):577–584, 2019.

[64] Simon Hönl, Youri Popoff, Daniele Caimi, Alberto Beccari, Tobias J Kippenberg, and Paul Seidler. Microwave-to-optical conversion with a gallium phosphide photonic crystal cavity. *arXiv preprint arXiv:2105.13242*, 2021.

[65] BG Mytsyk, NM Demyanyshyn, and OM Sakharuk. Elasto-optic effect anisotropy in gallium phosphide crystals. *Applied Optics*, 54(28):8546–8553, 2015.

[66] Ahmed Nabih Zaki Rashed. Best candidate materials for fast speed response and high transmission performance efficiency of acousto optic modulators. *Optical and Quantum Electronics*, 46(6):731–750, 2014.

[67] Stefano Valle and Krishna C Balram. Cryogenic operation of mems-based suspended high overtone bulk acoustic wave resonators for microwave to optical signal transduction. *arXiv preprint arXiv:2109.11838*, 2021.

[68] R. Raussendorf and H. J. Briegel. A one-way quantum computer. *Phys. Rev. Lett.*, 86:5188, 2001.

[69] Simon C Benjamin, Daniel E Browne, Joe Fitzsimons, and John J L Morton. Brokered graph-state quantum computation. *New Journal of Physics*, 8(8):141–141, August 2006.

[70] Simon C. Benjamin, Brendon W. Lovett, and Jason M. Smith. Prospects for measurement-based quantum computing with solid state spins. *Laser and Photonics Reviews*, 3:556, 2009.

[71] Tim Schröder, Sara L. Mouradian, Jiabao Zheng, Matthew E. Trusheim, Michael Walsh, Edward H. Chen, Luozhou Li, Igal Bayn, and Dirk Englund. Quantum nanophotonics in diamond. *J. Opt. Soc. Am. B*, 33:B65–B83, 2016.

[72] Andrei Faraon, Charles Santori, Zhihong Huang, Victor M. Acosta, and Raymond G. Beausoleil. Coupling of Nitrogen-Vacancy Centers to Photonic Crystal Cavities in Monocrystalline Diamond. *Physical Review Letters*, 109(3):033604, July 2012.

[73] C. Cabrillo, J. I. Cirac, P. García-Fernández, and P. Zoller. Creation of entangled states of distant atoms by interference. *Physical Review A*, 59:1025, 1999.

[74] H. Bernien, B. Hensen, W. Pfaff, G. Koolstra, M. S. Blok, L. Robledo, T. H. Taminiau, M. Markham, D. J. Twitchen, L. Childress, and R. Hanson. Heralded entanglement between solid-state qubits separated by three metres. *Nature*, 497:86 EP –, 04 2013.

[75] Paul E. Barclay, Kai-Mei C. Fu, Charles Santori, Andrei Faraon, and Raymond G. Beausoleil. Hybrid nanocavity resonant enhancement of color center emission in diamond. *Phys. Rev. X*, 1:011008, 2011.

[76] Michael Gould, Srivatsa Chakravarthi, Ian R. Christen, Nicole Thomas, Shabnam Dadgostar, Yuncheng Song, Minjoo Larry Lee, Fariba Hatami, and Kai-Mei C. Fu. Large-scale gap-on-diamond integrated photonics platform for nv center-based quantum information. *J. Opt. Soc. Am. B*, 33(3):B35–B42, Mar 2016.

[77] K.-M. C. Fu, C. Santori, P. E. Barclay, and R. G. Beausoleil. Conversion of neutral nitrogen-vacancy centers to negatively charged nitrogen-vacancy centers through selective oxidation. *Applied Physics Letters*, 96:121907, 2010.

[78] E. Yablonovitch, D.M. Hwang, T. J. Gmitter, L. T. Florez, and J. P. Harbison. Van der waals bonding of gaas epitaxial liftoff films onto arbitrary substrates. *Applied Physical Letters*, 56:2419–2421, 1990.

[79] Michale Gould, Emma R. Schmidgall, Shabnam Dadgostar, Fariba Hatami, and Kai-Mei C. Fu. Efficient extraction of zero-phonon-line photons from single nitrogen-vacancy centers in an integrated gap-on-diamond platform. *Phys. Rev. Applied*, 6:011001, 2016.

[80] V.M. Acosta, C. Santori, A. Faraon, Z. Huang, K.-M. C. Fu, A. Stacey, D.A. Simpson, K. Ganesan, S. Tomljenovic-Hanic, K. Ganesan, A.D. Greentree, S. Prawer, and R. G. Beausoleil. Dynamic stabilization of the optical resonances of single nitrogen-vacancy centers in diamond. *Phys. Rev. Lett.*, 108:206401, 2012.

[81] Yiwen Chu and Mikhail D. Lukin. Quantum optics with nitrogen-vacancy centers in diamond. *arXiv:1504.05990 [quant-ph]*, April 2015. arXiv: 1504.05990.

[82] Curtis T. Rueden, Johannes Schindelin, Mark C. Hiner, Barry E. DeZonia, Alison E. Walter, Ellen T. Arena, and Kevin W. Eliceiri. Imagej2: Imagej for the next generation of scientific image data. *BMC Bioinformatics*, 18(1):529, 2017.

[83] Johannes Schindelin, Ignacio Arganda-Carreras, Erwin Frise, Verena Kaynig, Mark Longair, Tobias Pietzsch, Stephan Preibisch, Curtis Rueden, Stephan Saalfeld, Benjamin Schmid, Jean-Yves Tinevez, Daniel James White, Volker Hartenstein, Kevin Eliceiri, Pavel Tomancak, and Albert Cardona. Fiji: an open-source platform for biological-image analysis. *Nature Methods*, 9(7):676–682, 2012.

[84] P. Siyushev, H. Pinto, M. Vörös, A. Gali, F. Jelezko, and J. Wrachtrup. Optically controlled switching of the charge state of a single nitrogen-vacancy center in diamond at cryogenic temperatures. *Phys. Rev. Lett.*, 110:167402, Apr 2013.

[85] N Aslam, G Waldherr, P Neumann, F Jelezko, and J Wrachtrup. Photo-induced ionization dynamics of the nitrogen vacancy defect in diamond investigated by single-shot charge state detection. *New Journal of Physics*, 15(1):013064, jan 2013.

[86] Scott T. Alsid, John F. Barry, Linh M. Pham, Jennifer M. Schloss, Michael F. O'Keeffe, Paola Cappellaro, and Danielle A. Braje. Photoluminescence decomposition analysis: A technique to characterize N-v creation in diamond. *Phys. Rev. Applied*, 12:044003, Oct 2019.

[87] Xiang-Dong Chen, Chang-Ling Zou, Fang-Wen Sun, and Guang-Can Guo. Optical manipulation of the charge state of nitrogen-vacancy center in diamond. *Applied Physics Letters*, 103(1):013112, 2013.

[88] A. M. Edmonds, U. F. S. D'Haenens-Johansson, R. J. Cruddace, M. E. Newton, K.-M. C. Fu, C. Santori, R. G. Beausoleil, D. J. Twitchen, and M. L. Markham. Production of oriented nitrogen-vacancy color centers in synthetic diamond. *Physical Review B*, 86(3):035201, July 2012.

[89] Robin Cruddace. *Magnetic resonance and optical studies of point defects in single crystal CVD diamond*. PhD thesis, University of Warwick, 2007.

[90] R U A Khan, B L Cann, P M Martineau, J Samartseva, J J P Freeth, S J Sibley, C B Hartland, M E Newton, H K Dhillon, and D J Twitchen. Colour-causing defects and their related optoelectronic transitions in single crystal CVD diamond. *Journal of Physics: Condensed Matter*, 25(27):275801, July 2013.

[91] Gordon Davies, Simon C. Lawson, Alan T. Collins, Alison Mainwood, and Sarah J. Sharp. Vacancy-related centers in diamond. *Physical Review B*, 46(20):13157–13170, November 1992.

[92] Christian Osterkamp, Martin Mangold, Johannes Lang, Priyadharshini Balasubramanian, Tokuyuki Teraji, Boris Naydenov, and Fedor Jelezko. Engineering preferentially-aligned nitrogen-vacancy centre ensembles in cvd grown diamond. *Scientific Reports*, 9(1):5786, 2019.

[93] D. J. Twitchen, M. E. Newton, J. M. Baker, T. R. Anthony, and W. F. Banholzer. Electron-paramagnetic-resonance measurements on the divacancy defect center $r4/w6$ in diamond. *Phys. Rev. B*, 59:12900–12910, May 1999.

[94] S. J. Breuer and P. R. Briddon. Ab initio investigation of the native defects in diamond and self-diffusion. *Phys. Rev. B*, 51:6984–6994, Mar 1995.

[95] Tobias Luhmann, Nicole Raatz, Roger John, Margarita Lesik, Jasper Rv?diger, Marc Portail, Dominik Wildanger, Felix Kleißler, Kai Nordlund, Alexander Zaitsev, Jean-François Roch, Alexandre Tallaire, Jan Meijer, and Sébastien Pezzagna. Screening and engineering of colour centres in diamond. *Journal of Physics D: Applied Physics*, 51(48):483002, oct 2018.

[96] Christian Osterkamp, Martin Mangold, Johannes Lang, Priyadharshini Balasubramanian, Tokuyuki Teraji, Boris Naydenov, and Fedor Jelezko. Engineering preferentially-aligned nitrogen-vacancy centre ensembles in CVD grown diamond. *Scientific Reports*, 9(1):5786, December 2019.

[97] Claire Glover, M. E. Newton, P. M. Martineau, Samantha Quinn, and D. J. Twitchen. Hydrogen Incorporation in Diamond: The Vacancy-Hydrogen Complex. *Physical Review Letters*, 92(13):135502, March 2004.

[98] F. Fuchs, C. Wild, K. Schwarz, W. Müller-Sebert, and P. Koidl. Hydrogen induced vibrational and electronic transitions in chemical vapor deposited diamond, identified by isotopic substitution. *Applied Physics Letters*, 66(2):177–179, January 1995.

[99] J. P. Goss, R. Jones, M. I. Heggie, C. P. Ewels, P. R. Briddon, and S. Öberg. Theory of hydrogen in diamond. *Physical Review B*, 65(11):115207, March 2002.

[100] S.P. Mehandru, Alfred B. Anderson, and John C. Angus. Hydrogen binding and diffusion in diamond. *Journal of Materials Research*, 7(03):689–695, March 1992.

[101] Simone Salustro, Francesco Silvio Gentile, Alessandro Erba, Philippe Carbonniére, Khaled E. El-Kelany, and Roberto Dovesi. The characterization of the VN x H y defects in diamond through the infrared vibrational spectrum. A quantum mechanical investigation. *Carbon*, 132:210–219, June 2018.

[102] S. Salustro, F.S. Gentile, P. D'Arco, B. Civalleri, M. Rérat, and R. Dovesi. Hydrogen atoms in the diamond vacancy defect. A quantum mechanical vibrational analysis. *Carbon*, 129:349–356, April 2018.

[103] J.-P. Tetienne, R. W. de Gille, D. A. Broadway, T. Teraji, S. E. Lillie, J. M. McCoey, N. Dontschuk, L. T. Hall, A. Stacey, D. A. Simpson, and L. C. L. Hollenberg. Spin properties of dense near-surface ensembles of nitrogen-vacancy centers in diamond. *Phys. Rev. B*, 97:085402, Feb 2018.

[104] T. Yamamoto, T. Umeda, K. Watanabe, S. Onoda, M. L. Markham, D. J. Twitchen, B. Naydenov, L. P. McGuinness, T. Teraji, S. Koizumi, F. Dolde, H. Fedder, J. Honert, J. Wrachtrup, T. Ohshima, F. Jelezko, and J. Isoya. Extending spin coherence times of diamond qubits by high-temperature annealing. *Phys. Rev. B*, 88:075206, Aug 2013.

[105] Hayato Ozawa, Hitoshi Ishiwata, Mutsuko Hatano, and Takayuki Iwasaki. Thermal stability of perfectly aligned nitrogen-vacancy centers for high sensitive magnetometers. *physica status solidi (a)*, 215(22):1800342, 2019/06/25 2018.

[106] S Pezzagna, B Naydenov, F Jelezko, J Wrachtrup, and J Meijer. Creation efficiency of nitrogen-vacancy centres in diamond. *New Journal of Physics*, 12(6):065017, June 2010.

[107] H. Pinto, R. Jones, D. W. Palmer, J. P. Goss, P. R. Briddon, and S. Öberg. On the diffusion of NV defects in diamond. *physica status solidi (a)*, 209(9):1765–1768, September 2012.

[108] Todd Karin, Scott Dunham, and Kai-Mei Fu. Alignment of the diamond nitrogen vacancy center by strain engineering. *Applied Physics Letters*, 105(5):053106, August 2014.

[109] H. Pinto, R. Jones, D. W. Palmer, J. P. Goss, P. R. Briddon, and S. Öberg. On the diffusion of nv defects in diamond. *physica status solidi (a)*, 209(9):1765–1768, 2019/06/25 2012.

[110] S. Molesky, P. Chao, W. Jin, and A. W. Rodriguez. Global T operator bounds on electromagnetic scattering: Upper bounds on far-field cross sections. *arXiv*, page 2001.11531, 2020.

[111] Sean Molesky, Zin Lin, Alexander Y. Piggott, Weiliang Jin, Jelena Vuckovic, and Alejandro W. Rodriguez. Inverse design in nanophotonics. *Nature Photonics*, 12(11):659–670, November 2018.

[112] Charles Santori, Paul E. Barclay, Kai-Mei C. Fu, and Raymond G. Beausoleil. Vertical distribution of nitrogen-vacancy centers in diamond formed by ion implantation and annealing. *Physical Review B*, 79(12):125313, March 2009.

[113] E. Yablonovitch, D. M. Hwang, T. J. Gmitter, L. T. Florez, and J. P. Harbison. Van der Waals bonding of GaAs epitaxial liftoff films onto arbitrary substrates. *Applied Physics Letters*, 56(24):2419–2421, June 1990.

[114] L. Marseglia, J. P. Hadden, A. C. Stanley-Clarke, J. P. Harrison, B. Patton, Y.-L. D. Ho, B. Naydenov, F. Jelezko, J. Meijer, P. R. Dolan, J. M. Smith, J. G. Rarity, and J. L. O'Brien. Nanofabricated solid immersion lenses registered to single emitters in diamond. *Applied Physics Letters*, 98(13):133107, March 2011.

[115] NB Manson, JP Harrison, and MJ Sellars. Nitrogen-vacancy center in diamond: Model of the electronic structure and associated dynamics. *Physical Review B*, 74(10):104303, 2006.

[116] Idan Meirzada, Y Hovav, SA Wolf, and N Bar-Gill. Negative charge enhancement of near-surface nitrogen vacancy centers by multicolor excitation. *Physical Review B*, 98(24):245411, 2018.

[117] DPL Aude Craik, P Kehayias, AS Greenspon, X Zhang, MJ Turner, JM Schloss, E Bauch, CA Hart, EL Hu, and RL Walsworth. Microwave-assisted spectroscopy technique for studying charge state in nitrogen-vacancy ensembles in diamond. *Physical Review Applied*, 14(1):014009, 2020.

[118] Hiromitsu Kato, Marco Wolfer, Christoph Schreyvogel, Michael Kunzer, Wolfgang Müller-Sebert, Harald Obloh, Satoshi Yamasaki, and Christoph Nebel. Tunable light emission from nitrogen-vacancy centers in single crystal diamond PIN diodes. *Applied Physics Letters*, 102(15):151101, April 2013.

[119] P. Siyushev, H. Pinto, M. Vörös, A. Gali, F. Jelezko, and J. Wrachtrup. Optically Controlled Switching of the Charge State of a Single Nitrogen-Vacancy Center in Diamond at Cryogenic Temperatures. *Physical Review Letters*, 110(16):167402, April 2013.

[120] Sebastian Knauer, John P. Hadden, and John G. Rarity. In-situ measurements of fabrication induced strain in diamond photonic-structures using intrinsic colour centres. *npj Quantum Information*, 6(1):50, December 2020.

[121] Hiroki Takesue. Erasing distinguishability using quantum frequency up-conversion. *Phys. Rev. Lett.*, 101:173901, Oct 2008.

[122] Linran Fan, Chang-Ling Zou, Menno Poot, Risheng Cheng, Xiang Guo, Xu Han, and Hong X. Tang. Integrated optomechanical single-photon frequency shifter. *Nature Photonics*, 10(12):766–770, 2016.

[123] C. J. Widmann, C. Giese, M. Wolfer, S. Kono, and C. E. Nebel. F- and Cl-terminations of (100)-oriented single crystalline diamond. *physica status solidi (a)*, 211(10):2328–2332, 2014. _eprint: https://onlinelibrary.wiley.com/doi/pdf/10.1002/pssa.201431188.

[124] Y. Tao, J. M. Boss, B. A. Moores, and C. L. Degen. Single-crystal diamond nanomechanical resonators with quality factors exceeding one million. *Nature Communications*, 5(1):3638, May 2014.

[125] Hayate Yamano, Sora Kawai, Kanami Kato, Taisuke Kageura, Masafumi Inaba, Takuma Okada, Itaru Higashimata, Moriyoshi Haruyama, Takashi Tanii, Keisuke Yamada, Shinobu Onoda, Wataru Kada, Osamu Hanaizumi, Tokuyuki Teraji, Junichi Isoya, and Hiroshi Kawarada. Charge state stabilization of shallow nitrogen vacancy centers in diamond by oxygen surface modification. *Japanese Journal of Applied Physics*, 56(4S):04CK08, April 2017.

[126] A. M. Dibos, M. Raha, C. M. Phenicie, and J. D. Thompson. Atomic Source of Single Photons in the Telecom Band. *Physical Review Letters*, 120(24):243601, June 2018.

[127] J. P. Hadden, J. P. Harrison, A. C. Stanley-Clarke, L. Marseglia, Y.-L. D. Ho, B. R. Patton, J. L. O'Brien, and J. G. Rarity. Strongly enhanced photon collection from diamond defect centres under micro-fabricated integrated solid immersion lenses. *Applied Physics Letters*, 97(24):241901, December 2010. arXiv: 1006.2093.

[128] Thomas M. Babinec, Birgit J. M. Hausmann, Mughees Khan, Yinan Zhang, Jeronimo R. Maze, Philip R. Hemmer, and Marko Loncar. A diamond nanowire single-photon source. *Nature Nanotechnology; London*, 5(3):195–9, March 2010. Num Pages: 5 Place: London, United States, London Publisher: Nature Publishing Group.

[129] Luozhou Li, Edward H. Chen, Jiabao Zheng, Sara L. Mouradian, Florian Dolde, Tim Schröder, Sinan Karaveli, Matthew L. Markham, Daniel J. Twitchen, and Dirk Englund. Efficient Photon Collection from a Nitrogen Vacancy Center in a Circular Bullseye Grating. *Nano Letters*, 15(3):1493–1497, March 2015.

[130] Tzu-Yung Huang, Richard R. Grote, Sander A. Mann, David A. Hopper, Annemarie L. Exarhos, Gerald G. Lopez, Garrett R. Kaighn, Erik C. Garnett, and Lee C. Bassett. A monolithic immersion metalens for imaging solid-state quantum emitters. *Nature Communications*, 10(1):2392, June 2019. Number: 1 Publisher: Nature Publishing Group.

[131] Noel H. Wan, Brendan J. Shields, Donggyu Kim, Sara Mouradian, Benjamin Lienhard, Michael Walsh, Hassaram Bakhru, Tim Schröder, and Dirk Englund. Efficient Extraction of Light from a Nitrogen-Vacancy Center in a Diamond Parabolic Reflector. *Nano Letters*, 18(5):2787–2793, May 2018.

[132] Amir Karamlou, Matthew E. Trusheim, and Dirk Englund. Metal-dielectric antennas for efficient photon collection from diamond color centers. *Optics Express*, 26(3):3341, February 2018.

[133] Jennifer T. Choy, Birgit J. M. Hausmann, Thomas M. Babinec, Irfan Bulu, Mughees Khan, Patrick Maletinsky, Amir Yacoby, and Marko Loncar. Enhanced single-photon emission from a diamond-silver aperture. *Nature Photonics; London*, 5:738–743, December 2011. Num Pages: 6 Place: London, United States, London Publisher: Nature Publishing Group.

[134] Nitzan Livneh, Moshe G. Harats, Daniel Istrati, Hagai S. Eisenberg, and Ronen Rapaport. Highly Directional Room-Temperature Single Photon Device. *Nano Letters*, 16(4):2527–2532, April 2016. Publisher: American Chemical Society.

[135] Sebastian K. H. Andersen, Simeon Bogdanov, Oksana Makarova, Yi Xuan, Mikhail Y. Shalaginov, Alexandra Boltasseva, Sergey I. Bozhevolnyi, and Vladimir M. Shalaev. Hybrid Plasmonic Bullseye Antennas for Efficient Photon Collection. *ACS Photonics*, 5(3):692–698, March 2018.

[136] F. Jelezko and J. Wrachtrup. Single defect centres in diamond: A review. *physica status solidi (a)*, 203(13):3207–3225, 2006.

[137] M. H. Abobeih, J. Cramer, M. A. Bakker, N. Kalb, M. Markham, D. J. Twitchen, and T. H. Taminiau. One-second coherence for a single electron spin coupled to a multi-qubit nuclear-spin environment. *Nature Communications*, 9(1):2552, December 2018.

[138] H Jeff Kimble. The quantum internet. *Nature*, 453(7198):1023–1030, 2008.

[139] C. E. Bradley, J. Randall, M. H. Abobeih, R. C. Berrevoets, M. J. Degen, M. A. Bakker, M. Markham, D. J. Twitchen, and T. H. Taminiau. A Ten-Qubit Solid-State Spin Register with Quantum Memory up to One Minute. *Physical Review X*, 9(3):031045, September 2019.

[140] Norbert Kalb, Andreas A Reiserer, Peter C Humphreys, Jacob JW Bakermans, Sten J Kamerling, Naomi H Nickerson, Simon C Benjamin, Daniel J Twitchen, Matthew Markham, and Ronald Hanson. Entanglement distillation between solid-state quantum network nodes. *Science*, 356(6341):928–932, 2017.

[141] Tim Schröder, Sara L. Mouradian, Jiabao Zheng, Matthew E. Trusheim, Michael Walsh, Edward H. Chen, Luozhou Li, Igal Bayn, and Dirk Englund. Quantum nanophotonics in diamond [Invited]. *Journal of the Optical Society of America B*, 33(4):B65, April 2016.

[142] Noel H Wan, Tsung-Ju Lu, Kevin C Chen, Michael P Walsh, Matthew E Trusheim, Lorenzo De Santis, Eric A Bersin, Isaac B Harris, Sara L Mouradian, Ian R Christen, et al. Large-scale integration of artificial atoms in hybrid photonic circuits. *Nature*, 583(7815):226–231, 2020.

[143] Srivatsa Chakravarthi, Pengning Chao, Christian Pederson, Sean Molesky, Andrew Ivanov, Karine Hestroffer, Fariba Hatami, Alejandro W. Rodriguez, and Kai-Mei C. Fu. Inverse-designed photon extractors for optically addressable defect qubits. *Optica*, 7(12):1805, December 2020.

[144] S. B. van Dam, M. Walsh, M. J. Degen, E. Bersin, S. L. Mouradian, A. Galiullin, M. Ruf, M. IJspeert, T. H. Taminiau, R. Hanson, and D. R. Englund. Optical coherence of diamond nitrogen-vacancy centers formed by ion implantation and annealing. *Physical Review B*, 99(16):161203, April 2019.

[145] M Kasperczyk, JA Zuber, A Barfuss, J Kölbl, V Yurgens, S Flågan, T Jakubczyk, B Shields, RJ Warburton, and P Maletinsky. Statistically modeling optical linewidths of nitrogen vacancy centers in microstructures. *Physical Review B*, 102(7):075312, 2020.

[146] S. J. Breuer and P. R. Briddon. *Ab initio* investigation of the native defects in diamond and self-diffusion. *Physical Review B*, 51(11):6984–6994, March 1995.

[147] X J Hu, Y B Dai, R B Li, H S Shen, and X C He. The diffusion of vacancies near a diamond (001) surface. *Solid State Communications*, page 4, 2002.

[148] Y. Chu, N.P. de Leon, B.J. Shields, B. Hausmann, R. Evans, E. Togan, M. J. Burek, M. Markham, A. Stacey, A.S. Zibrov, A. Yacoby, D.J. Twitchen, M. Loncar, H. Park, P. Maletinsky, and M.D. Lukin. Coherent Optical Transitions in Implanted Nitrogen Vacancy Centers. *Nano Letters*, 14(4):1982–1986, April 2014.

[149] Maximilian Ruf, Mark IJspeert, Suzanne van Dam, Nick de Jong, Hans van den Berg, Guus Evers, and Ronald Hanson. Optically Coherent Nitrogen-Vacancy Centers in Micrometer-Thin Etched Diamond Membranes. *Nano Letters*, 19(6):3987–3992, June 2019.

[150] C.L. Lee, E. Gu, M.D. Dawson, I. Friel, and G.A. Scarsbrook. Etching and micro-optics fabrication in diamond using chlorine-based inductively-coupled plasma. *Diamond and Related Materials*, 17(7-10):1292–1296, July 2008.

[151] James F Ziegler, Matthias D Ziegler, and Jochen P Biersack. Srim–the stopping and range of ions in matter (2010). *Nuclear Instruments and Methods in Physics Research Section B: Beam Interactions with Materials and Atoms*, 268(11-12):1818–1823, 2010.

[152] J-P Tetienne, L Rondin, P Spinicelli, M Chipaux, T Debuisschert, J-F Roch, and V Jacques. Magnetic-field-dependent photodynamics of single NV defects in diamond: an application to qualitative all-optical magnetic imaging. *New Journal of Physics*, 14(10):103033, October 2012.

[153] T Yamamoto, S Onoda, T Ohshima, T Teraji, K Watanabe, S Koizumi, T Umeda, L P McGuinness, C Muller, B Naydenov, F Dolde, H Fedder, J Honert, M L Markham, D J Twitchen, J Wrachtrup, F Jelezko, and J Isoya. Isotopic identification of engineered nitrogen-vacancy spin qubits in ultrapure diamond. *PHYSICAL REVIEW B*, page 6, 2014.

[154] Charles Santori, Philippe Tamarat, Philipp Neumann, Jörg Wrachtrup, David Fattal, Raymond G. Beausoleil, James Rabeau, Paolo Olivero, Andrew D. Greentree, Steven Prawer, Fedor Jelezko, and Philip Hemmer. Coherent Population Trapping of Single Spins in Diamond under Optical Excitation. *Physical Review Letters*, 97(24):247401, December 2006.

[155] Kai-Mei C. Fu, Charles Santori, Paul E. Barclay, Lachlan J. Rogers, Neil B. Manson, and Raymond G. Beausoleil. Observation of the Dynamic Jahn-Teller Effect in the Excited States of Nitrogen-Vacancy Centers in Diamond. *Physical Review Letters*, 103(25):256404, December 2009.

[156] Ignas Lekavicius, Thein Oo, and Hailin Wang. Diamond Lamb wave spin-mechanical resonators with optically coherent nitrogen vacancy centers. *Journal of Applied Physics*, 126(21):214301, December 2019.

[157] Sorawis Sangtawesin, Bo L. Dwyer, Srikanth Srinivasan, James J. Allred, Lila V. H. Rodgers, Kristiaan De Greve, Alastair Stacey, Nikolai Dontschuk, Kane M. O'Donnell, Di Hu, D. Andrew Evans, Cherno Jaye, Daniel A. Fischer, Matthew L. Markham, Daniel J. Twitchen, Hongkun Park, Mikhail D. Lukin, and Nathalie P. de Leon. Origins of Diamond Surface Noise Probed by Correlating Single-Spin Measurements with Surface Spectroscopy. *Physical Review X*, 9(3):031052, September 2019.

[158] Gwan-Hyoung Lee, Chul-Ho Lee, Arend M Van Der Zande, Minyong Han, Xu Cui, Ghidewon Arefe, Colin Nuckolls, Tony F Heinz, James Hone, and Philip Kim. Heterostructures based on inorganic and organic van der waals systems. *Apl Materials*, 2(9):092511, 2014.

[159] Paul Seidler, Kevin Lister, Ute Drechsler, Jens Hofrichter, and Thilo Stöferle. Slotted photonic crystal nanobeam cavity with an ultrahigh quality factor-to-mode volume ratio. *Optics express*, 21(26):32468–32483, 2013.

[160] Hyeongrak Choi, Mikkel Heuck, and Dirk Englund. Self-similar nanocavity design with ultrasmall mode volume for single-photon nonlinearities. *Physical review letters*, 118(22):223605, 2017.

[161] Shuren Hu and Sharon M Weiss. Design of photonic crystal cavities for extreme light concentration. *ACS photonics*, 3(9):1647–1653, 2016.

[162] Parag B Deotare, Murray W McCutcheon, Ian W Frank, Mughees Khan, and Marko Lončar. High quality factor photonic crystal nanobeam cavities. *Applied Physics Letters*, 94(12):121106, 2009.

[163] Ruffin Eley Evans. *An integrated diamond nanophotonics platform for quantum optics*. PhD thesis, Harvard University, 2018.

[164] Janine Riedrich-Moller, Carsten Arend, Christoph Pauly, Frank Mucklich, Martin Fischer, Stefan Gsell, Matthias Schreck, and Christoph Becher. Deterministic coupling of a single silicon-vacancy color center to a photonic crystal cavity in diamond. *Nano letters*, 14(9):5281–5287, 2014.

[165] Marta Arcari, Immo Söllner, Alisa Javadi, S Lindskov Hansen, Sahand Mahmoodian, Jin Liu, Henri Thyrrestrup, Eun Hye Lee, Jin Dong Song, Søren Stobbe, et al. Near-unity coupling efficiency of a quantum emitter to a photonic crystal waveguide. *Physical review letters*, 113(9):093603, 2014.

[166] Steven G Johnson and John D Joannopoulos. Block-iterative frequency-domain methods for maxwell's equations in a planewave basis. *Optics express*, 8(3):173–190, 2001.

[167] Ardavan F Oskooi, David Roundy, Mihai Ibanescu, Peter Bermel, John D Joannopoulos, and Steven G Johnson. Meep: A flexible free-software package for electromagnetic simulations by the fdtd method. *Computer Physics Communications*, 181(3):687–702, 2010.

[168] Mouktik Raha. *A Telecom-Compatible Quantum Memory in the Solid-State: Single Erbium Ions Coupled to Silicon Nanophotonic Circuits*. PhD thesis, Princeton University, 2021.

[169] Ding Huang. *Building Quantum Network Nodes Based on Neutral Silicon Vacancy Centers in Diamond*. PhD thesis, Princeton University, 2021.

[170] Katharina Schneider, Pol Welter, Yannick Baumgartner, Herwig Hahn, Lukas Czornomaz, and Paul Seidler. Gallium phosphide-on-silicon dioxide photonic devices. *Journal of Lightwave Technology*, 36(14):2994–3002, 2018.

[171] Biswarup Guha, Felix Marsault, Fabian Cadiz, Laurence Morgenroth, Vladimir Ulin, Vladimir Berkovitz, Aristide Lemaître, Carmen Gomez, Alberto Amo, Sylvain Combrié, et al. Surface-enhanced gallium arsenide photonic resonator with quality factor of 6× 10 6. *Optica*, 4(2):218–221, 2017.

[172] Jean Wei, Joel M Murray, Jacob O Barnes, Douglas M Krein, Peter G Schunemann, and Shekhar Guha. Temperature dependent sellmeier equation for the refractive index of gap. *Optical Materials Express*, 8(2):485–490, 2018.

[173] Chong-Ki Hong, Zhe-Yu Ou, and Leonard Mandel. Measurement of subpicosecond time intervals between two photons by interference. *Physical review letters*, 59(18):2044, 1987.

[174] Lilian Childress and Ronald Hanson. Diamond nv centers for quantum computing and quantum networks. *MRS Bulletin*, 38(2):134–138, 2013.

[175] Javier Navas, Daniel Araujo, José Carlos Piñero, Antonio Sánchez-Coronilla, Eduardo Blanco, Pilar Villar, Rodrigo Alcántara, Josep Montserrat, Matthieu Florentin, David Eon, et al. Oxygen termination of homoepitaxial diamond surface by ozone and chemical methods: An experimental and theoretical perspective. *Applied Surface Science*, 433:408–418, 2018.

[176] Eliezer Oliveira, Chenxi Li, Xiang Zhang, Anand Puthirath, Mahesh R Neupane, James Weil, A Glen Birdwell, Tony Ivanov, Seoyun Kong, Tia Grey, et al. Stability of oxygenated groups on pristine and defective diamond surfaces. *arXiv preprint arXiv:2201.09690*, 2022.

[177] Robert G Ryan, Alastair Stacey, Kane M O'Donnell, Takeshi Ohshima, Brett C Johnson, Lloyd CL Hollenberg, Paul Mulvaney, and David A Simpson. Impact of surface functionalization on the quantum coherence of nitrogen-vacancy centers in nanodiamonds. *ACS applied materials & interfaces*, 10(15):13143–13149, 2018.

[178] Akira Daicho, Tatsuya Saito, Shinichiro Kurihara, Atsushi Hiraiwa, and Hiroshi Kawarada. High-reliability passivation of hydrogen-terminated diamond surface by atomic layer deposition of al2o3. *Journal of Applied Physics*, 115(22):223711, 2014.

[179] Nick S Jones and TM Stace. Photon frequency-mode matching using acousto-optic frequency beam splitters. *Physical Review A*, 73(3):033813, 2006.

[180] André Stefanov, Hugo Zbinden, Nicolas Gisin, and Antoine Suarez. Quantum entanglement with acousto-optic modulators: Two-photon beats and bell experiments with moving beam splitters. *Physical Review A*, 67(4):042115, 2003.

[181] David Levonian, Ralf Riedinger, Bartholomeus Machielse, Erik Knall, Mihir Bhaskar, Can Knaut, Rivka Bekenstein, Hongkun Park, Marko Loncar, and Mikhail Lukin. Optical entanglement of distinguishable quantum emitters. *arXiv preprint arXiv:2108.10928*, 2021.

[182] Linbo Shao, Neil Sinclair, James Leatham, Yaowen Hu, Mengjie Yu, Terry Turpin, Devon Crowe, and Marko Lončar. Integrated microwave acousto-optic frequency shifter on thin-film lithium niobate. *Optics Express*, 28(16):23728–23738, 2020.

[183] Huan Li, Qiyu Liu, and Mo Li. Electromechanical brillouin scattering in integrated planar photonics. *APL Photonics*, 4(8):080802, 2019.

[184] Carsten Schuck, Wolfram HP Pernice, and Hong X Tang. Waveguide integrated low noise nbtin nanowire single-photon detectors with milli-hz dark count rate. *Scientific reports*, 3:1893, 2013.

[185] Simone Ferrari, Oliver Kahl, Vadim Kovalyuk, Gregory N Goltsman, Alexander Korneev, and Wolfram HP Pernice. Waveguide-integrated single-and multi-photon detection at telecom wavelengths using superconducting nanowires. *Applied physics letters*, 106(15):151101, 2015.

[186] Patrik Rath, Oliver Kahl, Simone Ferrari, Fabian Sproll, Georgia Lewes-Malandrakis, Dietmar Brink, Konstantin Ilin, Michael Siegel, Christoph Nebel, and Wolfram Pernice. Superconducting single-photon detectors integrated with diamond nanophotonic circuits. *Light: Science & Applications*, 4(10):e338–e338, 2015.

[187] James D Siverns, John Hannegan, and Qudsia Quraishi. Neutral-atom wavelength-compatible 780 nm single photons from a trapped ion via quantum frequency conversion. *Physical Review Applied*, 11(1):014044, 2019.

[188] Xiyuan Lu, Qing Li, Daron A Westly, Gregory Moille, Anshuman Singh, Vikas Anant, and Kartik Srinivasan. Chip-integrated visible–telecom entangled photon pair source for quantum communication. *Nature physics*, 15(4):373–381, 2019.

[189] Prem Kumar. Quantum frequency conversion. *Optics letters*, 15(24):1476–1478, 1990.

[190] Matthias Bock, Pascal Eich, Stephan Kucera, Matthias Kreis, Andreas Lenhard, Christoph Becher, and Jürgen Eschner. High-fidelity entanglement between a trapped ion and a telecom photon via quantum frequency conversion. *Nature communications*, 9(1):1–7, 2018.

[191] Sebastian Zaske, Andreas Lenhard, Christian A. Keßler, Jan Kettler, Christian Hepp, Carsten Arend, Roland Albrecht, Wolfgang-Michael Schulz, Michael Jetter, Peter Michler, and Christoph Becher. Visible-to-telecom quantum frequency conversion of light from a single quantum emitter. *Phys. Rev. Lett.*, 109:147404, Oct 2012.

[192] Alexander W Bruch, Xianwen Liu, Xiang Guo, Joshua B Surya, Zheng Gong, Liang Zhang, Junxi Wang, Jianchang Yan, and Hong X Tang. 17 000%/w second-harmonic conversion efficiency in single-crystalline aluminum nitride microresonators. *Applied Physics Letters*, 113(13):131102, 2018.

[193] Ashutosh Rao, Kamal Abdelsalam, Tracy Sjaardema, Amirmahdi Honardoost, Guillermo F Camacho-Gonzalez, and Sasan Fathpour. Actively-monitored periodic-poling in thin-film lithium niobate photonic waveguides with ultrahigh nonlinear conversion efficiency of 4600% w- 1 cm- 2. *Optics express*, 27(18):25920–25930, 2019.

[194] Jia-Yang Chen, Zhao-Hui Ma, Yong Meng Sua, Zhan Li, Chao Tang, and Yu-Ping Huang. Ultra-efficient frequency conversion in quasi-phase-matched lithium niobate microrings. *Optica*, 6(9):1244–1245, 2019.

[195] Yuxiang Liu, Marcelo Davanço, Vladimir Aksyuk, and Kartik Srinivasan. Electromagnetically induced transparency and wideband wavelength conversion in silicon nitride microdisk optomechanical resonators. *Physical review letters*, 110(22):223603, 2013.

[196] Xiyuan Lu, Gregory Moille, Qing Li, Daron A Westly, Anshuman Singh, Ashutosh Rao, Su-Peng Yu, Travis C Briles, Scott B Papp, and Kartik Srinivasan. Efficient telecom-to-visible spectral translation through ultralow power nonlinear nanophotonics. *Nature Photonics*, 13(9):593–601, 2019.

[197] Michael Volk and Wolfgang Stolz. Determination of refractive index and direct bandgap of lattice matched bgap and (bga)(asp) materials on exact oriented silicon. *Journal of Applied Physics*, 122(23):235702, 2017.

[198] Nadir Hossain, TJC Hosea, Stephen J Sweeney, Sven Liebich, Martin Zimprich, Kerstin Volz, Bernardette Kunert, and Wolfgang Stolz. Band structure properties of novel bxga1- xp alloys for silicon integration. *Journal of Applied Physics*, 110(6):063101, 2011.

[199] S Rogowsky, M Baeumler, M Wolfer, L Kirste, R Ostendorf, J Wagner, S Liebich, W Stolz, K Volz, and B Kunert. Vibrational mode and dielectric function spectra of bgap probed by raman scattering and spectroscopic ellipsometry. *Journal of Applied Physics*, 109(5):053504, 2011.

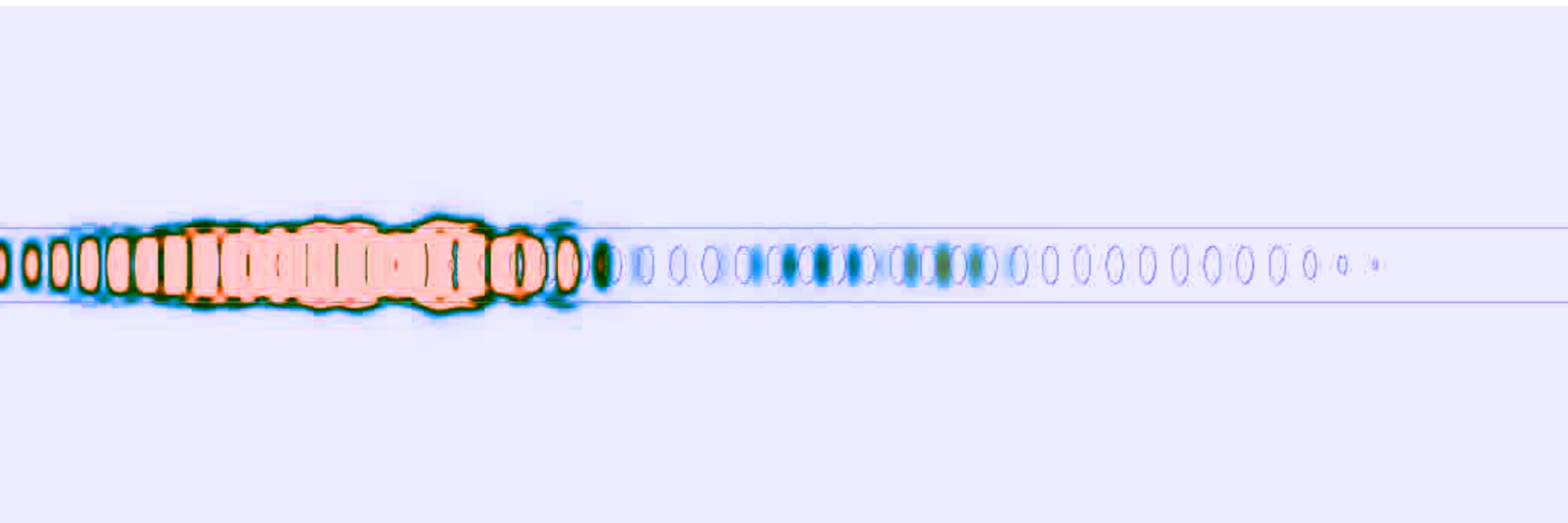

The cover images depict electromagnetic simulations of light transmission through nanophotonic devices; disk-resonators (front) and 1-D photonic crystal resonator (back).

Defects qubits in diamond (nitrogen-vacancy and silicon-vacancy) are coupled to long-lived optical modes visible within the disks and the photonic crystal resonators.

Cover design by Srivatsa Chakravarthi

UNIVERSITY *of* WASHINGTON

National Nanotechnology Coordinated Infrastructure

INSTITUTE FOR NANO-ENGINEERED SYSTEMS

NSF